Final Report

The Charles Pankow Foundation

Research Grant Agreement #05-19

Steel Coupling Beams in Low-Seismic and Wind Applications

University of Cincinnati, Cincinnati, OH

Sushil Kunwar

Bahram M. Shahrooz, PE, FACI, FASCE, FSEI

This page left blank intentionally.

Table of Contents

List of Tables

List of Figures

This page left blank intentionally.

Executive Summary

Research Overview

Coupled structural (shear) walls (CSW) are a common structural system. This system is comprised of two or more structural walls that are linked, typically, at each floor by coupling beams. Based on the expected level of inelastic deformations, composite structural (shear) walls can be classified as Composite Ordinary Shear Wall (COSW) or Composite Special Shear Wall (CSSW). One common composite system involves linking reinforced concrete wall piers by steel (or steel-concrete composite) coupling beams that are embedded in the wall piers. Design and detailing of steel coupling beam-wall connection in COSW was the focus of the research reported herein.

In the 2010 and earlier versions of AISC 341 *Seismic Provisions*, the coupling beam-wall connection was designed to develop the coupling beam's expected capacity. This provision in the 2016 version was replaced by the requirement that the connection in COSW be designed only to develop the demand from the coupling beam as calculated by linear-elastic analysis with no ductile detailing requirements. As a result, the design and detailing of the embedment region has been relaxed. This change leads to shorter embedment lengths and smaller reinforcement in the embedment region.

Analytical studies conducted at the University of Cincinnati indicated the shorter embedment length could accelerate the loss of coupling beam-wall connection integrity, leading to a reduction in the level of coupling action between the wall piers. The loss of coupling action will affect the demands in the wall piers, and their capacities could be exceeded. Moreover, inter-story and overall drifts could surpass acceptable limits. Primarily to remedy these observations, AISC 341 *Seismic Provisions* was modified in 2022 by specifying a minimum embedment length of not being less than the coupling beam's depth and requiring additional longitudinal reinforcement along the embedded region.

A coordinated experimental (consisting of two half-scale and four three-quarter beam-wall subassemblies) and analytical study was conducted to examine the current design provisions for steel coupling beams in COSW outlined in AISC 341-2022. It is important to note that the current (and previous) AISC *Seismic Provisions* for coupling beams in COSW and CSSW are solely based on experimental research focused on coupling beam-wall connection details intended to resist high seismic loads. To the best of the authors' knowledge, no experimental research had been conducted to understand the performance of COSW prior to the study presented in this report. The research data were used to evaluate the current AISC 341 *Seismic Provisions* and to develop new design and detailing provisions for COSW.

Summary and Observations

The following conclusions and observations are made:

1. The additional longitudinal reinforcement required by AISC 341-22 did not appreciably impact the connection performance in terms of the initial stiffness, stiffness degradation, dissipated energy, maximum load that could be resisted, and mode of failure.
2. Except for the specimens with embedment length/coupling beam depth ≤ 1 and the specimen with auxiliary transfer bars attached to the flanges, the other specimens did not fully develop their target nominal shear strength (V_n).
3. For the specimens without face bearing plates, which act as a bearing stiffener, the coupling beam's flange and web experienced local bending and buckling. In one specimen with face bearing plates, which failed prematurely due to excessive damage in the connection region, the flange experienced a small amount of bending within the

connection region – the bending occurred at a location that was away from the face bearing plates.

4. The applicability of current AISC Eq H4-1 for determining the required embedment length is questionable for cases with embedment length/coupling beam depth ≤ 1 because strain distribution is not linear for such cases. One of the implicit assumptions in AISC Eq H4-1 is that strain varies linearly along the embedment length. Although Eq. H4-1 underestimates the connection capacity and is conservative for cases with embedment length/coupling beam depth ≤ 1, the use of strut-and-tie models is more appropriate.

$$V_n = 1.54\sqrt{f_c'}\left(\frac{b_w}{b_f}\right)^{0.66}\beta_1 b_f L_e\left[\frac{0.58-0.22\beta_1}{0.88+\frac{g}{2L_e}}\right] \qquad \text{AISC Eq H4-1}$$

5. The auxiliary transfer bars provide a direct load path for transferring the forces in the coupling beam to the surrounding concrete. This direct load path is not offered by longitudinal reinforcement along the embedment length. The lack of a direct load path is deemed to be the main reason for the similarities of the performance of the specimens with or without the higher longitudinal reinforcement required by AISC 341-22.

6. Based on analysis of the test results, the following equation was developed for calculating the required embedment length:

$$V_n = \frac{0.19 f_c' b_f L_e}{0.56+\frac{g}{2L_e}}$$

7. The measured capacities were found to be on average within 3% of the capacities calculated by the new equation. Additional analytical studies of archetypes from several previous research indicate an excellent correlation between the capacities determined by using a detailed, mechanistic procedure and those from the new equation. Not only does the new equation closely capture the connection capacity but it is also simpler than the current equation (AISC Eq. H4-1).
8. The use of the new equation results in longer embedment lengths than the values computed from the current AISC Eq. H4-1. However, the embedment lengths are much shorter than those needed to develop the member capacity, which was required in the 2010 or earlier versions of AISC 341 *Seismic Provisions*.
9. With 95% confidence, the average value of the experimental stiffness is between 0.678 and 0.692 times the value obtained by using the effective moment of inertia calculated from AISC Eq. C-H4-1. Therefore, the coefficient of 0.6 in this equation needs to be changed to 0.4.

$$I_{eff} = 0.60I\left(1 + \frac{12\lambda EI}{g^2 G A_w}\right)^{-1} \qquad \text{Eq C-H4-1}$$

10. The archetype, which was used to select and detail the test specimens, had been designed by using the current AISC Eq. C-H4-1. By using the modified version of this equation (i.e., using 0.4 instead of 0.6), the first-floor wall piers of the archetype were found to be slightly inadequate (demand/capacity became 1.03 instead of 0.97 in the original design). Furthermore, the wind load inter-story drifts for several stories exceeded the limit of h/450, where h is the story height, but all the inter-story drifts remained below h/400.

Recommendations

In view of the results presented in this report, the following revisions to AISC 341 seismic provisions are recommended.

1. Replace the current AISC Eq. H4-1 by

$$V_n = \frac{0.19 f_c' b_f L_e}{0.56 + \frac{g}{2L_e}}$$

2. Replace the current AISC Eq. C-H4-1 by

$$I_{eff} = 0.40I\left(1 + \frac{12\lambda EI}{g^2 G A_w}\right)^{-1}$$

3. Require a bearing stiffener (“face bearing plates”) at the interface between steel coupling beams and reinforced concrete walls. This requirement may be waived if the adequacy of flanges and web against bending and buckling is ensured. Note that face bearing plates could simplify the formwork around the flanges and web.

Acknowledgements

The research presented in this report was funded by the Charles Pankow Foundation and co-funded by the American Institute of Steel Construction and the Magnusson Klemencic Associates (MKA) Foundation. These foundations are gratefully thanked for their financial support. The authors express their gratitude to Ms. Anne Ellis, former Executive Director of the Charles Pankow Foundation, who continued to support the project as the research team overcame several delays because of lab closure during the Covid pandemic and equipment problems. Mr. Ron Klemencic and Mr. Kevin Aswegan at Magnusson Klemencic Associates are acknowledged for their technical advice and informative discussions throughout the project. Dr. Devin Huber at the American Institute of Steel Construction is thanked for facilitating the fabrication of several test fixtures and taking care of their associated costs. Dr. Christopher Motter at Washington State University is thanked for discussions throughout the project. The members of AISC Task Committee 5 (Composite Design) are acknowledged for their feedbacks during various phases of the project.

Material donations and support from the following companies are gratefully acknowledged: reinforcing bars by Contractors Materials Co. (CMC) in Cincinnati, Ohio; auxiliary transfer bars and their associated hardware by LENTON in Solon, Ohio; Baker Concrete in Monroe, Ohio provided the forms for the phase one test specimens; Terracon in Cincinnati, Ohio performed many of the concrete cylinder tests. Mr. Floyd Tharpe, Mr. Garrett Tharpe, and Mr. Terry Tincher at Family Tradition in Spring Valley, Ohio helped with the fabrication of phase two test specimens; their assistance is gratefully acknowledged. Mr. Terry Tincher's endless support throughout the experimental phase is acknowledged and gratefully appreciated. Ms. Sarah Jobe of K&M industry in Spring Valley, Ohio is sincerely thanked for her help with the logistics of fabrication and delivery of the second phase test specimens.

The authors express their gratitude to Mr. TJ Brown at the University of Cincinnati Large Scale Test Facility and Mr. Curtis Fox from the Department of Aerospace Engineering at the University of Cincinnati for their technical support. The following former and current students at the University are thanked for their help with various aspects of the experimental phase of the reported research: Mr. Samuel Blesi, Dr. Sandip Chhetri, Dr. Abdullah Haroon, and Ms. Margaret Sullivan-Miller.

The authors dedicate this report to our friend and colleague Dr. Partick J. Fortney at the University of Cincinnati who unexpectedly passed away in 2019. His deep desire to understand behavior and performance of ordinary composite coupled walls was the genesis of the reported research. The proposed changes to AISC *Seismic Provisions* would not have been possible without Pat's passion to teaching, research, and practice of structural engineering.

This page left blank intentionally.

Chapter 1 Introduction and Background

1.1 Introduction

Coupled structural (shear) walls (CSW) are a common structural system. This system has become more widespread after the 9/11 attack because of its inherent redundancy and minimal impact on architectural versatility. The system consists of two or more wall piers connected by coupling (link) beams. The coupling beams allow the transfer of vertical forces between the adjacent wall piers, thus, creating a frame-like action. This action induces an axial force couple which opposes the global overturning moment from lateral forces. The coupling action provides three significant benefits. First, it decreases the moments that the individual wall piers must resist. Second, the coupling beams dissipate energy by undergoing inelastic deformations. Third, the coupled system has significantly larger stiffness than that from the individual wall piers, thereby, reducing the roof deflection and inter-story drifts.

For reinforced concrete (RC) coupling beams, special diagonal reinforcement (Figure 1.1) is necessary to prevent or reduce the likelihood of sliding failure at the beam-wall interface. The use of special diagonal reinforcement complicates the construction process and may increase the project's time and cost. The designer may also need to provide impractically deep beams because of the limited shear capacity of RC coupling beams (Harries et al., 2005). The impacts of these issues can be eliminated or reduced by replacing RC coupling beams with steel coupling beams. The resulting structural system, which uses steel beams for coupling action, is known as a Hybrid/Composite Coupled Wall System.

Based on the expected level of inelastic deformations, composite structural (shear) walls can be classified as Composite Ordinary Shear Wall (COSW) or Composite Special Shear Wall (CSSW). The design and detailing of COSW and CSSW are presented in Sections H4 and H5 of

AISC Seismic Provision 341-16 (AISC 341-16, 2016), respectively. COSW systems are used in regions with low-to-moderate seismic demands and are expected to undergo limited inelastic deformations. On the other hand, CSSW systems are used in regions with high seismic demands and are expected to undergo significant inelastic deformations. The design and detailing of the coupling beam-wall connection in COSW is the focus of this research.

In the 2010 and earlier versions of AISC 341 seismic provisions (AISC 341-10, 2010), the coupling beam-wall connection was designed to develop the coupling beam's expected capacity. This provision in the 2016 version (AISC 341-16, 2016) was removed and replaced by the requirement that the beam-wall connection in COSW be designed only to develop the demand from the coupling beam as calculated by linear-elastic analysis with no ductile detailing requirements. It is important to note that the current provisions for coupling beams in COSW and CSSW are solely based on experimental research focused on coupling beam-wall connection details intended to resist high seismic loads. There is little experimental research to support the revised provisions for COSW.

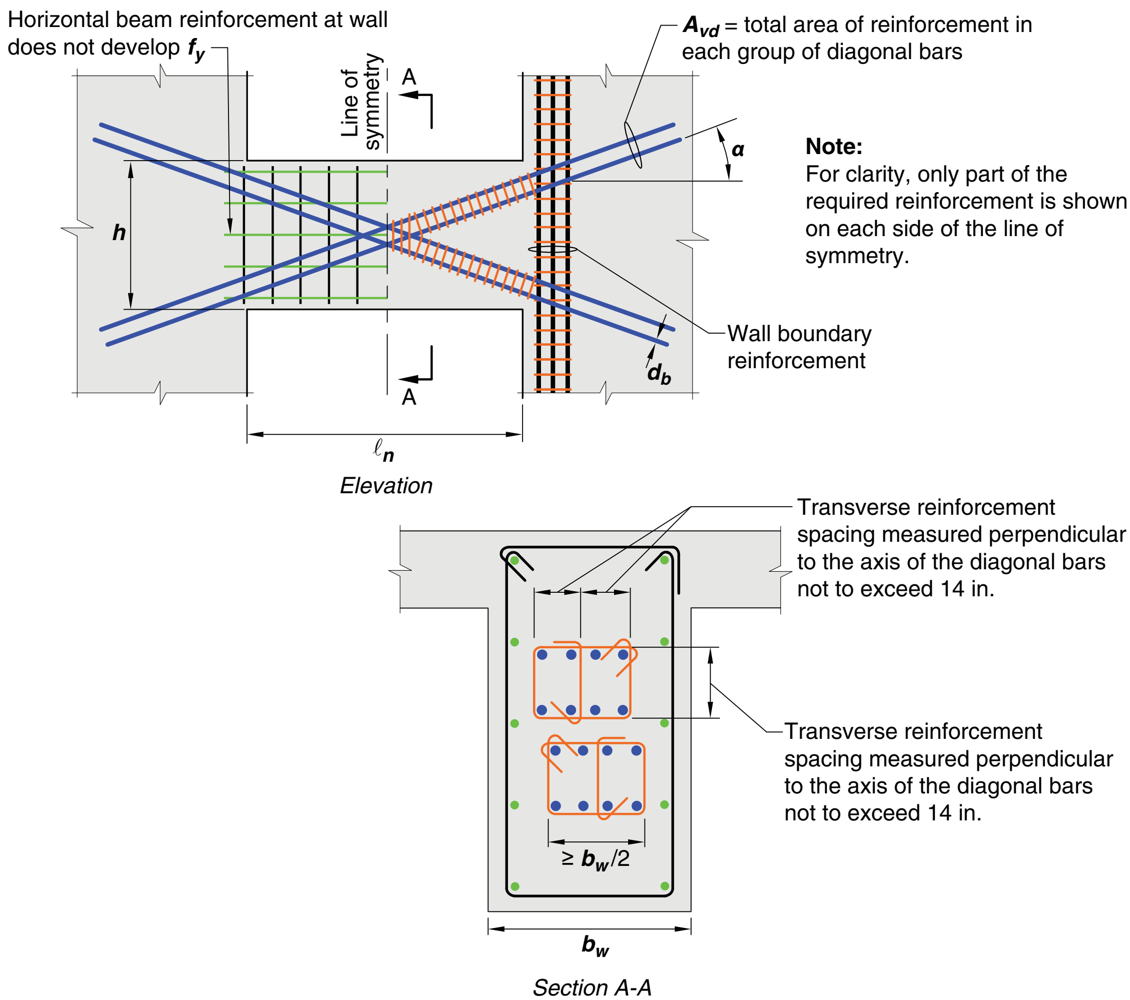

Figure 1.1 Diagonal reinforcement of reinforced concrete coupling beams (source: ACI 318-19).

1.2 Review of Past Research and Design Provisions

1.2.1 Background of coupling beam-wall connection design

The coupling beam's embedment length is calculated using an equation developed by Mattock and Gaafar (1982), which was originally formulated to find the strength of embedded steel brackets/corbels cast in precast concrete columns. The equation is based on satisfying force and moment equilibrium in the embedment region and is shown in Eq 1.1.

$$V_n = 1.54\sqrt{f_c'}\left(\frac{b_w}{b_f}\right)^{0.66}\beta_1 b_f L_e\left[\frac{0.58-0.22\beta_1}{0.88+\frac{g}{2L_e}}\right] \qquad \textbf{Eq 1.1}$$

b_f = coupling beam flange width, in.

b_w = thickness of wall pier, in.

f_c' = specified concrete compressive strength, ksi

g = coupling beam clear span, in.

L_e = embedment length, in.

$$\beta_1 = \begin{cases} 0.85 \text{ if } f_c' \leq 4 \text{ ksi} \\ 0.65 - 0.2\left(\dfrac{f_c' - 8}{4}\right) \text{ for } 4 \leq f_c' < 8 \text{ ksi} \\ 0.65 \text{ if } f_c' \geq 8 \text{ ksi} \end{cases}$$

1.2.2 AISC 341-10 vs. AISC 341-16

The provisions for coupling beams in COSW were significantly changed in 2016. These changes are discussed in this section and contrasted against those in the 2010 version of AISC 341. The impacts of these changes are illustrated through simulation studies of a 25-story prototype structure. The differences between these two provisions are discussed for (a) calculation of design force and (b) detailing of embedment region.

1.2.2.1 Design force

According to AISC 341-10, the coupling beam-wall connections are designed such that the strength is at least equal to the expected strength of the coupling beam as shown in Eq 1.2

$$V_{connection} = V_n = \frac{2R_y M_p}{g} \leq R_y V_p \qquad \textbf{Eq 1.2}$$

M_p = coupling beam plastic moment capacity
R_y = ratio of expected yield strength to specified minimum yield strength
V_p = coupling beam plastic shear capacity

In the 16th edition of AISC 341, the requirement that the connection be designed to develop the coupling beam's expected strength was changed to designing the connection for the demands from linear elastic analysis which is shown in Eq 1.3.

$$\phi V_{connection} \geq V_{elastic} \quad \textbf{Eq 1.3}$$

$\phi = 0.9$

Concrete spalling may occur at the beam-wall connection during cyclic wind or low seismic loading. The loss of concrete cover will reduce the embedment length available for transferring forces. AISC 341-10 took this effect into account, in part, by assuming the embedment length to begin inside the wall from the first wall longitudinal bar in the boundary element. In contrast, AISC 341-16 does not consider the wall spalling and assumes that the calculated embedment length begins from the face of the wall.

1.2.2.2 Embedment region detailing

Past research (Harries et al.,1997) demonstrated the need for longitudinal reinforcement in embedded regions to control gap opening at coupling beam flange-wall boundary interface under cyclic loading, which is shown schematically in Figure 1.2. AISC 341-10 specified vertical wall reinforcement over the embedment length with a nominal axial strength of at least equal to the coupling beam's expected shear strength. On the other hand, AISC 341-16 requires vertical wall reinforcement to resist the coupling beam's linear elastic shear demand. The required reinforcement (A_{st}) is computed from Eq 1.4, in which V_n is the coupling beam's expected strength based on ASIC 341-10 and is linear elastic shear demand of coupling beam according to AISC 341-16 and f_y is reinforcement yield strength.

$$f_y A_{st} \geq V_n \quad \textbf{Eq 1.4}$$

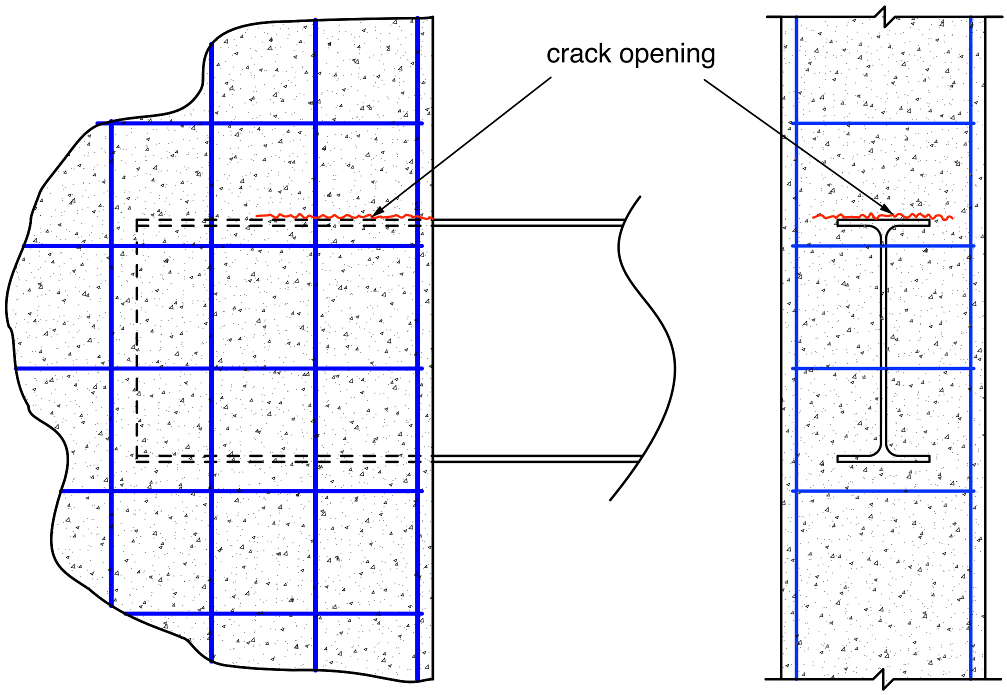

Figure 1.2 Gap opening at coupling beam-wall interface.

Both versions require distributing the longitudinal reinforcement such that two-thirds of the calculated reinforcement is within the first half of the embedment length. The reinforcement must extend at least one tension development length above and below the flanges.

1.2.2.3 Summary

The above discussions indicate that the embedment region design and detailing have been relaxed in the 2016 version of AISC 341. This change will lead to a smaller embedment length and smaller reinforcement in the embedment region. The implications of these relaxations have yet to be determined.

1.2.3 Expected impacts of changes made in AISC 341-16

In an attempt to examine the potential impacts of AISC 341-16 provisions, an analytical study of COSW was conducted by Mirza (2018). A 25-story office building located in Cincinnati (a low seismic region) was selected and designed. Due to the absence of a boundary element in the wall for an ordinary system, the embedment region can be vulnerable if the calculated embedment length is short, and connection degradation is expected to occur. Gradual degradation of connection was simulated in the ETABS (2016). For this purpose, the embedment length was progressively reduced by 1 in., 2 in., or 4 in. to model cracking at the coupling beam-wall interface. For each value, rotational springs (Figure 1.3) were calibrated such that the calculated demands match the available capacities after inducing damage. The shear and moment capacities before damage (V and M) and their counterparts after damage (V' and M') are shown in Eq 1.5.

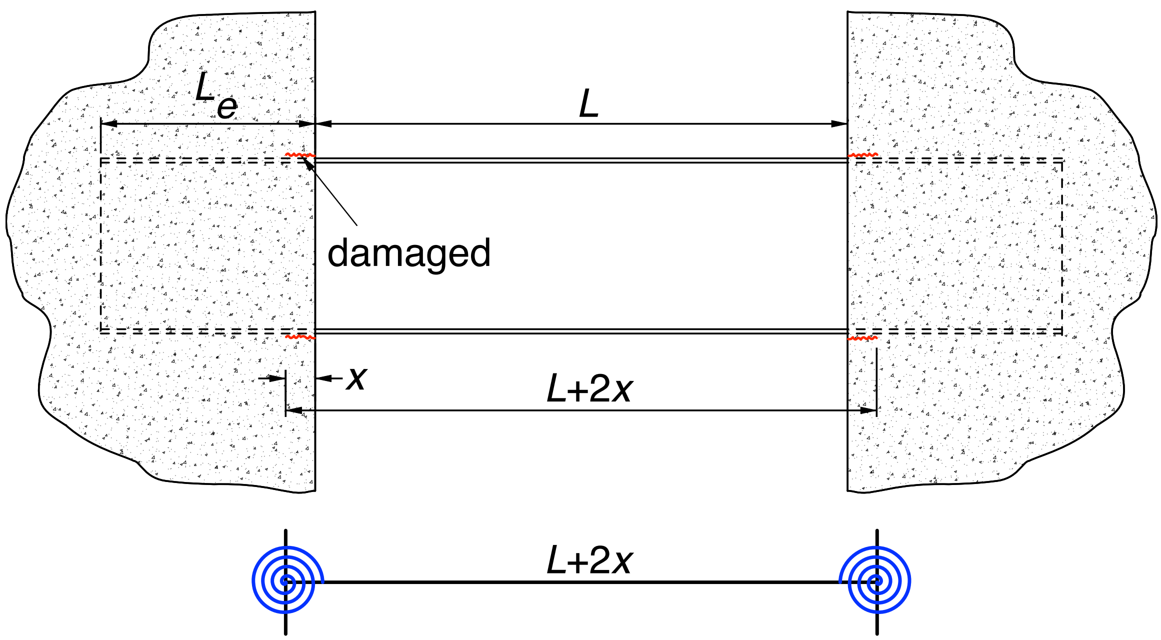

Figure 1.3 Simulation of stiffness by rotational springs.

$$V = \phi 1.54\sqrt{f_c'}\left(\frac{b_w}{b_f}\right)^{0.66}\beta_1 b_f L_e\left[\frac{0.58-0.22\beta_1}{0.88+\frac{L}{2L_e}}\right]$$

Eq 1.5

$$V' = \phi 1.54\sqrt{f_c'}\left(\frac{b_w}{b_f}\right)^{0.66}\beta_1 b_f (L_e-x)\left[\frac{0.58-0.22\beta_1}{0.88+\frac{L+2x}{2(L_e-x)}}\right]$$

$$\frac{M'}{M}=\frac{V'}{V}\left(\frac{L+2x}{L}\right)$$

As the level of damage was progressively increased the overall stiffness dropped, leading to larger inter-story drifts. As shown in Figure 1.4, the inter-story drifts in floors above the 8th floor exceeded $h/450$ (h = inter-story height) and floors above the 11th floor exceeded $h/400$ with the introduction of 2 in. of connection degradation. For 4-in. degradation, the inter-story drifts above the 3rd floor exceeded both limits. A similar trend was observed when considering lateral drifts, see Figure 1.5.

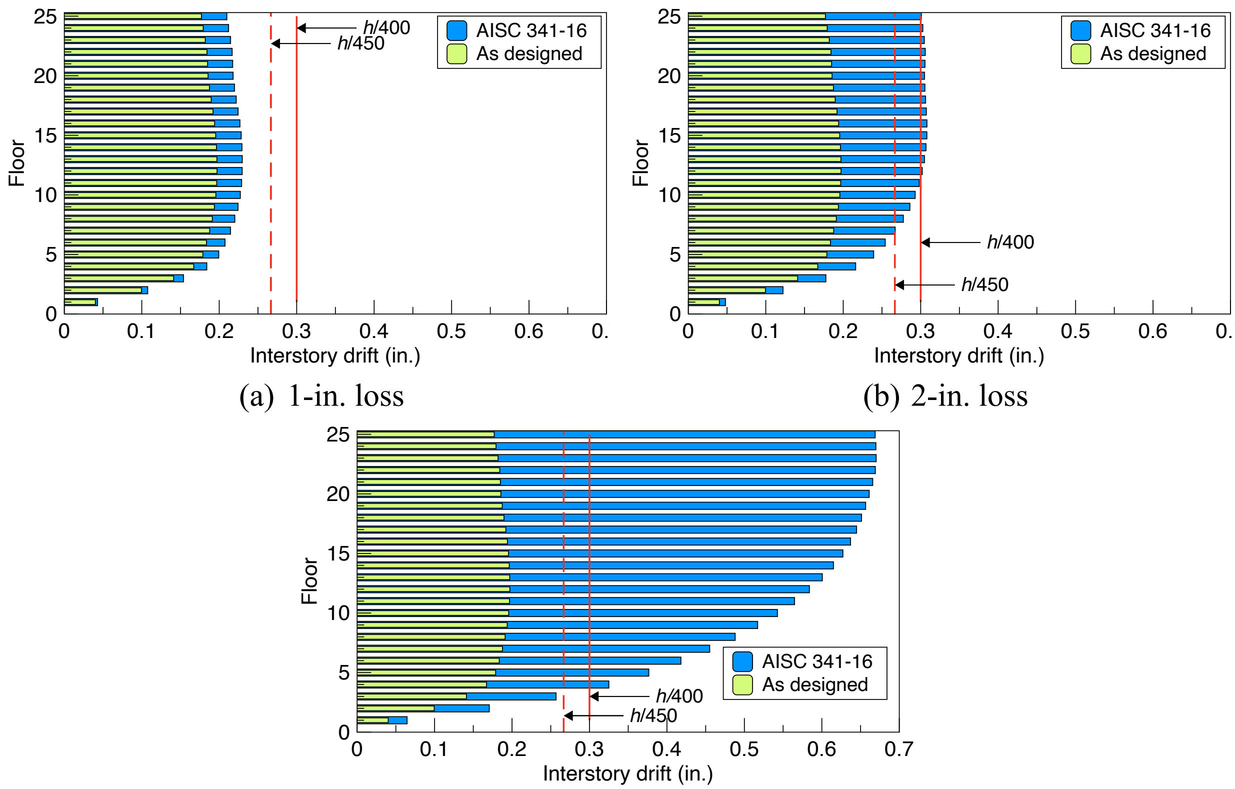

(a) 1-in. loss

(b) 2-in. loss

(c) 4-in. loss

Figure 1.4 Changes in inter-story drifts for different losses of embedment length.

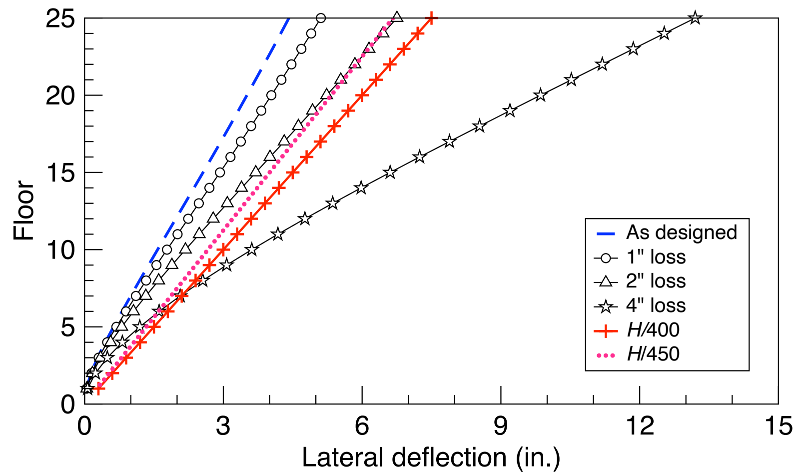

Figure 1.5 Impact of connection degradation on lateral drift.

With the loss of coupling beam-wall connection integrity, the level of coupling action was reduced. As a result, the demands in the wall piers were impacted. In general, the wall pier capacities were exceeded as the level of damage (simulated by reducing the "effective" embedment length) became larger, i.e., wall demand to capacity exceeded 1 as shown in Figure 1.6. For several locations, e.g., at floor 5, the introduction of damage lowered the wall demand to capacity ratio. This trend can be explained with reference to Figure 1.7. After accounting for loss of embedment length, the coupling action was reduced and moment in the coupled direction increased from -1394 k-ft to -5698 k-ft. At the same time, the axial tension induced by coupling action was decreased, increasing the axial load from 1460 kips to 2028 kips. As a result of these shifts, the moment demand was moved farther away from the moment contour, which reduced the demand-to-capacity ratio.

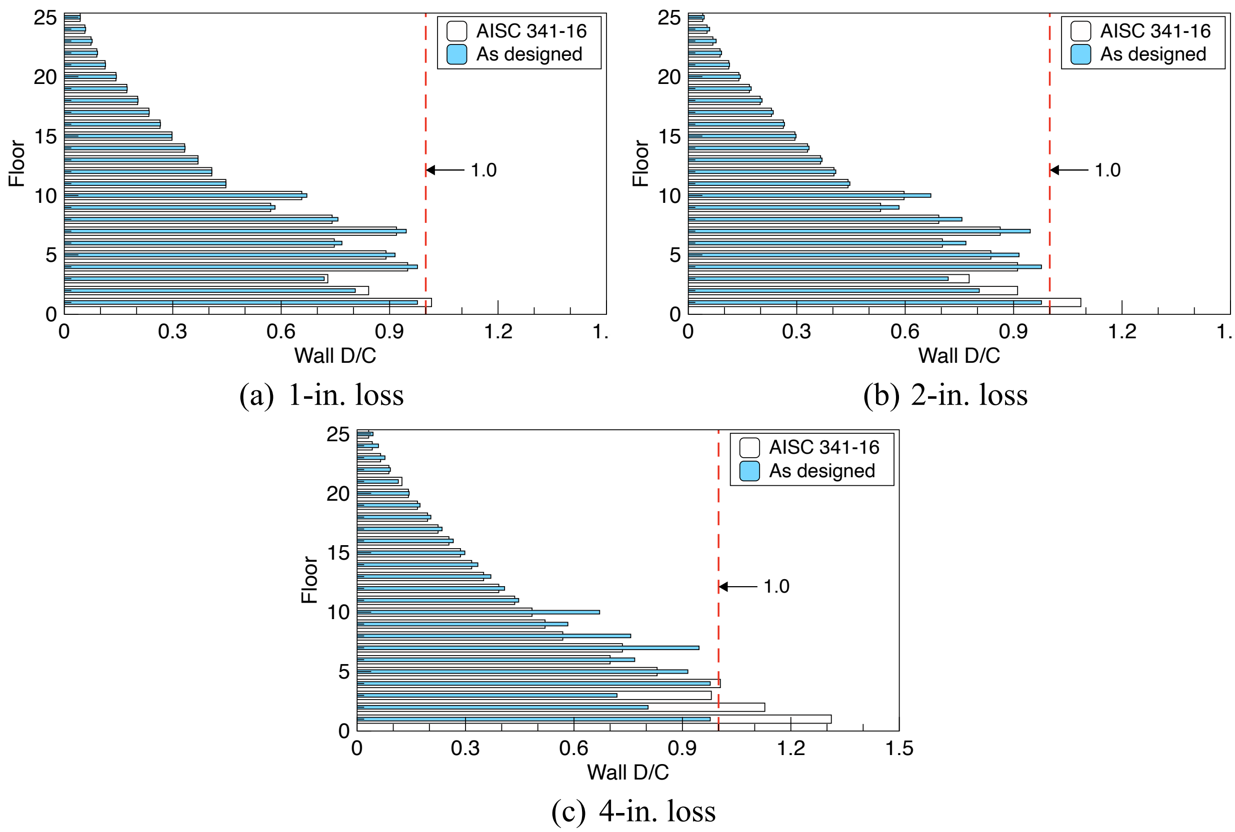

Figure 1.6 Impact of connection degradation on capacity of wall piers.

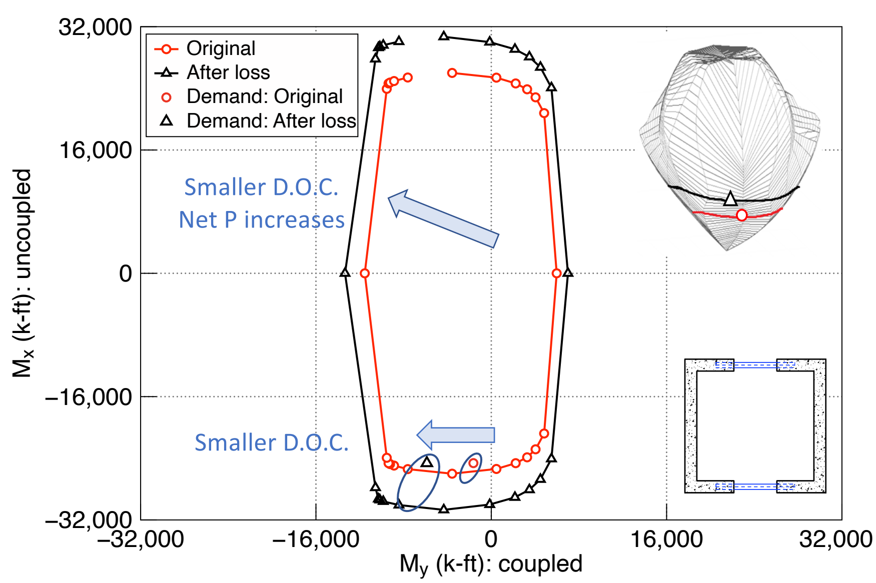

Figure 1.7 Comparison of wall pier axial load and bending moment with and without damage.

1.2.4 AISC 341-22

The elastic demands at the top and bottom stories are typically small. If connections are required to develop such low values of elastic demands (as recommended by AISC 341-16), the calculated embedment length could be unrealistically small. Driven primarily based on the results of the analyses performed by Mirza (2018), which was discussed in Section1.2.3, several changes have been proposed to remedy the potential issues observed in the simulations. The key changes are as follows:

(a) Specify a minimum embedment length equal to coupling beam depth.

(b) Revise the reinforcement needed to control gap opening, as discussed in Section 1.2.2.2. Eq 1.4 is replaced by Eq 1.6.

$$f_y A_{st} \geq C_b$$

where

A_{st} = area of reinforcement

Eq 1.6

$$C_b = \text{greater of} \left(\frac{\frac{g}{2L_e} + 0.33\beta_1}{0.88 - 0.33\beta_1} \right) V_n \quad \text{and } V_n$$

f_y = reinforcement yield strength

V_n = coupling beam elastic shear demand

1.3 Project overview and objectives

A coordinated experimental and analytical study was conducted to examine design provisions for steel coupling beams in COSW. Large-scale test specimens were selected based on a 25-story prototype structure located in Cincinnati. The test specimens consisted of two half-scale beam-wall subassemblies and four three-quarter scale beam-wall components. The experimental test data were utilized to scrutinize AISC 341-16 and AISC 341-22 design and detailing provisions for COSW with the ultimate objective of proposing revisions.

Chapter 2 Experimental Program

2.1 Introduction

As discussed in Chapter 1, the test specimens were selected based on a 25-story archetype. An overview of the design of the archetype is provided in this chapter. Additionally, the test specimen details, measured material properties, key features of the testing apparatus, and instrumentations are presented.

2.2 Selection and design of archetype

A twenty-five-story office building was selected and designed. The plan view of the archetype is shown in Figure 2.1. Cincinnati, Ohio, which is in a low seismic region, was selected as the location of the building. Two C-shaped composite ordinary shear walls (COSW) linked by steel coupling beams (two per floor) form the lateral force-resisting system. The gravity load resisting system consists of columns, spandrel beams, and post-tensioned floor slabs. Design of the archetype is discussed in Kunwar (2020).

As seen from Table 2.1, minimum reinforcement (0.25%) controlled the transverse reinforcement for all the floors except for the first three stories. Minimum reinforcement also controlled the longitudinal reinforcement for the walls above story 8. Four groups of coupling beams were selected (see Table 2.2). The maximum coupling beam shear demand (185 kips) was in story 9. Three rolled wide flange shapes were selected based on the maximum calculated shear demand in each group.

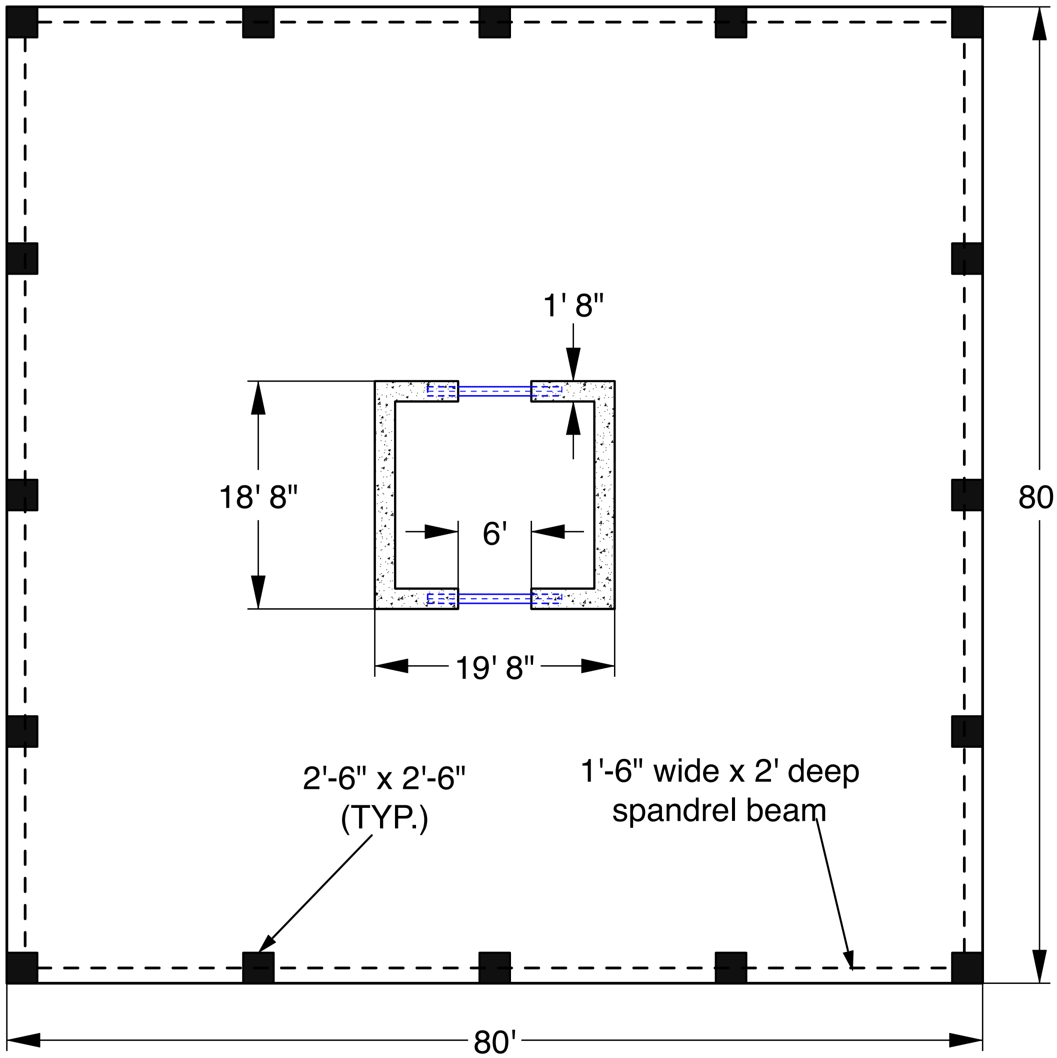

Figure 2.1 Archetype plan view.

Table 2.1 Wall reinforcement ratio.

Story	Reinforcement ratio (%)	
	Longitudinal	Transverse
1-3	0.92	0.41
4-6	0.68	0.25
7-8	0.43	0.25
9-25	0.25	0.25

Table 2.2 Summary of coupling beam demands and capacities.

Group	Story	Beam size	Maximum shear demand in a group (kips)	Beam capacity (kips)
1	1-2	W12 x 53	53	98
2	3-9	W16 x 77	185	187
3	10-16	W14 x 74	142	157
4	17-25	W12 x 53	68	98

To highlight the differences between the 2010, 2016, and 2022 versions of AISC 341 *Seismic Provisions*, the required embedment lengths and reinforcement over the embedment portion (to control gap opening) are compared in Figure 2.2a and Figure 2.2b, respectively. As expected, AISC 341-10 requires the longest embedment lengths than those from AISC 341-16 and AISC 341-22 because the embedment lengths are determined to develop the member capacity according to AISC 341-10. There is no difference between the development lengths from AISC 341-16 and AISC 341-22 except for cases that are controlled by the minimum depth requirement of AISC 341-22. The amount of reinforcement needed to control gap opening based on AISC-22 is noticeably larger than the other two versions. On average, AISC 341-22 provisions require 3.8 times and 2.1 times larger longitudinal reinforcement than AISC 341-16 and AISC 341-10, respectively.

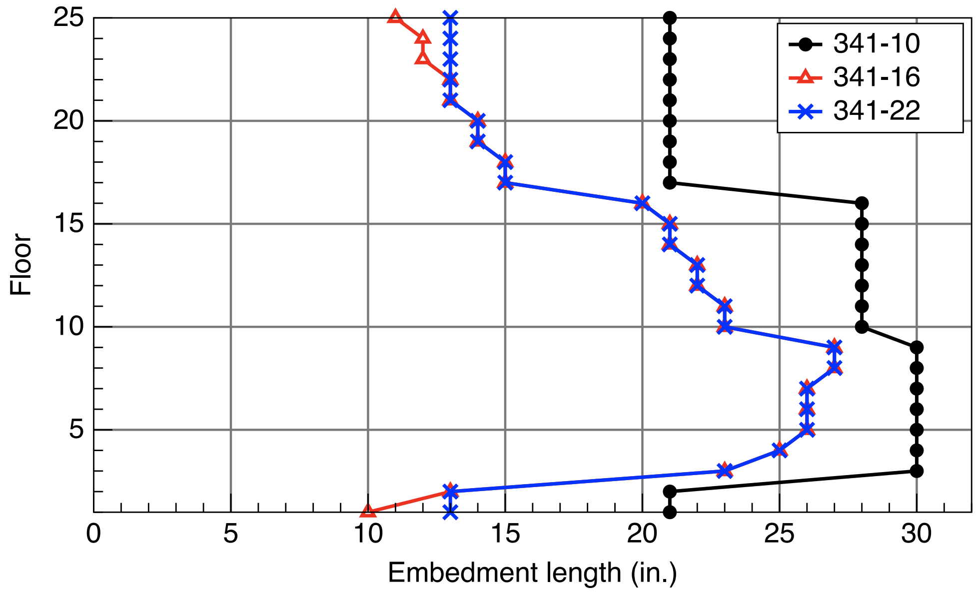

(a) Embedment length.

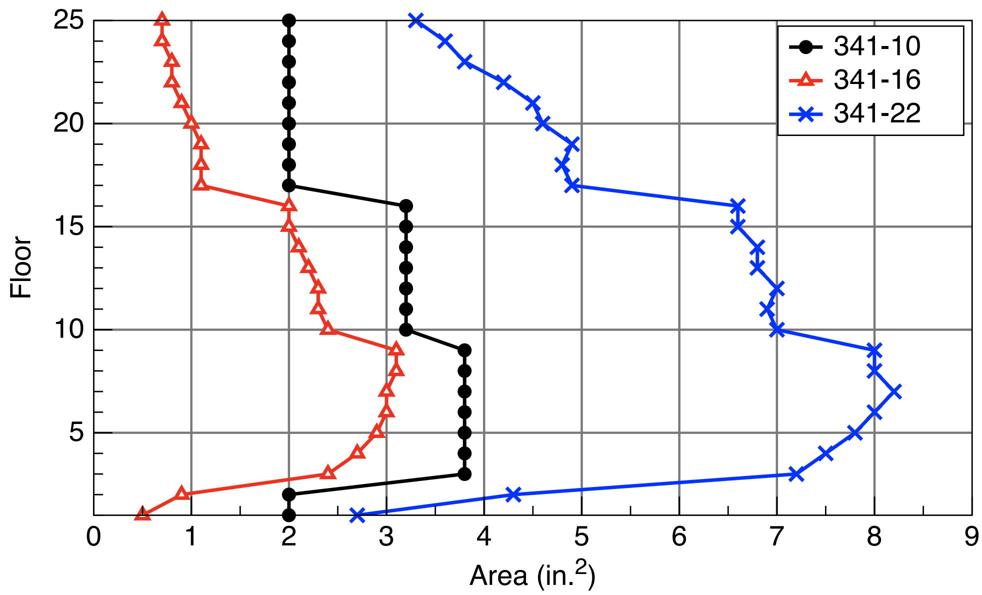

(b) Reinforcement for controlling gap opening.

Figure 2.2 Comparisons of ASIC 341-10, AISC 341-16, and AISC 341-22.

2.3 Test specimens

A total of six specimens were fabricated in two phases, two in phase 1 and four in phase 2. The specimens in both phases consisted of a portion of the wall pier and one-half of a steel coupling beam embedded in the wall pier. The specimens in phase 1 had two coupling beams, one at each end of the wall pier. One connection was designed according to AISC 341-16 and the other one based on AISC 341-22. Each coupling beam was tested separately; hence, four different tests were conducted in the first phase. Four specimens were fabricated and tested in the second phase. Therefore, the data from eight tests were obtained. There were major differences in terms of loading, scale, and overall configuration of the specimens in phase 1 and phase 2. Therefore, the specimens from the two phases are described separately.

2.3.1 Phase 1 specimens

Two half-scale specimens were tested in the first phase. Specimens 1a and 1b were selected based on the demands in the 24th story to simulate cases with short embedment lengths. Specimens 2a and 2b were based on the demands and wall details in the 9th story of the archetype because the wall at this location is governed by minimum reinforcement but coupling beam has the largest shear force. The design forces from these two floors were used to proportion the specimens. Additional details are provided in Kunwar (2020).

2.3.1.1 Wall pier

The walls in the archetype are C-shaped whereas a rectangular wall was chosen in the test specimens. The rectangular wall represents one flange of the C-shaped walls. As a result, standard similitude concepts cannot be used to determine the wall reinforcement for the half-scale test specimens. Considering that the amount of wall reinforcement is expected to influence the performance of coupling beam-wall connection, it was decided to maintain the same percentage of wall reinforcement in the test specimen and one flange of the archetype C-shaped wall. The wall thickness was taken as 10 in. to represent half-scale equivalent of the archetype wall thickness of 20 in. The other dimensions were selected based on constraints such as the spacing of tie downs of the laboratory's strong floor, dimensions of hydraulic actuators, etc. The wall geometry and reinforcement for specimens 1a and 1b and specimens 2a and 2b are shown in

Figure 2.3 and Figure 2.4, respectively. Photographs in Figure 2.5 show various stages of fabrication of the first phase specimens.

2.3.1.2 Coupling beams

The shear force in a half-scale coupling beam is equivalent to the full-scale value divided by 4. Using the scaled shear force, the coupling beams were designed and detailed according to AISC 341-16 and AISC 341-22. W8x21 (to represent story 9) and W6x16 (to represent story 24) were selected based on having adequate strength and matching as close as possible the ½-scale equivalents[1] of key cross-sectional properties of the full-scale beams as close as possible.

2.3.1.3 Embedment length and detailing

As discussed previously, each specimen has two coupling beams – one designed and detailed according to AISC 341-16 and the other one based on AISC 341-22. The details of coupling beam-wall pier connection as well as additional wall longitudinal reinforcement, if any, are summarized in Table 2.3.

Table 2.3 Phase 1 test matrix and wall-beam connection details.

Specimen ID	Test ID	Story in archetype	Governing code	Coupling beam	Embedment length (in.)	Additional reinforcement
1a	Test 1	24	341-16	W6x16	6	----
1b	Test 2	24	341-22	W6x16	7	4 No. 3
2a	Test 3	9	341-16	W8x21	13	2 No. 3
2b	Test 4	9	341-22	W8x21	13	2 No. 4 and 4 No. 5

[1] Dimensions = ½ of full-scale values, area = ¼ of full-scale area, plastic section modulus = 1/8 of full-scale value, moment of inertia = 1/16 of full-scale value

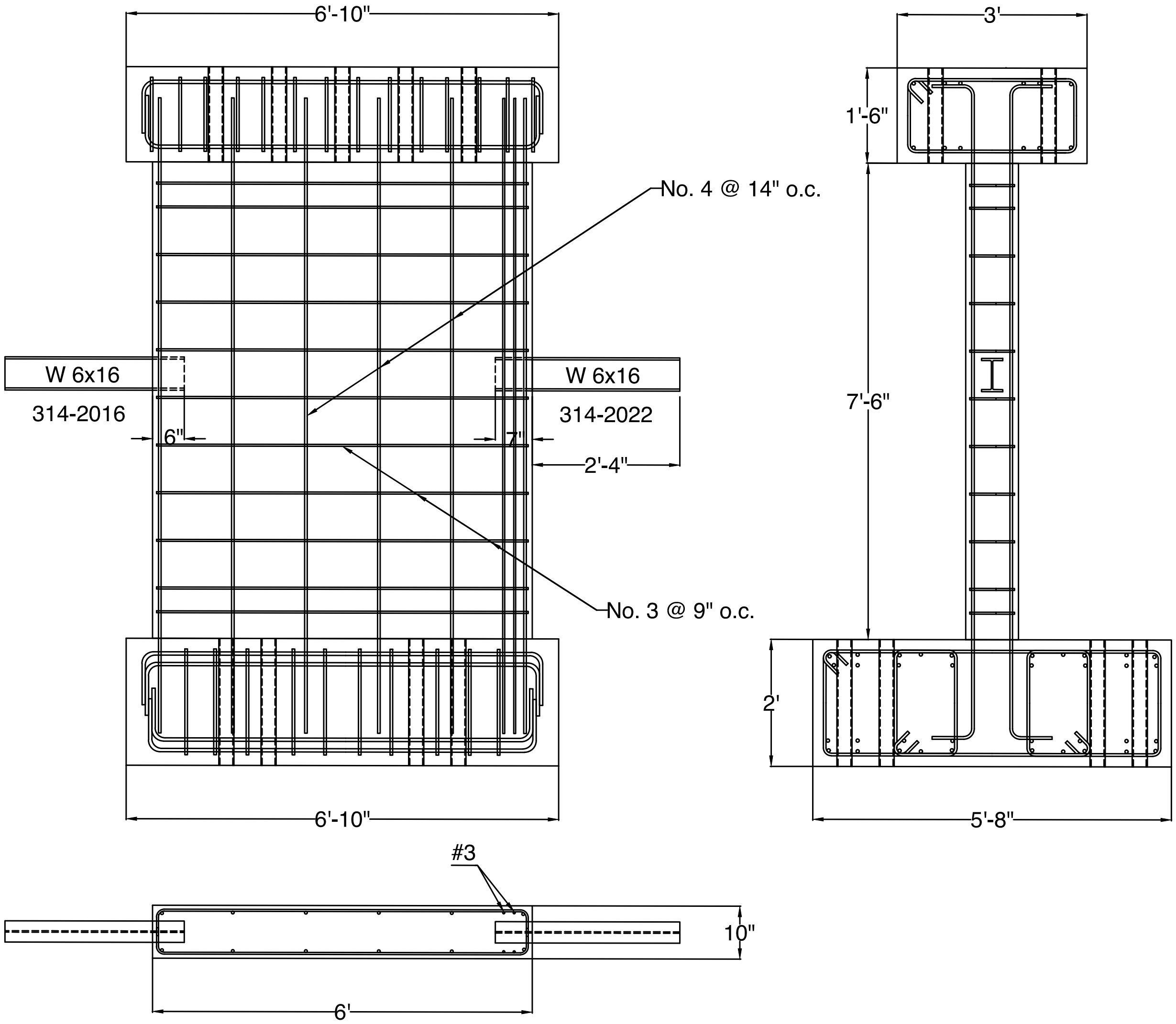

Figure 2.3 Details of specimens 1a and 1b (tests 1 and 2).

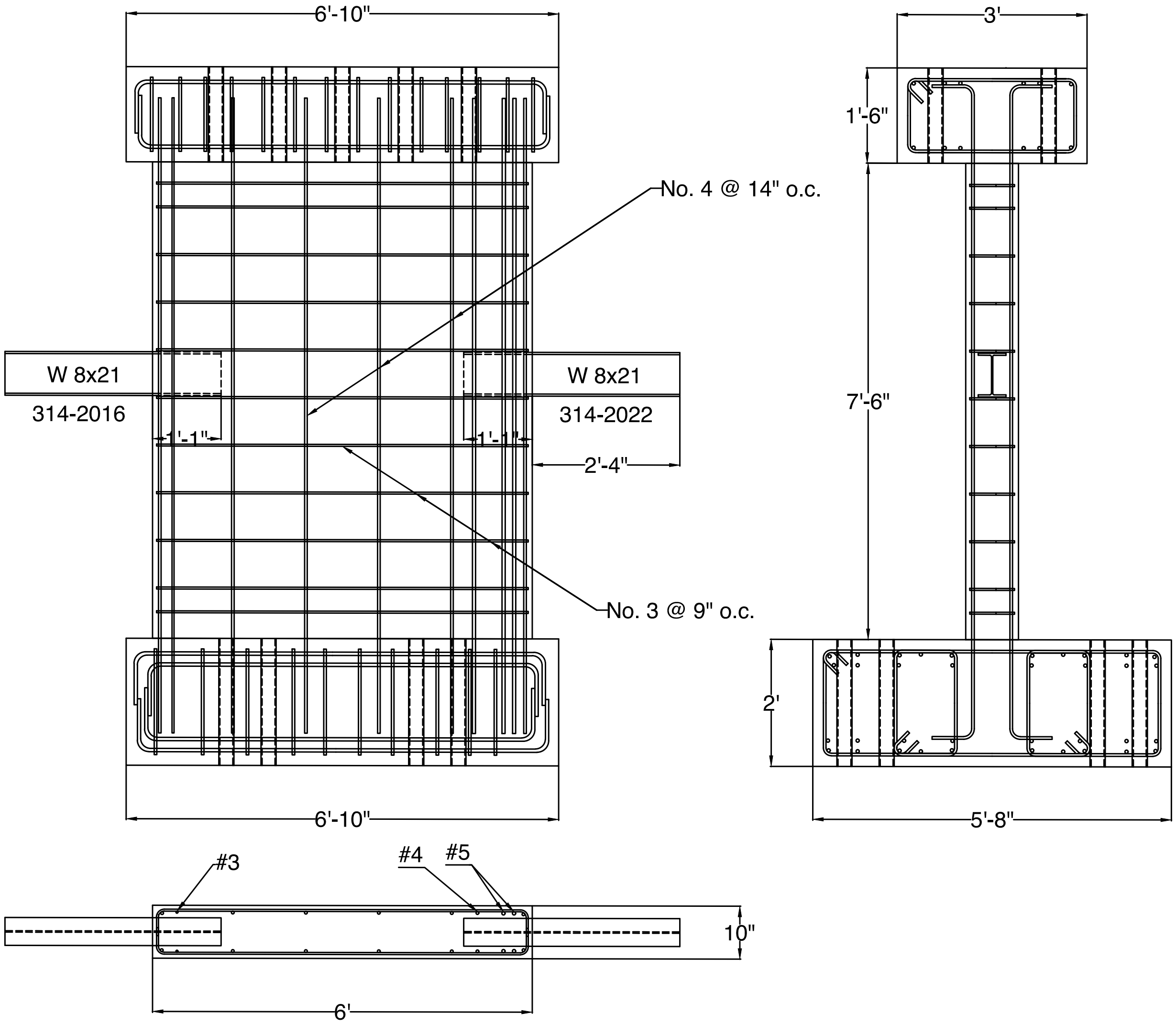

Figure 2.4 Details of specimens 2a and 2b (tests 3 and 4).

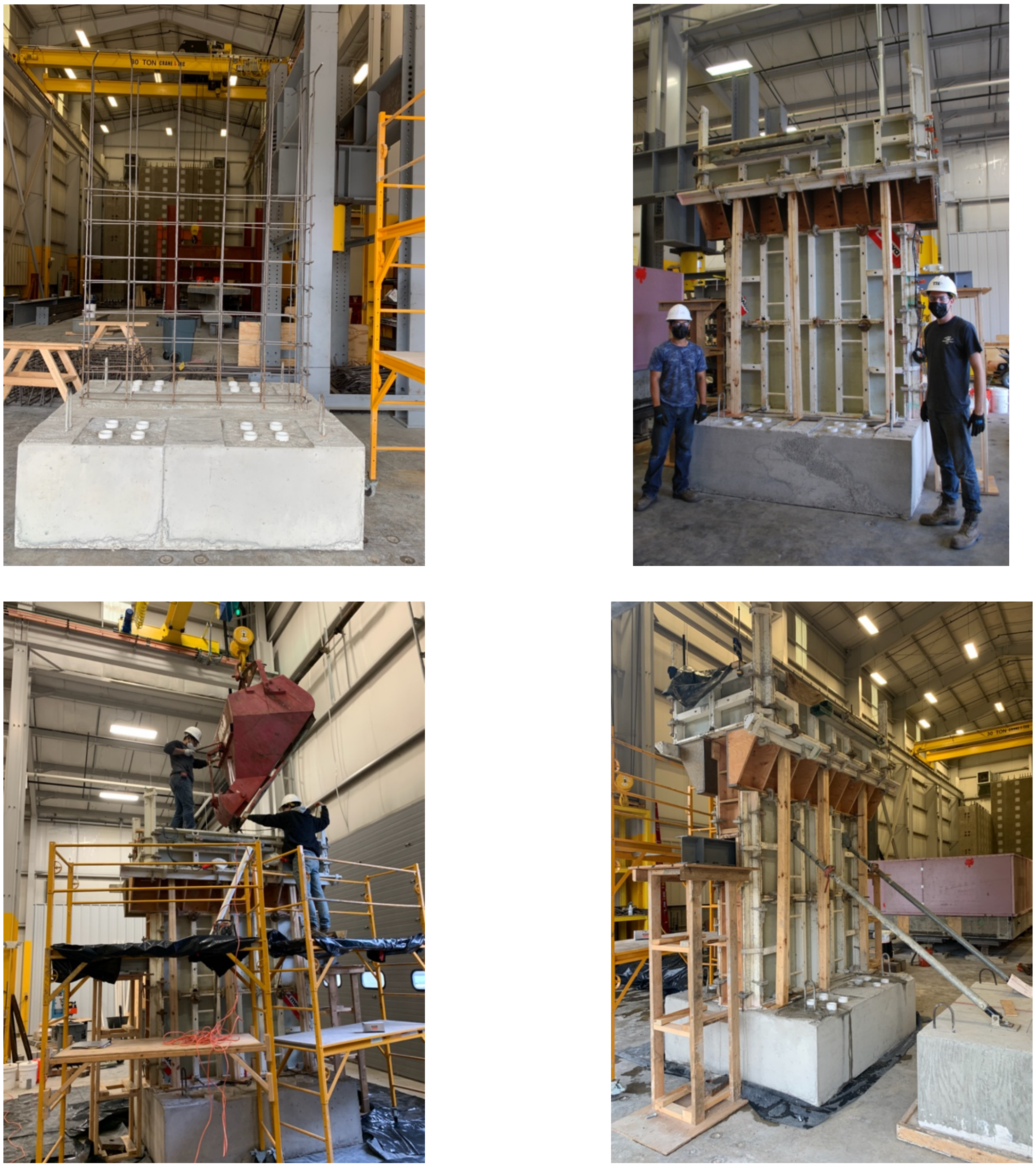

Figure 2.5 Fabrication of first-phase specimens.

2.3.2 Phase 2 specimens

The maximum coupling beam shear demand is in story 9 of the archetype. The test specimens were designed and detailed based on the demands in this story and corresponding wall reinforcement. The specimens in the second phase are approximately ¾ scale, whereas ½-scale specimens were used in the first phase. The test matrix is summarized in Table 2.4. Based on the observations made in the first phase (discussed in Chapter 3), it was decided to add face-bearing plates in all the second phase specimens. The embedment length was determined using the current AISC 341 (2022) equation (Eq 2.1) and a revised equation (Eq 2.2). Derivation of the revised equation is provided in Appendix A. The calculated embedment length according to ASIC 341 and the revised equation is 19 in. and 24 in., respectively.

AISC 341-22 $$V_n = 1.54\sqrt{f_c'}\left(\frac{b_w}{b_f}\right)^{0.66} \beta_1 b_f L_e \left[\frac{0.58 - 0.22\beta_1}{0.88 + \frac{g}{2L_e}}\right] \quad \textbf{Eq 2.1}$$

Revised $$V_n = \frac{0.227 f_c' b_f L_e}{0.845 + \frac{g}{2L_e}} \quad \textbf{Eq 2.2}$$

Table 2.4 Phase 2 test matrix.

Specimen ID	Test ID	Embedment length	Auxiliary transfer reinforcement	Confinement	Face bearing plate
3	5	AISC 341-22	No	No	Yes
4	6	Revised	No	No	Yes
5	7	AISC 341-22	Yes	No	Yes
6	8	AISC 341-22	No	Yes	Yes

The amount of auxiliary transfer reinforcement was calculated using Eq 2.3, which is the same as Eq. H5-3 in AISC 341-2022. The auxiliary transfer reinforcement was added to mitigate stiffness degradation observed in the first phase (discussed in Chapter 3). Considering that stiffness is primarily a serviceability issue, F_{ysr} was taken as $0.5F_{ysr}$, i.e., 30 ksi for ASTM A615 Gr. 60 reinforcement that was used. A total of 8 No. 5 bars (4 on each flange) were used. The manufacturer had threaded the bars into couplers and torqued them according to their specifications. The coupler of the assembly was welded to the flanges before placing the coupling beam in the form. In actual construction, couplers would have been welded to the flanges before threading and torquing the headed bars.

$$A_{tb} \geq 0.03 f_c' L_e b_f / F_{ysr} \quad \textbf{Eq 2.3}$$

Confinement in specimen 6 (test ID 8) consisted of two layers of cross ties along the embedment length. Confinement was provided for both flanges. Specimen details and photographs before casting are shown in Figure 2.6 and Figure 2.7, respectively.

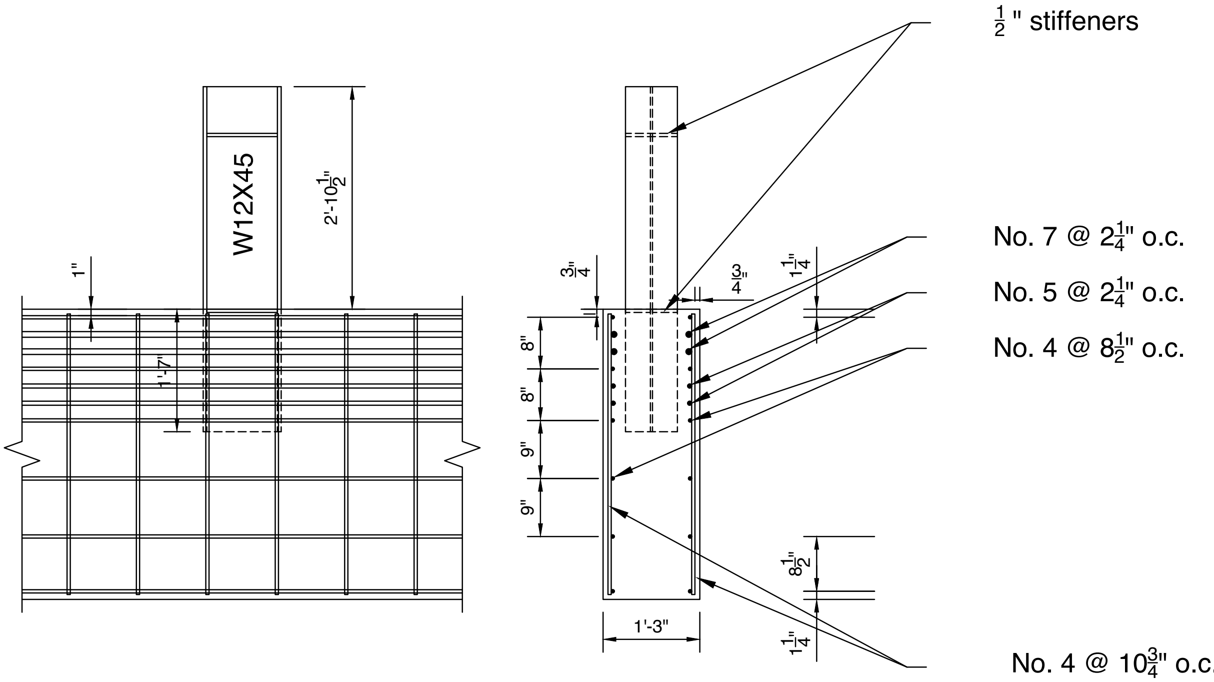

(a) Specimen 3 (test 5)

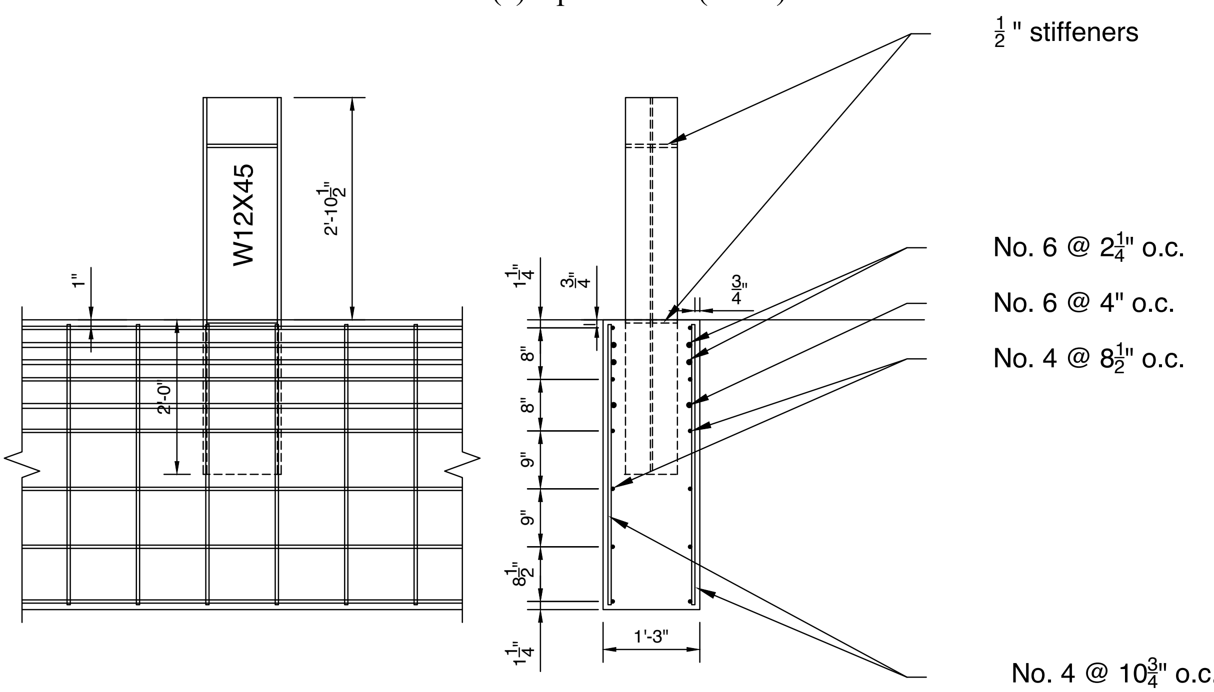

(b) Specimen 4 (test 6)

Figure 2.6 Specimen details.

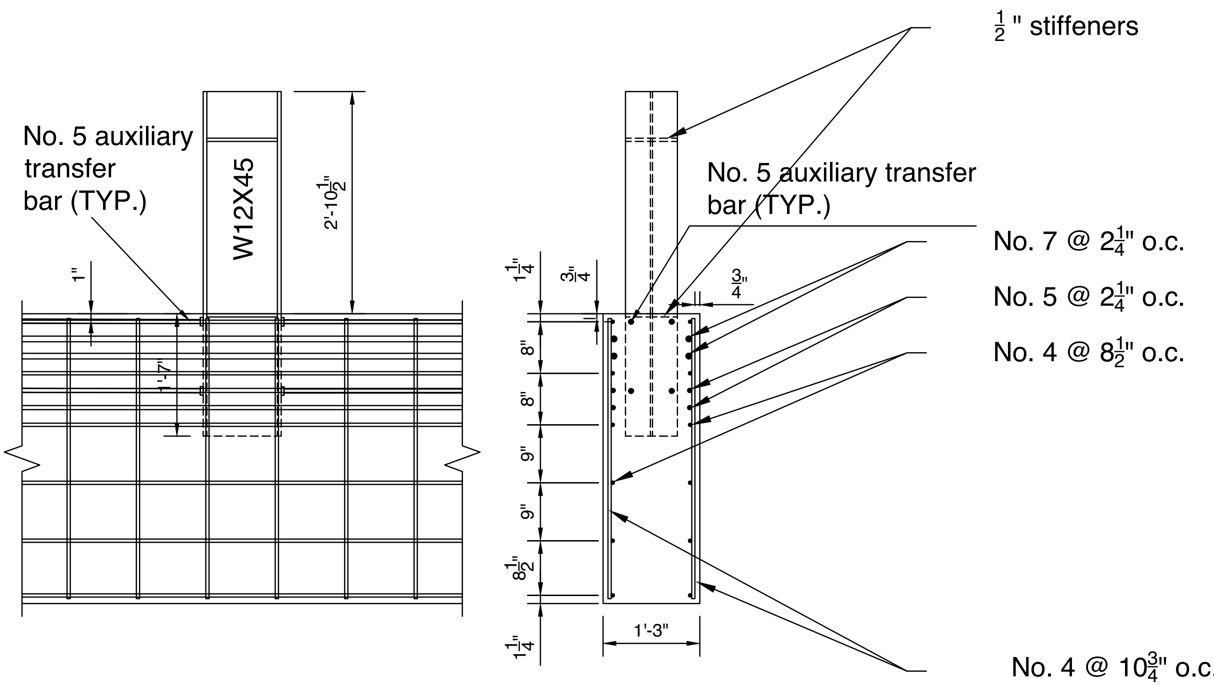

Auxiliary transfer bars will be as close as possible to the web while maintaining ACI spacing requirements for headed bars

(c) Specimen 5 (test 7)

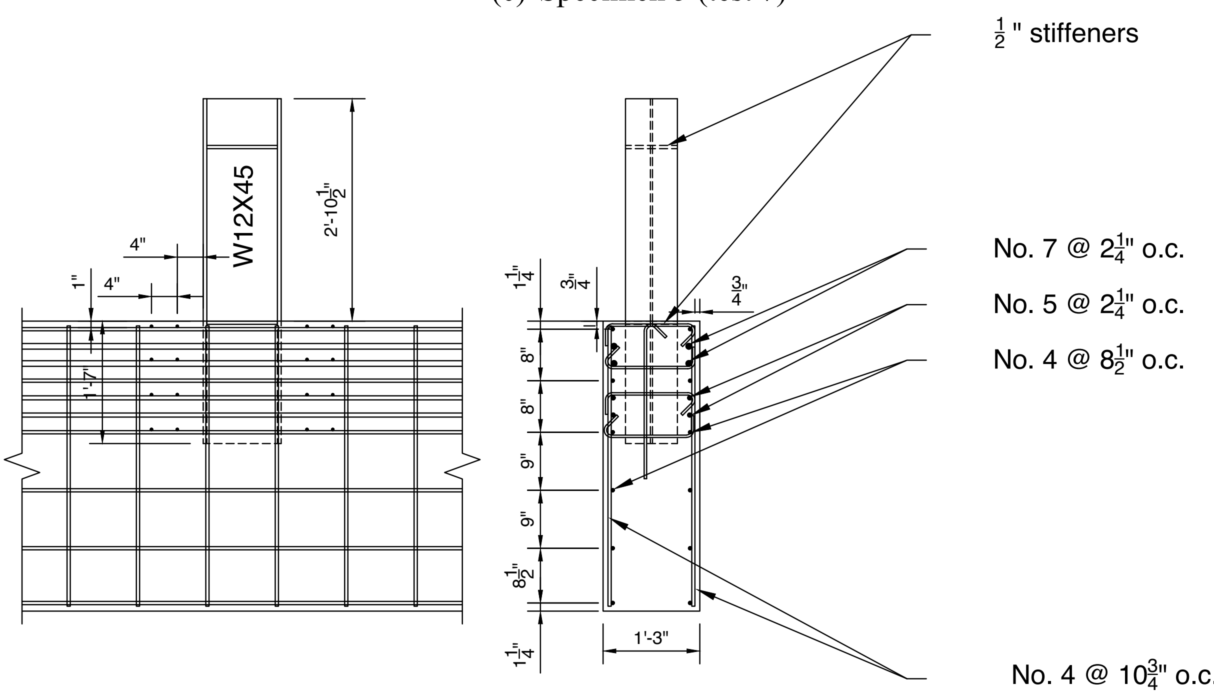

(d) Specimen 6 (test 8)

Figure 2.6 Specimen details (cont.).

(a) Specimen 4 (test 6) [specimen 3 (test 5) was similar but with a shorter embedment length]

(b) Specimen 5 (test 7)

(c) Specimen 6 (test 8)

Figure 2.7. Photographs of specimens before casting

2.4 Material properties

Design concrete compressive strength (f'_c) was 5,000 psi. The reinforcing bars were A615 Gr. 60 and structural steel was A572 Gr. 50. The material properties were determined by testing samples according to the relevant ASTM test methods.

2.4.1 Concrete

The concrete compressive strength was determined using "field cured" 6-in. diameter by 12-in. high cylinders and 4-in. diameter by 8-in. high cylinders tested in accordance with ASTM C39 (2021). Additionally, 4-in. cores were obtained from a number of the test specimens. The cores were tested and processed according to ASTM C42 (2020). Splitting tensile strength was determined using ASTM C496 (2017). The measured compressive and tensile strengths are summarized in Table 2.5.

Table 2.5 Measured concrete compressive and tensile strengths.

Specimen ID	Test ID	Compressive Strength (psi)	Tensile Strength (psi)
1a	1	4133[a]	363
1b	2	4133[a]	363
2a	3	6954[b]	529
2b	4	6954[b]	529
3	5	6983[a]	520
4	6	4700[b]	460
5	7	6730[a]	450
6	8	6150[c]	480

[a] from cylinders (ASTM C39)
[b] from cores (ASTM C42)
[c] average of the strengths from cylinders and cores

2.4.2 Reinforcement

Full-section specimens were tested according to ASTM A370 (2022). The values of yield strength (f_y), ultimate strength (f_u), and rupture strain are summarized in Table 2.6. These values are the averages from three samples. The measured stress-strain diagrams are provided in Appendix B.

Table 2.6 Measured material properties of reinforcement.

Phase	size	f_y (ksi)		f_u (ksi)		rupture strain	
		Average	COV	Average	COV	Average	COV
1	#3	75.3	0.021	97.0	0.0068	0.123	0.405
	#4	76.7	0.026	105.6	0.0017	0.118	0.460
	#5	71.9	0.031	101.0	0.0073	0.096	0.109
2	#3	75.3	0.021	97.0	0.0068	0.123	0.405
	#4	71.5	na[a]	100	0.017	nr[b]	na
	#5	70.2	0.005	86.3	0.004	> 0.1225[c]	na
	#6	71.4	0.004	88.1	0.003	> 0.1265	na
	#7	75.2	0.005	91	0.004	> 0.1375	na
	[a] due to issues with extensometer, yield strength could be obtained from only one sample. [b] the value was not reported. [c] rupture occurred outside of the gage length						

2.4.3 Structural Steel

Using subsize specimens fabricated and tested according to ASTM E8 (2022), the yield and ultimate strength of the flanges and webs of the steel coupling beams were determined. The results, which are the average values from testing two samples, are tabulated in Table 2.7. The measured stress-strain diagrams are shown in Appendix B.

Table 2.7 Measured material properties of steel coupling beams.

Phase	Specimen I.D.	Test I.D.	Shape	Location	F_y (ksi)	F_u (ksi)
1	1a, 1b	1, 2	W6×16	Flange	52.8	66.9
				Web	60.1	72.5
	2a, 2b	3, 4	W8×21	Flange	58.8	75.9
				Web	63.8	79.1
2	3, 4, 5, 6	5, 6, 7, 8	W12×45	Flange	53.6	68.1
				Web	56.8	70.2

2.5 Test setup

Two vastly different setups were utilized for testing the specimens in phase 1 and phase 2. The test setups are described separately in this section.

2.5.1 Phase 1 test setup

Four servo-valve controlled actuators were used to load the coupling beam and subject the wall pier to gravity load, axial force, shear force, and bending moment, refer to Figure 2.8. Actuator 1 was controlled to follow a predefined load or displacement history. The force measured by this actuator, which is the shear force in the coupling beam, was used as the input to control the force in the other three actuators according to the relationships tabulated in Table 2.8. These relationships were determined to keep the stresses in the test specimen equal to those in the archetype. The procedure for determining these ratios is discussed in Appendix C.

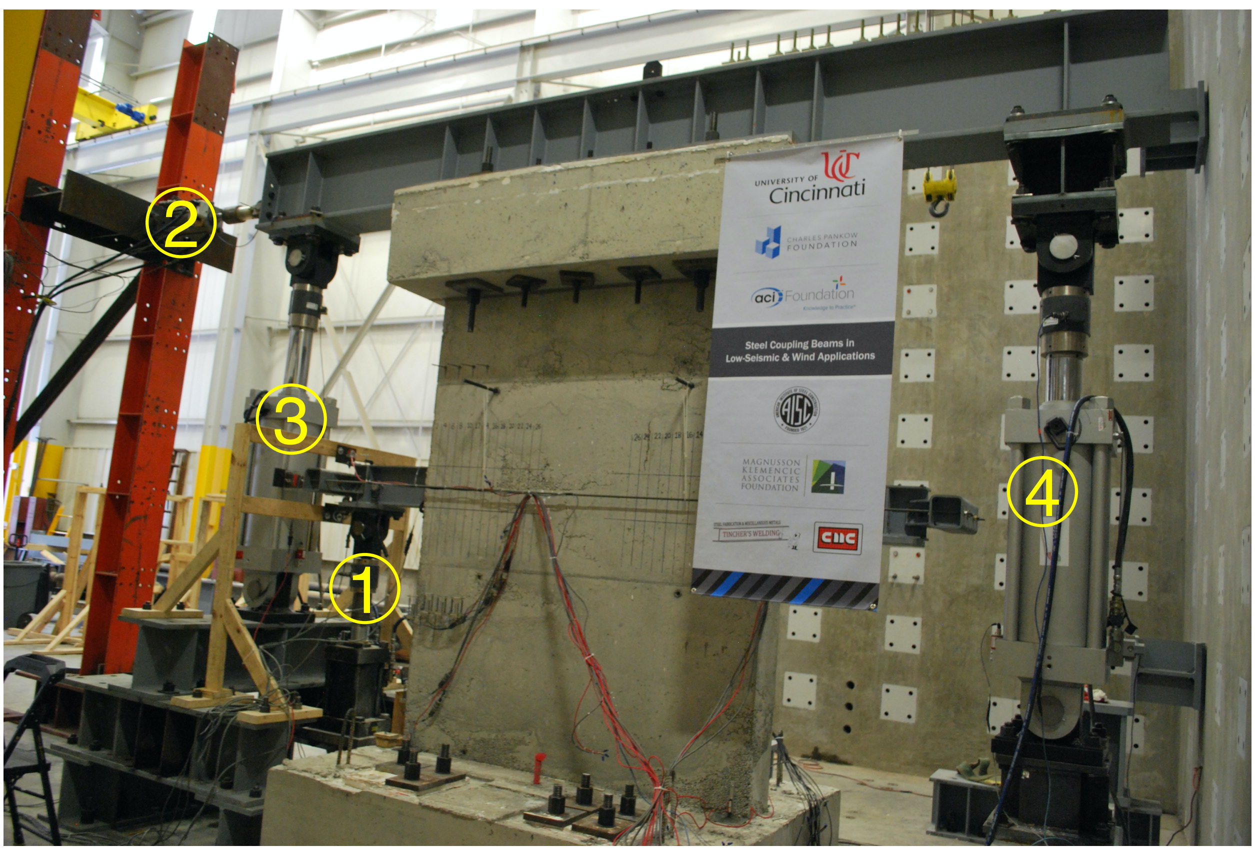

Figure 2.8 Test setup for specimens in phase 1.

Table 2.8 Force relationships between secondary and primary actuators.

Actuator (See Figure 2.8)	Relationships for Specimens 1a and 1b (test 1 and test 2)	Relationships for Specimen 2a and 2b (test 3 and test 4)
2	Force = 0.026 x force in actuator 1	Force = 0.143 x force in actuator 1
3	Force = 0.229 x force in actuator 1	Force = 0.682 x force in actuator 1
4	Force = 0.035 x force in actuator 1	Force = 0.831 x force in actuator 1

The directions of applied forces are provided in Figure 2.9. It should be noted that the wall curvature in specimens 1a and 1b, which represented the 24th floor connection, is opposite to that in the lower floors. Considering the complexity of simultaneous control of four actuators, a bespoke test frame was fabricated and used to debug programming of the controller. The four actuators during debugging process are shown in Figure 2.10. It was anticipated that the coupling beam would be "pulled out" of the wall when the primary actuator (actuator 1) pushes the beam up. This axial deformation would be restrained by the floor diaphragm in the archetype. Therefore, an assembly was mounted to restrain the axial deformation. A pair of assemblies were bolted to the coupling beams at each end of the wall pier and were connected by 5/8-in. A193-B7 threaded rods, see Figure 2.11. A similar concept has been used by other researchers (Motter, 2013).

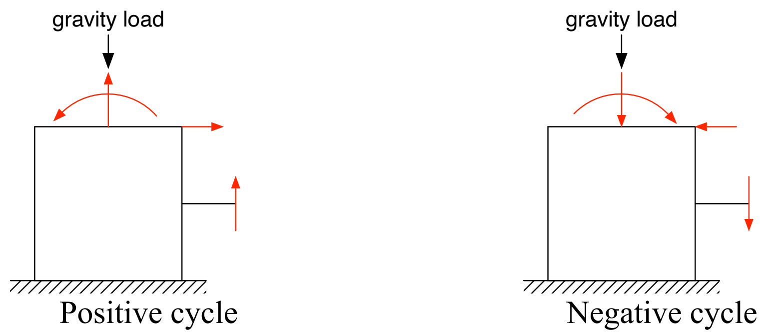

(a) Specimens 1a and 1b – Floor 24 (test 1 and test 2)

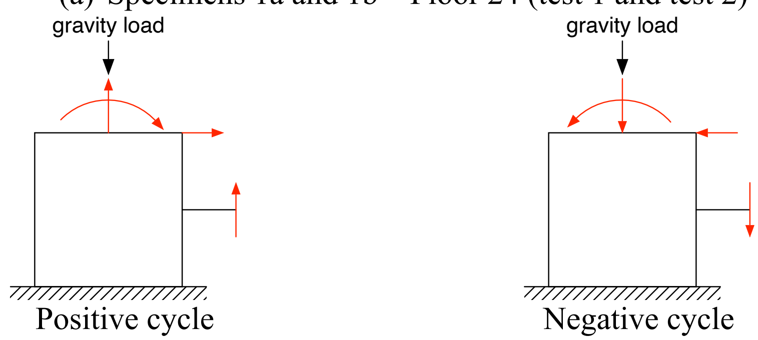

(b) Specimens 2a and 2b – Floor 9 (test 3 and test 4)

Figure 2.9 Direction of applied forces and moment.

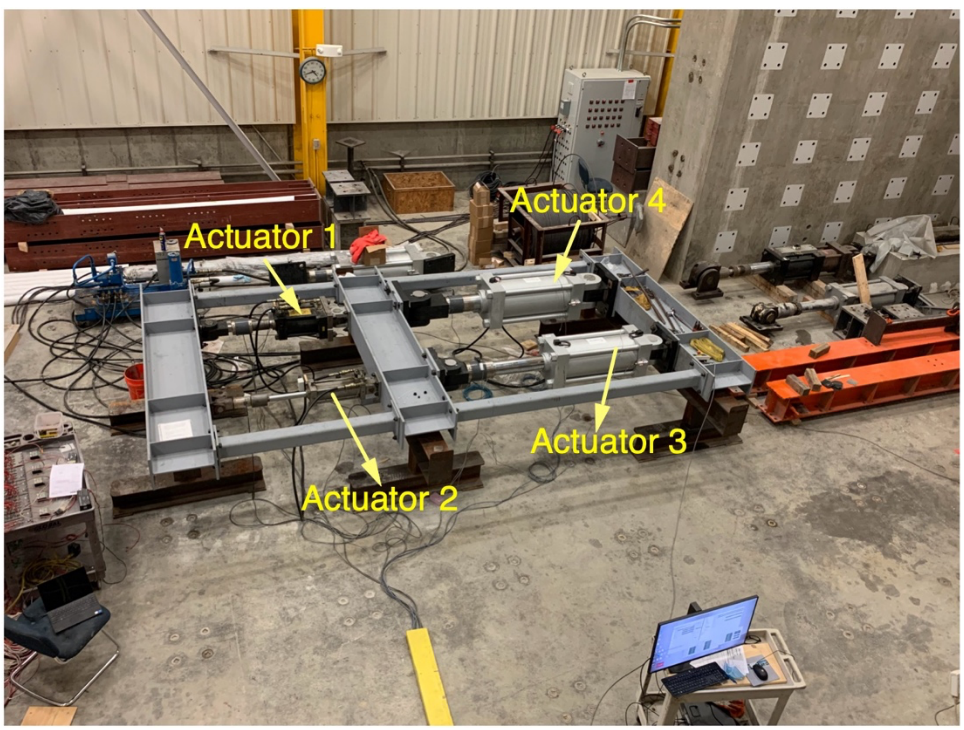

Figure 2.10 Setup for debugging controller.

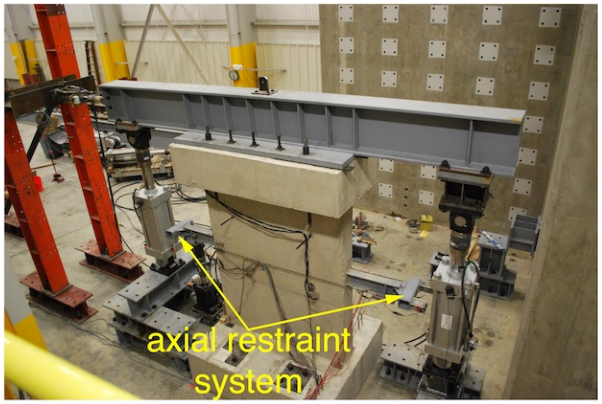

(a) Overall view

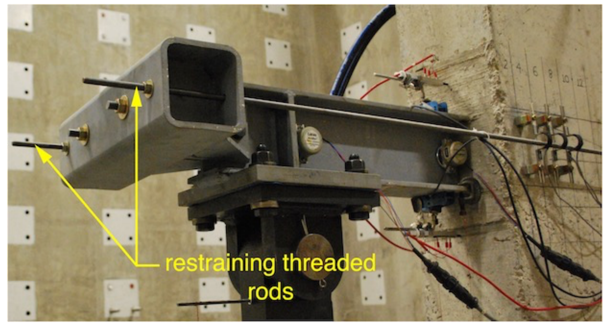

(b) Closeup view

Figure 2.11 Coupling beam axial deformation restraint apparatus for phase 1 specimens.

2.5.2 Phase 2 test setup

The test specimen was post-tensioned to the laboratory's strong floor using two strong "tie backs". A constant axial load was applied by using eight 1-in. high-strength threaded rods. The level of applied axial load was intended to match the axial stress at the 9th story of the archetype. A single servo-controlled actuator was used to apply load and displacement cycles to the coupling beam. The test setup is shown in Figure 4.1. The positive direction of applied load and displacement is indicated in this figure.

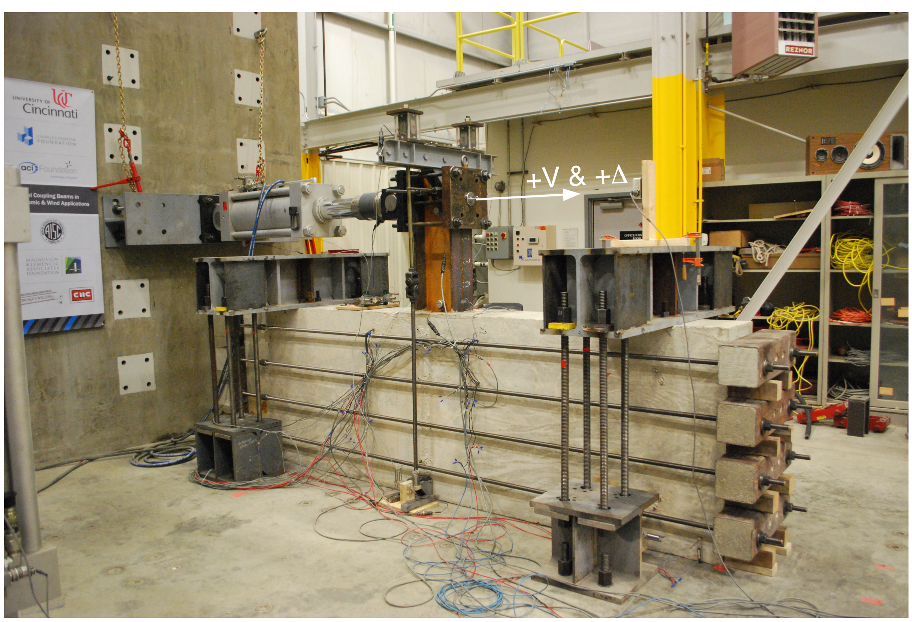

Figure 2.12 Test setup for specimens in phase 2.

Similar to phase 1 specimens, the axial deformation of the coupling beam was restrained. As seen from Figure 2.13, the apparatus consisted of a strong tie back beam that was bolted to the coupling beam. A pair of 1-in. high-strength threaded rods connected the strong tie-back beam to the bottom of the wall. Universal joints in line with the threaded rods were used to minimize deformation of the rods.

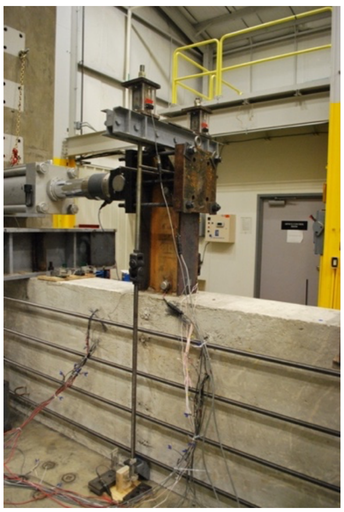

(a) Overview

(b) Universal joint in line with threaded rods

Figure 2.13 Coupling beam axial deformation restraint apparatus for phase 2 specimens.

2.6 Instrumentation

Various internal and external sensors were installed to measure several key responses. Strain gages were attached to the wall longitudinal reinforcement at various locations and auxiliary transfer bars (for phase 2 specimen 5 [test 7]), see Figure 2.14. The gages were located at 2 in. from the flanges. The strain gages for the auxiliary transfers were placed at the development length. Strain gages were also attached to the coupling beam flanges at 1 in. from the face of the wall. Strain gage rosettes, also at 1 in. above the wall, were also installed on the web of the phase 2 specimens.

The following external instruments were utilized to monitor various responses: (a) actuator's load cell and displacement transducer measured the applied force and resulting displacement, (b) external displacement transducers were used to measure the deflection of the coupling beam at the location of applied shear force, (c) tilt meters recorded the coupling beam rotation, (d) displacement transducers monitored the axial deformation of the coupling beam, (e) sensors were used to measure the horizontal displacement of the flange relative to the wall, (f) load cells recorded the force required to restrain coupling beam axial deformation, (g) potential uplift of the wall was measured by vertical displacement transducers attached to the specimen and targeted against the strong floor, and (h) potential slip of the specimen relative to the strong floor was monitored by displacement transducers. In phase 1 specimens, concrete strain along the embedment length using clip gages, which did not measure reliable data due to spalling and damage around the embedment length, or vertical DC LVDTs. The external instrumentations are illustrated in Figure 2.15 and Figure 2.16 for phase 1 and phase 2 specimens, respectively. The locations of these sensors are provided in Figure 2.17, Figure 2.18, and Figure 2.19.

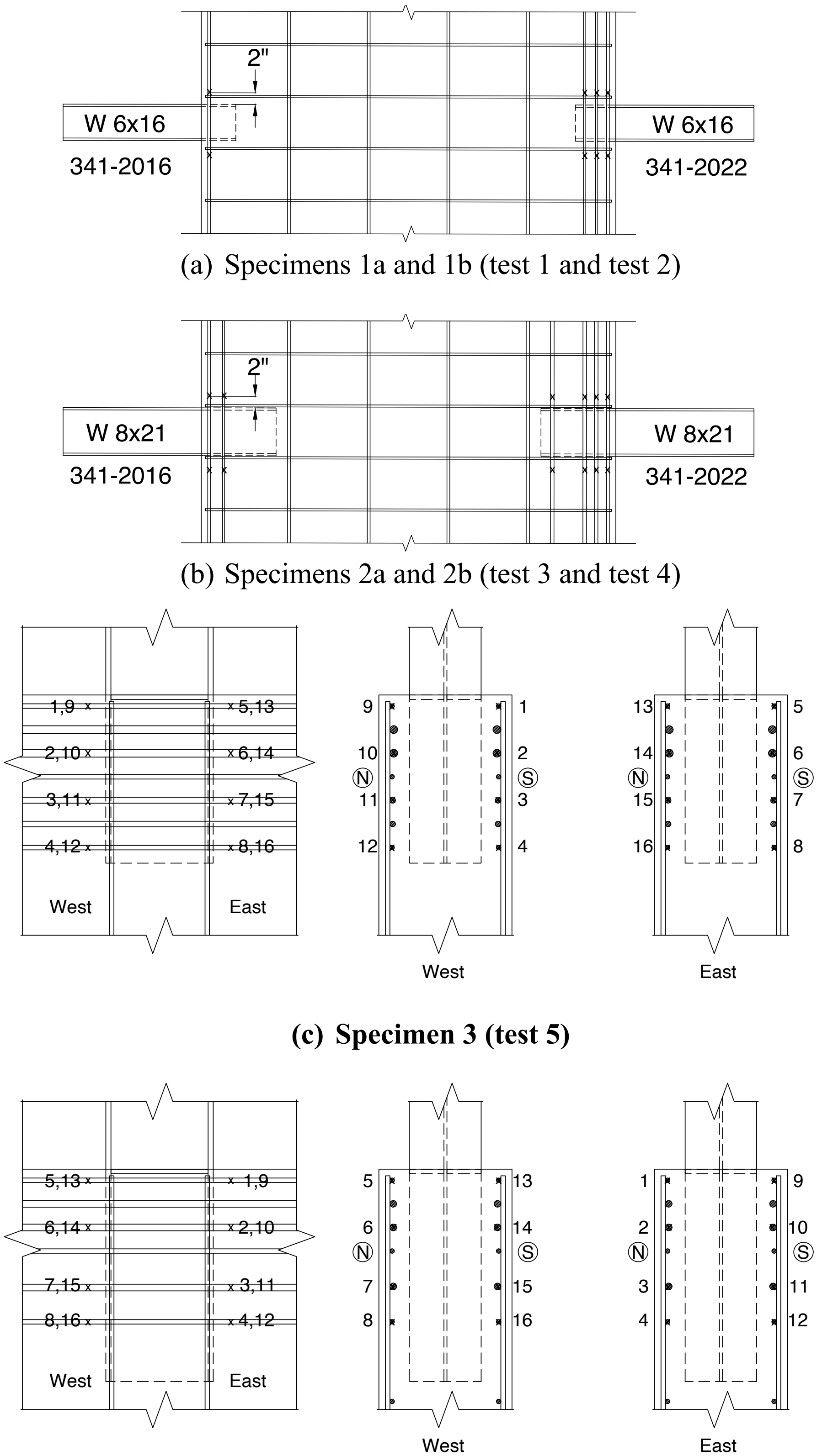

(a) Specimens 1a and 1b (test 1 and test 2)

(b) Specimens 2a and 2b (test 3 and test 4)

(c) Specimen 3 (test 5)

(d) Specimen 4 (test 6)

Figure 2.14 Locations of strain gages shown with x.

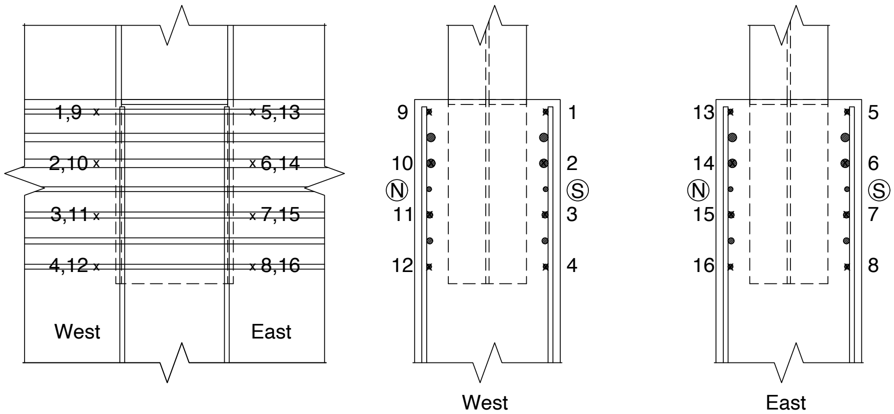

(e) Specimen 5 (test 7)

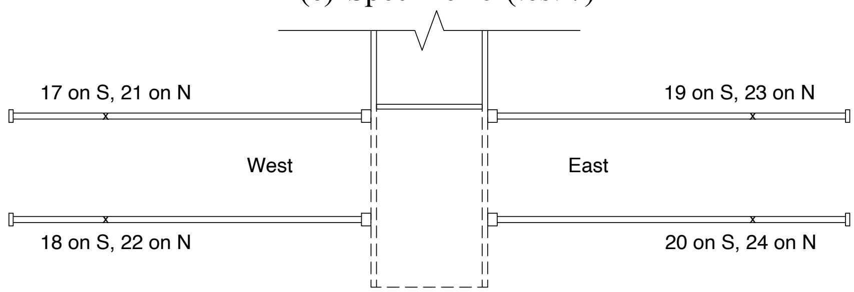

(f) Specimen 5 (test 7) – auxiliary transfer bars0

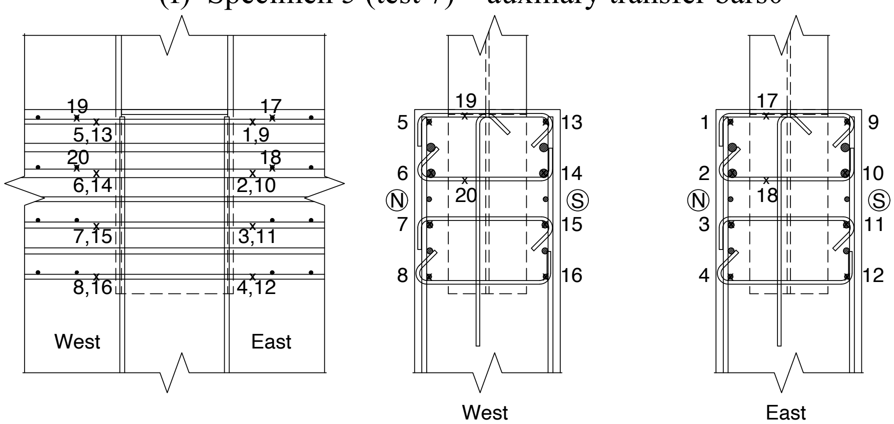

(g) Specimen 6 (test 8)

Figure 2.14 Locations of strain gages shown with x (cont.).

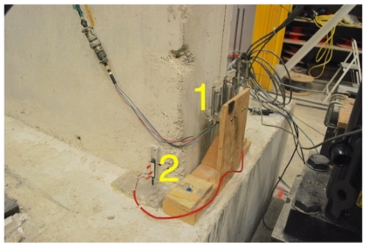

(a) 1: transducer for measuring beam deflection at support, 2: transducer for measuring potential wall uplift

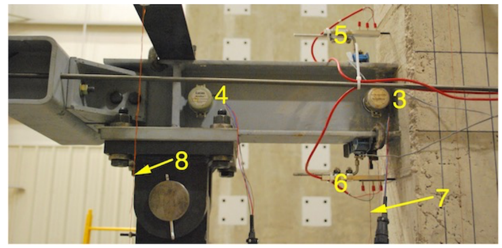

(b) 3 & 4: tilt meters for measuring rotations, 5 & 6: transducers for determining initiation of spalling, 7: copper wire for sensor 1 (see a), 8: copper wire for sensor 9 (see c)

(c) 9: additional measurement of beam deflection at load point

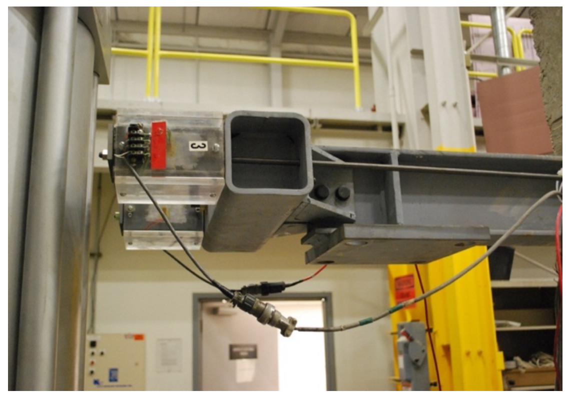

(d) measurement of coupling beam axial force

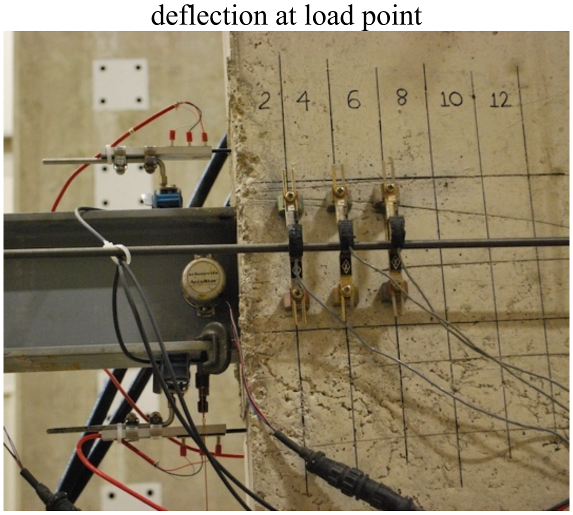

(e) Measurement of concrete surface strain Specimens 1a and 1b (tests 1 and 2): clip gages

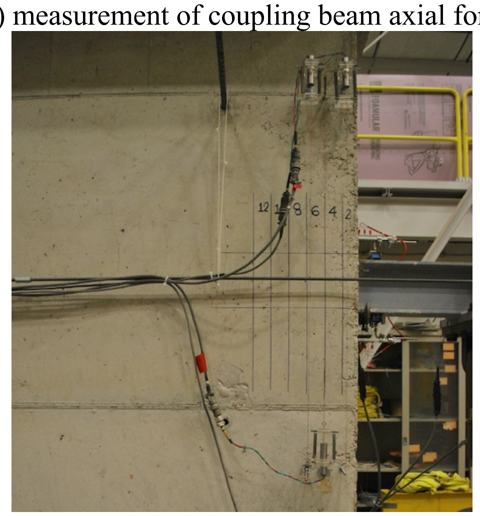

(f) Measurement of concrete surface strain Specimens 2a and 2b (tests 3 and 4): DC LVDTs

Figure 2.15 External instrumentation for phase 1 specimens.

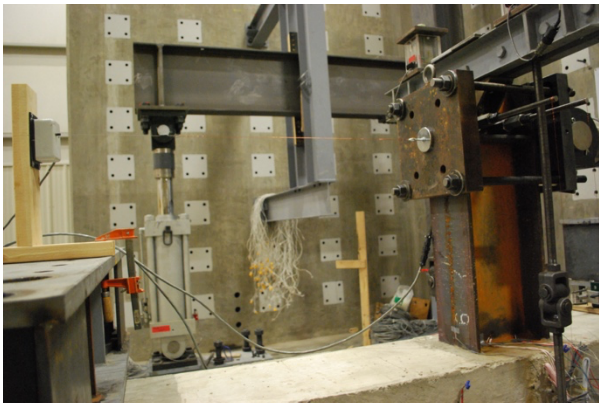

(a) External displacement transducer to measure beam deflection

(b) Tilt meters

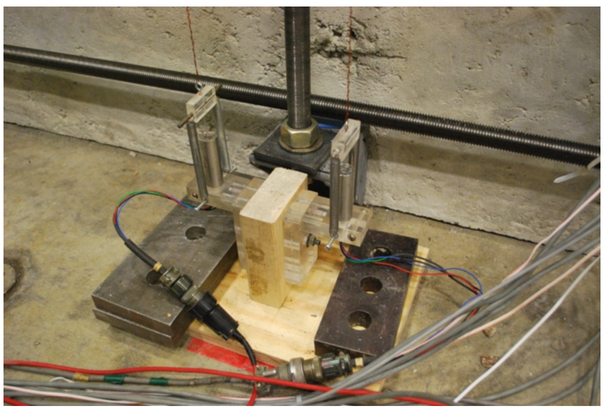

(c) Two out of four displacement transducers used to monitor beam axial deformation

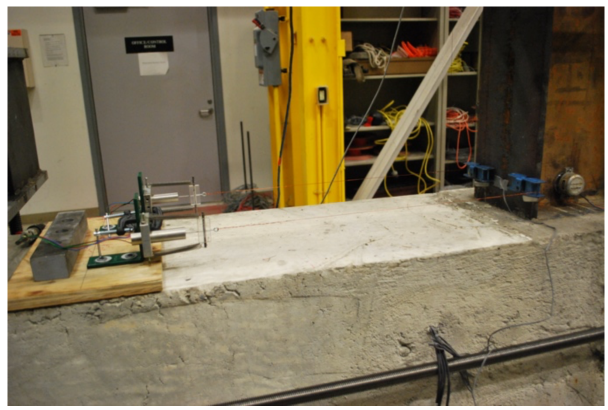

(d) Displacement transducers to measure deflection of the beam near its base

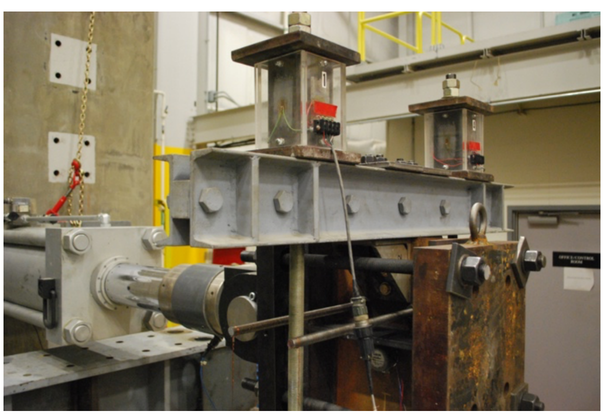

(e) Load cells to measure force in axial restraining apparatus

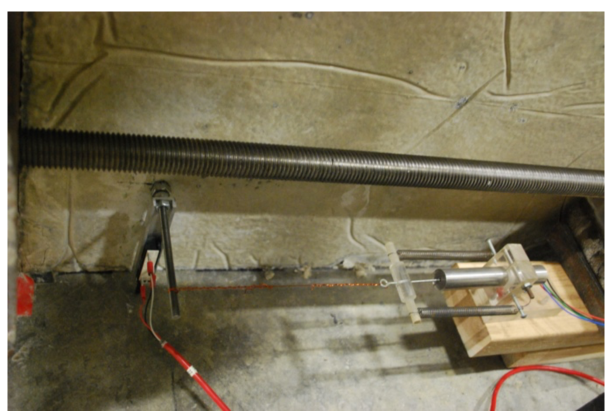

(f) Displacement transducers to monitor potential wall uplift and slip

Figure 2.16 External instrumentation for phase 2 specimens.

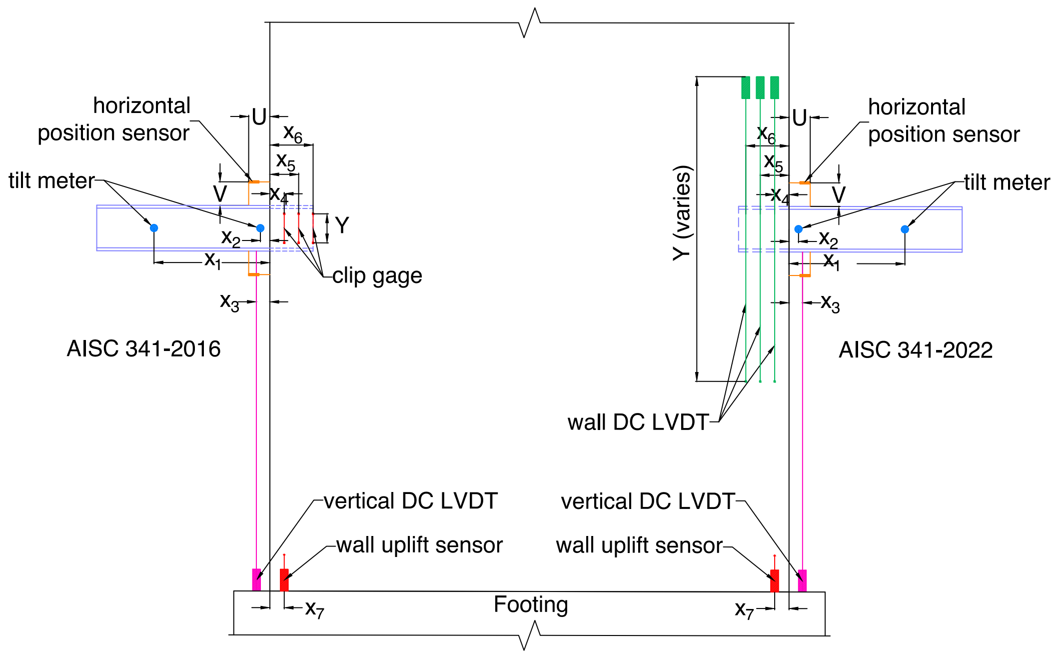

Sensors for specimen 1a (AISC 341-2016)	Position	
Tilt meter 1	X_1 = 16-1/16 in.	
Tilt meter 2	X_2 = 1-1/16 in.	
Vertical DC LVDT	X_3 = 1-7/8 in.	
Clip gage 1	X_4 = 2 in.	Y = 4 in. (south and north faces)
Clip gage 2	X_5 = 4 in.	Y = 4 in. (south and north faces)
Clip gage 3	X_6 = 6 in.	Y = 4 in. (south and north faces)
Wall uplift sensor	X_7 = 2 in.	
Horizontal position sensor (top and bottom)	U = 2-15/16 in.	V = 3-1/4 in.
Sensors for specimen 1b (AISC 341-2022)	**Position**	
Tilt meter 1	X_1 = 16-1/16 in.	
Tilt meter 2	X_2 = 1-1/16 in.	
Vertical DC LVDT	X_3 = 1-7/8 in.	
Wall DC LVDT 1	X_4 = 2 in.	Y = 42-13/16 in. (south face) Y = 42-1/16 in. (north face)
Wall DC LVDT 2	X_5 = 4 in.	could not be installed on the south face Y = 42-15/16 in. (north face)
Wall DC LVDT 3	X_6 = 6 in.	Y = 43-1/16 in. (south face) Y = 42-15/16 in. (north face)
Wall uplift sensor	X_7 = 2 in.	
Horizontal position sensor (top and bottom)	U = 2-15/16 in.	V = 3-1/4 in.

Figure 2.17 Locations of external instruments for specimens 1a and 1b (test 1 and test 2).

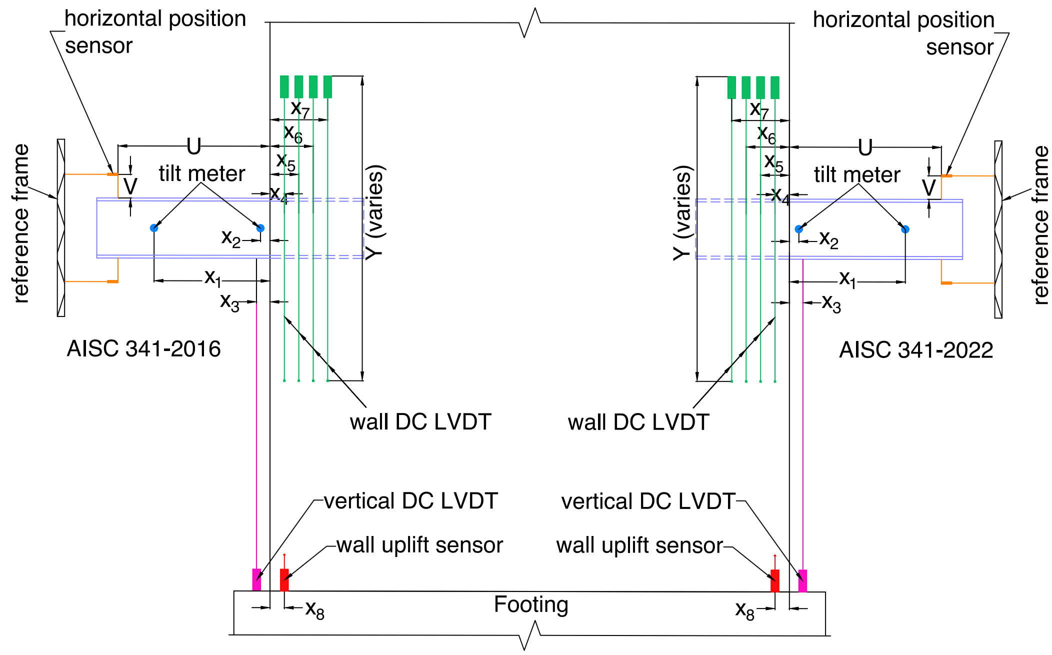

Sensors for specimen 2a (AISC 341-2016)	Position	
Tilt meter 1	X_1 = 16-1/16 in.	
Tilt meter 2	X_2 = 1-5/16 in.	
Vertical DC LVDT	X_3 = 2 in.	
Wall DC LVDT 1	X_4 = 2 in. (south face) X_4 = 2 in. (north face)	Y = 48-1/4 in. (south face) Y = 48-1/4 in. (north face)
Wall DC LVDT 2	X_5 = 5.5 in. (south face) X_5 = 6 in. (north face)	Y = 48-1/4 In. (south face) Y = 48-1/4 In. (north face)
Wall DC LVDT 3	X_6 = 9 in. (south face) X_6 = 9 in. (north face)	Y = 48-1/4 in. (south face) Y = 48-1/4 in. (north face)
Wall DC LVDT 4	X_7 = 12.5 in. (south face) X_7 = 12.5 in. (north face)	Y = 48-1/4 in. (south face) Y = 48-1/4 in. (north face)
Wall uplift sensor	X_8 = 2 in.	
Horizontal position sensor (top and bottom)	U = 25-1/8 in.	V = 2-1/8 in.
Sensors for specimen 2b (AISC 341-2022)	**Position**	
Tilt meter 1	X_1 = 16-1/4 in.	
Tilt meter 2	X_2 = 1-1/2 in.	
Vertical DC LVDT	X_3 = 2-5/8 in.	
Wall DC LVDT 1	X_4 = 2 in.	Y = 49-3/4 in. (south face) Y = 48-1/4 in. (north face)
Wall DC LVDT 2	X_5 = 5.5 in.	Y = 48-1/4in. (south face) Y = 48-1/4 in. (north face)
Wall DC LVDT 3	X_6 = 9 in.	Y = 48-1/4 in. (south face) Y = 48-1/4 in. (north face)
Wall DC LVDT 4	X_7 = 12.5 in.	Y = 48-1/4 in. (south face) Y = 48-1/4 in. (north face)
Wall uplift sensor	X_8 = 2 in.	
Horizontal position sensor (top and bottom)	U = 24-3/4 in.	V = 2-1/8 in.

Figure 2.18 Locations of external instruments for specimens 2a and 2b (test 3 and test 4).

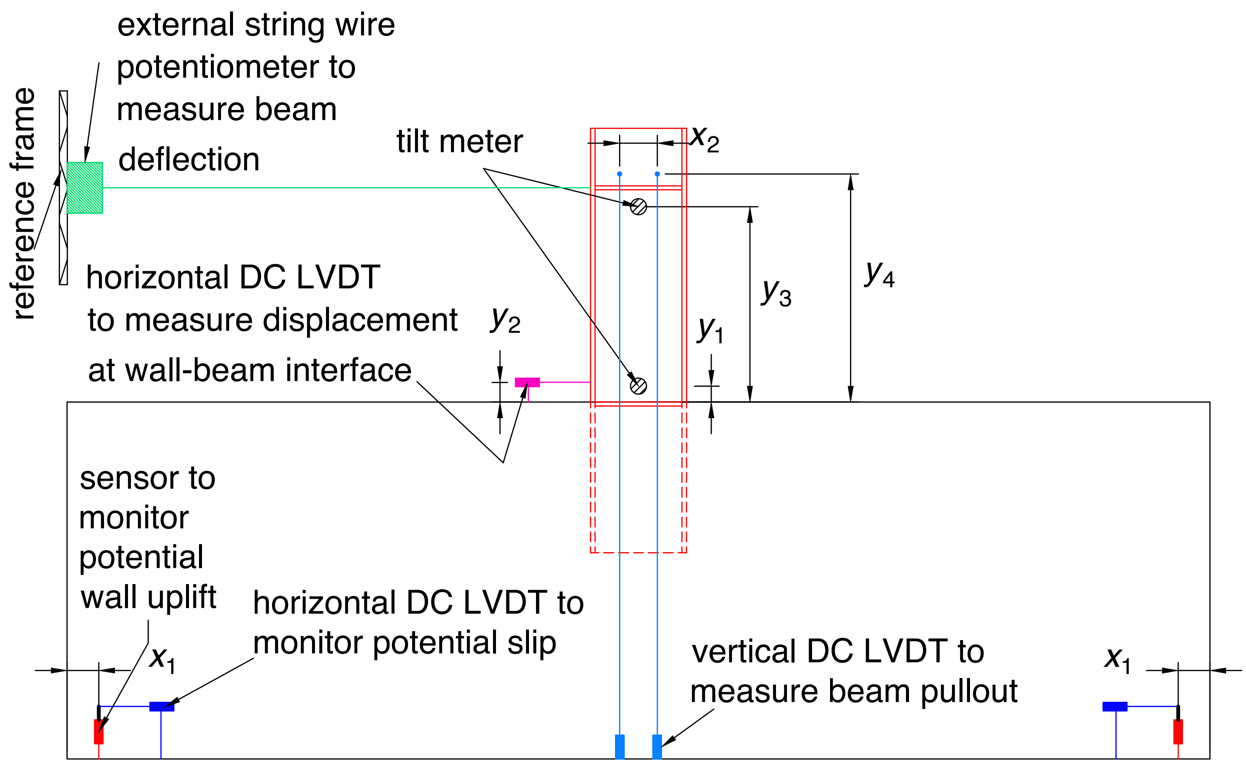

Specimen I.D.	Test I.D.	x_1 (in.)	x_2 (in.)	y_1 (in.)	y_2 (in.)	y_3 (in.)	y_4 (in.)
2	5	4	5-1/2	2	2-5/8	24-5/8	28-1/8
3	6	4	5-1/2	2	2-5/8	24-5/8	28-3/4
4	7	4	5-1/2	2	2-9/16	24-1/2	29
5	8	4	4-3/4	2	2-1/2	24-5/8	28-3/4

Figure 2.19 Locations of external instruments for phase 2 specimens.

2.7 Testing protocol

The loading protocol for specimen 1a (test 1) was different from that for the remaining tests. For test 1, the goal was to subject the connection to: 250 cycles at $0.15M_{pr}$, 500 cycles at $0.40M_{pr}$, 75 cycles at $0.75M_{pr}$, 5 cycles at $1.2\theta_y$, 2 cycles at $1.5\theta_y$, 5 cycles at $1.2\theta_y$, 75 cycles at $0.75M_{pr}$, 500 cycles at $0.40M_{pr}$, and 250 cycles at $0.15M_{pr}$, where M_{pr} is coupling beam probable moment capacity and θ_y is coupling beam yield rotation. However, due to an issue with data acquisition computer, the connection was subjected to 495 cycles at $0.15M_{pr}$ (corresponding to $0.54V_n$ where V_n is the nominal shear force for which the connection was designed) and testing was terminated after 40 cycles at $0.40M_{pr}$ (equivalent to $1.43V_n$) as the connection had lost its integrity and could not resist additional loads.

Based on the lessons learned from the first test, the loading protocol was changed for the remaining specimens. The goal was to subject each specimen to 543 cycles with increasing and decreasing force amplitudes. If possible, the remaining specimens were to be subjected to a series of load-controlled cycles followed by a “standard” seismic protocol. The intended testing protocol is summarized in Table 2.9. As noted in this table; however, not all the steps/cycles could be completed for some of the specimens due to unanticipated failure, or additional cycles were conducted because an instrument had malfunctioned and had to be replaced.

Table 2.9 Testing protocol.

Wind		Seismic	
Load Step	Description	Displacement Cycle	Description
1	100 cycles @ $0.25V_n$	1	3 cycles @ θ[a]= 0.50%
2	100 cycles @ $0.40V_n$	2	3 cycles @ θ = 0.75%
3	50 cycles @ $0.50V_n$	3	3 cycles @ θ = 1.0%
4	15 cycles @ $0.67V_n$	4	3 cycles @ θ = 1.5%
5	5 cycles @ $0.83V_n$	5	3 cycles @ θ = 2.0%
6	3 cycles @ V_n	6	3 cycles @ θ = 3.0%
7	5 cycles @ $0.83V_n$	7	2 cycles @ θ = 4.0%
8	15 cycles @ $0.67V_n$	8	2 cycles @ θ = 6.0%
9	50 cycles @ $0.50V_n$	9	1 cycle@ θ = 8.0%
10	100 cycles @ $0.40V_n$		
11	100 cycles @ $0.25V_n$		

[a] θ = chord rotation

Variations from the target testing protocol:

- Specimen 1b (test 2): 45 additional cycles @ $0.50V_n$ and 15 additional cycles @ $0.67V_n$, 2 cycles @ θ = 1.5%, 1 cycle @ θ = 2.0%, 1 cycle @ θ = 3.0%, 1 cycle @ θ = 4.0%, 1 cycle @ θ = 6.0%, cycle 9 (1 cycle @ θ = 8.0%) could not be completed.
- Specimen 2a (test 3): 1 cycle @ V_n, load steps 7–11 were not conducted, displacement cycles 1 and 2 were not performed, 1 cycle @ θ = 1.5%, displacement cycles 8–9 were not conducted.
- Specimen 2b (test 4): 1 cycle @ V_n, load steps 9-11 were not conducted, displacement cycles 1–3 were not performed, 1 cycle @ θ = 1.5%.
- Specimen 3 (test 5): Only one-half of cycle for load step 6 could be completed. The following protocols were not conducted: load steps 7–11 and displacement cycles 1–2. Due to excessive damage, displacement cycles 8–9 were not performed.
- Specimen 4 (test 6): Only one complete cycle for load step 6 could be completed. Due to excessive damage, loading was stopped during one-half cycle of the second cycle at V_n. Seismic displacement cycles were not conducted.
- Specimen 5 (test 7): The wind loading protocol was completed. Displacement cycles 1–2 were not conducted. Testing of this specimen was stopped after completing displacement cycle 7 because of excessive damage.
- Specimen 6 (test 8): The connection lost its integrity during the first half cycle of loading step 5. Seismic displacement cycles were not conducted.

This page left blank intentionally.

Chapter 3 Test Results and Discussions

3.1 Introduction

The performances of the connections are described through visual observations and synthesis of the measured test data. The results for each test are first presented separately. The influence of different design method and detailing is discussed by evaluating comparable specimens.

3.2 Specimen 1a (test 1)

The applied shear was normalized with respect to the connection nominal shear strength V_n = 10 kips. The relationship between the normalized shear and chord rotation (tip displacement divided by the shear span) is shown in Figure 3.1. Using the actual embedment length, as-built dimensions, and measured concrete strength, the connection capacity was determined to be 11.8 kips. This capacity, referred to as "provided", was used to normalize the applied shear shown on the secondary y-axis.

Through the first 495 cycles at $0.54V_n$, the chord rotation became progressively larger indicating gradual loss of stiffness. No damage was detected during or at the conclusion of these cycles. The research team (RT) hypothesizes this behavior is because of small, localized deterioration of the bearing of the steel coupling flanges against the surrounding concrete over the embedment length; such damage is not visible on the wall surface. The stiffness was noticeably reduced after the first excursion beyond V_n (i.e., when the normalized shear strength on the primary y-axis is 1). When subjected to 40 cycles of loading at $1.43V_n$, the connection stiffness significantly deteriorated leading to major pinching of the hysteretic response. The results from the last 10 cycles of $1.43V_n$ are not included in Figure 3.1 because the target force could not be reached due to excessive damage.

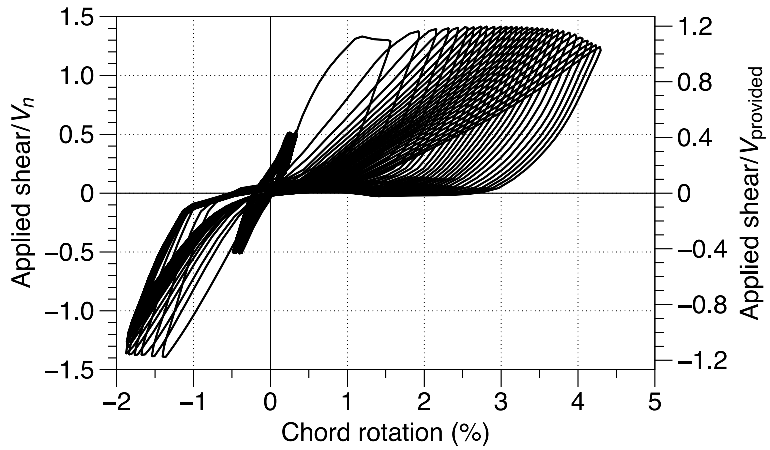

Figure 3.1 Normalized applied shear vs. chord rotation – specimen 1a (test 1).

The coupling beam did not yield, the largest measured flange strain (excluding the last 10 cycles at $1.43V_n$) was 815 micro strains, which corresponds to 24 ksi. Considering that the beam remained elastic, the relationship between the applied shear and deflection is expected to remain elastic. Hence, the nonlinearity seen in Figure 3.1 is attributed to damage in the connection region. The connection flexibility is also evident from Figure 3.2. The coupling beam displacement at 1-7/8 in. from the face reached a maximum value of nearly 0.15 in., which is nearly 0.19 times the maximum tip deflection and significantly larger than the expected value had the coupling beam been fixed at the face of the wall.

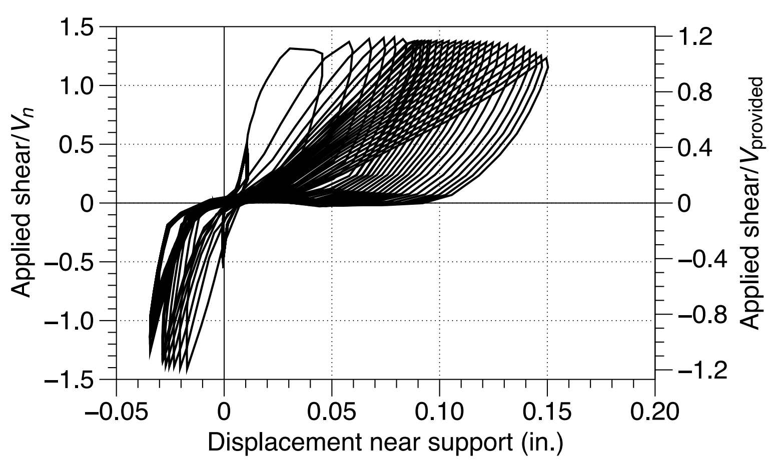

Figure 3.2 Normalized applied shear vs. displacement near support – specimen 1a (test 1).

The photograph in Figure 3.3 illustrates the level of damage at the conclusion of loading. After 5 cycles at 1.43V_n, a major crack was found between the flanges. The concrete within the flanges was completely lost on one side. The damage penetrated 3 in., i.e., one-half of the total provided embedment length, into the wall. The damage shown in the photograph corroborates the loss of stiffness and pinching behavior observed in Figure 3.1.

Figure 3.3 State of connection at the conclusion of testing – specimen 1a (test 1).

3.3 Specimen 1b (test 2)

The applied shear was normalized with respect to the connection nominal shear strength V_n = 10 kips. The relationship between the normalized shear and chord rotation is shown in Figure 3.4. Using the actual embedment length, as-built dimensions, and measured concrete strength, the connection capacity was determined to be 15.5 kips. This capacity, referred to as "provided", was used to normalize the applied shear shown on the secondary y-axis. The wind loading protocol consisted of 543 cycles with 3 cycles at V_n. As evident from the inset in Figure 3.4, the connection response during wind load protocol was nonlinear with some pinching. Visual inspection did not, however, indicate any cracking around the connection. The nonlinearity is attributed to the localized bearing failure of concrete around the flanges in the embedded region. The level of nonlinearity increased during seismic tests. Prior to failure, the connection was subjected to several cycles of shears that exceeded the nominal and "provided" capacities. The connection suddenly lost its load carrying capacity during the negative half of the first cycle at 6% chord rotation as indicated in Figure 3.4. The failure occurred after reaching $2.03V_n$ (1.32 times the "provided" connection capacity) at 4.74% chord rotation.

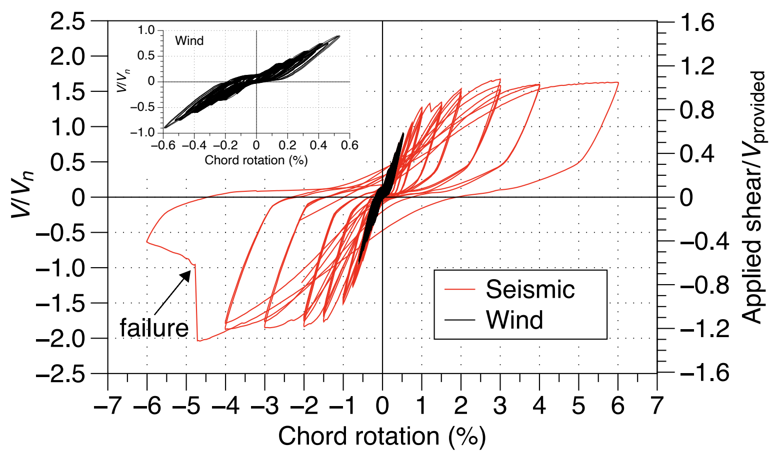

Figure 3.4 Normalized applied shear vs. chord rotation – specimen 1b (test 2).

Similar to specimen 1a (test 1), the coupling beam remained elastic during both the wind and seismic test protocols. The maximum flange strain indicates a maximum stress of $0.66F_y$, where F_y is the measured flange yield strength. Considering that the beam remained elastic, the observed nonlinearities are due to the damage in the connection region, which is also evident from the displacement measured at 1-7/8 in. from the face of the support, see Figure 3.5. During wind load tests, the maximum displacement near the support, which is expected to be small, was 0.10 times the peak tip deflection. For the seismic cycle at 6%, the ratio between maximum displacement near support and tip deflection was 0.22.

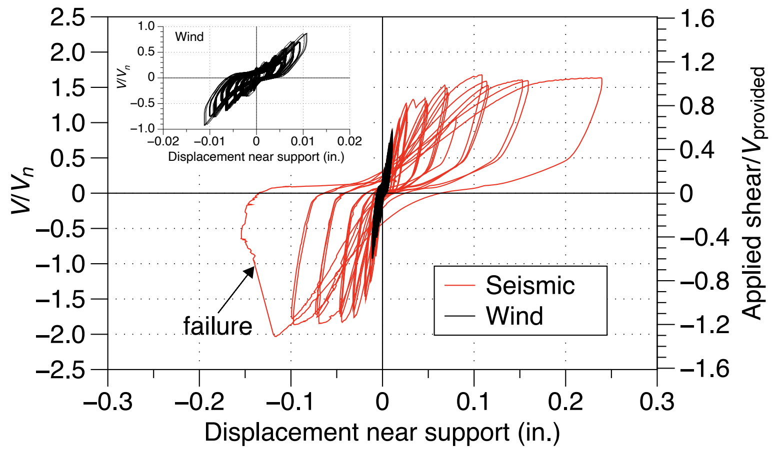

Figure 3.5 Normalized applied shear vs. displacement near support – specimen 1b (test 2).

The damage after completing the wind protocol load cycle and subjecting the connection to a series of chord rotations reaching a maximum value of 6% is shown in Figure 3.6. The loss of load-carrying capacity is primarily attributed to crushing above the top flange and between the flanges.

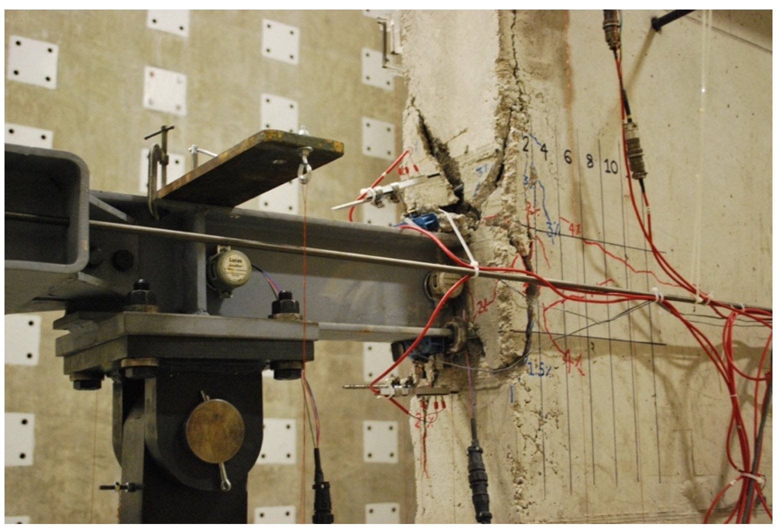

Figure 3.6 State of connection at the conclusion of testing – specimen 1b (test 2).

3.4 Specimen 2a (test 3)

The applied shear was normalized with respect to V_n (49.4 kips) and the "provided" connection capacity (56.0 kips) that was calculated using the measured material strengths and as-built dimensions. The normalized applied shear versus the chord rotation is plotted in Figure 3.7.

The connection lost significant stiffness during the first cycle of wind load step 6 (i.e., 3 cycles at V_n). For instance, the chord rotation was increased by a factor of 4.1 when the shear was increased from $0.83V_n$ to $0.95V_n$ (from 0.73 to 0.84 times the "provided" capacity). The condition of the specimen after unloading and removal of loose concrete is documented in Figure 3.8. It should be noted that prior to this stage of loading, the specimen had been subjected to a total of 270 cycles with increasing load amplitudes less than V_n (100 cycles @ $0.25V_n$, 100 cycles @ $0.40V_n$, 50 cycles @ $0.50V_n$, 15 cycles @ $0.50V_n$, and 5 cycles @ $0.83V_n$). Considering the significant loss of connection integrity, the remaining wind load steps (see Table 2.9) were not conduced. Deterioration of connection integrity is evident from the seismic tests: the load resisted by the connection was at most $0.77V_n$ and $0.96V_n$ for the positive and negative half cycles, respectively, even though the connection was subjected to 6% chord rotation.

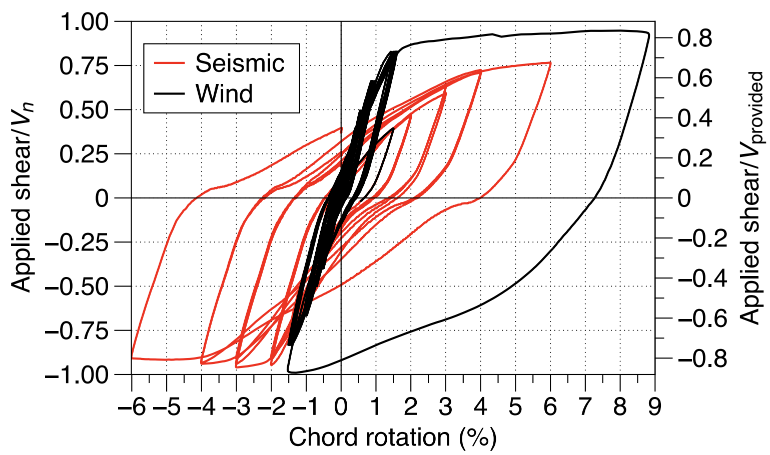

Figure 3.7 Normalized applied shear vs. chord rotation – specimen 2a (test 3).

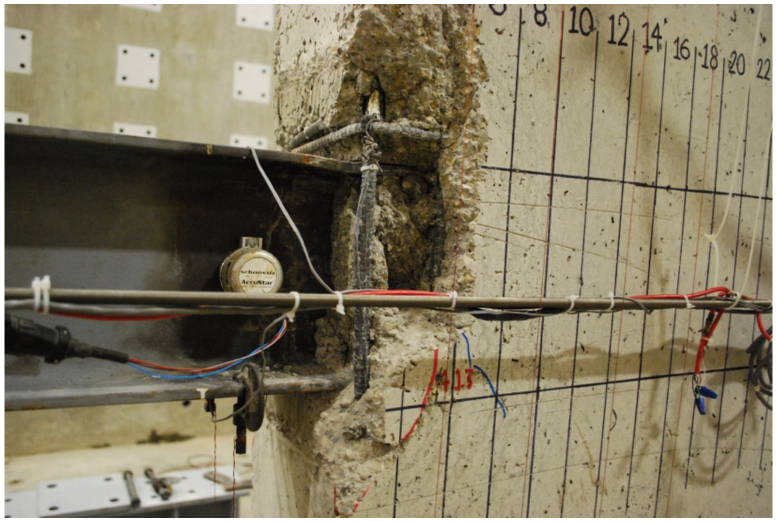

Figure 3.8 Condition of connection at the conclusion of wind load protocol tests – specimen 2a (test 3).

A still image captured from video recordings (Figure 3.9) suggests the formation of a "plastic hinge" in the coupling beam. The "plastic hinge" is attributed to excessive yielding, local flange bending, and web buckling. Flange yielding is seen from Figure 3.10. At $0.93V_n$, the bottom flange yielded. The strain in the top flange began to change sign, which is attributed to local flange bending, at $0.94V_n$. The maximum strain in the top and bottom flange was $2.83\varepsilon_y$ (ε_y = yield strain) and $1.65\varepsilon_y$, respectively. The residual bottom flange strain was nearly twice the yield strain. Flange bending and web buckling can be seen in the photographs shown in Figure 3.11.

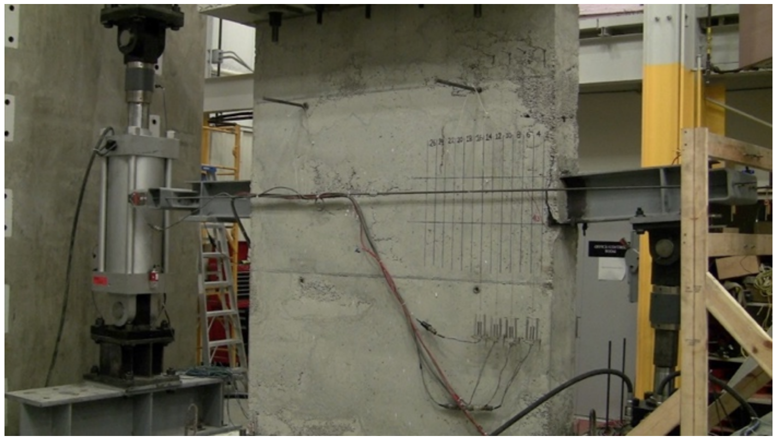

Figure 3.9 Deformation at peak chord rotation = 8.76% – specimen 2a (test 3)

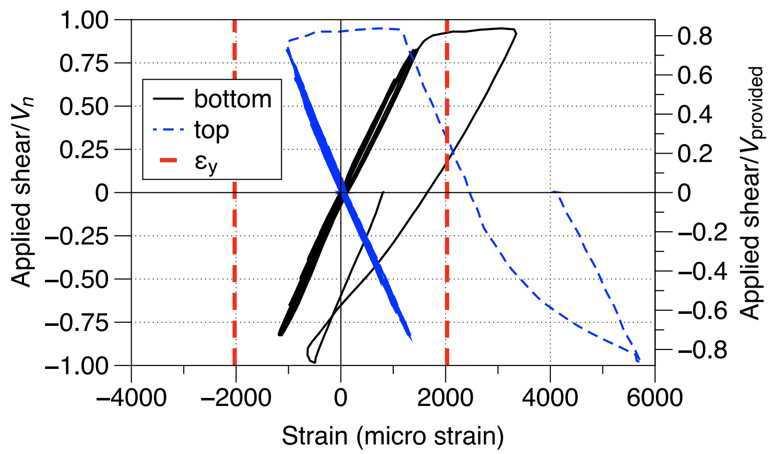

Figure 3.10 Normalized applied shear vs. beam flange strains – specimen 2a (test 3) during wind loading protocol.

(a) After one cycle at V_n (b) At the completing seismic cycles

Figure 3.11 Flange bending and web buckling – specimen 2a (test 3).

The relationship between the normalized applied shear and beam displacement at 2 in. from the face of the wall is shown in Figure 3.12. Prior to the sudden loss of stiffness, the beam displacement at this location was nearly 0.05 in., which corresponds to 17% of the maximum tip displacement. The hysteretic loops up to the sudden increase and relatively large displacement near the wall suggest connection flexibility. The same trend was observed for specimen 1b (test 2).

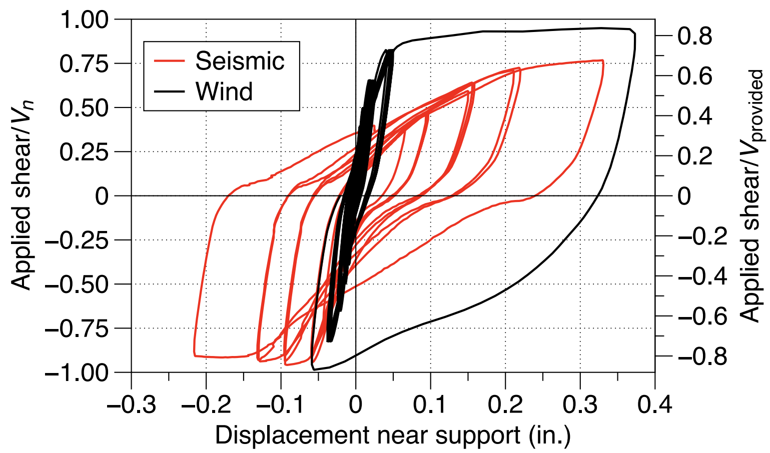

Figure 3.12 Normalized applied shear vs. displacement near support – specimen 2a (test 3).

As evident from Figure 3.13, the coupling beam was progressively being "pulled out" of the wall leading to an increase in the axial restraint apparatus's force. This trend is consistent with the results discussed previously. The permanent axial deformation and corresponding force were 0.25 in. and 6.1 kips at the conclusion of the first 270 cycles.

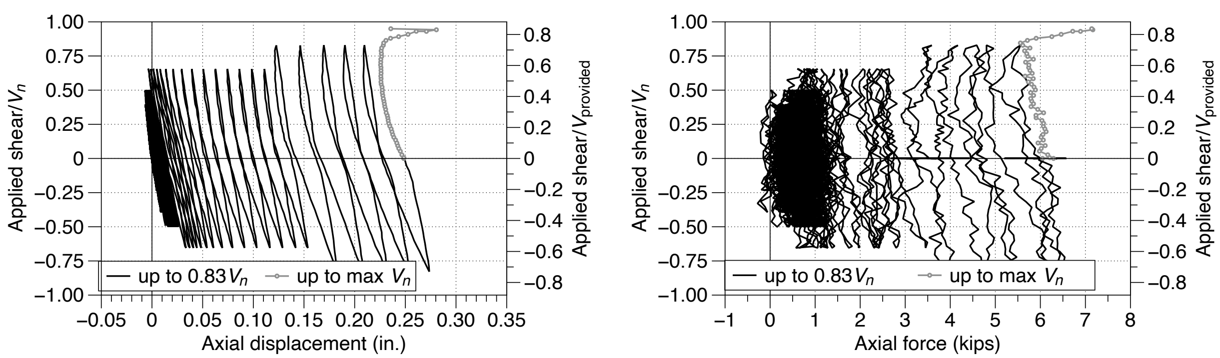

(a) Axial displacement (b) Axial force

Figure 3.13 Normalized applied shear vs. coupling beam axial displacement and axial force during wind load protocol tests – specimen 2a (test 3).

The excessive loss of stiffness correlates with the condition of the connection at the conclusion of wind load protocol testing, see Figure 3.14. The steel coupling beam flange was found to have bent, and the web had buckled (Figure 3.15). Damage had penetrated the wall between 5 in. and 6 in., reducing the available embedment length to approximately 0.58 times the original length (13 in.). After subjecting the connection to the post-wind seismic displacement protocol (see Table 2.9), the connection experienced further damage. The available embedment length had been reduced to between 4.5 in. and 6 in., i.e., a loss of more than 50%. Furthermore, the flange experienced more bending, web buckling became more pronounced, and the wall longitudinal bar buckled. These damages are shown in Figure 3.15.

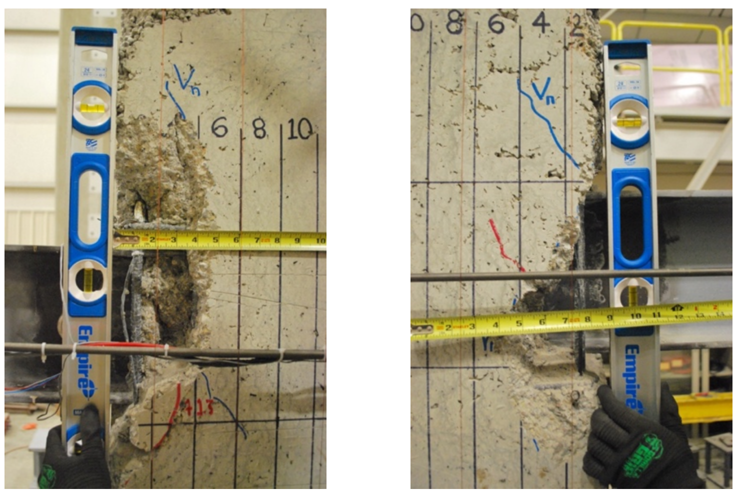

(a) South face (b) North face

Figure 3.14 Damage at the conclusion of wind load protocol testing and after removing loose concrete – specimen 2a (test 3).

(a) Flange bending and extent of damage

(b) Buckling of web and wall longitudinal reinforcement

Figure 3.15 Damage at the conclusion of seismic load protocol testing and after removing loose concrete – specimen 2a (test 3).

3.5 Specimen 2b (test 4)

The difference between this specimen and specimen 2a was the additional longitudinal reinforcement along the embedment length. Despite having more reinforcement, the performance of specimen 2b (test 4) was rather similar to specimen 2a (test 3). The connection lost a significant amount of stiffness during the first cycle at V_n (see Figure 3.16), which was also observed for specimen 2a (Figure 3.7). The sudden loss of stiffness is apparent by, for example, comparing the chord rotation of 1.43% at $0.83V_n$ versus 5.36% at $0.96V_n$, which was the largest shear that the connection could resist. The chord rotation was increased by a factor of nearly 4 when the applied shear was increased by $0.13V_n$ (6.43 kips).

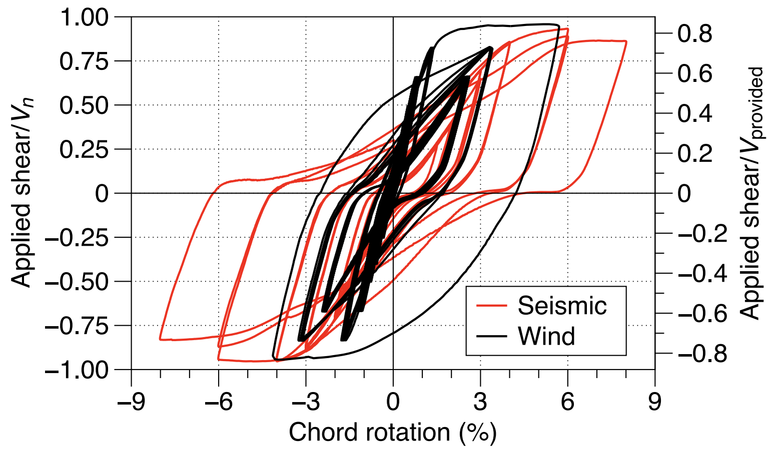

Figure 3.16 Normalized applied shear vs. chord rotation – specimen 2b (test 4).

The effect of the sudden loss of stiffness is also evident from Figure 3.17, which shows the relationship between the normalized applied shear and the beam displacement measured at 2-5/8 in. from the wall. The hysteresis loops prior to the rapid increase in the displacement point to the connection flexibility.

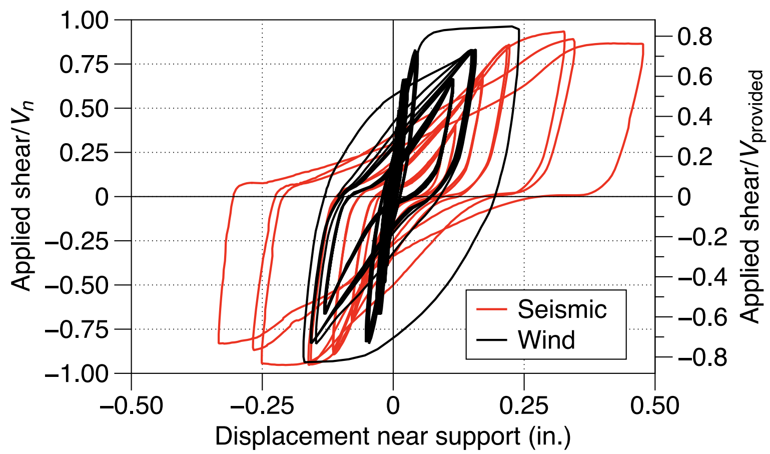

Figure 3.17 Normalized applied shear vs. displacement near support – specimen 2b (test 4).

The trends of the strains in the coupling beam top and bottom flanges are like those in specimen 2a (Figure 3.18). During the last cycle of wind-load protocol, which was aimed at subjecting the connection to V_n, the bottom flange yielded at an applied shear equal to $0.96V_n$. At nearly the same load, the sign of top flange strain began to reverse (from being in compression to becoming positive), which suggests flange bending. Prior to load reversal, i.e., at peak chord rotation of 5.70%, the bottom flange strain was 1.24ε_y (ε_y = yield strain). The residual stress on the bottom flange was nearly equal to the yield stress. Although compression strain was expected in the top flange, flange bending resulted in a tensile strain equal to 0.34ε_y.

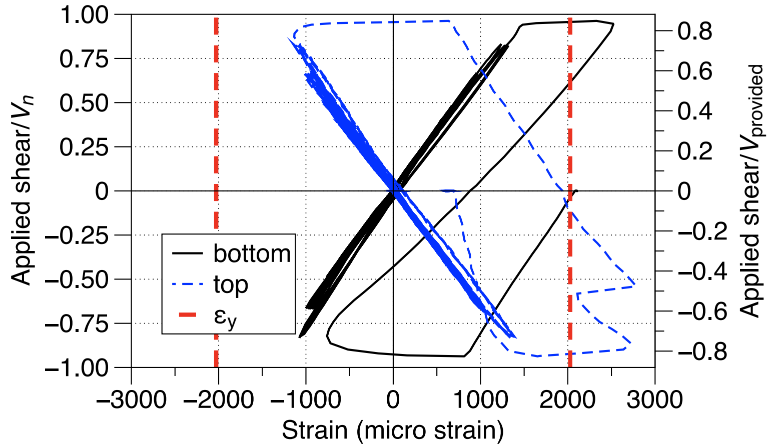

Figure 3.18 Normalized applied shear vs. beam flange strains – specimen 2b (test 4) during wind loading protocol.

The coupling beam in this specimen was also progressively "pulled out" of the wall as the level of the applied shear was increased, see Figure 3.19. Prior to attempting to subject the connection to V_n, the coupling beam had been "pulled out" 0.30 in. The corresponding force in the axial restraint apparatus was 7.2 kips.

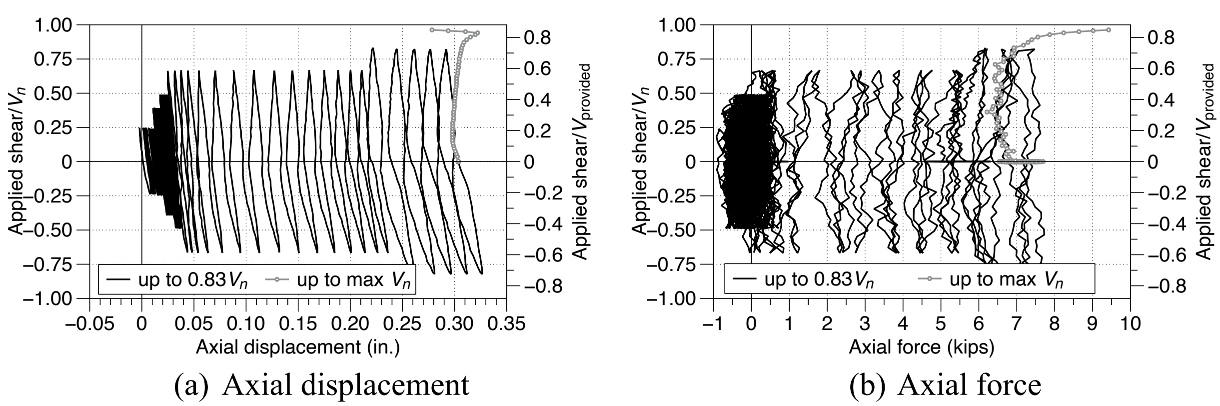

Figure 3.19 Normalized applied shear vs. coupling beam axial displacement and axial force during wind load protocol tests – specimen 2b (test 4).

At the conclusion of the wind load protocol, the wall above and below the beam had been damaged extensively. The extensive level of damage had reduced the available embedment length to between 9 in. and 11 in., i.e., between 15% and 31% of the embedment length had been lost. The smaller embedment reduces the connection stiffness, which is consistent with a sudden increase of chord rotation observed in Figure 3.16. The level of damage was, expectedly, increased with additional applications of wind load protocol (5 cycles at $0.83V_n$ and 15 cycles at $0.67V_n$) and seismic protocol (see Table 2.9). At the conclusion of the tests, between 5 in. and 7.5 in. of embedment length had been lost (0.39 and 0.58 times the embedment length). Moreover, both the top and bottom flanges were bent, and the web clearly had buckled. The condition of specimen 2b at the conclusion of the testing program is illustrated in Figure 3.21.

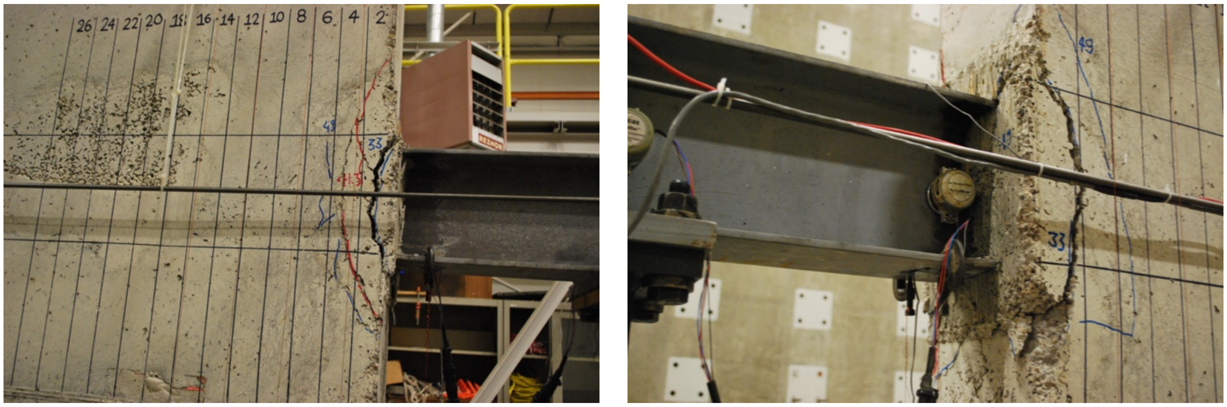

(a) North face (b) South face

Figure 3.20 Damage at the conclusion of wind load protocol testing (loose concrete was not removed) – specimen 2b (test 4).

(a) Penetration of damage into wall (b) Flange bending and web buckling

Figure 3.21 Damage at the conclusion of seismic load protocol testing and after removing loose concrete – specimen 2b (test 4).

3.6 Specimen 3 (test 5)

The applied shear was normalized with respect to the target value of V_n = 113 kips. The relationship between the normalized shear chord rotation is shown in Figure 3.22. Using the actual embedment length, as-built dimensions, and measured concrete strength, the "provided" connection capacity is 122 kips. This capacity was used to normalize the applied shear shown on the secondary y-axis. During the first cycle of step 6 (3 cycles at V_n), the connection suddenly lost stiffness after reaching $0.96V_n$. As a result, the tip deflection abruptly jumped to 1.03 in. (corresponding to 3.8% chord rotation), exceeding the safety displacement limit set in the controller, and loading was stopped. The photographs in Figure 3.23 show the status of the connection at this stage. The excessive permanent deformation of the beam is evident from Figure 3.23(b). As intended, the face bearing plates prevent local bending and buckling of the flanges and web.

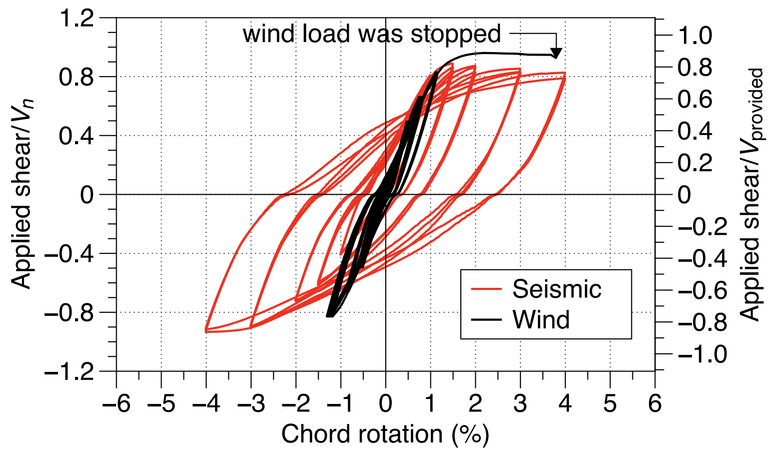

Figure 3.22 Normalized applied shear vs. chord rotation – specimen 3 (test 5).

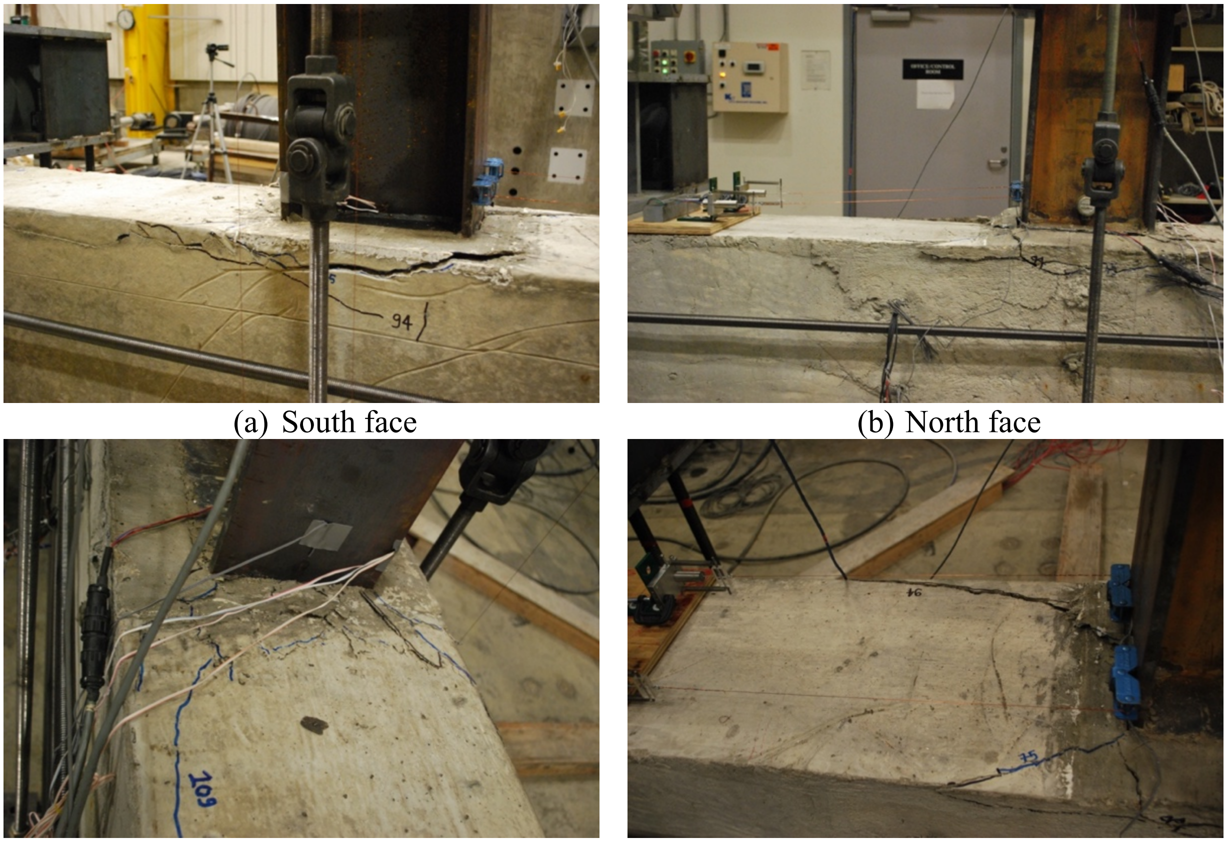

(a) South face (b) North face

(c) West side (d) East side

Figure 3.23 Damage at 0.96V_n for specimen 3 (test 5).

Although the specimen had failed before reaching V_n, the connection was subjected to the seismic protocol shown in Table 2.9 in an attempt to get data regarding post-damage behavior. The influence of damage is easily seen in the curves for the seismic segment. The maximum shear that could be resisted during seismic cycles was 0.89V_n. Considering the significant level of damage at the end of the wind load protocol and the performance during 3 cycles at 1.5%, 2%, and 3% chord rotation, loading was stopped after completing 2 cycles at 4% chord rotation.

The connection flexibility can be seen from Figure 3.24, which shows the coupling beam displacement at 2-5/8 in. from the face of the wall. Prior to failure, reflected by the sudden jump, the peak displacement near the support was nearly 0.14 times the peak deflection at the load point. At the conclusion of wind load protocol tests, the flanges did not yield (Figure 3.25); the maximum strain was 0.88ε_y, where ε_y is the yield strain. Figure 3.27 shows the shear stress (V/dt_w) vs. maximum shear strain determined from a rosette strain gage bonded to the web at the coupling beam's mid-depth – see Figure 3.26 for the relevant formulae. The shear strain at yield ($\gamma_y = \left(F_y/\sqrt{3}\right)/G$ with G taken as $0.39E$ by assuming the Poisson ratio is 0.27) is also plotted in Figure 3.27. A sudden increase in shear strain is observed when the applied shear reached $0.89V_n$; however, the largest maximum shear strain did not exceed γ_y– it was 0.98γ_y. Therefore, the sudden loss of stiffness leading to a jump in the displacements at the tip or near the support is primarily attributed to the loss of connection integrity. When subjected to seismic protocol, both the flange and web yielded. Although the level of yielding was more significant for the web, the maximum flange strain was 1.07ε_y and the maximum shear strain in the web at the coupling beam's mid-depth reached a value of nearly 2γ_y.

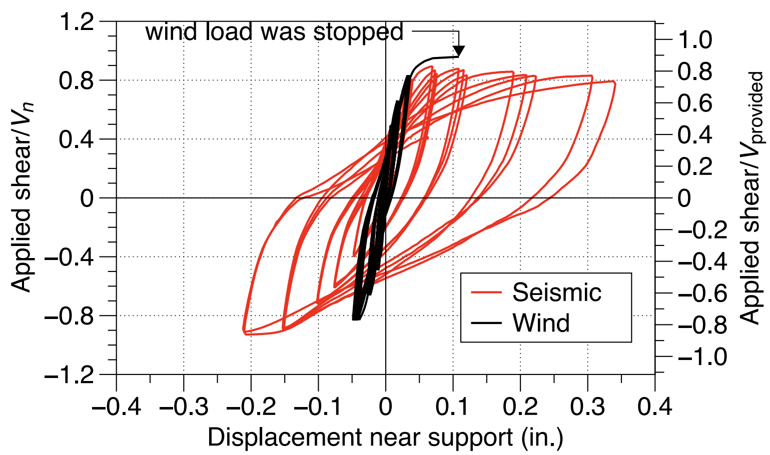

Figure 3.24 Normalized applied shear vs. displacement near support – specimen 3 (test 5).

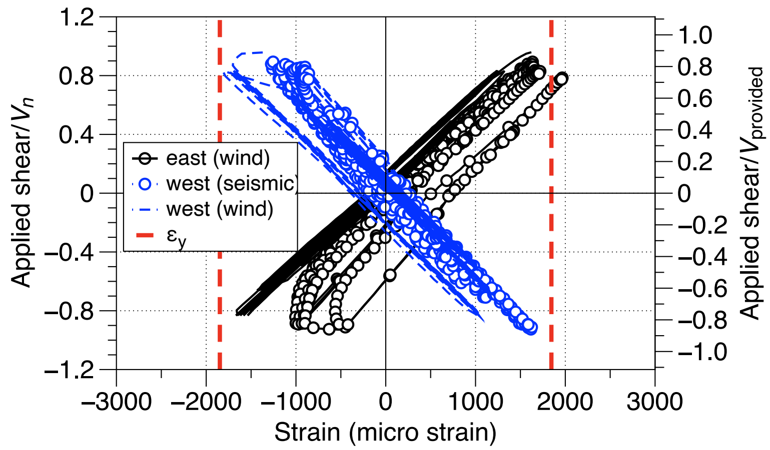

Figure 3.25 Normalized applied shear vs. beam flange strains – specimen 3 (test 5).

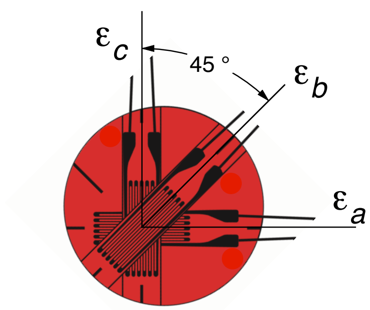

image modified from https://tml.jp/e

maximum and minimum principal strains:

$$\varepsilon_{max} = 0.5\left\{\varepsilon_a + \varepsilon_c + \sqrt{2[(\varepsilon_a - \varepsilon_b)^2 + (\varepsilon_b - \varepsilon_c)^2]}\right\}$$

$$\varepsilon_{min} = 0.5\left\{\varepsilon_a + \varepsilon_c - \sqrt{2[(\varepsilon_a - \varepsilon_b)^2 + (\varepsilon_b - \varepsilon_c)^2]}\right\}$$

maximum shear strain:

$$\gamma_{max} = \sqrt{2[(\varepsilon_a - \varepsilon_b)^2 + (\varepsilon_b - \varepsilon_c)^2]}$$

Figure 3.26 Calculation of peak normal and shear strains from rosette strain gage data.

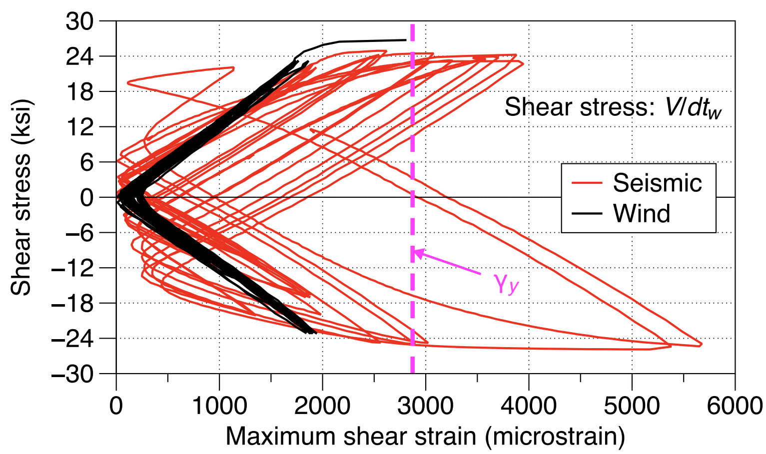

Figure 3.27 Shear stress vs. maximum shear strain – specimen 3 (test 5).

The coupling beam in this specimen was also progressively "pulled out" of the wall as the level of applied shear was increased, see Figure 3.28. At the end of wind load protocol testing, the connection had been moved axially by 0.17 in. (0.0063 times the original shear span of 27 in.) with a corresponding force of 15.8 kips (0.15 times the maximum applied shear) in the axial restraint apparatus.

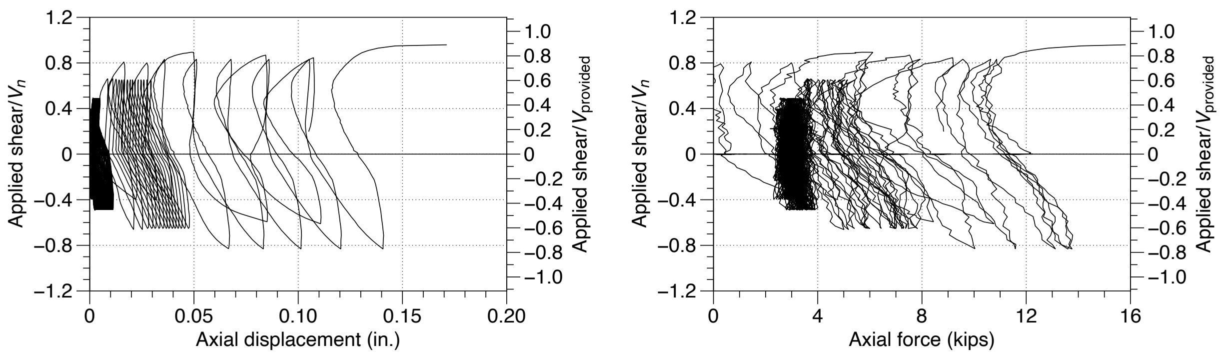

(a) Axial displacement (b) Axial force

Figure 3.28 Normalized applied shear vs. coupling beam axial displacement and axial force during wind load protocol tests – specimen 3 (test 5).

The connection had been damaged significantly at the conclusion of the seismic loading protocol, see Figure 3.29. Out of the total embedment length of 19 in., 7 and 9.5 in. of concrete between the flanges had been damaged significantly on the South and North face, respectively (Figure 3.29c). Over a depth ranging between 4 and 8.5 in., there was a gap between the flange and wall, suggesting bearing failure (Figure 3.29d). At the conclusion of loading, no evidence of local bending and buckling of the flanges and web was found; the face bearing plates performed at expected.

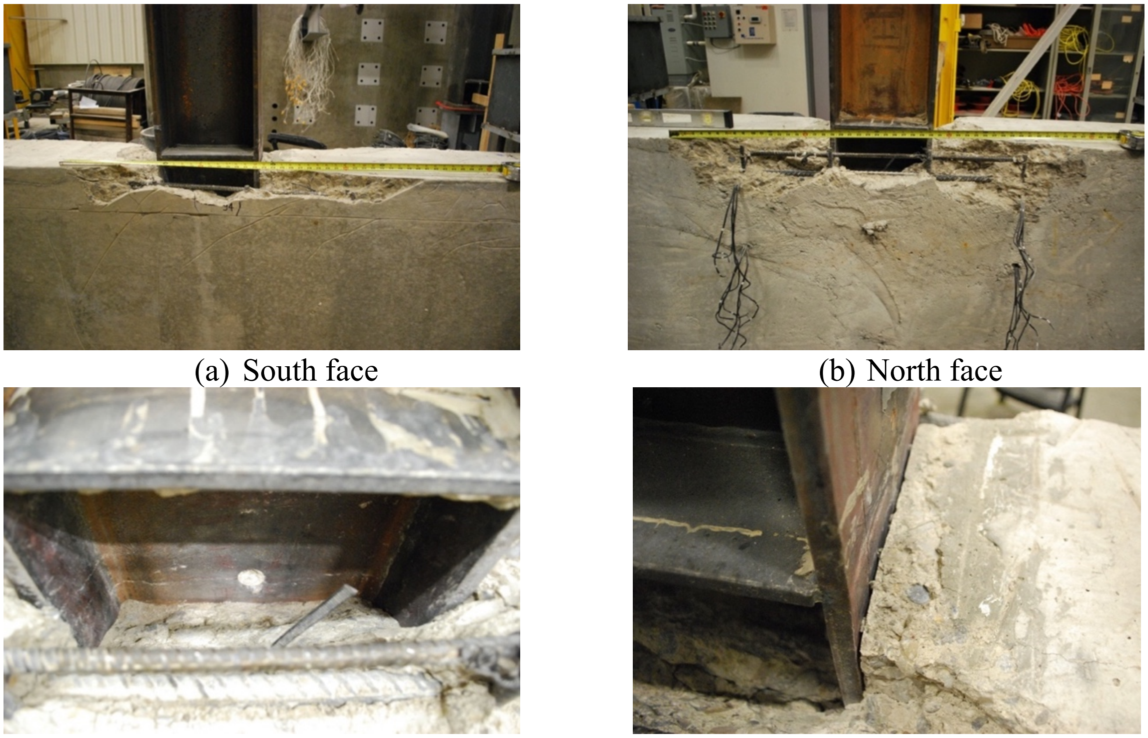

(a) South face (b) North face

(c) Damage penetration (d) Gap opening between flange and wall

Figure 3.29 Damage at the conclusion of seismic load protocol testing and after removing loose concrete – specimen 3 (test 5).

3.7 Specimen 4 (test 6)

The embedment length was 24 in. compared to 19 in. for specimen 3 (test 5). In contrast to specimen 3, one cycle at V_n could be applied, but the connection failed after reaching $0.99V_n$ during the application of the second cycle at 5.7% chord rotation. The connection had experienced significant damage during the first cycle at V_n as evident from the normalized applied shear force versus chord rotation shown in Figure 3.30. The positive chord rotation increased substantially with little increase in shear. This connection was not subjected to seismic protocol considering the large chord rotation at which it failed. Similar sudden increases are observed in the displacement at 2-5/8 in. from the wall (Figure 3.31), axial displacement (Figure 3.32a), and axial force in the axial restraint apparatus (Figure 3.32b). Due to delays in placing concrete in this specimen, water had to be added onsite to the concrete mix. The unexpected bad performance of this specimen is attributed to the concrete quality.

During the first cycle at V_n, the flange on the west side yielded (see Figure 3.33): the maximum strain $1.24\varepsilon_y$ (ε_y = yield strain based on the measured yield strength) with a residual strain (after completing the first cycle at V_n) of $0.33\varepsilon_y$. At the conclusion of loading, the residual strain in the west flange was $0.94\varepsilon_y$. The east flange remained elastic except during the last cycle before failure (i.e., the attempt to conduct the second cycle at V_n) when it marginally yielded: the maximum strain was $1.02\varepsilon_y$. The residual strain in the east flange was $0.084\varepsilon_y$ at the conclusion of loading.

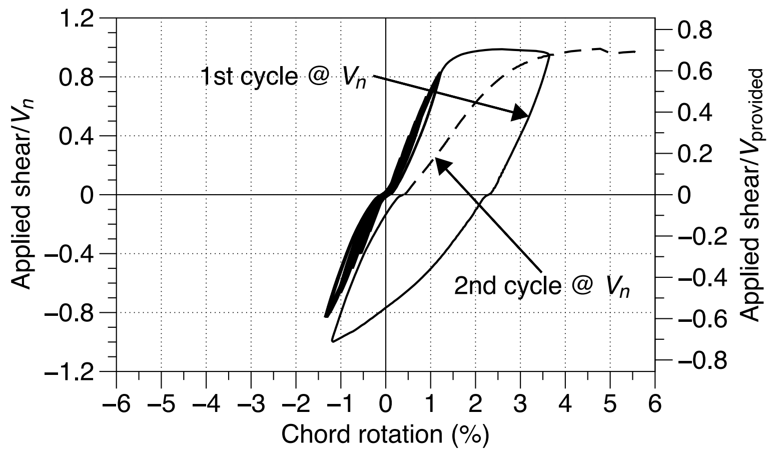

Figure 3.30 Normalized applied shear vs. chord rotation – specimen 4 (test 6).

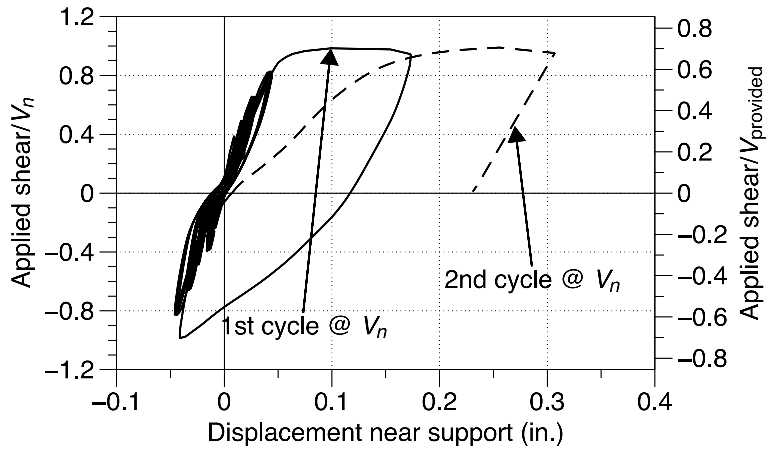

Figure 3.31 Normalized applied shear vs. displacement near support – specimen 4 (test 6).

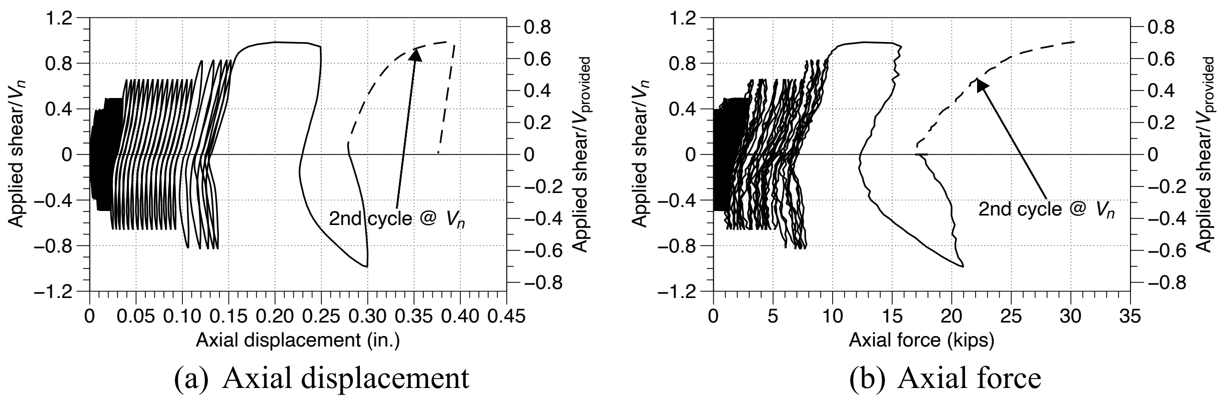

Figure 3.32 Normalized applied shear vs. coupling beam axial displacement and axial force – specimen 4 (test 6).

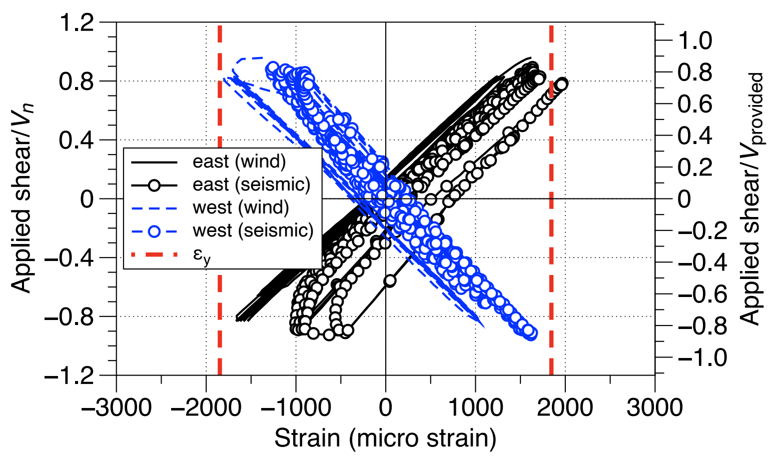

Figure 3.33 Normalized applied shear vs. beam flange strains – specimen 4 (test 6).

During the first 265 cycles (100 cycles @ $0.25V_n$, 100 cycles @ $0.40V_n$, 50 cycles @ $0.50V_n$, and 15 cycles @ $0.67V_n$), the relationship between shear stress and maximum shear strain (determined from the data measured by a rosette strain gage placed on the web at the mid-depth) does not depict any sudden increase (Figure 3.34). However, the maximum shear strain increased suddenly and exceeded γ_y during the first 2 cycles at $0.83V_n$; it reached a value of $1.09\gamma_y$. When subjected to 3 additional cycles at $0.83V_n$, the maximum shear strain did not increase noticeably (it was increased by 128 microstrains to $1.13\gamma_y$). The maximum shear strain more than doubled after the connection underwent one cycle at V_n: the maximum shear strain was $2.53\gamma_y$, i.e., 2.24 times larger than the value for the previous cycles. Before failure, the maximum shear strain was $3.01\gamma_y$, which is 1.19 times larger than the value measured during the first cycle at V_n. The sudden jumps of chord rotation and displacement near the support are not attributed to the extent of yielding of the web but primarily due to the damage in the connection region. This assessment is supported by examining the performance of specimen 5 (test 7) discussed in Section 3.8.

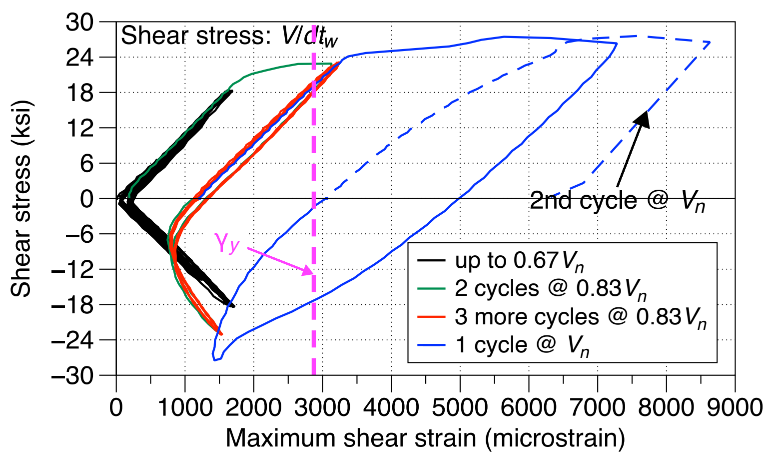

Figure 3.34 Shear stress vs. maximum shear strain – specimen 4 (test 6).

The level of damage, shown in Figure 3.35, is less than that observed in specimen 3 (test 5). In contrast to specimen 3, distributed cracks were found in the wall. Moreover, approximately 3 in. of loose/crushed concrete between the flanges could be removed, and the maximum depth of gap between the flange and wall was 3-3/8 in. The longer embedment length reduced the level of damage, but this specimen could resist only one cycle of V_n, whereas specimen 3 failed during the first attempt at applying V_n. Similar to specimen 4 (test 6), the face bearing plates prevented flange and web local bending and buckling.

(a) South face

(b) North face

(c) Damage penetration

Figure 3.35 Damage in specimen 4 (test 6) after removing loose concrete.

3.8 Specimen 5 (test 7)

In contrast to specimens 3 and 4 (tests 5 and 6), the entire wind loading protocol could be completed for this specimen that had auxiliary transfer bars. The specimen could develop its target V_n with a maximum chord rotation of nearly 1.6%. Due to localized damages in the connection region during wind loading, the specimen could resist only $0.91V_n$ when subjected to the seismic protocol. At the maximum applied chord rotation of 4%, the load-carrying capacity was between $0.82V_n$ and $-0.86V_n$. The benefits of auxiliary transfer bars are evident from the coupling displacement measured at 2-9/16 in. from the face of the wall (Figure 3.37), axial displacement of the coupling beam (Figure 3.38a), and force in the axial restraint apparatus (Figure 3.38b). For specimen 4 (test 6), which could only resist one cycle at V_n, the displacement near the support, axial displacement, and the axial restraint apparatus force were 2.9, 6.0, and 5.9 times their counterparts in specimen 5 (test 7), respectively. The lower values suggest the benefits of using auxiliary transfer bars in specimen 5. These bars are attached to the flange and provide a direct transfer of forces into the concrete rather than just relying on bearing stresses. The connection integrity was gradually lost during seismic tests as evident from higher values of displacement near the face of the wall, axial deformation of the coupling beam, and force in the axial restraint apparatus.

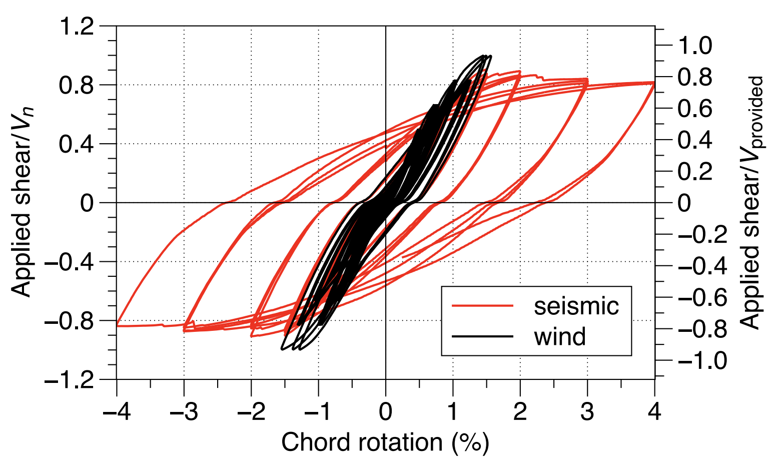

Figure 3.36 Normalized applied shear vs. chord rotation – specimen 5 (test 7).

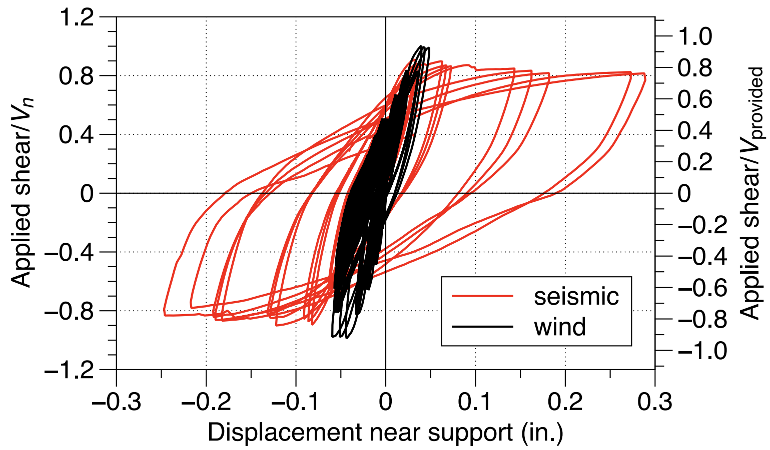

Figure 3.37 Normalized applied shear vs. displacement near support – specimen 5 (test 7).

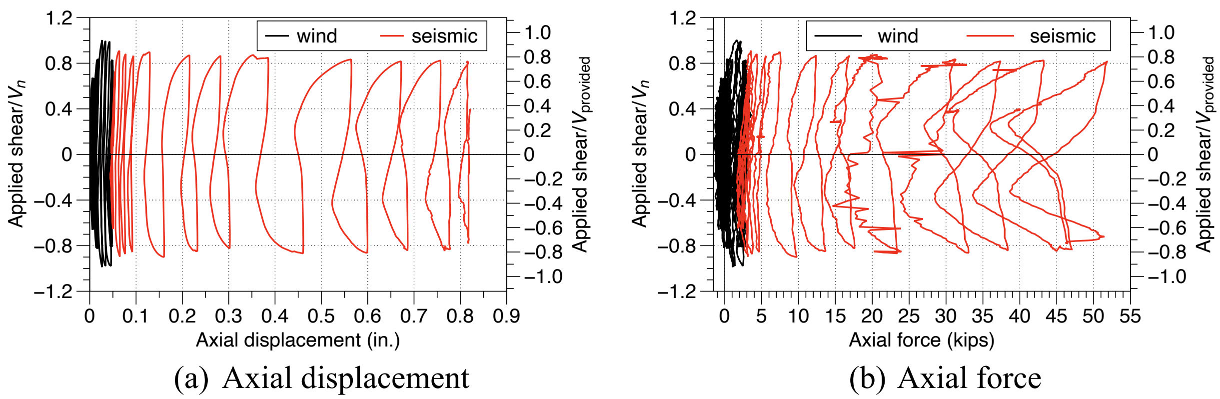

Figure 3.38 Normalized applied shear vs. coupling beam axial displacement and axial force – specimen 5 (test 7).

The flanges yielded during the application of wind load protocol, see Figure 3.39. The maximum strain in the west flange and east flange was 1.29 and 1.06 times the yield strain, respectively. The variation of maximum shear strain in the web at the midspan is plotted against the applied shear stress in Figure 3.40. For clarity, the results are shown separately for wind and seismic protocols. Up to $0.83V_n$, there is no sudden jump in the maximum shear strain and the maximum shear strain remained below shear yield strain, but the web at the mid-depth of the beam in specimen 4 (test 6) yielded when it was subjected to $0.83V_n$. During the first cycle at V_n, the web in specimens 4 and 5 yielded although the strain in specimen 4 ($2.53\gamma_y$) was about 1.3 times larger than in specimen 5 ($1.47\gamma_y$). The maximum shear strain in specimen 4 increased appreciably before failure when subjected to the second cycle at V_n whereas the maximum shear strain in specimen 5 became slightly smaller: $3.01\gamma_y$ vs. $1.34\gamma_y$. When subjected to seismic cycles, the maximum shear strain did not increase because the shear forces that could be resisted were smaller than V_n as a result of damage in the connection region that reduced the stiffness during the win loa tests.

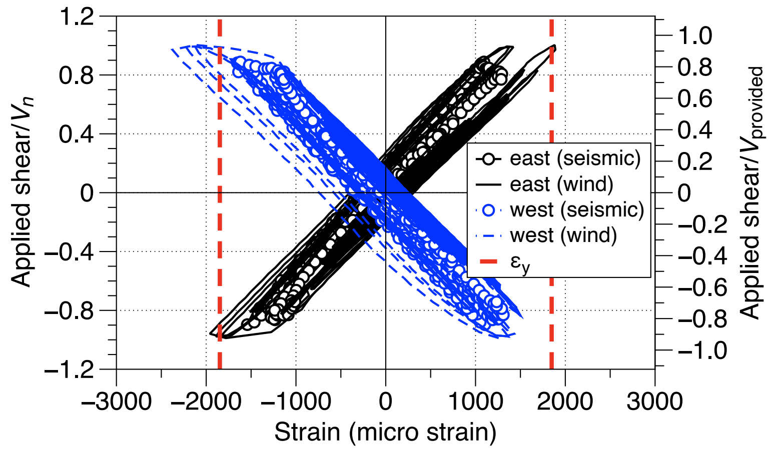

Figure 3.39 Normalized applied shear vs. beam flange strains – specimen 5 (test 7).

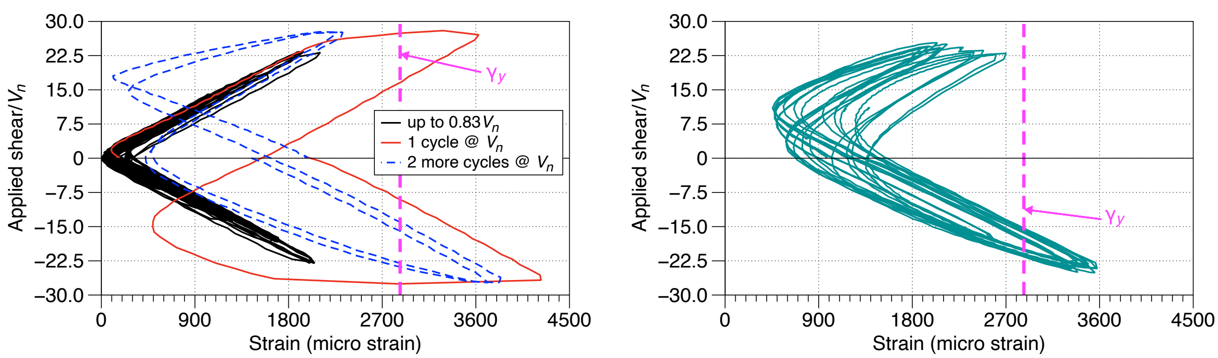

(a) Wind protocol (b) Seismic protocol

Figure 3.40 Shear stress vs. maximum shear strain – specimen 5 (test 7).

Specimen 4 had a longer embedment length than specimen 5 but did not have auxiliary transfer bars. Although the web in both specimens yielded, the responses of these two specimens were quite different. Specimen 4 failed after one cycle at V_n, but specimen 5 did not fail and the entire wind load protocol could be completed. Therefore, the sudden loss of stiffness of specimen 4 (Figure 3.30 or Figure 3.31) and its eventual failure is attributed to connection failure and not yielding of the coupling beam. The auxiliary transfer bars in specimen 5 prevented connection failure.

The level of damage was generally similar to specimen 3 (test 5), which had the same embedment length as specimen 5 (test 7), see Figure 3.41. No evidence of flange and web local bending and buckling could be found. On the South and North face, 8 in. and 9.75 in. of concrete had been crushed between the flanges and could be removed. However, the depth of the gap between the flange and wall was less than specimen 3: 5-3/8 in. compared to 8.5 in. The auxiliary transfer bars served two purposes: (1) they provided an additional source to resist bearing forces against the coupling beam's flanges in the embedment region, and (2) they contributed significantly towards restraining the "ratcheting effect" from the actuator. The latter contribution is evident from Figure 3.41c and Figure 3.41d that show excessive bending of the bars and weld fracture of the couplers. The presence of auxiliary transfer bars is attributed to specimen 5 (test 7) being able to resist V_n and completing the full wind load protocol followed by performing the seismic cycles.

(a) South face

(b) North face

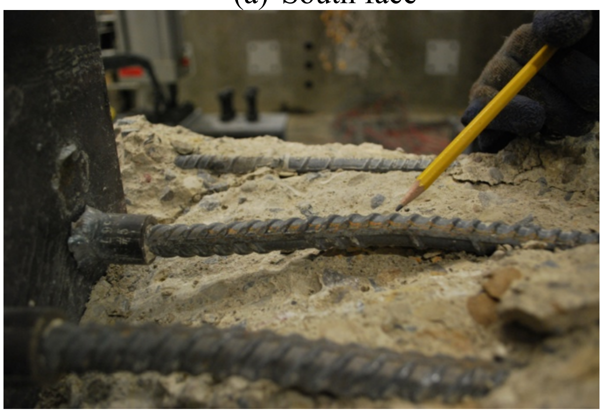

(c) Bending in auxiliary transfer bar

(d) Coupler weld fracture

Figure 3.41 Damage in specimen 5 (test 7) at the conclusion of seismic load protocol testing after removing loose concrete.

3.9 Specimen 6 (test 8)

The difference between this specimen and specimen 3 (test 5) and specimen 5 (test 7) is the presence of additional reinforcement to confine the concrete around the embedment length. However, specimen 6 suddenly failed at $0.79V_n$ during the first cycle aimed at achieving $0.83Vn$. The sudden loss of stiffness leading to failure is evident from Figure 3.42 and Figure 3.43. The chord rotation was increased from nearly 2% at the maximum applied shear of $0.79V_n$ to 5.6% when the applied shear was $0.76V_n$, or the coupling displacement at 2-1/2 in. from the face of the support was increased more than threefold. A similar trend is observed from the axial displacement of the coupling beam and the axial restraint apparatus's force shown in Figure 3.44a and Figure 3.44b, respectively. The flange on the east side had marginally yielded (the strain was 1.06 times the yield strain) before failure, see Figure 3.45. Immediately before the loss of load-carrying capacity, the web at the mid-depth yielded – the maximum shear strain reached a value of $1.05\gamma_y$ at $0.76V_n$. Considering the level of strains in the flange and web, the sudden loss of stiffness and failure is attributed to extensive damage in the connection region. It is not clear why the connection performed poorly despite having confining reinforcement.

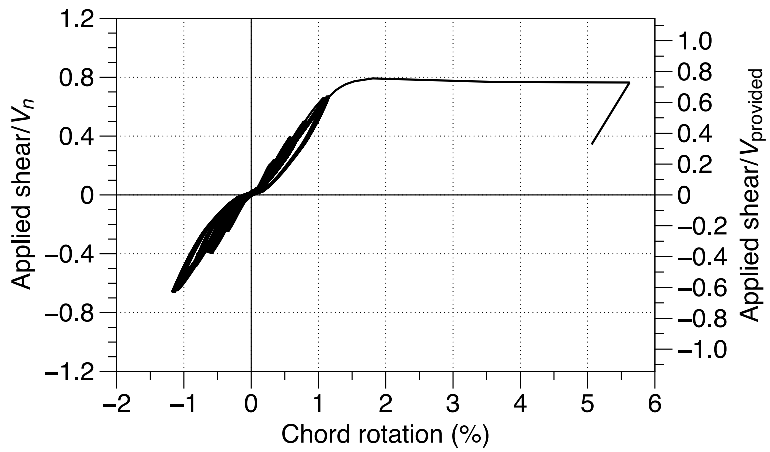

Figure 3.42 Normalized applied shear vs. chord rotation – specimen 6 (test 8).

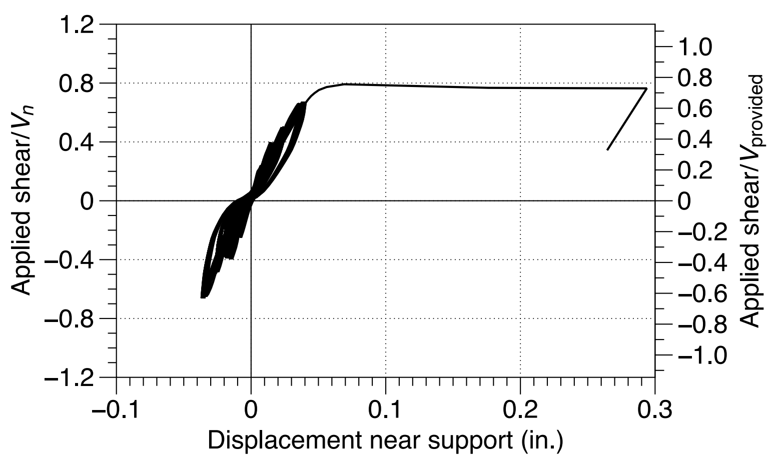

Figure 3.43 Normalized applied shear vs. displacement near support – specimen 6 (test 8).

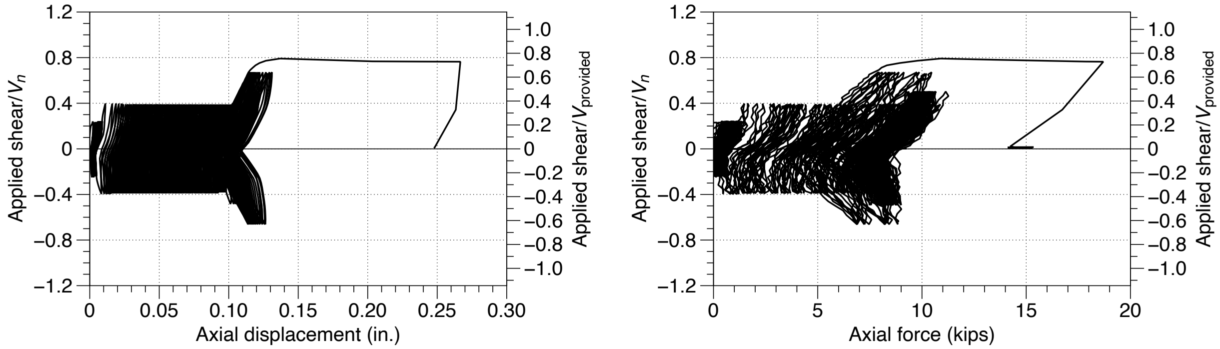

(a) Axial displacement (b) Axial force

Figure 3.44 Normalized applied shear vs. coupling beam axial displacement and axial force – specimen 6 (test 8).

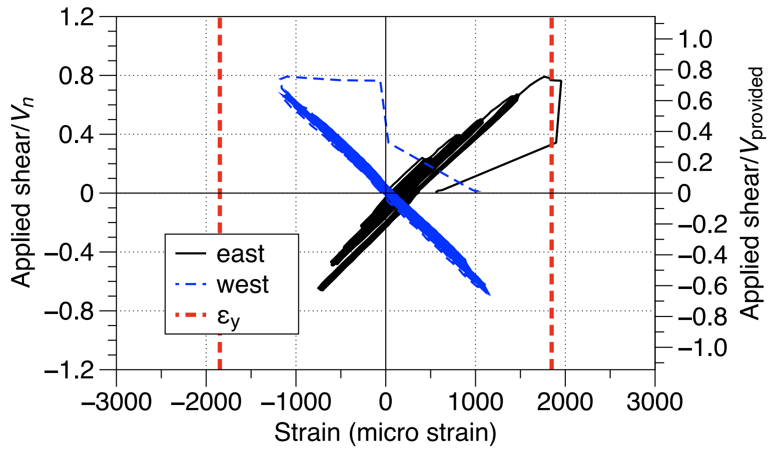

Figure 3.45 Normalized applied shear vs. beam flange strains – specimen 6 (test 8).

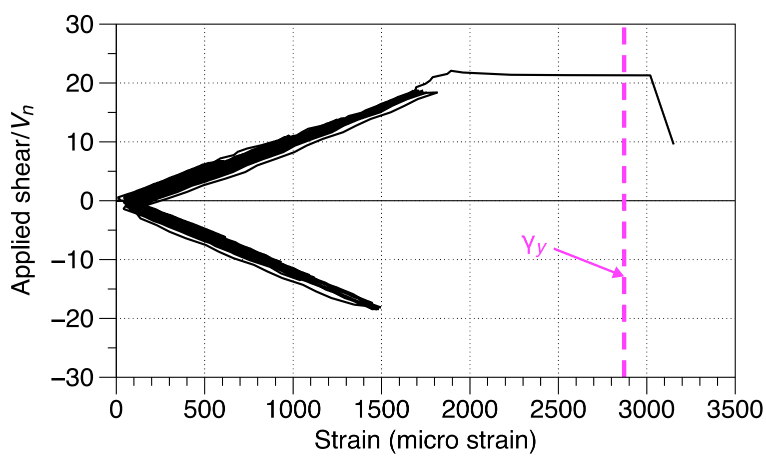

Figure 3.46 Shear stress vs. maximum shear strain – specimen 6 (test 8).

The level of damage was similar to the other specimens that could undergo more cycles and larger forces (Figure 3.47a and Figure 3.47b). Despite the presence of confinement reinforcement, major crushing occurred near the flanges (Figure 3.47e). Approximately 3 in. of concrete had been crushed and could easily be removed. A 4.5-in. deep gap was found between the flange and wall. The concrete between the flanges had been crushed and could easily be removed. The depth of the crushed concrete between the flanges was 9-5/8 in. on the North face and 10 in. on the South face (Figure 3.47c). Additionally, the flange on the north-west corner was found to have been locally bent below the face bearing plates (Figure 3.47d), but the web did not bend nor did it buckle locally.

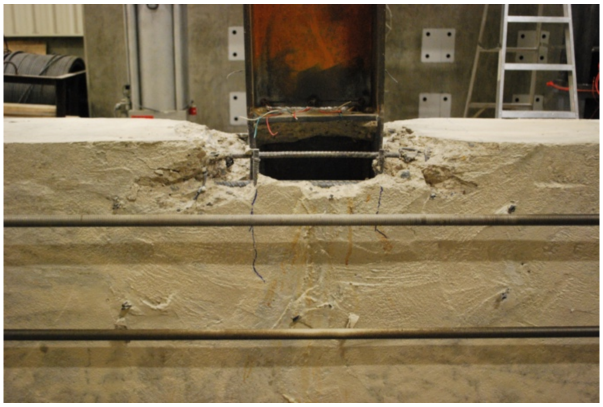

(a) South face

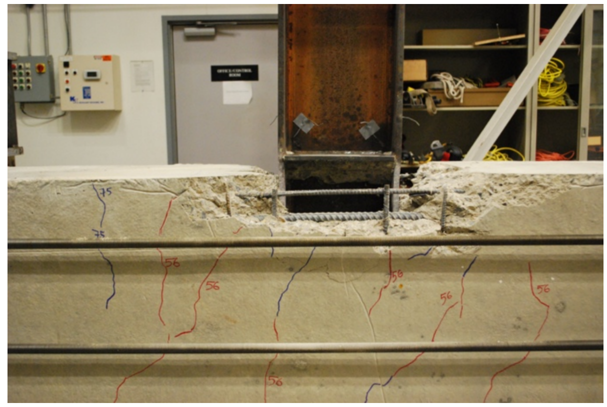

(b) North face

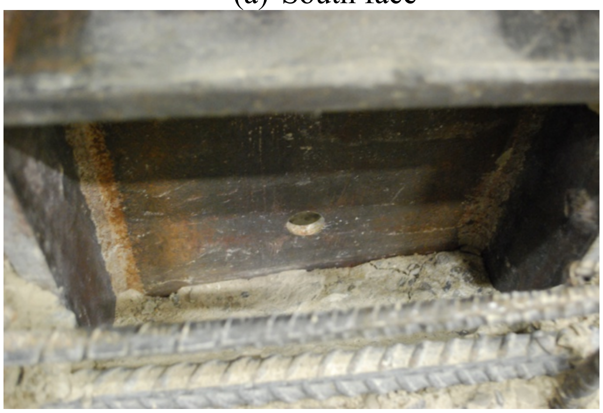

(c) Crushing between flanges

(d) Local flange bending

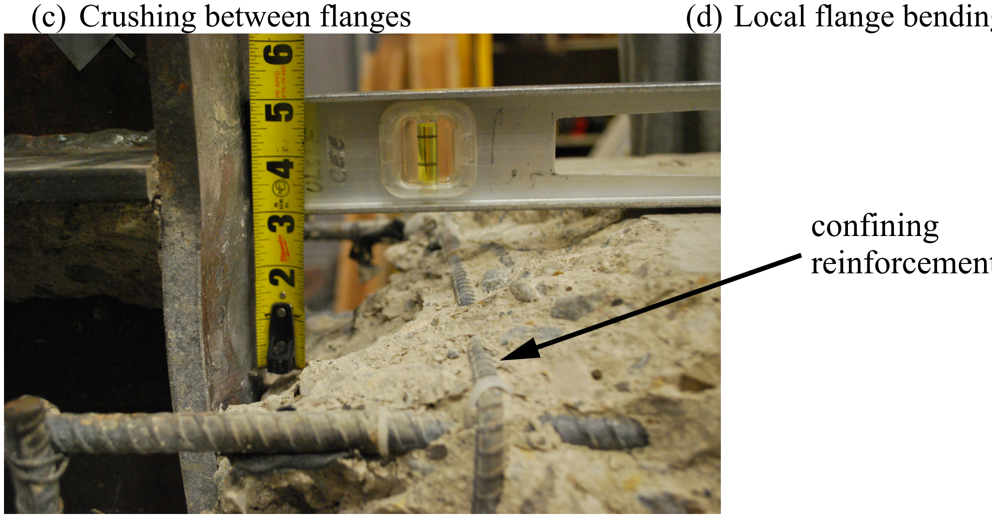

(e) Damage around flange

Figure 3.47 Damage in specimen 6 (test 8) after removing loose concrete.

3.10 Evaluation of comparable specimens

Several metrics were used to assess the impact of embedment length and detailing of the embedded region. Most of these comparisons are limited to the results obtained from wind load protocol tests.

3.10.1 Backbone curves and stiffness

The peak value of the applied load and the corresponding displacement at the coupling beam's tip were determined for each cycle. These values were averaged to obtain the peak values for each load step. The resulting values were used to define the backbone curves that are shown in Figure 3.48. In the following discussions, the backbone curves of similar specimens are compared. To see potential differences, only the data within $V/V_n = \pm 1.2$ and chord rotation = ± 2% are shown. Additionally, peak-to-peak stiffness for each cycle was determined. The variation of stiffness throughout testing is illustrated in Figure 3.49. As expected, the connection stiffness degraded as the load level was increased. For a few cases, the stiffness during the second set of loading became larger than that during the first set of loading. This trend, which also has been observed by others (Hill et al., 2023), is deemed to be because the "shakedown" effects occurring during the first set of loading were overcome when the load was increased in the subsequent loading steps.

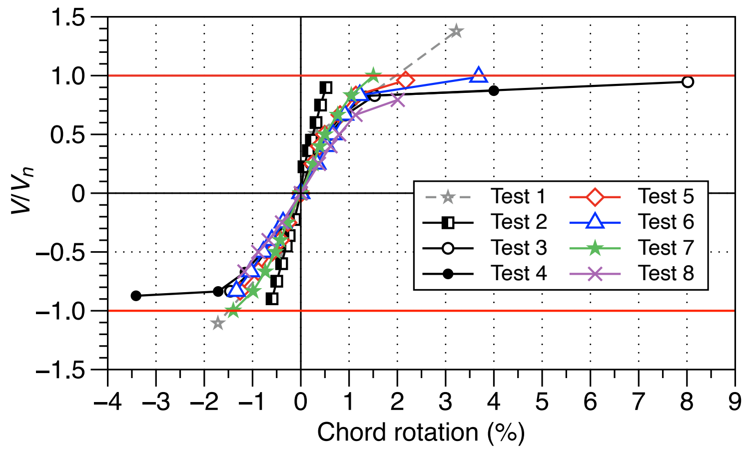

Figure 3.48 Backbone curves.

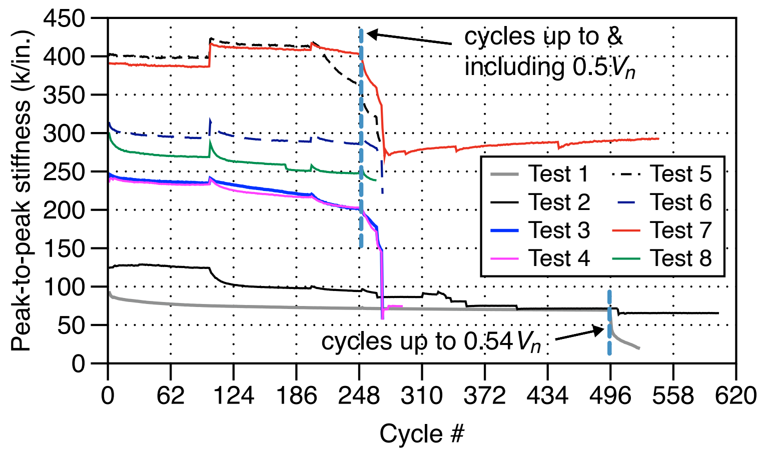

Figure 3.49 Variation of peak-to-peak stiffness.

Specimens 1a (test 1) and 1b (test 2) were identical except for the embedment length and reinforcement along the embedded region; specimen 1a was designed per AISC 341-16 while specimen 1b was designed according to AISC 341-22. As discussed in Chapter 2, specimen 1a was subjected to 495 load cycles corresponding to $0.54V_n$ before being subjected to $1.43V_n$. Up to approximately $0.54V_n$, specimen 1b was subjected to 100 cycles at $0.25V_n$, 100 cycles at $0.40V_n$, and 50 cycles at $0.50V_n$. As seen from Figure 3.50, specimen 1a exhibits a smaller stiffness (indicated by a shallower slope of the normalized applied shear – chord rotation backbone curve) than specimen 1b. A similar trend is observed by comparing the peak-to-peak stiffness (Figure 3.49). The lower stiffness is attributed to specimen 1a being subjected to more cycles with larger load levels than specimen 1b. Specimen 1a lost a significant amount of stiffness when subjected to $1.43V_n$, which should be expected as the load exceeded the design force (V_n) by 43%.

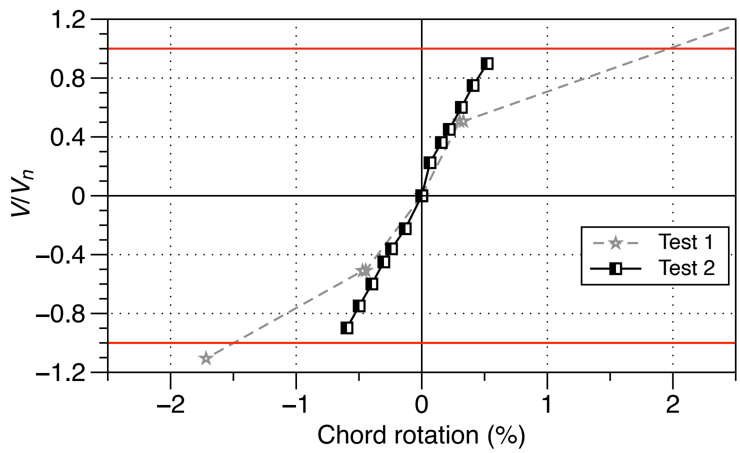

Figure 3.50 Comparison of backbone curves of specimen 1a (test 1) and specimen 1b (test 2).

Specimens 2a and 2b (test 3 and test 4, respectively) were also comparable except for the additional longitudinal reinforcement required by AISC 341-22 over the embedment length. These two specimens were subjected to identical loading protocols. The backbone curves of these two specimens are nearly identical (Figure 3.51) even though specimen 2b (test 4), which had been designed according to AISC 341-22, had more longitudinal reinforcement than specimen 2b (test 3). The stiffness of these two specimens is also similar (Figure 3.49).

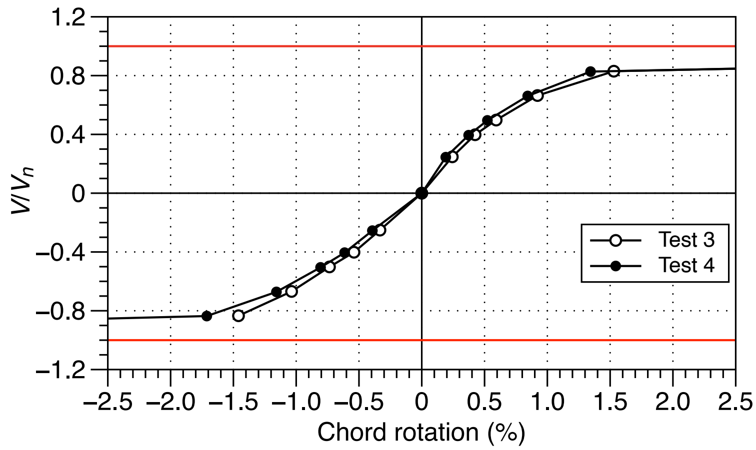

Figure 3.51 Comparison of backbone curves of specimen 2a (test 3) and specimen 2b (test 4).

In terms of the amount of longitudinal reinforcement along the embedment length, specimens 3 to 6 (tests 5 to 8) were very similar as they all had been designed per AISC 341-22. The longer embedment length in specimen 4 (test 6) resulted in a slightly different amount of longitudinal reinforcement. As discussed in Section 3.9, specimen 6 (test 8) performed much worse than the other specimens. This trend is visible from Figure 3.52; specimen 6 (test 8) had the lowest stiffness (among tests 5-8), particularly for the positive cycles. The peak-to-peak stiffness shown in Figure 3.49 also indicates the same observation. Although specimen 4 (test 6) had the longest embedment length, its stiffness (assessed from the backbone curve's slope and peak-to-peak stiffness) was less than what specimen 3 (test 5) or specimen 5 (test 7) could achieve. The concrete quality in specimen 4 is somewhat questionable due to the extra water that had to be added onsite to the concrete mix. The difference between specimen 3 (test 5) and specimen 5 (test 7) was the presence of auxiliary transfer bars in specimen 5. There is no discernable difference between the backbone curves of these specimens up to $0.87V_n$ for the positive cycles. Specimen 5 (test 7) exhibited a larger stiffness (i.e., a steeper slope) for the negative cycles, but its peak-to-peak stiffness is rather similar to specimen 3 (test 5) as evident from Figure 3.49. The auxiliary transfer bars did not apparently enhance stiffness but increased the load-carrying capacity.

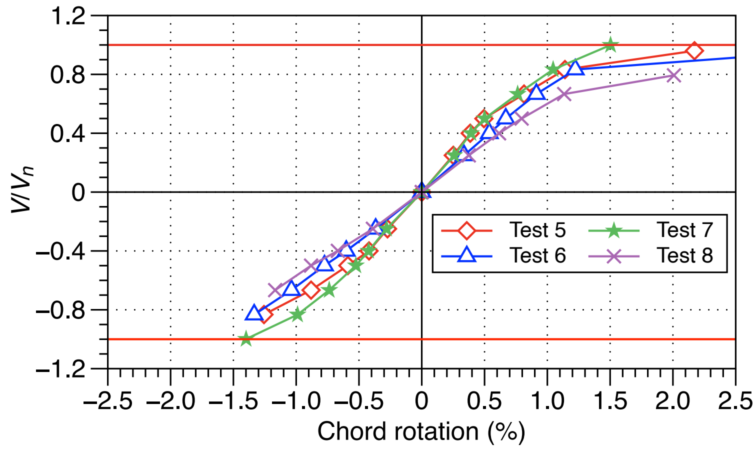

Figure 3.52 Comparison of backbone curves of specimens 3–6 (tests 5–8).

3.10.2 Strains in reinforcing bars

As discussed in Chapter 1, one of the changes in AISC 341-2022 results in more longitudinal reinforcement over the embedment length. Strain gages were bonded to a number of key reinforcing bars (see Chapter 2) primarily to examine the influence of the additional reinforcement. The strains corresponding to the largest applied shear are summarized in Table 3.1 and Table 3.2 for the specimens in phase 1 and phase 2, respectively in terms the yield strain (ε_y) determined from material testing. In specimen 6 (test 8), which failed suddenly when the applied shear was only $0.79V_n$, the longitudinal reinforcing bars farthest from the face of the wall marginally yielded – the maximum strain was 1.1 ε_y. For the other specimens, the longitudinal reinforcing bars did not yield. The maximum strain in specimens 2a and 2b (tests 3 and 4) is not appreciably different even though specimen 2b had more longitudinal reinforcement as required by AISC 341-22, e.g., $0.29\varepsilon_y$ vs. $0.19\varepsilon_y$ for specimen 2a and specimen 2b, respectively for the reinforcing bars closest to the exterior face of the wall (gage 1). The additional reinforcement in specimen 2b could not be engaged, i.e., did not yield, before the connection failed.

The discussions in Section 3.10.1 indicate that specimen 3 (test 5) and specimen 5 (test 7) performed similarly in terms of the backbone curves and peak-to-peak stiffness. However, the strains in comparable reinforcing bars in specimen 5 are much smaller than their counterparts in specimen 3, e.g., the largest strain during wind load tests is $0.90\varepsilon_y$ in specimen 3 vs. $0.093\varepsilon_y$ in specimen 5. The additional resistance mechanism provided by the auxiliary transfer bars reduced the demands in the longitudinal reinforcing bars.

Table 3.1 Strains in instrumented reinforcement at peak load– phase 1 specimens.

Specimen 1a (test 1)			Specimen 2a (test 3)		
Gage ID[a]	497 cycles @ 0.54Vn	30 cycles @ 1.43Vn	Gage ID	Wind	Seismic
SG 1	$0.0070\varepsilon_y$	$0.39\varepsilon_y$	SG 1	$0.29\varepsilon_y$	$0.15\varepsilon_y$
SG 2	$0.0081\varepsilon_y$	$0.41\varepsilon_y$	SG 2	$0.13\varepsilon_y$	$0.046\varepsilon_y$
Specimen 1b (test 2)			SG 3	$0.12\varepsilon_y$	$0.042\varepsilon_y$
Gage ID	Wind	Seismic	SG 4	$0.11\varepsilon_y$	$0.15\varepsilon_y$
SG 1	$0.038\varepsilon_y$	$0.54\ \varepsilon_y$	Specimen 2b (test 4)		
SG 2	$0.029\varepsilon_y$	$0.71\varepsilon_y$	Gage ID	Wind	Seismic
SG 3	$0.024\varepsilon_y$	$0.98\varepsilon_y$	SG 1	$0.19\varepsilon_y$	$0.13\varepsilon_y$
SG 4	$0.059\varepsilon_y$	$0.39\varepsilon_y$	SG 2	$0.16\varepsilon_y$	$0.11\varepsilon_y$
SG 5	$0.054\varepsilon_y$	$0.61\varepsilon_y$	SG 3	$0.10\varepsilon_y$	$0.015\varepsilon_y$
SG 6	$0.037\varepsilon_y$	$0.43\varepsilon_y$	SG 4	$0.087\varepsilon_y$	$0.17\varepsilon_y$
			SG 5	$0.052\varepsilon_y$	---[b]
			SG 6	$0.087\varepsilon_y$	$0.068\varepsilon_y$
			SG 7	$0.070\varepsilon_y$	$0.056\varepsilon_y$
			SG 8	$0.081\varepsilon_y$	$0.17\varepsilon_y$

[a] see Figure 3.53
[b] strain gage was lost.

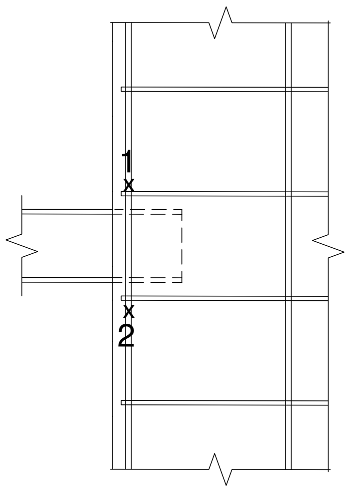

(a) Specimen1a (test 1)

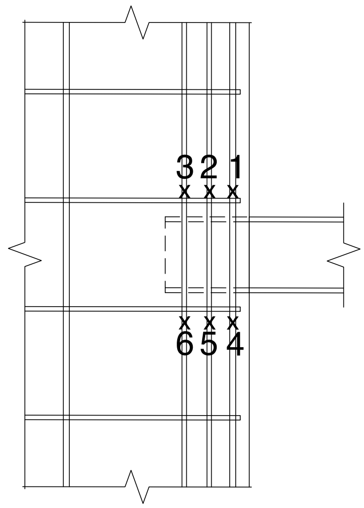

(b) Specimen 1b (test 2)

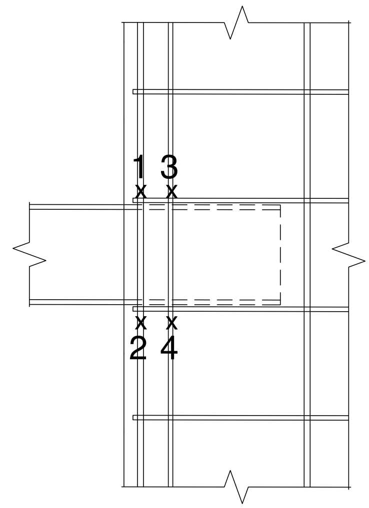

(c) Specimen 2a (test 3)

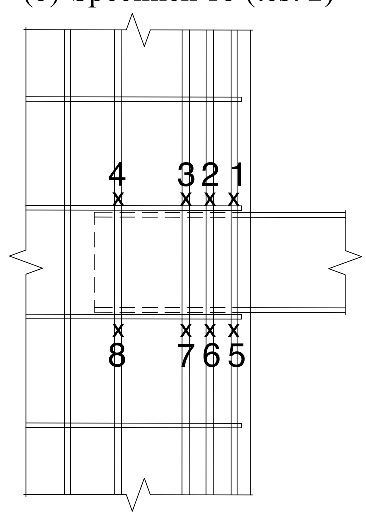

(d) Specimen 2b (test 4)

Figure 3.53 Locations of strain gages – phase1 specimens.

Table 3.2 Strains in instrumented reinforcement at peak load – phase 2 specimens.

Specimen 3 (test 5)			Specimen 4 (test 6)		
Gage ID[a]	Wind	Seismic	Gage ID	Wind	Seismic
SG1	$0.27\varepsilon_y$	$0.17\varepsilon_y$	SG1	$0.70\varepsilon_y$	not conducted
SG2	$0.063\varepsilon_y$	$0.061\varepsilon_y$	SG2	$0.30\varepsilon_y$	
SG3	$0.90\varepsilon_y$	$0.54\varepsilon_y$	SG3	$0.74\varepsilon_y$	
SG4	$0.20\varepsilon_y$	$0.057\varepsilon_y$	SG4	$0.35\varepsilon_y$	
SG5	$0.039\varepsilon_y$	$0.052\varepsilon_y$	SG5	$0.18\varepsilon_y$	
SG6	$0.25\varepsilon_y$	$0.03\varepsilon_y$	SG6	$0.28\varepsilon_y$	
SG7	$0.27\varepsilon_y$	$0.43\varepsilon_y$	SG7	$0.34\varepsilon_y$	
SG8	$0.033\varepsilon_y$	$0.038\varepsilon_y$	SG8	$0.30\varepsilon_y$	
Specimen 5 (test 7)			Specimen 6 (test 8)		
Gage ID	Wind	Seismic	Gage ID	Wind	Seismic
SG1	$0.087\varepsilon_y$	$0.16\varepsilon_y$	SG1	$0.45\varepsilon_y$	not conducted
SG2	$0.086\varepsilon_y$	$0.023\varepsilon_y$	SG2	$0.21\varepsilon_y$	
SG3	$0.025\varepsilon_y$	$0.022\varepsilon_y$	SG3	$0.20\varepsilon_y$	
SG4	$0.018\varepsilon_y$	$0.041\varepsilon_y$	SG4	$1.1\varepsilon_y$	
SG5	$0.078\varepsilon_y$	$0.32\varepsilon_y$	SG5	$0.94\varepsilon_y$	
SG6	$0.026\varepsilon_y$	$0.045\varepsilon_y$	SG6	$0.26\varepsilon_y$	
SG7	$0.093\varepsilon_y$	$0.017\varepsilon_y$	SG7	$0.38\varepsilon_y$	
SG8	$0.062\varepsilon_y$	$0.094\varepsilon_y$	SG8	$1.0\varepsilon_y$	

[a] see Figure 3.54

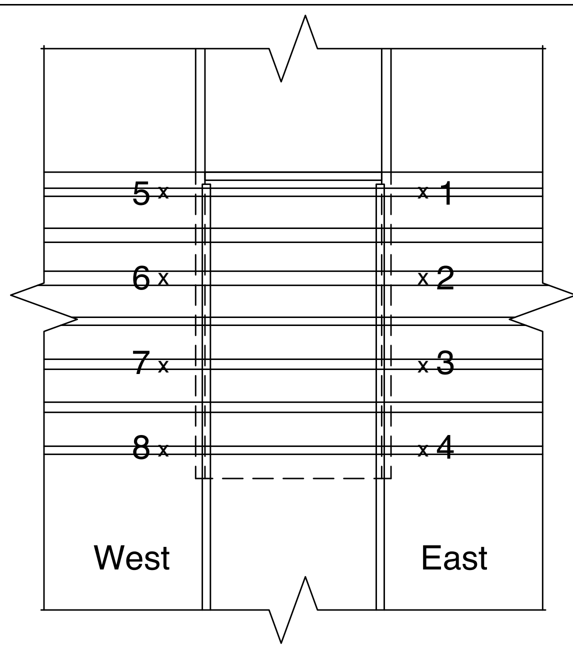

Figure 3.54 Locations of strain gages – phase2 specimens.

3.10.3 Energy dissipation

The area of the hysteresis loops from beam applied shear-tip deflection curves indicates the dissipated energy. The level of energy dissipation denotes the level of inelasticity and damage. The cumulative dissipated energies are compared in Figure 3.55. The x-axis denotes the wind loading steps presented in Table 2.9. The comparison is made separately for the specimens in phase 1 and phase 2 because of their differences. The loading protocol was different for specimen 1a and 1b (tests 1 and 2); therefore, the energy dissipation of these two specimens is not compared.

Consistent with the previous observations made from backbone curves, stiffness, and strains in longitudinal reinforcement along the embedment length, no discernable difference is observed between specimen 2a (test 3) and specimen 2b (test 4) even though specimen 2b had more longitudinal reinforcement per AISC 341-22. Specimen 6 (test 8), which failed at a much smaller load than the other second phase specimens, dissipated the most amount of energy. The larger energy dissipation is consistent with this specimen having the lowest stiffness. Specimen 5 (test 7), which had auxiliary transfer bars, dissipated the least amount of energy up to the last step that the other specimens could be tested. The additional resistance mechanism provided by the auxiliary transfer bars minimized the level of damage in the connection region.

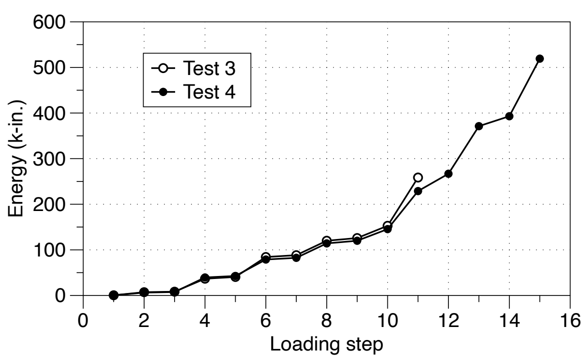

(a) Phase 1 specimens

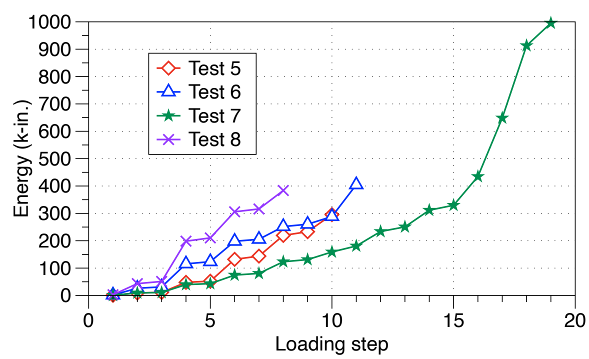

(a) Phase 2 specimens

Figure 3.55 Comparison of dissipated energy.

3.11 Strength

The connections were designed using Eq 3.1, which is the current equation H4-1 in AISC 341-22. Using the measured material properties and the as-built dimensions, the connection capacities were calculated according to Eq 3.1. Table 3.3 compares the maximum applied shear against the design shear and the calculated value.

$$V_n = 1.54\sqrt{f_c'}\left(\frac{b_w}{b_f}\right)^{0.66}\beta_1 b_f L_e\left[\frac{0.58-0.22\beta_1}{0.88+\frac{g}{2L_e}}\right] \quad \textbf{Eq 3.1}$$

Only specimen 1a (test 1), specimen 1b (test 2), specimen 4 (test 6), and specimen 5 (test 7) could reach their target design V_n although specimen 4 failed during the second application of V_n. However, none of the specimens could develop their respective calculated capacities except for specimens 1a and 1b (tests 1 and 2). Therefore, the application of Eq 3.1 for low seismic regions needs to be reexamined. This equation is based on assuming a linear strain distribution, maximum concrete strain (ε_f) of 0.003, and the ratio of the neutral axis depth to the embedment length (c/L_e) = 0.66 – see Figure 3.56.

Table 3.3 Calculated and measured connection capacity.

Specimen ID	Test ID	Design V_n (kips)	V_n (kips) from Eq 3.1[a]	Test V_{max} (kips)	Test/ Design V_n	Test/ Calculated
1a	1	10	11.8	14.2	1.42	1.20
1b	2	10	15.5	20.4	2.04	1.32
2a	3	49.4	56	49	0.99	0.88
2b	4	49.4	56	47.4	0.96	0.85
3	5	113	122	109	0.96	0.89
4	6	113	158	113[b]	1.00	0.72
5	7	113	121	113[c]	1.00	0.93
6	8	113	118	89.7	0.79	0.76

[a] based on as-built dimensions and measured material properties
[b] failed during the second application of V_n
[c] maximum load used for testing

Eq 3.1 has been found to be adequate based on a large of number of past studies focused on special coupled walls (with boundary element reinforcement) for which the embedment length had been calculated to develop the coupling member capacity, i.e., the lesser of $2(1.1R_y)M_p/g$ and $1.1R_yV_p$. The past specimens were subjected to a relatively small number of cycles (approximately 60 or less) of loads/displacements with increasing amplitudes. The experimental data from the current research indicate Eq 3.1 is inadequate for ordinary coupled walls with no boundary element reinforcement, cases in which the embedment length is determined to develop V_n, and when the connection is subjected to many cycles (more than 500) of loads/displacements with increasing amplitudes. Therefore, a new equation is necessary for computing the required embedment length in ordinary coupled walls.

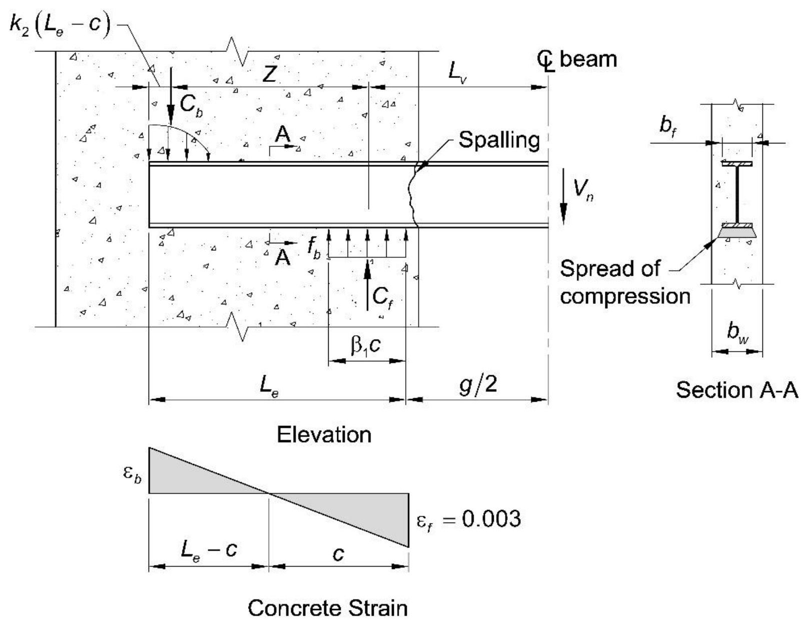

Figure 3.56 Modeling assumptions for Eq 3.1 (Source: AISC 341-22).

3.11.1 Development of a new design equation

The model shown in Figure 3.57 was used to assess the measured capacities. The strain at the wall-coupling beam interface (ε_f) and the depth of the neutral axis (c) were allowed to vary in order to maintain equilibrium of the vertical forces and moment. The concrete constitutive relationship consisted of a parabolic ascending branch with a linear post-peak descending branch. The selected model is illustrated in Figure 3.58. The peak concrete strength (f_c) was taken as $0.85f'_c$. Figure 3.57 illustrates two cases with $\varepsilon_f \leq \varepsilon_{01}$ and $\varepsilon_f > \varepsilon_{01}$ with strain at the end of the connection (ε_b) being less than ε_{01}. However, the actual calculations were based on $\varepsilon_b \leq \varepsilon_{01}$ or $\varepsilon_b > \varepsilon_{01}$. The bearing forces were determined using the coupling beam flange width, i.e., no "spreading" beyond the flange width was considered. On the other hand, in the derivation of Eq 3.1, the term $1.54\sqrt{f_c'}\left(b_w/b_f\right)^{0.66}$ implicitly is based on relying on the bearing stresses beyond the flange width. The value of applied shear (V) was incrementally increased, and the values of ε_f and c were iterated until equilibrium could be achieved. The connection capacity was taken as the maximum V for which equilibrium was possible.

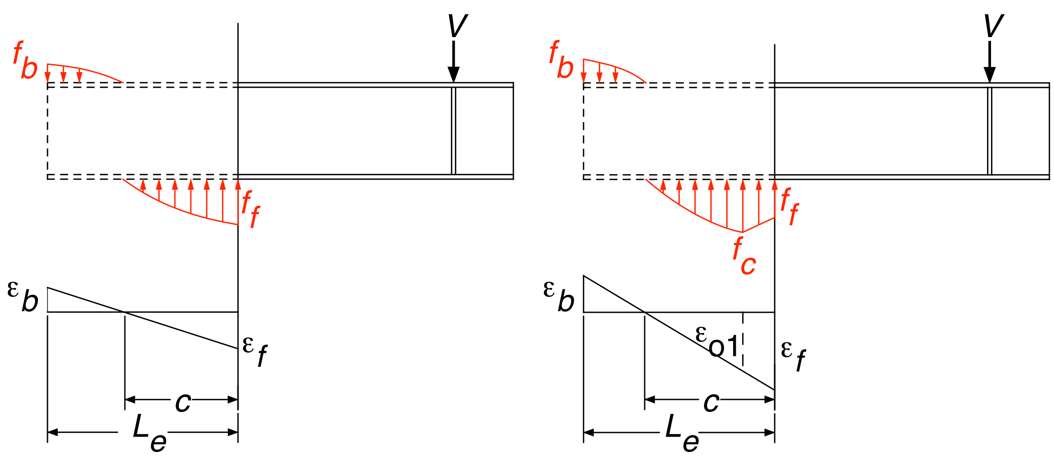

Figure 3.57 Model for computing connection capacity.

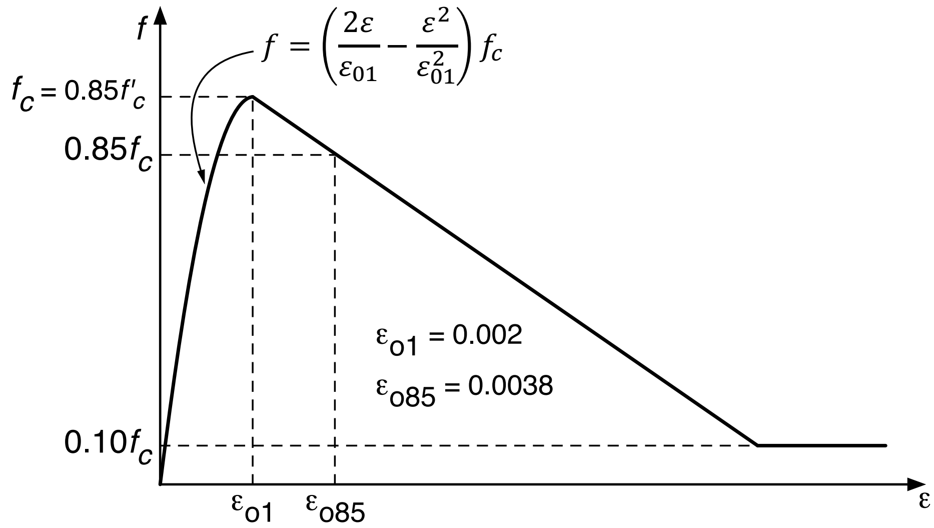

Figure 3.58 Concrete constitutive model.

For specimen 5 (test 7), which had auxiliary transfer bars, the same modeling approach was used except for adding forces from the auxiliary transfer bars – see Figure 3.59. The strain in the bars was limited to the maximum measured strain.

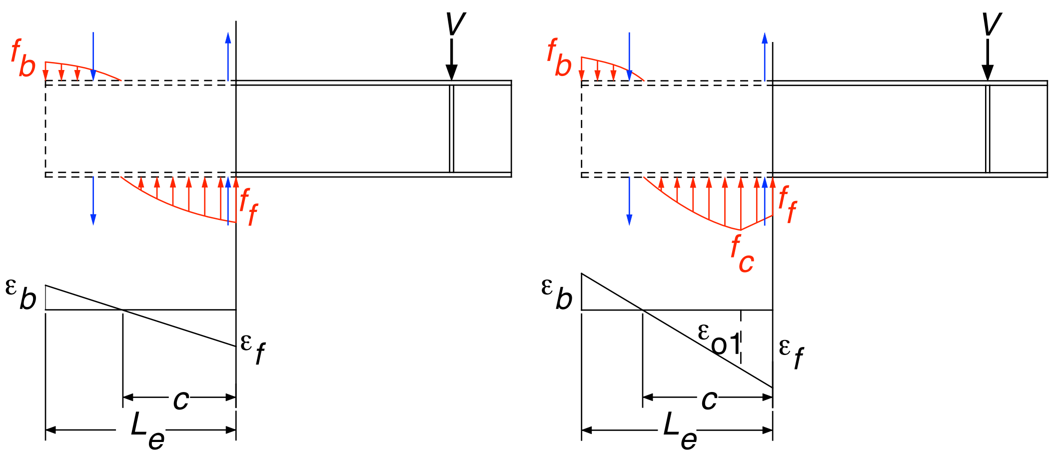

Figure 3.59 Model for computing connection capacity for specimen 5 (test 7) with auxiliary transfer bars.

Using the aforementioned methodology, the capacity of specimens 2a through 6 (tests 3 through 8) was determined. For specimens 1a and 1b (tests 1 and 2), the ratio of embedment length to coupling beam depth (L_e/d) is 1 or smaller. For such scenarios, a linear distribution of strain is not appropriate. The strut-and-tie model shown in Figure 3.60 was developed to compute the capacities of specimens 1a and 1b. Similar to the model used for the other specimens, the strut forces were computed by limiting the bearing width to the coupling beam flange width. The strut capacity was based on using $0.85f'_c$. The value of applied shear (V) was incrementally increased, and the locations of vertical bearing forces (y_1 and y_2) were iterated until equilibrium could be achieved. The connection capacity was taken as the maximum V for which equilibrium was possible.

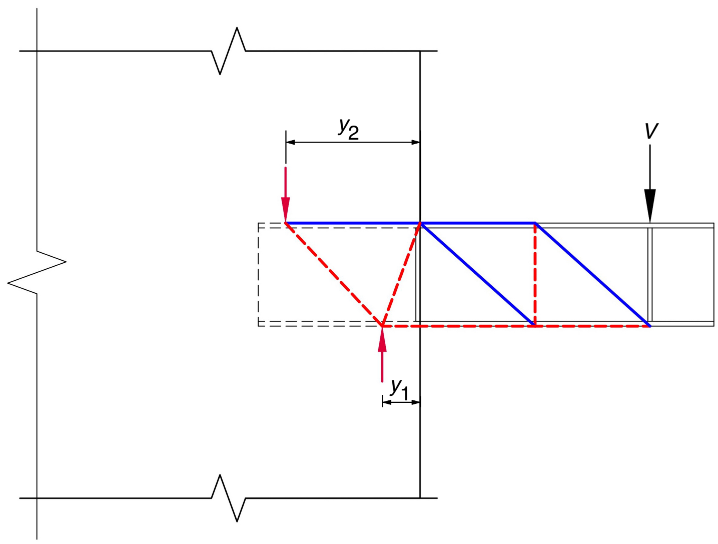

Figure 3.60 Strut-and-tie model.

As evident from Table 3.4, the calculated capacities are reasonably close to the measured values. The largest difference is for specimen 4 (test 6). As mentioned previously, water had to be added onsite to the concrete mix because of delays in casting this specimen. As a result, the "exact" concrete compressive strength for this specimen is somewhat unclear. For instance, if the concrete compressive strength is assumed to be 300 psi higher than the value obtained from the cores taken from this specimen, the measured capacity is 1.02 times the calculated capacity instead of 1.09 times.

Table 3.4 Measured vs. calculated capacity.

Specimen ID	Test ID	Measured/ Calculated	ε_f	c/L_e
1a	1	1.04	---[a]	---
1b	2	1.04	---	---
2a	3	1.03	0.00342	0.564
2b	4	1.00	0.00342	0.564
3	5	1.04	0.00337	0.563
4	6	1.09[b]	0.00370	0.575
5	7	1.04	0.00370	0.569
6	8	0.98	0.00346	0.563
		Average = 1.03 COV = 0.031 [a] Not applicable as a strut-and-tie model was used for specimens 1a and 1b. [b] Concrete strength is not reliably available for this specimen.		

3.11.2 Proposed equation

Ignoring specimen 4 (test 6), the average values of ε_f and c/L_e (provided in Table 3.4) are 0.0035 and 0.56, respectively. Ensuring equilibrium with reference to the model shown in Figure 3.61, the following equation is derived.

$$V_n = \frac{0.193 f_c' b_f L_e}{0.56 + \frac{g}{2L_e}} \qquad \textbf{Eq 3.2}$$

Using this equation, the capacities were computed. The measured and calculated equations are compared in Table 3.5. As discussed previously, a strut-and-tie model is more appropriate for specimens 1a and 1b (tests 1 and 2) with L_e/d being 1 or less than 1. Specimen 5 (test 7) had auxiliary transfer bars, which are not considered in the proposed equation nor in Eq 3.1 (AISC Eq. H4-1). The relatively large difference for specimen 4 (test 6) is attributed to the "exact" concrete strength not being known due to adding extra water onsite to the concrete mix. Excluding test 1a, 1b, and 4, the measured capacities, on average, are 3% higher than the value obtained from the proposed equation. To simplify and be slightly conservative, it is proposed to change 0.193 to 0.19 in Eq 3.2, i.e., use Eq 3.3.

$$V_n = \frac{0.19 f_c' b_f L_e}{0.56 + \frac{g}{2L_e}} \qquad \textbf{Eq 3.3}$$

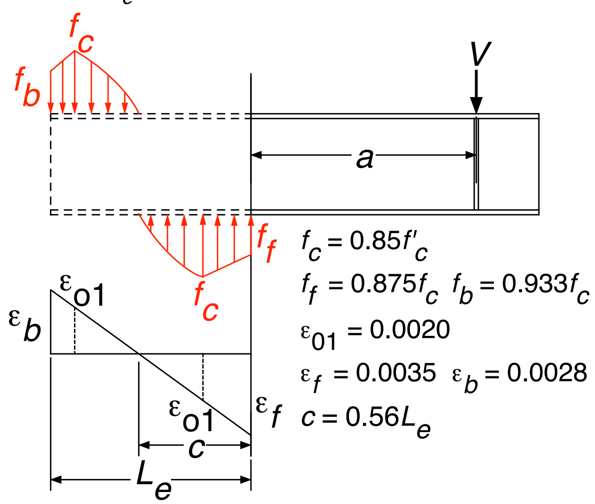

Figure 3.61 Model for derivation of proposed equation.

Table 3.5 Comparison of measured capacity vs. proposed equation.

Specimen ID	Test ID	Measured/Eq 3.3
1a	1	2.62[a]
1b	2	2.84[a]
2a	3	1.04
2b	4	1.00
3	5	1.04
4	6	1.09
5	7	1.13[b]
6	8	0.98
	Average [c]	1.03
	COV [c]	0.04

[a] Strut-and-tie model needs to be used because $L_e/d \leq 1$
[b] Specimen 5 had auxiliary transfer bars
[c] Average and COV by ignoring specimens 1a, 1b, and 5

3.11.3 Evaluation of proposed equation

The proposed equation (Eq 3.3) was further evaluated through a case study involving the archetypes used in several previous studies (Fortney, 2005; Gong, 1998; Kunwar, 2020; Remmetter, 1992; Shahrooz et al., 2018). Knowing the shear design forces, wall geometry, and selected coupling beam dimensions, the embedded length was determined from Eq 3.1. The larger of the calculated length and coupling beam depth was selected and rounded up to the nearest whole number. Using the provided embedment length, the connection capacity (V_n) was obtained by using Eq 3.1. The modeling procedure described in Section 3.11.1 was employed to compute the capacities. Considering the very good correlation of the measured capacities of the test specimens, the resulting capacities are deemed to represent the "actual" connection capacity. The connection capacity was also determined according to the proposed equation (Eq 3.3). Excluding the cases for which a strut-and-tie model is appropriate (i.e., those with $L_e/d \leq 1$), a total of 102 cases (including the test specimens) were evaluated. As seen from Figure 3.62, the current equation overestimates the calculated connection capacity, which is consistent with the observations made for the test specimens. On average, Eq 3.1 overestimates the connection capacity on average by a factor of 1.5 and by as much as a factor of 2 (see Table 3.6). For all the cases, Eq 3.1 (AISC Eq. H4-1) overestimates the connection capacity; the minimum value of V_n from Eq 3.1 is 1.17 times the computed capacity. Overestimation of the connection capacity suggests the embedment length obtained from Eq 3.1 would be insufficient. However, the capacity from the proposed equation is nearly identical to the calculated connection capacity (Figure 3.62). Similar conclusions may be arrived from the average, maximum, and minimum values of the ratio of the proposed equation (Eq 3.3) to the calculated connection capacity: 0.99, 1.00, and 0.98, respectively. Therefore, the proposed equation provides a simple yet slightly conservative method to determine the connection capacity of steel coupling beams interfaced with ordinary structural walls, and the embedment length from the proposed equation would be adequate to develop the connection capacity.

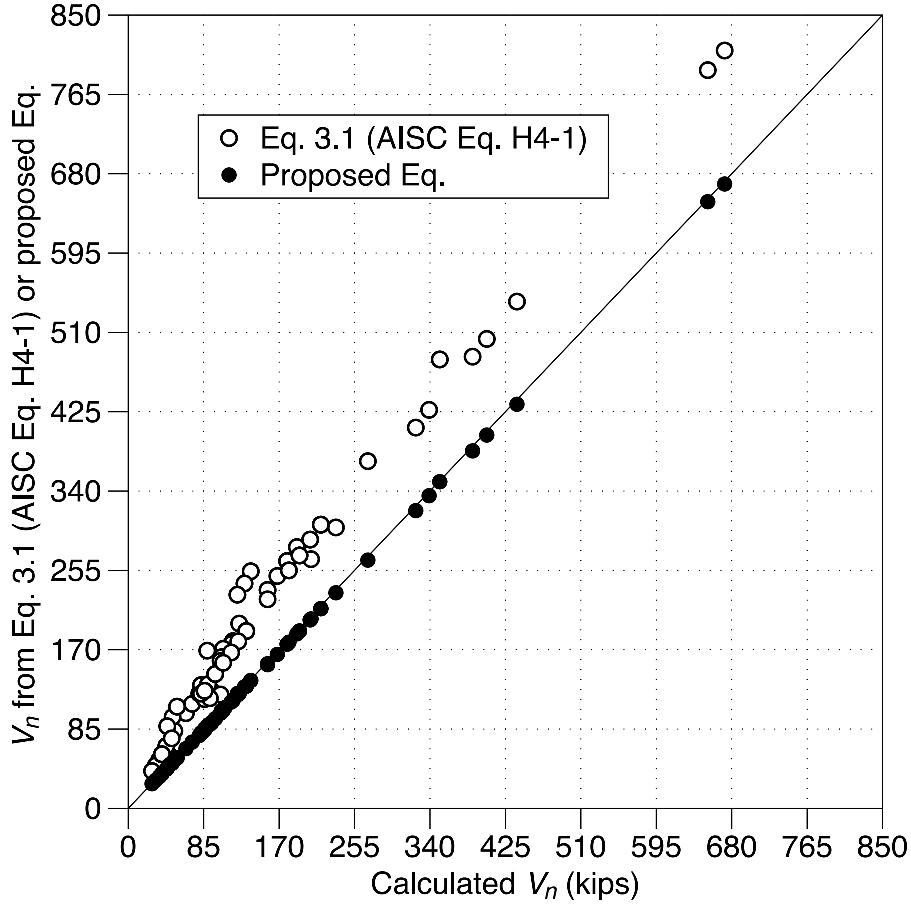

Figure 3.62 Calculated capacity vs. capacity from Eq 3.1 (AISC Eq. H4-1) and proposed equation (Eq 3.3).

Table 3.6 Comparison of V_n from Eq 3.1 and Eq 3.3 against calculated connection capacity.

	Eq 3.1 / Calculated	Eq 3.3 / Calculated
Average	1.50	0.99
COV	0.12	0.0043
Maximum	2.00	1.00
Minimum	1.17	0.98

3.11.4 Comparison of embedment length from proposed equation and current equation

The proposed equation results in a longer embedment length than the value determined from the current equation Eq 3.1. To assess the additional length, the embedment lengths for the design cases discussed in Section 3.11.3 were calculated by using the current and proposed equations, i.e., Eq 3.1 and Eq 3.3.

Figure 3.63 illustrates the change in the required embedment lengths as calculated by the proposed equation versus the values obtained from Eq 3.1 (current AISC Eq. H4-1). In this figure, the embedment lengths required to develop the member capacity (R_yV_p) are also compared against those from Eq 3.1. The proposed equation increases the required embedment by at most 52% and 23% on average. As expected, significantly longer embedment lengths are required to develop the member capacity: 107% and 217% on average and maximum, respectively. The embedment length from the proposed equation is the same as that found from Eq 3.1, i.e., 0% change, if the beam depth controls the final value. The values shown in Figure 3.63 indicate that the proposed equation does not result in excessively long embedment lengths.

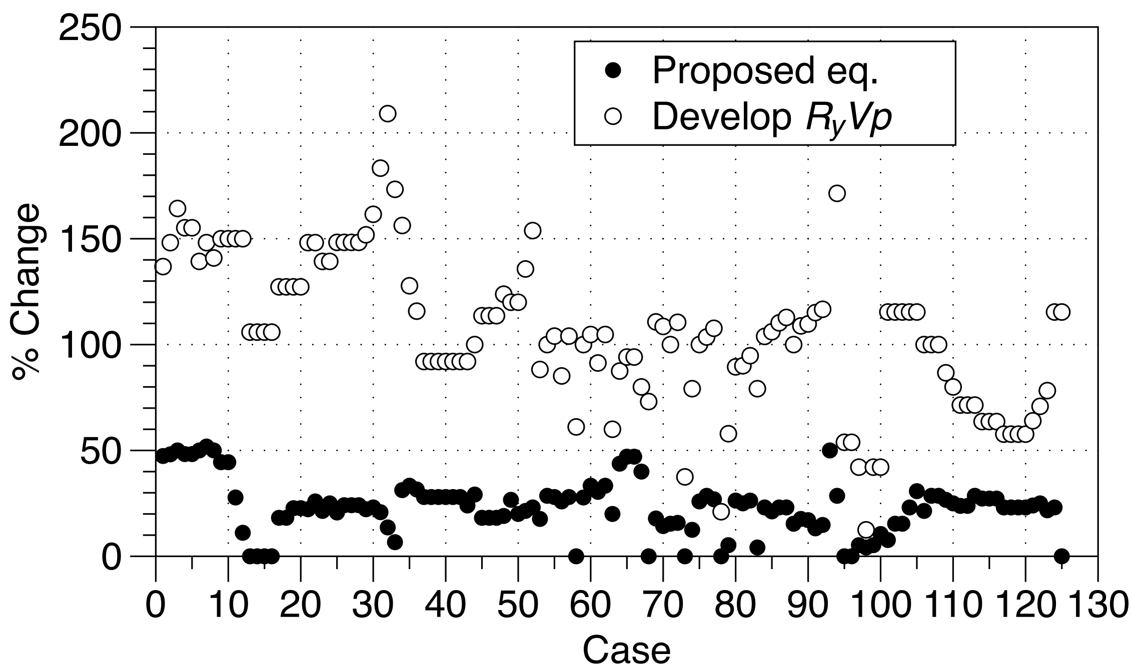

Figure 3.63 Change in embedment length compared to Eq 3.1 (AISC Eq. H4-1).

3.12 Stiffness

3.12.1 Evaluation of current equation for effective moment of inertia

The values of peak-to-peak stiffness were normalized with respect to the stiffness obtained by using the effective moment of inertia calculated from AISC Eq C-H4-1, which is provided herein as Eq 3.4.

$$I_{eff} = 0.60I\left(1 + \frac{12\lambda EI}{g^2 G A_w}\right)^{-1} \qquad \textbf{Eq 3.4}$$

The normalized peak-to-peak stiffness for each cycle is plotted in Figure 3.64. As expected, the connection stiffness degraded as the load level was increased. With few exceptions, the experimentally obtained stiffness is smaller than the value calculated from Eq 3.4 (AISC Eq C-H4-1). With 95% confidence, the average of measured stiffness (0.722) is between 0.713 and 0.730 times the value calculated using Eq 3.4 for cycles up to and including $0.54V_n$. If all the cycles are considered, the average value (0.685) is between 0.678 and 0.692 with 95% confidence.

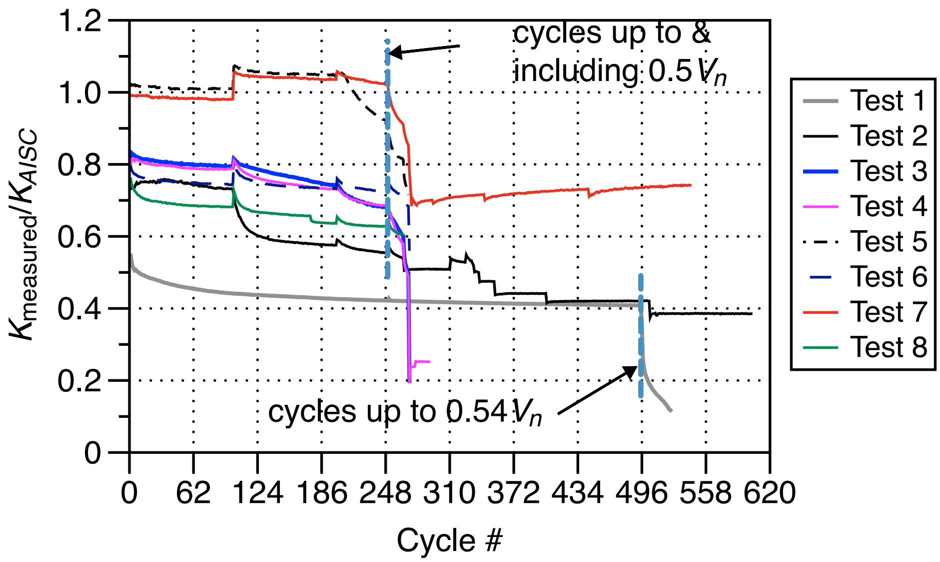

Figure 3.64 Comparison of measured stiffness vs. stiffness based on AISC I_{eff}.

The results demonstrate that the coefficient 0.60 needs to be 0.43 or 0.41 if cycles up to and including $0.5V_n$ or all cycles are considered, respectively. Therefore, it is proposed to change 0.60 to 0.40 for steel coupling beams linking ordinary reinforced concrete walls.

3.12.2 Impact of revision of effective moment of inertia

The archetype was designed based on the effective moment of inertia (I_{eff}) from Eq 3.4, which is intended to account for connection flexibility. The computer program used for design (ETABS) accounts for shear deformation; therefore, the equation's parenthetical term need not be included in the model. The coupling beam moment of inertia was multiplied by 0.6 in the computer model for design. The experimental data described in Section 3.12.1 indicate that this multiplier should be taken as 0.4. To understand the impact of this change, the archetype was reanalyzed for the same loads used in the original design but the coupling beams' moment of inertias were multiplied by 0.4.

The revised model of the archetype has lower coupling beam moments of inertia than those in the original design; hence, the distribution of forces in the wall piers are affected and the drifts are expected to be larger than the original values. The potential implications of these changes were examined by evaluating the performance of the archetype subjected to the design wind loads. The demand-to-capacity ratios of the wall piers shown in Figure 65a indicate the strength of the first-story wall is marginally insufficient; the capacity is exceeded by about 3%. More importantly, the inter-story drifts between stories 9 and 21 exceed $h/450$, but all the values are lower than $h/400$, where h is the story height. The archetype, as designed originally, had sufficient capacity, and the inter-story drift limits were satisfied.

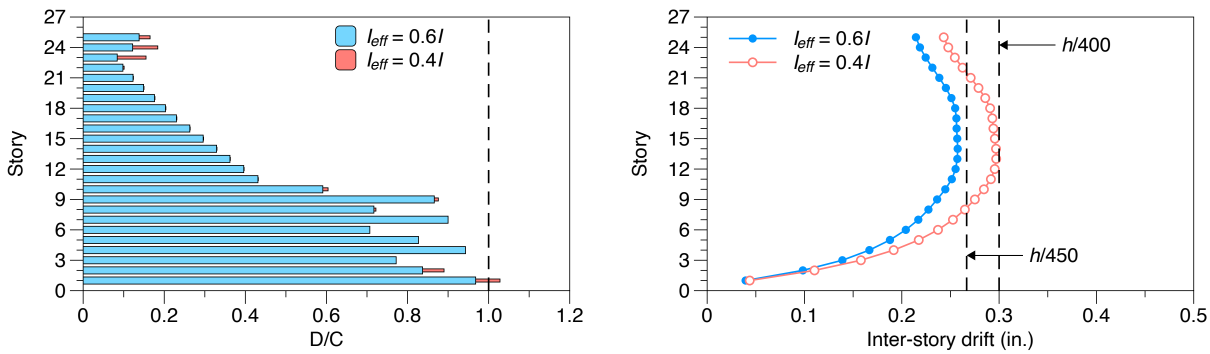

(a) Wall demand-to-capacity ratios for wind loads

(b) Inter-story drifts for wind loads

Figure 65 Comparison of original and revised performances of archetype.

Chapter 4 Summary, Conclusions, and Recommendations

4.1 Project overview

Coupled structural (shear) walls (CSW) are a common structural system. This system is comprised of two or more structural walls that are typically linked at each floor by coupling beams. Based on the expected level of inelastic deformations, composite structural (shear) walls can be classified as Composite Ordinary Shear Wall (COSW) or Composite Special Shear Wall (CSSW). The design and detailing of COSW and CSSW are presented in Sections H4 and H5 of AISC 341 *Seismic Provision*, respectively. COSW systems are used in regions with low-to-moderate seismic demands and are expected to undergo limited inelastic deformations. On the other hand, CSSW systems are used in regions with high seismic demands and are expected to undergo significant inelastic deformations. One common composite system involves linking reinforced concrete wall piers by steel (or steel-concrete composite) coupling beams that are embedded in the wall piers. Design and detailing of steel coupling beam-wall connection in COSW was the focus of the research herein.

In the 2010 and earlier versions of AISC 341 *Seismic Provisions*, the coupling beam-wall connection was designed to develop the coupling beam's expected capacity. This provision in the 2016 version was replaced by the requirement that the connection in COSW be designed only to develop the demand from the coupling beam as calculated by linear-elastic analysis with no ductile detailing requirements. As a result, design and detailing of embedment region has been relaxed. This change leads to shorter embedment lengths and smaller reinforcement in the embedment region.

Analytical studies conducted at the University of Cincinnati indicated the shorter embedment length could accelerate the loss of coupling beam-wall connection integrity, leading to a reduction in the level of coupling action between the wall piers. The loss of coupling action will affect the demands in the wall piers, and their capacities could be exceeded. Moreover, inter-story and overall drifts could surpass acceptable limits. Partly to remedy these observations, AISC 341 was modified in 2022 by specifying a minimum embedment length of not being less than the coupling beam's depth and requiring additional longitudinal reinforcement along the embedded region.

A coordinated experimental and analytical study was conducted to examine the current design provisions for steel coupling beams in COSW outlined in AISC 341-2022. It is important to note that the current (and previous) AISC 341 *Seismic Provisions* for coupling beams in COSW and CSSW are mostly (if not entirely) based on experimental research focused on coupling beam-wall connection details intended to resist high seismic loads. To the best of the authors' knowledge, no experimental research had been conducted to understand the performance of COSW prior to the study presented in this report.

The test specimens were selected based on a 25-story archetype located in Cincinnati, Ohio. With the exception of a few upper stories, where seismic demands were slightly higher than those from wind loads, the design was controlled by wind loads. Two half-scale and four three-quarter beam-wall subassemblies, each representing a steel coupling beam-wall connection, were fabricated and tested. The experimental test data were used to evaluate the current AISC 341 requirements and develop new design and detailing provisions for COSW.

4.2 Observations and conclusions

The following conclusions and observations are based on the information presented in this report.

1. The additional longitudinal reinforcement required by AISC 341-22 did not appreciably impact the connection performance in terms of the initial stiffness, stiffness degradation, dissipated energy, maximum load that could be resisted, and mode of failure.
2. Except for the specimens with embedment length/coupling beam depth ≤ 1 and the specimen with auxiliary transfer bars attached to the flanges, the other specimens did not fully develop their target shear of V_n. These specimens failed at $0.96V_n$ or $0.99V_n$, failed after the application of one cycle with the applied shear being equal to V_n, or failed prematurely at $0.79V_n$. The force resistance mechanism with short embedment lengths (i.e., when embedment length/coupling beam depth ≤ 1) is attributed to the formation of struts and ties instead of the formulation used in the development of the current ASIC 341-22 equation for determining the required embedment length. AISC 341-22 embedment length equation is based on assuming a linear strain distribution, which becomes questionable for cases with embedment length/coupling beam depth ≤ 1. Although AISC 341-22 equation underestimates the connection capacity and is conservative for cases with embedment length/coupling beam depth ≤ 1, the use of strut-and-tie models is more appropriate. The addition of auxiliary transfer bars provides additional resistance from the couple formed by the forces in the bars. Furthermore, the auxiliary transfer bars reduce the magnitude of the forces that need to be developed from the flange-concrete bearing stresses. Due to these benefits, the specimen with auxiliary transfer bars could successfully be subjected to the complete wind load and seismic displacement protocols.

3. The auxiliary transfer bars provide a direct load path for transferring the forces in the coupling beam to the surrounding concrete. This direct load path is not offered by longitudinal reinforcement along the embedment length. The lack of a direct load path is deemed to be the main reason for the similarities of the performance of the specimens with or without the higher longitudinal reinforcement required by AISC 341-22.
4. For the specimens without face bearing plates, which act as a bearing stiffener, the coupling beam's flange and web experienced local bending and buckling. In one specimen with face bearing plates, the flange experienced a small amount of bending within the connection region – the bending occurred at a location that was away from the face bearing plates. This specimen failed prematurely at $0.79V_n$, and its connection had experienced excessive damage.
5. Except for the specimens with embedment length/coupling beam depth ≤1, none of the specimens could develop the capacities calculated from the current equation (AISC Eq. H4-1) if the as-built dimensions and measured properties are used in the calculations. This trend is attributed to the fundamental assumptions in the derivation of the current equation, i.e., the depth of neutral axis/embedment length is taken as 0.66, concrete strain is 0.003 at the interface between the beam and wall pier, and the implicit hypothesis of "spreading" of bearing stresses beyond the flange width. It should be noted that loading for the specimen with auxiliary transfer was stopped prior to reaching the full capacity. For this reason, the measured maximum load for this specimen is less than its calculated capacity.
6. A new equation for calculating the required embedment length was developed based on analysis of the test results. In this equation, the strain at the coupling beam-wall interface

is taken as 0.0035 (instead of 0.003 in the current ASIC Eq. H4-1), and the depth of the neutral axis is set equal to 0.56 times the embedment length (compared to 0.66 in ASIC Eq. H4-1). The measured capacities were found to be within 3% of the capacities calculated by the new equation. Additional analytical studies of archetypes from a number of previous research indicate an excellent correlation between the capacities determined based on a detailed, mechanistic procedure and those from the new equation. Not only does the new equation closely capture the connection capacity but it is also simpler than the current equation (AISC Eq. H4-1).

7. The use of the new equation results in longer embedment lengths than the values computed from the current AISC Eq. H4-1. However, the embedment lengths are much shorter than those needed to develop the member capacity, which was required in the 2010 or earlier versions of AISC 341 *Seismic Provisions*.
8. With 95% confidence, the average value of the experimental stiffness is between 0.678 and 0.692 times the value obtained by using the effective moment of inertia calculated from AISC Eq. C-H4-1. Therefore, the coefficient of 0.6 in this equation needs to be changed to 0.4.
9. The archetype, which was used to select and detail the test specimens, had been designed by using the current AISC Eq. C-H4-1. By using the modified version of this equation (i.e., using 0.4 instead of 0.6), the first-floor wall piers of the archetype were found to be slightly inadequate (demand/capacity became 1.03 instead of 0.97 in the original design). Furthermore, the wind load inter-story drifts for several stories exceeded the limit of $h/450$, where h is the story height, but all the inter-story drifts remained below $h/400$.

4.3 Recommendations

Based on the results presented in this report, the following revisions to AISC 341 seismic provisions are recommended.

1. Replace the current AISC Eq. H4-1 by

$$V_n = \frac{0.19 f_c' b_f L_e}{0.56 + \frac{g}{2L_e}}$$

2. Replace the current AISC Eq. C-H4-1 by

$$I_{eff} = 0.40I\left(1 + \frac{12\lambda EI}{g^2 G A_w}\right)^{-1}$$

3. Require a bearing stiffener at the interface between steel coupling beams and reinforced concrete walls. This requirement may be waived if the adequacy of flanges and web against bending and buckling is ensured. It should be noted that face bearing plates could also simplify the formwork around the flanges and web.

Ballot items reflecting these proposed changes have been developed and are currently being reviewed by AISC Task Committee 5 (Composite Design).

References

AISC 341 (2010) *Seismic Provisions for Structural Steel Buildings-ANSI/AISC 341-10*, American Institute of Steel Construction, Chicago, IL.

AISC 341 (2016) *Seismic Provisions for Structural Steel Buildings-ANSI/AISC 341-16*, American Institute of Steel Construction Chicago, IL.

AISC 341 (2022) *Seismic Provisions for Structural Steel Buildings-ANSI/AISC 341-22*, American Institute of Steel Construction Chicago, IL.

American Concrete Institute (ACI) Committee 318, (2019) *Building Code Requirements for Structural Concrete (ACI 318-19) and Commentary (ACI 318R-19)*, American Concrete Institute, Farmington Hills, MI, 623 pp.

ASTM (2017) ASTM C496/C496M *Standard Test Method for Splitting Tensile Strength of Cylindrical Concrete Specimens*, ASTM International, West Conshohocken, PA, 5 pp.

ASTM (2020) ASTM C42/C42M *Standard Test Method for Obtaining and Testing Drilled Cores and Sawed Beams of Concretes*, ASTM International, West Conshohocken, PA, 7 pp.

ASTM (2021) ASTM C39/C39M *Standard Test Method for Compressive Strength of Cylindrical Concrete Specimens*, ASTM International, West Conshohocken, PA, 8 pp.

ASTM (2022) ASTM C39/C39M *Standard Test Methods and Definitions for Mechanical Testing of Steel Products*, ASTM International, West Conshohocken, PA, 51 pp.

ASTM (2022) ASTM E8/E8M *Standard Test Methods for Tension Testing of Metallic Materials, ASTM International*, West Conshohocken, PA, 31 pp.

Computers and Structures Inc. (2016), *ETABS version 16.2*, Berkeley, CA.

Fortney, J.P. (2005) *The Next Generation of Coupling Beams*, PhD Dissertation, University of Cincinnati, Cincinnati, OH, 370 pp. (http://rave.ohiolink.edu/etdc/view?acc_num=ucin1115837131)

Gong, B. (1998) Seismic Behavior of Composite Coupled Wall Systems, PhD Dissertation, University of Cincinnati, Cincinnati, OH, 293 pp.

Harries, K.A., Fortney, P.J., Shahrooz, B.M. Brienen, P.J. (2005) *Design of Practical Diagonally Reinforced Concrete Coupling Beams – A Critical Review of ACI 318 Requirements*, ACI Structural Journal, Vol. 102, No. 6, 876-882.

Harries, K.A., Mitchell, D., Redwood, R.G. and Cook, W.D. (1997). *Seismic Design of Coupling Beams—A Case for Mixed Construction*, Canadian Journal of Civil Engineering, Vol. 24, No. 3, pp. 448–459.

Hill, J., Forbes, J., Motter, C.J. (2023) *Nonlinear Wind Design of Steel Reinforced Concrete (SRC) Coupling Beams: Final Report and Design Recommendations*, Washington State University, Pullman, WA, 155 pp.

Kunwar, S. (2020) *Comprehensive Evaluation of Composite Core Walls for Low-Seismic Force and Wind Load Applications*, MS Thesis, University of Cincinnati, Cincinnati, OH, 72 pp. (http://rave.ohiolink.edu/etdc/view?acc_num=ucin1613750905724949)

Mattock, A. H., Gaafar, G. H. (1982) *Strength of Embedded Steel Sections as Brackets*, ACI Structural Journal, Vol. 79, No. 2, 83-93.

Mirza, A.R. (2018) *Evaluation of AISC Coupling Beam Embedment Length in Composite Ordinary Shear Walls*, MS Thesis, University of Cincinnati, Cincinnati, OH, 105 pp. (http://rave.ohiolink.edu/etdc/view?acc_num=ucin1543577095290297)

Motter, C.J. (2013), *Large-Scale Testing of Steel Reinforced Concrete (SRC) Coupling Beams Embedded into RC Shear Walls*, PhD Dissertation, University of California – Los Angeles, 199 pp.

Remmetter, M.E. (1992) *Investigation of Composite Connections for Coupled Shear Walls Utilizing Steel Coupling Beams*, MS Thesis, University of Cincinnati, Cincinnati, OH, 185 pp.

Shahrooz, B.M., Fortney, P.J., Harries K.A. (2018) *Steel Coupling Beams with a Replaceable Fuse*, Journal of Structural Engineering, ASCE, (144)(2)(2018): 04017210_1:11.

This page left blank intentionally.

Appendix A
Derivation of development length equation for specimen 4 (test 6)

A.1 Introduction

Figure A.1 shows the compressive stresses developed above and below the embedded steel section due to the applied load V_n acting at a distance a from the face of the wall. A linear strain distribution with a strain of 0.003 at the outer face of the wall is assumed. Hognestad concrete model (see Figure A.2) gives the parabolic stress-strain relationship for the concrete stresses and is mathematically represented by Eq. A.1. A strain of 0.002 is assumed for the maximum stress of f_c.

$$f_c = 1000 f_{max}[\varepsilon - 250\varepsilon^2] \quad \textbf{Eq. A.1}$$

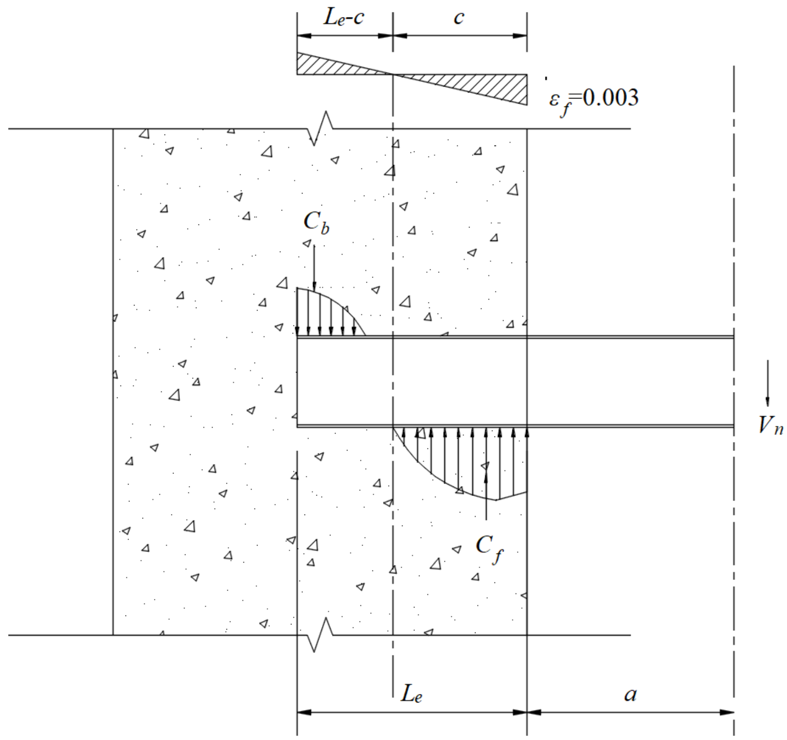

Figure A.1 Stresses in the embedment region.

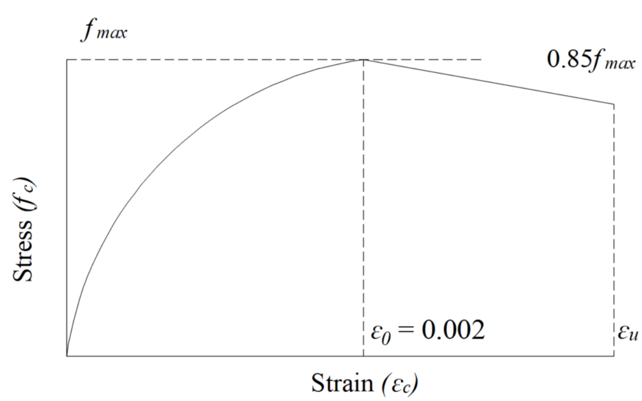

Figure A.2 Hognestad concrete model.

A.2 Calculation of front bearing force (C_f)

The front bearing force (C_f) is determined by recognizing that the stress-strain distribution consists of a parabolic section and a trapezoidal section, as shown in Figure A.3. For each section, the magnitude of forward bearing force and its location is calculated separately.

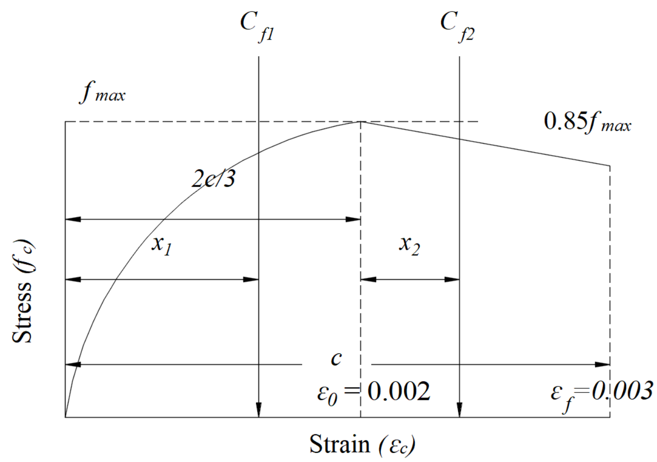

Figure A.3 Front bearing forces and their locations.

A.2.1 Parabolic segment

Force

$$C_{f_1} = \int_0^{\frac{2c}{3}} 1000 f_{max}\,(\varepsilon - 250\varepsilon^2) b_f\, dx \text{ where, } b_f \text{ is flange width and } \varepsilon = \frac{x\varepsilon_f}{c}$$

$$C_{f_1} = 1000 f_{max} b_f \frac{4\varepsilon_f c}{9}\left[\frac{1}{2} - \frac{500}{9}\varepsilon_f\right]$$

$$Substituting\ \varepsilon_f = 0.003$$

$$C_{f_1} = \frac{4}{9} f_{max} b_f c$$

Location

$$\bar{x} = \frac{\int_0^{\frac{2c}{3}} x 1000 f_{max}(\varepsilon - 250\varepsilon^2)\,dx}{\int_0^{\frac{2c}{3}} 1000 f_{max}(\varepsilon - 250\varepsilon^2)\,dx}$$

$$\bar{x} = \frac{\frac{2c}{3}\left(\frac{1}{3} - \frac{125}{3}\varepsilon_f\right)}{\left(\frac{1}{2} - \frac{500}{9}\varepsilon_f\right)}$$

$$Substituting\ \varepsilon_f = 0.003$$

$$\bar{x} = x_1 = \frac{5c}{12}$$

A.2.2 Trapezoidal segment

Force

$$C_{f_2} = \left(\frac{f_{max} + 0.85f_{max}}{2}\right)\frac{c}{3}b_f$$

$$C_{f_2} = 0.308f_{max}cb_f$$

Location

$$\bar{x} = \frac{\frac{c}{3}(1.7f_{max} + f_{max})}{3(f_{max} + 0.85f_{max})}$$

$$\bar{x} = x_2 = \frac{6c}{37}$$

A.3 Back bearing force (C_b)

A parabolic stress distribution is assumed for the back portion of the connection, see Figure A.4.

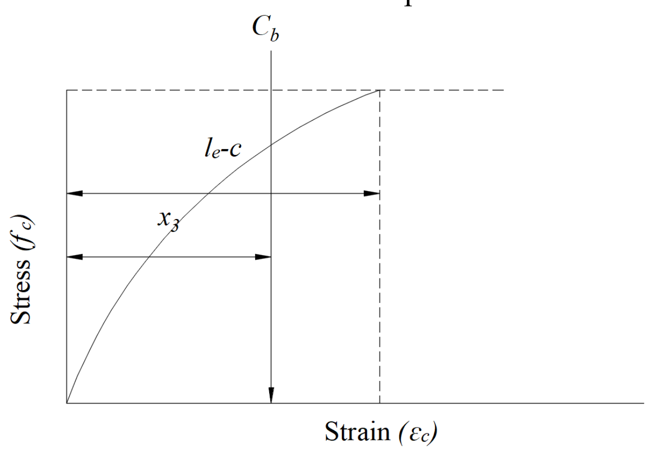

Figure A.4 Back bearing force.

Force

$$C_b = \int_0^{L_e-c} 1000f_{max}(\varepsilon - 250\varepsilon^2)\, b_f dx \; where \; \varepsilon = \frac{\varepsilon_f x}{c}$$

$$C_b = 1000f_{max}b_f\frac{\varepsilon_f}{c}(L_e - c)^2\left[\frac{1}{2} - \frac{250}{3}\varepsilon_f\left(\frac{L_e}{c} - 1\right)\right]$$

$$Substituting \; \varepsilon_f = 0.003$$

$$C_b = 3f_{max}\frac{b_f}{c}(L_e - c)^2\left[\frac{1}{2} - \frac{1}{4}\left(\frac{L_e}{c} - 1\right)\right]$$

Location

$$\bar{x} = \frac{\int_0^{L_e-c} x1000f_{max}(\varepsilon - 250\varepsilon^2)dx}{\int_0^{L_e-c} 1000f_{max}(\varepsilon - 250\varepsilon^2)dx}$$

$$\bar{x} = \frac{(L_e - c)\left[\frac{1}{3} - \frac{250}{4}\varepsilon_f\left(\frac{L_e - c}{c}\right)\right]}{\left[\frac{1}{2} - \frac{250}{3}\varepsilon_f\left(\frac{L_e - c}{c}\right)\right]}$$

$Substituting\ \varepsilon_f = 0.003$

$$\bar{x} = x_3 = \frac{(L_e - c)\left[\frac{1}{3} - \frac{3}{16}\left(\frac{L_e - c}{c}\right)\right]}{\left[\frac{1}{2} - \frac{1}{4}\left(\frac{L_e - c}{c}\right)\right]}$$

The summary of forces and their locations are shown in Figure A.5.

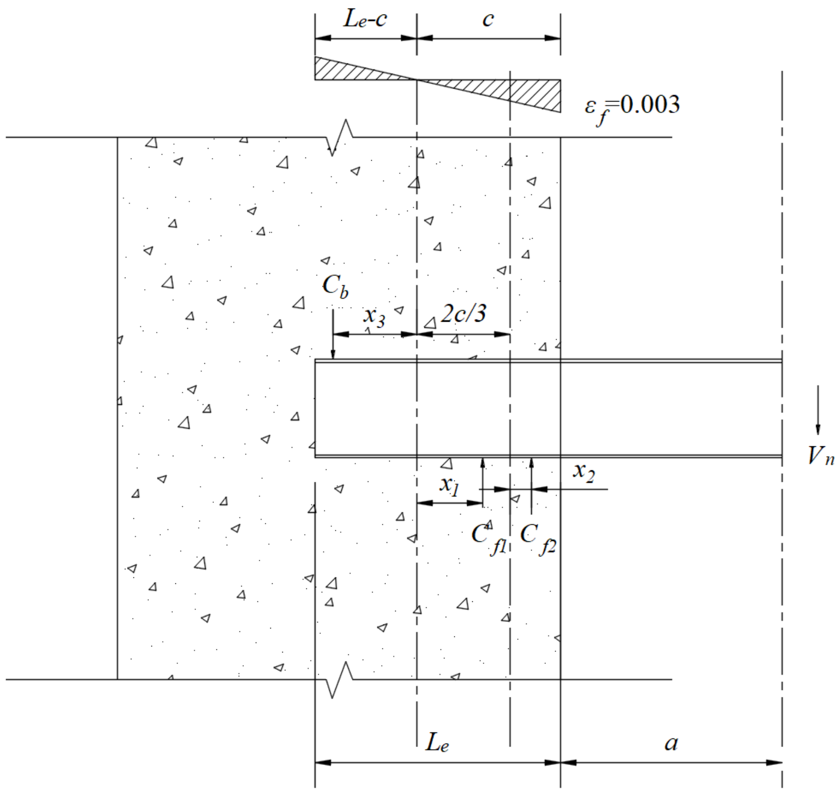

Figure A.5 Forces and their locations.

A.4 Relationship between depth of compressive zone (c) and embedment length (L_e)

In Figure A.5, sum the moments about V_n

$$C_b \times (x_3 + c + a) = C_{f_1} \times (a + c - x_1) + C_{f_2} \times \left(a + c - \frac{2c}{3} - x_2\right)$$

$$3f_{max}\frac{b_f}{c}(L_e-c)^2\left[\frac{(L_e-c)\left(\frac{1}{3}-\frac{3}{16}\left(\frac{L_e-c}{c}\right)\right)}{\frac{1}{2}-\frac{1}{4}\left(\frac{L_e-c}{c}\right)}+c+a\right]$$
$$=\frac{4}{9}f_{max}b_f c\left(a+c-\frac{5c}{12}\right)+\frac{37}{120}f_{max}cb_f\left(a+\frac{c}{3}-\frac{6c}{37}\right)$$

$$3\frac{c}{L_e}\left(\frac{L_e}{c}-1\right)^2\left(\frac{3}{4}-\frac{1}{4}\frac{L_e}{c}\right)\left[\frac{\left(1-\frac{c}{L_e}\right)\left(\frac{25}{58}-\frac{3}{16}\frac{L_e}{c}\right)}{\frac{3}{4}-\frac{1}{4}\frac{L_e}{c}}+\frac{c}{L_e}+\frac{a}{L_e}\right]$$
$$=\frac{4}{9}\frac{c}{L_e}\left(\frac{a}{L_e}+\frac{7}{12}\frac{c}{L_e}\right)+\frac{37}{120}\frac{c}{L_e}\left(\frac{a}{L_e}+\frac{19}{111}\frac{c}{L_e}\right)$$

Figure A.6 shows the variation of c/L_e for different values of a/L_e. The average value of c/L_e is found to be 0.59 with the coefficient of variation of 5.6%.

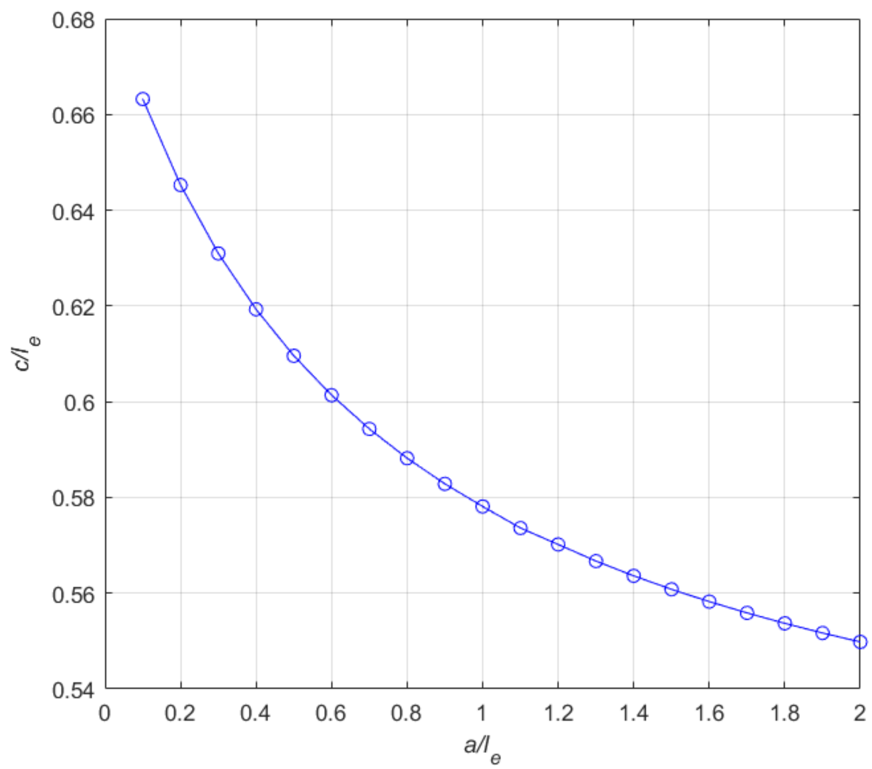

Figure A.6 Variation of c/L_e with respect to a/L_e.

A.5 Embedment length equation

In Figure A.5, sum the moments about the back bearing force

$$V_n\times(a+c+x_3)-C_{f_1}\times(x_1+x_3)-C_{f_2}\times\left(x_2+\frac{2c}{3}+x_3\right)=0$$

Simplify equations for $C_{f_1}, C_{f_2}, x_1, x_2$ and $x_3$by susbtituting ${}^{C}/_{L_e} = 0.59$.

$$V_n \times \left(\frac{a}{L_e} + \frac{c}{L_e} + \frac{0.255L_e}{L_e}\right) = \frac{4}{9} f_{max} b_f c \times 0.501L_e + \frac{37}{120} f_{max} b_f c \times 0.744L_e$$

$$V_n = \frac{0.267 f_{max} b_f L_e}{0.845 + \frac{a}{L_e}}$$

$Assume\ f_{max} = 0.85f_c'$

$$V_n = \frac{0.227 f_c' b_f L_e}{0.845 + \frac{a}{L_e}}$$

This page left blank intentionally.

Appendix B
Measured stress-strain diagrams of reinforcement and steel coupling beams

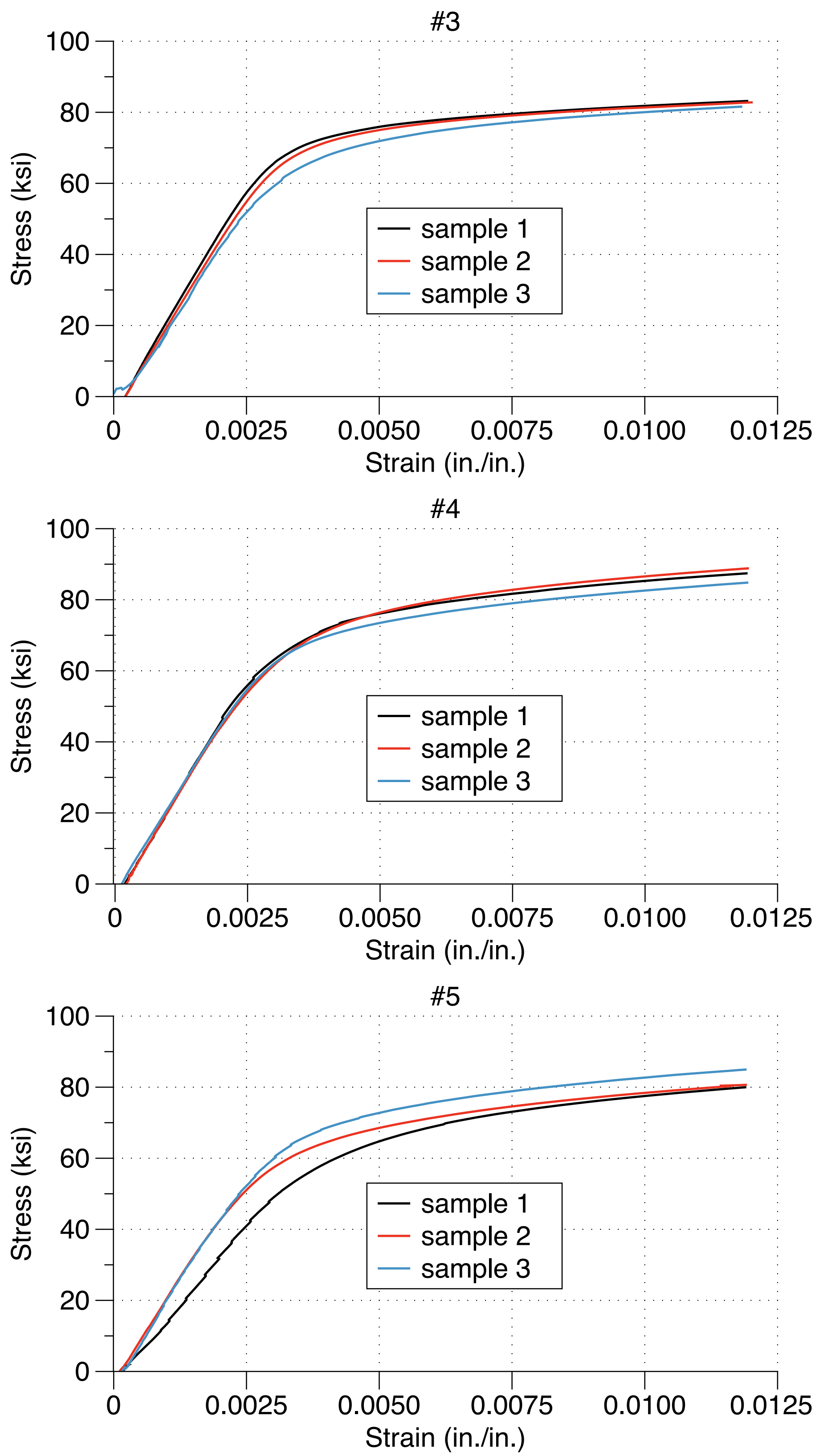

Figure B.1 Stress-strain diagrams – reinforcing bars in phase 1 specimens.

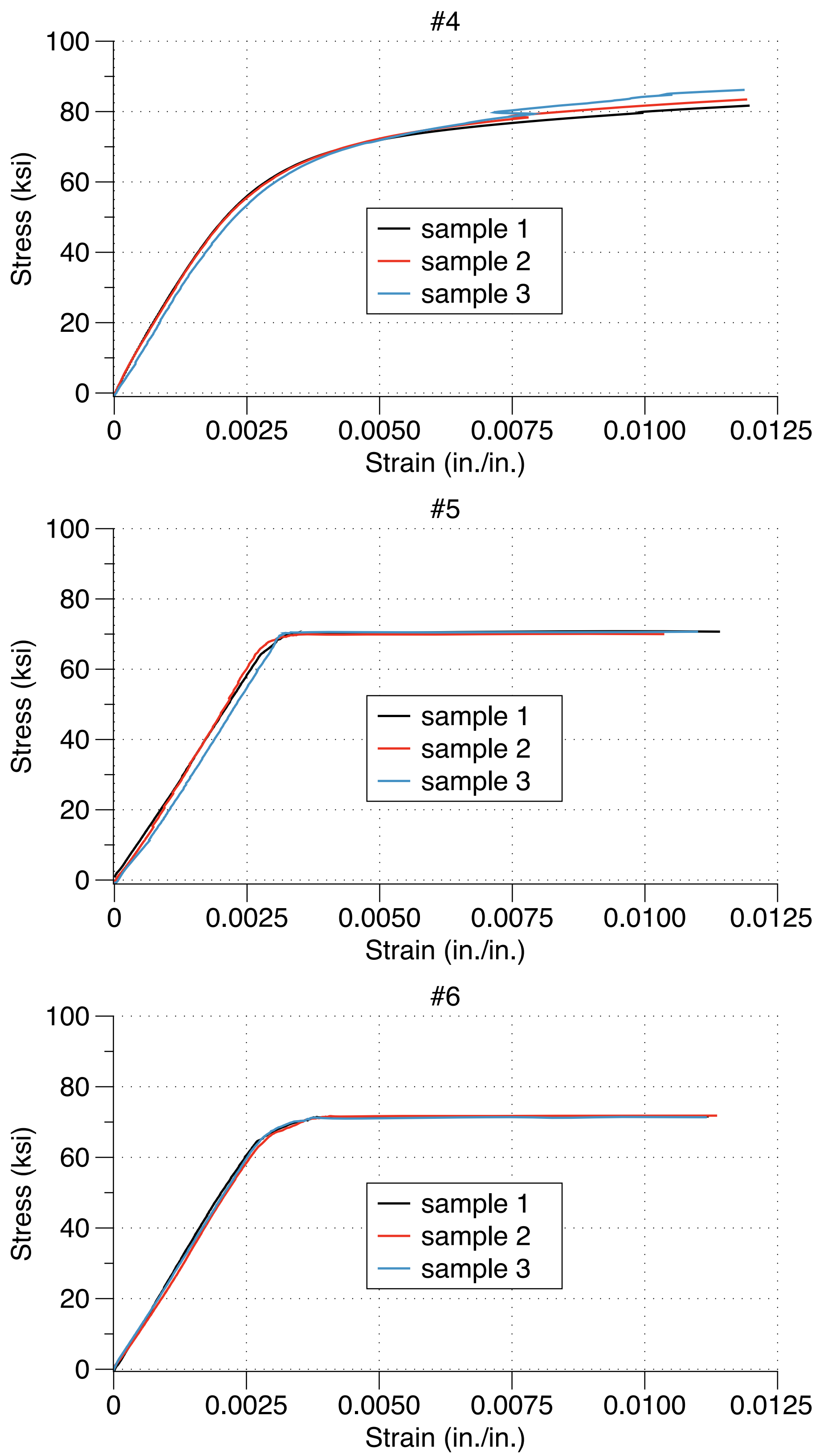

Figure B.2 Stress-strain diagrams – reinforcing bars in phase 2 specimens.

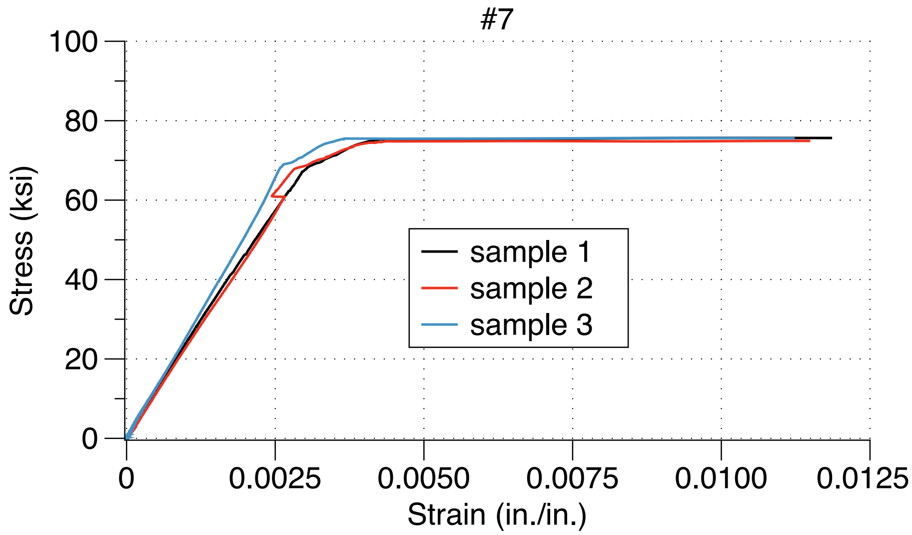

Figure B.2 Stress-strain diagrams – reinforcing bars in phase 2 specimens (cont.).

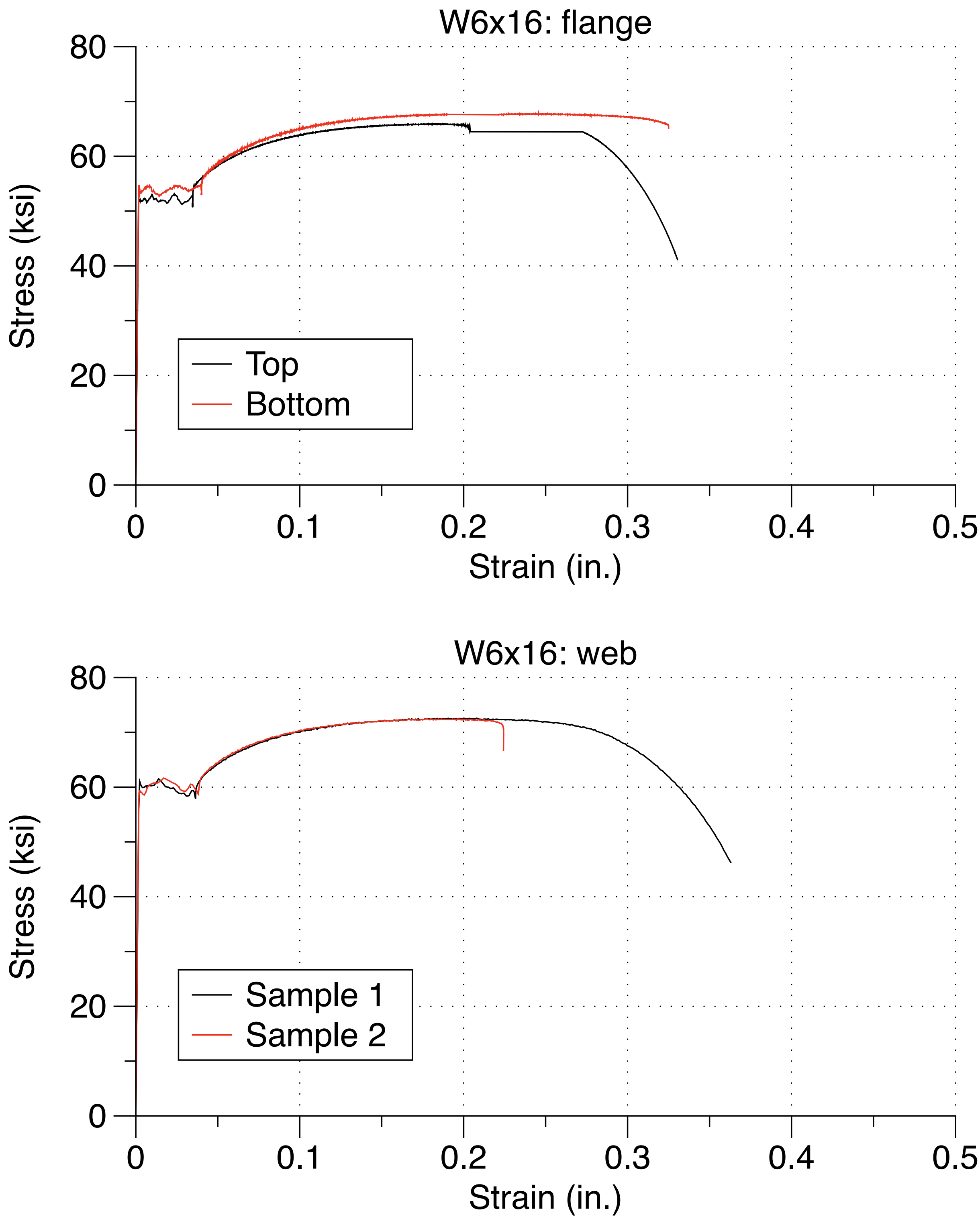

Figure B.3 Stress-strain diagram - steel coupling beam W6x16 (specimens 1a and 1b).

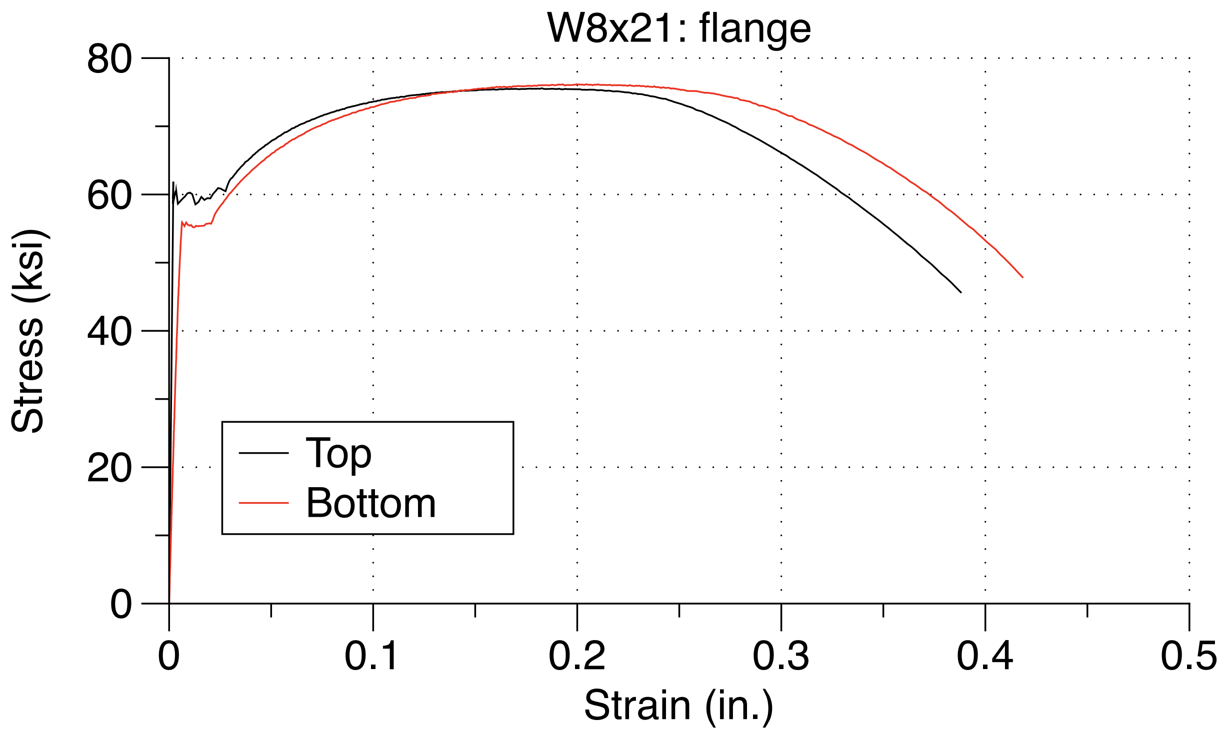

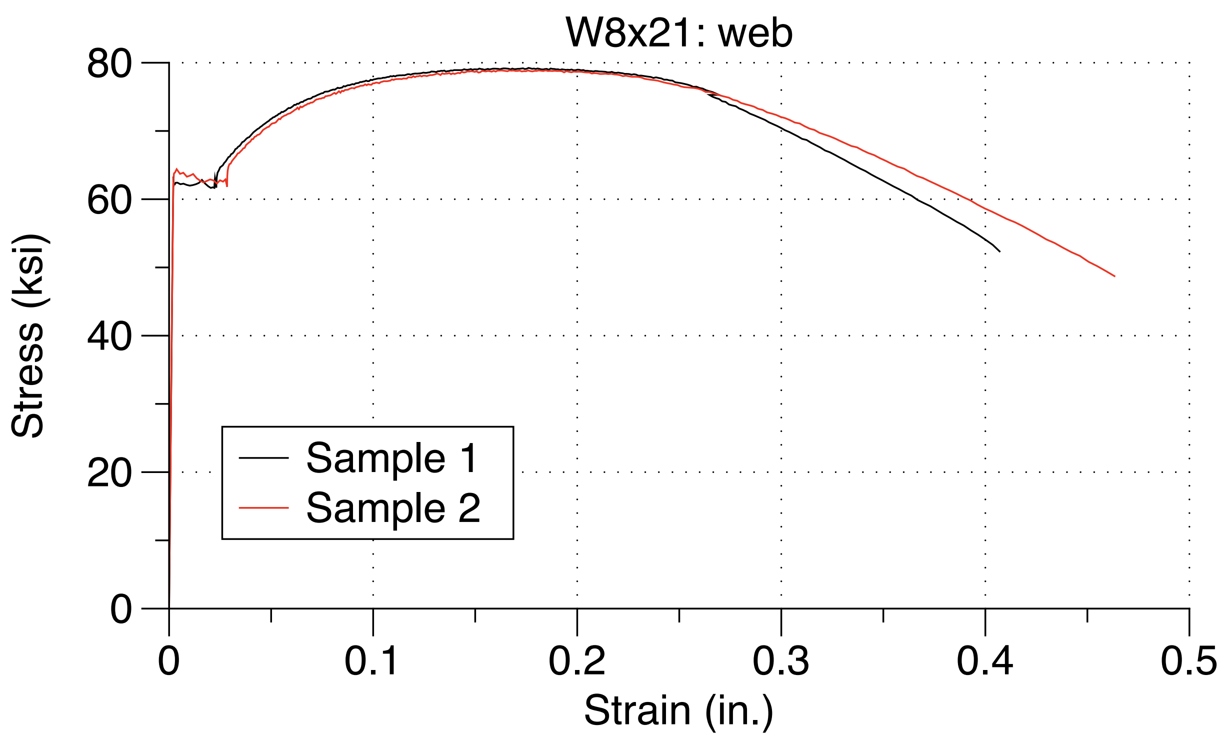

Figure B.4 Stress-strain diagram - steel coupling beam W8x21 (specimens 2a and 2b)

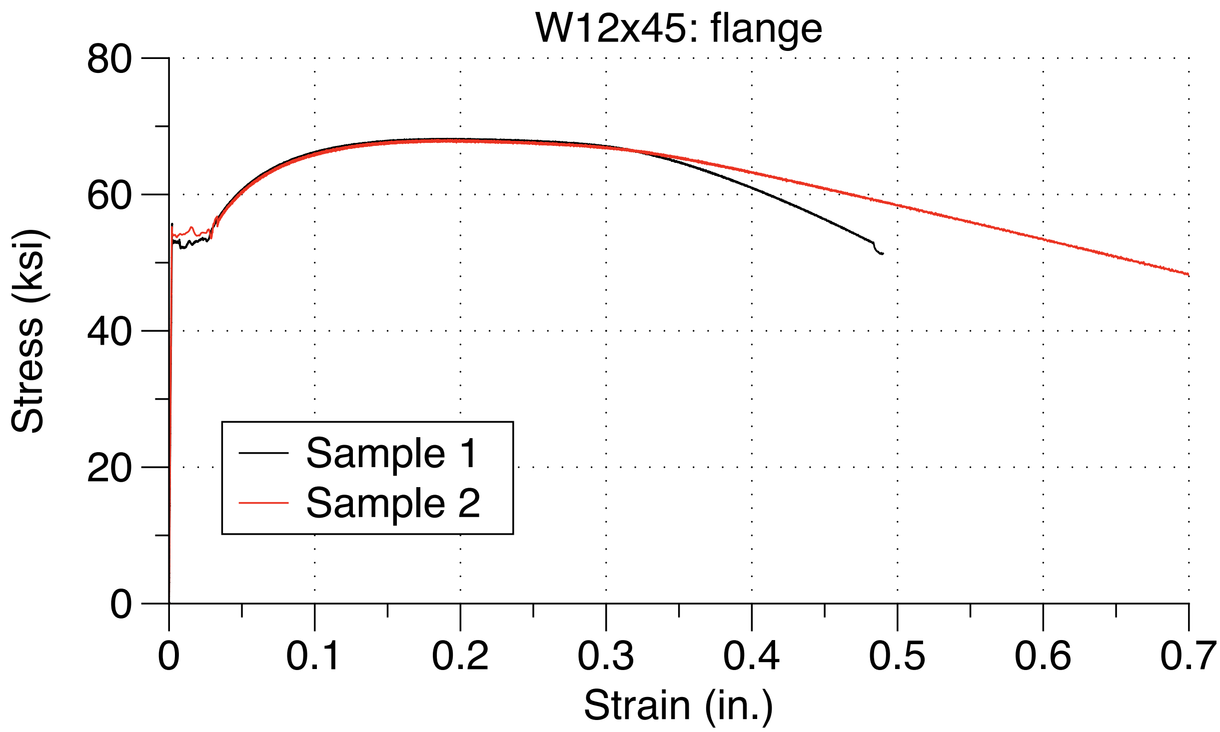

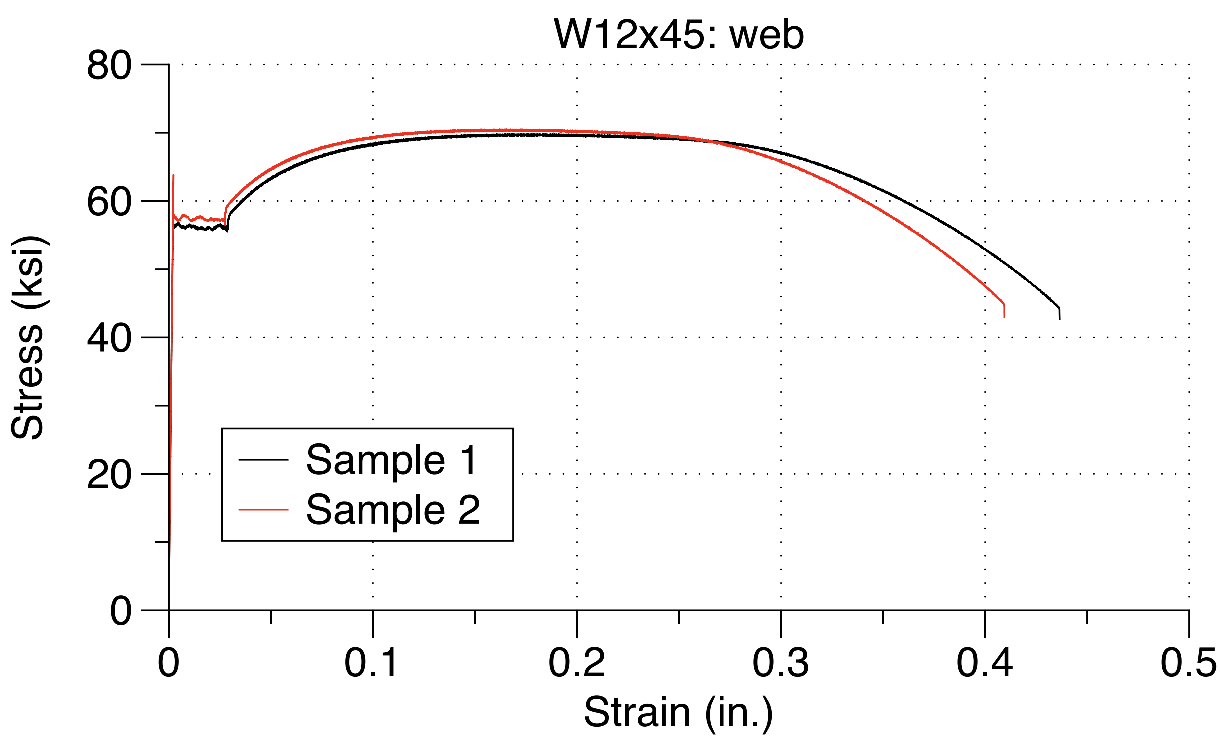

Figure B.5 Stress-strain diagram - steel coupling beam W12x45 (specimens 3-6).

This page left blank intentionally.

Appendix C
Force relationships between secondary and primary actuators

The forces in the secondary actuators need to be related to the coupling beam shear force. These relationships were determined to maintain equal stresses in the prototype C-shaped wall pier and test specimen rectangular wall. The procedure is explained in the following with reference to Figure C.1.

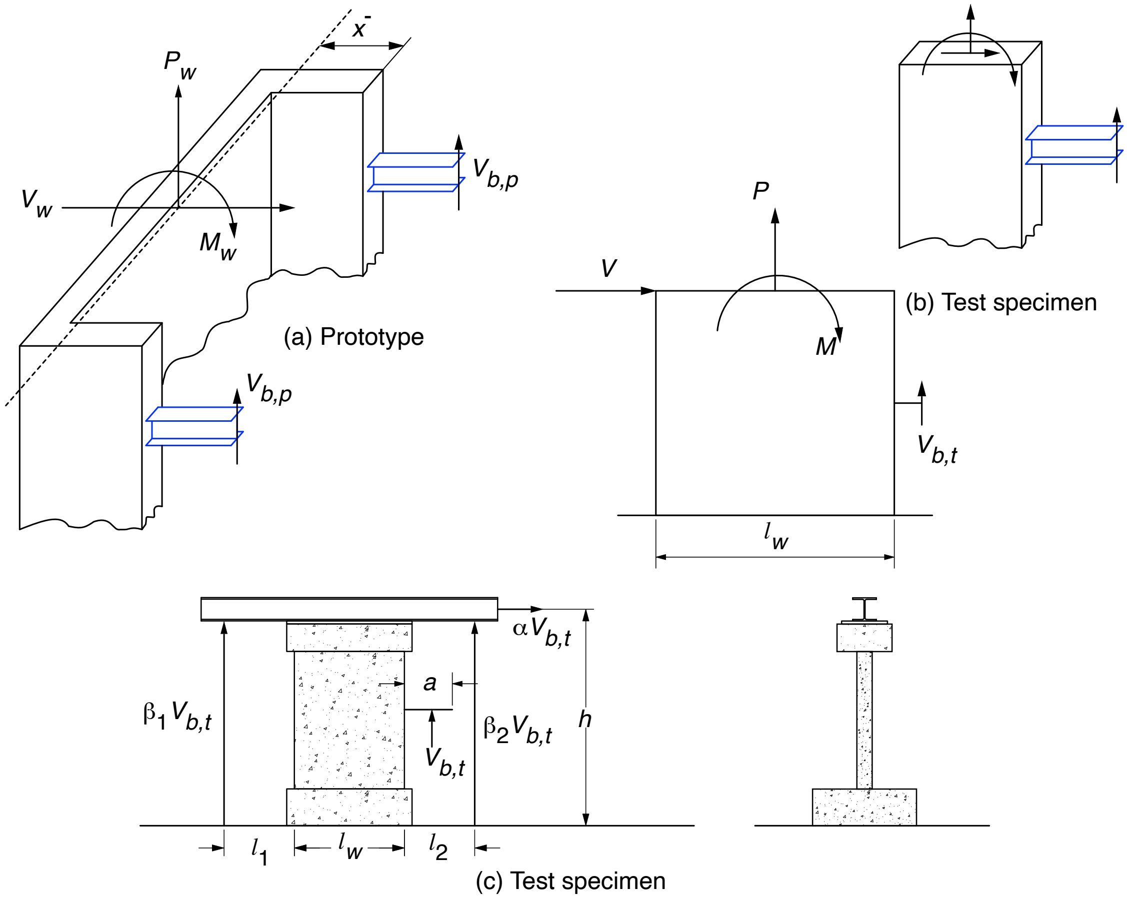

Figure C.1 Illustration of procedure for establishing relationships between actuators.

1. For the prototype structure, the relationships between coupling beam shear ($V_{b,p}$) and wall shear (V_w), wall axial force (P_w), and wall overturning moment (M_w) are established based on the calculated design forces obtained from analysis, i.e., factors R_1, R_2, and R_3 shown in Eq. C.1. These relationships are then used to express the axial stresses (σ) and shear stress (τ) in the prototype C-shaped wall pier in terms of coupling beam shear (Eq. C.1).

$$\frac{V_w}{2V_{b,p}} = R_1 \qquad \frac{P_w}{2V_{b,p}} = R_2 \qquad \frac{M_w}{2V_{b,p}} = R_3$$

$$\tau_{due\ to\ V_w} \approx \frac{V_w}{A_{c\ shaped\ wall}} \qquad \sigma_{due\ to\ P_w} = \frac{P_w}{A_{c\ shaped\ wall}} \qquad \sigma_{due\ to\ M_w} = \frac{M_w x^-}{I_{c\ shaped\ wall}} \qquad \textbf{Eq. C.1}$$

$$\tau_{due\ to\ V_w} \approx \frac{2V_{b,p}R_1}{A_{c\ shaped\ wall}} \qquad \sigma_{due\ to\ P_w} = \frac{2V_{b,p}R_2}{A_{c\ shaped\ wall}} \qquad \sigma_{due\ to\ M_w} = \frac{2V_{b,p}R_3 x^-}{I_{c\ shaped\ wall}}$$

2. The level of stress in wall piers is a key factor influencing the performance of coupling beam. Therefore, the axial stresses due to axial force and overturning moment as well as the shear

stress in the prototype C-shaped wall pier and rectangular are set equal. These stresses (Eq. C.2) can be simplified to find the relationships between the wall shear force (V), axial force (P), and overturning moment (M) and the coupling beam shear ($V_{b,t}$) in the test specimen as shown in Eq. C.3.

$$\sigma_{due\ to\ P} = \frac{P}{A_{rectangular\ wall}} = \sigma_{due\ to\ P_w} = \frac{2V_{b,p}R_2}{A_{c\ shaped\ wall}}$$
$$\sigma_{due\ to\ M} = \frac{M(0.5l_w)}{I_{rectangular\ wall}} = \sigma_{due\ to\ M_w} = \frac{2V_{b,p}R_3x^-}{I_{c\ shaped\ wall}} \qquad \textbf{Eq. C.2}$$
$$\tau_{due\ to\ V} \approx \frac{V}{A_{rectangular\ wall}} = \tau_{due\ to\ V_w} \approx \frac{2V_{b,p}R_1}{A_{c\ shaped\ wall}}$$

$$\frac{P}{V_{b,t}} = \frac{2(A_{rectangular\ wall})R_2}{A_{c\ shaped\ wall}} \rightarrow P = V_{b,t}\frac{2(A_{rectangular\ wall})R_2}{A_{c\ shaped\ wall}}$$
$$\frac{M}{V_{b,t}} = \frac{2(I_{rectangular\ wall})R_3x^-}{0.5l_w(I_{c\ shaped\ wall})} \rightarrow M = V_{b,t}\frac{2(I_{rectangular\ wall})R_3x^-}{0.5l_w(I_{c\ shaped\ wall})} \qquad \textbf{Eq. C.3}$$
$$\frac{V}{V_{b,t}} = \frac{2(A_{rectangular\ wall})R_1}{A_{c\ shaped\ wall}}$$

3. The value of α (see Figure C.1) is $V/V_{b,t}$ calculated from Eq. C.3. The value of R_1 is obtained from Eq. C.1. Equilibrium of forces shown in Figure C.1c is used to obtain the values of β_1 and β_2; the equilibrium equations are $P = \beta_1 V_{b,t} + \beta_2 V_{b,t}$ and $M = \beta_1 V_{b,t}(l_1 + 0.5l_w) - \beta_2 V_{b,t}(l_2 + 0.5l_w)$. From these two equations, the expressions for β_1 and β_2 become

$$\beta_1 V_{b,t} = \frac{M + P(l_2 + 0.5l_w)}{l_1 + l_2 + l_w} \qquad \beta_2 V_{b,t} = \frac{P(l_1 + 0.5l_w) - M}{l_1 + l_2 + l_w}$$

Substituting P and M by the expressions obtained in Eq. C.3, the values of β_1 and β_2 can be determined from Eq. C.4 in which R_2 and R_3 are from Eq. C.1.

$$\beta_1 = \frac{\frac{2(I_{rectangular\ wall})R_3x^-}{0.5l_w(I_{c\ shaped\ wall})} + \frac{2(A_{rectangular\ wall})R_2}{A_{c\ shaped\ wall}}(l_2 + 0.5l_w)}{l_1 + l_2 + l_w}$$
$$\textbf{Eq. C.4}$$
$$\beta_2 = \frac{\frac{2(A_{rectangular\ wall})R_2}{A_{c\ shaped\ wall}}(l_1 + 0.5l_w) - \frac{2(I_{rectangular\ wall})R_3x^-}{0.5l_w(I_{c\ shaped\ wall})}}{l_1 + l_2 + l_w}$$

This page left blank intentionally.

Nonlinear Wind Design of Steel Reinforced Concrete (SRC) Coupling Beams: Final Report

Alexander Hill

Jacob Forbes

Christopher J. Motter

Washington State University

RGA #06-19

CHARLES PANKOW FOUNDATION

Building Innovation through Research

aci Foundation Building the Future

MAGNUSSON KLEMENCIC ASSOCIATES FOUNDATION

Acknowledgements

This research was supported by funding from the Charles Pankow Foundation, with co-funding from the American Concrete Institute (ACI) Foundation and the Magnusson Klemencic Associates (MKA) Foundation. The authors express their gratitude to the Charles Pankow Foundation, ACI Foundation, and MKA Foundation. Any opinions, findings, and conclusions expressed in this material are those of the authors and do not necessarily reflect those of the Charles Pankow Foundation, ACI Foundation, or MKA Foundation. Thanks are extended to the members of the industry advisory panel, comprised of Viral Patel, Rafael Sabelli, Gregory Deierlein, Mark Denavit, Brad Malmsten, John Peronto, Roberto Leon, Amit Varma, Ron Klemencic, David Fields, John Hooper, Kevin Aswegan, Sean Clifton, Juliana Rochester, Russell Larsen, Jordan Jarrett, and Bahram Shahrooz. Thanks are extended to Scott Lewis, Joshah Jennings, Jesse Black, Levi Arnold, Britnie Casillas, Isaac Nisbet, Parker Likes, Kyle Doering, Nicholas Bonnington, Walker Smith, and Riley Haug for assistance with laboratory testing. This study on steel reinforced concrete (SRC) coupling beams was conducted in parallel with a companion study on steel coupling beams conducted at the University of Cincinnati. Sushil Kunwar, Bahram Shahrooz, and Patrick Fortney are thanked for collaborative discussions. This research is dedicated to the memory of Patrick J. Fortney.

Abstract

Structures are typically designed to yield and sustain damage in a controlled manner during design-level earthquakes. While a similar approach has traditionally not been used for design-level windstorms, the recently-published ASCE/SEI Prestandard for Performance Based Wind Design (ASEC/SEI, 2019) describes design for modest nonlinear response of select structural members such as coupling beams. In this study, four steel reinforced concrete (SRC) coupling beams, with steel sections that embedded into a reinforced concrete wall, were tested quasi-statically under fully reversed cyclic wind demands with peak beam deformation of three times the yield rotation. The beams and walls were designed in accordance with seismic provisions in AISC 341-22 Section H5, and the walls were compliant with ACI 318-19 Section 18.10.6.5. The exception was the wall reinforcement for two of the four tests, in order to examine potential reductions to that prescribed. For one of these tests, the ratio of the strength of wall longitudinal reinforcement crossing the embedment length to that prescribed was 0.53. For the other of these tests, this value was 0.22 and the wall boundary transverse reinforcement at the embedment zone was also less than that prescribed. During each test, the wall was subjected to constant axial gravity load and fully reversed-cyclic lateral loading that was linearly proportional to the load in the test beam. The ratio of wall shear to beam shear was constant for the four tests, while the ratio of wall moment to beam shear was the same for three tests and was larger for one of the tests with wall reinforcement compliant with AISC 341-22 Section H5.

For the test with the least wall reinforcement, significant damage was observed in the wall at the embedded connection. The load developed in the beam was limited by yielding in the wall. Significant pinching, characteristic of gapping, was observed in the load-deformation response. Significant stiffness degradation occurred for repeated loading cycles at 40% of the computed peak strength, and the beam was unable to develop 75% of the computed beam strength, despite being loaded to 6.0% chord rotation. The quantity of wall reinforcement was inadequate to promote favorable performance. Performance was more favorable for the other three tests, which were observed to have similarities in damage patterns and load-deformation responses. Damage concentrated at the beam-wall interface, with the majority of the coupling beam deformation at this location. Although the stiffness degradation for these three tests was much less than the test with wall yielding, stiffness degradation for repeated loading cycles at a given load level was found to be significant in these three tests, particularly for larger loading levels prior to yielding. However, significant strength degradation of initial cycles at new peak deformation demands was not observed in any tests, and significant pinching in the load-deformation response was not observed for the three tests with more favorable performance. Peak load resistance was reached at peak deformation demand, which was 5.70% chord rotation for the test with the largest wall demands, 4.80% chord rotation for two tests, and 6.0% for the test with wall yielding. The primary difference in load-deformation responses for the wind tests conducted in this study and previous seismic tests was the stiffness degradation with repeated loading cycles, noting that the number of cycles used in the wind tests was substantially higher than that used in typical seismic tests.

Stiffness for the first loading cycle at 75% of the expected strength was examined using the results from the three test beams from this study that reached this level and three SRC coupling beams from other studies. The difference between stiffness in the positive and negative direction was more significant for larger cyclic wall demands, with higher stiffness in the positive direction due to wall demands producing compression at the embedment region. The average of the positive and negative stiffness was larger for walls with higher compression force in the wall on the positive excursion. If cyclic stiffness degradation for repeated cycles at a given increment is not explicitly modeled, it is recommended to use a backbone model based on average values of all cycles at each increment, as this would lead to equal area under the curve for the backbone model and test data. Parameters for a bilinear backbone model for nonlinear wind design are suggested, with effective stiffness of 75% of that prescribed in AISC 341-22 for seismic design, a yield force computed using moment-curvature analysis at full yielding of the tension flange using expected material properties, a computed expected strength from AISC 341-22, and a post-yield slope based on 4.0% chord rotation from yield to expected strength. It is recommended that the hysteretic model be determined by modeling the test beams and calibrating to dissipated energy test data for the three tests with favorable performance. Each of the four backbone parameters were determined based on fit to test data.

This study did not include testing on SRC coupling beams that were designed using provisions in AISC 341-22 Section H4 and tested to peak deformation demands more consistent with ordinary walls. It is recommended that nonlinear wind design of steel reinforced concrete (SRC) coupling beams follow the seismic provisions in AISC 341-22 Section H5. It is recommended that the quantity of wall longitudinal reinforcement crossing the embedment length prescribed by AISC 341-22 Section H5 be reduced by 50% for cases in which wall demands do not exceed that applied for the test that supported this recommendation. These peak wall moment and tensile strain demands were $0.29M_y$ and 0.00019 tensile strain in outermost reinforcement at the coupling beam mid-height and an average of $0.04M_y$ and -0.00001 tensile strain (0.00001 compressive strain) in outermost reinforcement over one story height, taken as half a story above and below the coupling beam mid-height. These demands were determined from moment-curvature analysis for the moment and axial load in the wall determined by assuming transfer of coupling beam shear and moment to the wall at coupling beam mid-height. This recommendation applies for both seismic and wind design, due to favorable performance for this test under wind demands to a peak deformation of 4.65% chord rotation.

Table of Contents

List of Figures

List of Tables

1. Introduction

Reinforced concrete coupled walls are often used in buildings to provide lateral resistance to seismic and wind demands. Coupling beams are located at the top of story levels and connect to adjacent coplanar walls, creating openings beneath the coupling beams. Shear and moment demand from the coupling beams are transferred into the wall to provide coupling. The shear demands create axial load in the walls. Coupled walls are stiffer and stronger than uncoupled walls due to the moment resistance provided by beams and by the axial tension-compression force couple. During large earthquakes, plasticity is expected to concentrate at the ends of the coupling beams and at the base of the walls. Coupling beams are typically designed to yield prior to walls and provide ductility, energy dissipation, and redundancy. Rotational demands on coupling beams from lateral loads acting on coupled walls are typically higher than other structural components.

Seismic design provisions for diagonally and conventionally reinforced concrete coupling beams are provided in ACI 318-19. The use of diagonal reinforcement rather than conventional reinforcement is often necessary to satisfy shear demands. The use of diagonal reinforcement provides improved resistance to shear sliding relative to longitudinal reinforcement (Paulay and Binney, 1974). However, the need to develop the diagonal reinforcement into the wall leads to congestion of reinforcement at the wall boundaries that complicates construction. Steel and steel reinforced concrete (SRC) coupling beams are an alternative to rebar-reinforced concrete coupling beams that reduce reinforcement congestion in the wall to simplify construction. Relative to steel coupling beams, the concrete encasement used in SRC coupling beams provides fire protection and stability against flange and web buckling. From past studies on steel coupling beams (Shahrooz et al, 1993; Harries et al, 1993; Harries et al, 1997) and SRC coupling beams (Gong and Shahrooz, 2001a,b; Motter et al, 2017a,b), it is evident that the deformation capacity can meet or exceed that of rebar-reinforced concrete coupling beams. This previous research focused on seismic behavior in special coupled walls, which are designed for ductile post-yield response in earthquakes. This led to development of performance-based seismic design guidelines (Motter et al, 2013) and updates to the AISC Seismic Provisions (AISC 341-22) for prescriptive seismic design.

Research and resulting development of design provisions on coupling beams subjected to nonlinear demand from wind loading is lacking. This is largely due to the difference in design approach reflected in building codes for seismic and wind. Existing seismic design guidelines (e.g., PEER TBI, 2017) recommend an essentially elastic structural response for a service-level earthquake with 43-year return period, with significant nonlinearity permitted for the maximum considered earthquake with a 2475-year return period. Seismic design provisions in ASCE 7-16 similarly allow for significant nonlinearity in the design-level earthquake, which reflects a roughly 475-year return period. Wind design provisions in ASCE 7-16 are based on linear behavior for an approximately 1700-year design wind speed. Due to the inconsistency in design philosophy for wind and seismic, the design of buildings in U.S. regions with significant seismicity may be controlled by wind. Efforts to provide more consistency between wind and seismic design are reflected by the recently-published ASCE/SEI Prestandard for Performance Based Wind Design (ASEC/SEI, 2019), which describes design for modest nonlinear response of select structural members such as coupling beams. Previous research on the behavior of coupling beams subjected to many loading cycles at modest peak ductility demands is limited. There is a need to address this research gap in order to design for modest coupling beam nonlinearity using the ASCE/SEI Prestandard for Performance Based Wind Design (ASCE/SEI, 2019). This study focuses on characterization of the nonlinear response of SRC coupling beams under wind demands. Recent research was conducted on the nonlinear response of reinforced concrete coupling beams to wind demand (Abdullah et al, 2020). Abdullah et al (2020) tested one SRC coupling beam, with the steel section embedded into concrete blocks that were post-tensioned. To provide additional data on the behavior of SRC coupling beams under nonlinear wind demands, cyclic tests on SRC coupling beams embedded into structural walls were conducted in this study. Four tests were conducted, and the testing and data analysis are summarized in this report. Design recommendations were formulated and are also provided in this report.

2. Background

2.1. Previous Research on Steel and SRC Coupling Beams

For steel and SRC coupling beams, the steel section is embedded into the structural wall to make a connection through a bearing mechanism. Marcakis and Mitchell (1980) and Mattock and Gaafar (1982) studied embedment behavior of steel sections embedded into concrete columns and provided recommended equations to compute the embedment strength that were adopted into AISC 341-22 for steel and SRC coupling beams embedded into walls. The equations adopted into AISC 341-22 included modification of the embedment strength for spalling of wall cover concrete, as recommended by Harries et al (1993).

The vertical stresses in the structural wall at the embedded connection may vary considerably. Shahrooz et al (1993) conducted seismic testing on steel coupling beams embedded into cyclically loaded reinforced concrete structural walls, such that the wall stresses at the embedded connection could vary from compression to tension. Shahrooz et al (1993) observed asymmetric response in the coupling beams, with reduced fixity of the embedded steel section under wall tension demands compared to compression demands. This reduced the fixity of the embedded coupling beam to increase the effective beam length, and Shahrooz et al (1993) recommended that the effective length be increased by one third of the embedment length.

Gong and Shahrooz (2001a,b) conducted seismic tests on SRC coupling beams. Gong and Shahrooz (2001a) reported unfavorable performance when embedment length is based on capacity design for the beam excluding the reinforced concrete encasement. Conversely, Gong and Shahrooz (2001b) reported favorable performance when embedment length was based on capacity design for the beam including the reinforced concrete encasement. Gong and Shahrooz (2001b) provided a recommended equation for determining the peak shear strength of an SRC coupling beam and recommended that this peak strength be used for capacity design of the embedment for shear-controlled coupling beams.

Harries et al (1993, 1997) conducted seismic tests on steel coupling beams embedded into concrete wall segments. Harries et al (1993, 1997) recommended use of longitudinal reinforcement with strength exceeding the beam shear strength to control the crack opening along the flanges of the embedded steel section. This recommendation was adopted into AISC 341. The embedment creates local tensile demands in the wall at the connection region, due to the bearing forces in the embedded connection. The localized tensile demands can cause or exacerbate yielding in the wall in the connection region. Wall yielding was observed in tests in which it was not computed when modeling the transfer of beam shear and moment to the wall at a discrete point, potentially leading to significant damage if not accounted for in design (Motter et al, 2017a). Recognizing that this modeling approach is not uncommon, additional longitudinal reinforcement in the wall may be required to mitigate the effect of the additional demands at the embedment region (Harries et al, 1993, 1997; Motter et al, 2017b). Motter et al (2017b) recommended that the wall longitudinal reinforcement crossing the embedment length provide nominal strength that also meets or exceeds the resultant back bearing force in the coupling beam, and this provision was introduced into AISC 341-22.

2.2. Summary of Building Code Design Provisions for SRC Coupling Beams

Seismic design provisions for SRC coupling beams are provided in AISC 341-22. H4 applies to composite ordinary shear walls, and H5 applies to composite special shear walls. H4 and H5 provisions are summarized in this section.

For composite ordinary shear walls, provisions in H4.5b.2 specify that the beam shear demand determined from analysis not exceed the connection shear strength, $\phi_v V_{n,connection}$, with ϕ_v=0.9 and $V_{n,connection}$ determined from:

$$V_{n,connection} = 1.54\sqrt{f_c'}\left(\frac{b_w}{b_f}\right)^{0.66}\beta_1 b_f L_e\left(\frac{0.58-0.22\beta_1}{0.88+\frac{g}{2L_e}}\right) \tag{2-1}$$

where L_e is the embedment length of the coupling beam measured from the face of the wall, g is the clear span of the coupling beam, b_w is the thickness of the wall, b_f is the width of the steel section flange, f'_c is the specified compressive strength of concrete in ksi, and β_1 is a factor relating the depth of the equivalent rectangular compressive stress block to neutral axis depth, as defined in ACI 318-19. This provision may be used to determine the minimum L_e for satisfactory design. Provisions in H4.5b.2 also specify that the beam shear demand determined from analysis not exceed the design shear strength, $\phi_v V_{nc}$, with ϕ_v=0.9 and V_{nc} determined from:

$$V_{nc} = V_p + 0.0632\sqrt{f_c'}b_{wc}d_c + \frac{A_{sr}F_{ysr}d_c}{s} \tag{2-2}$$

where A_{sr} is the area of transverse reinforcement within s, F_{ysr} is the specified minimum yield stress of transverse reinforcement, b_{wc} is the width of concrete encasement, d_c is the effective depth of concrete encasement, s is the spacing of transverse reinforcement, and $V_p = 0.6F_yA_w$, where F_y is the specified yield strength of steel for the steel section, and A_w is the web area of the steel section. It is specified that the peak moment demand, M_u, in the coupling beam determined from analysis, which occurs at the beam-wall interface, be multiplied by $1+[(2L_e)/(3g)]$ to account for fixity at $L_e/3$ into the wall from the beam-wall interface, where L_e is the minimum embedment length computed from Eq. (2-1) to provide sufficient connection shear strength. The flexural strength of the beam is ϕ_bM_n, as defined in ANSI/AISC 360-22 Chapter I. Wall longitudinal reinforcement is required over the embedment length of the beam with nominal axial strength not less than:

$$\left(\frac{\frac{g}{2L_e}+0.33\beta_1}{0.88-0.33\beta_1}\right)V_u \geq V_u \tag{2-3}$$

where V_u is the maximum shear demand in the beam. This wall longitudinal reinforcement is prescribed to extend at least one tension development length above and below the flanges of the embedded steel section. Beam longitudinal and transverse reinforcement is prescribed to be distributed around the perimeter with total area in each direction of at least $0.002b_{wc}$ and spacing not exceeding 12". The beam longitudinal reinforcement is prescribed not to extend into the wall and not to be included in the computation of flexural strength.

For composite special shear walls, provisions in H5.5d specify that the embedment length of the steel section into the wall be determined from:

$$V_{be} = 1.54\sqrt{f_c'}\left(\frac{b_w}{b_f}\right)^{0.66}\beta_1 b_f L_e\left(\frac{0.58-0.22\beta_1}{0.88+\frac{g}{2L_e}}\right) \tag{2-4}$$

where L_e is the embedment length of the coupling beam considered to begin inside the first layer of confining reinforcement, nearest to the edge of the wall, in the wall boundary member, V_{be} is the expected shear strength of the coupling beam, and g is the clear span of the coupling beam plus the wall concrete clear cover at each end of the beam. V_{be} is specified to be the lesser of the expected flexural and shear strength, computed as:

$$V_{be} = \frac{2(1.1)M_{pbe}}{g} \leq V_{ce} \tag{2-5}$$

where M_{pbe} is the expected flexural strength calculated using the plastic stress distribution or the strain compatibility method, with applicable R_y and R_c factors used for different elements of the cross-section, and V_{ce} is computed as:

$$V_{ce} = 1.1R_yV_p + 0.08\sqrt{R_cf_c'}b_{wc}d_c + \frac{1.33R_{yr}A_{sr}F_{ysr}d_c}{s} \tag{2-6}$$

where R_c = 1.3 is a factor to account for the expected strength of concrete, R_y is the ratio of the expected yield stress to the specified yield stress for the structural steel section, and R_{yr} is the ratio of the expected yield stress to the specified yield stress for the transverse reinforcement, with values for R_y and R_{yr} taken from Table A3.2 in AISC 341-22 (2022). Wall longitudinal reinforcement is required over the embedment length of the beam with nominal axial strength not less than:

$$\left(\frac{\frac{g}{2L_e}+0.33\beta_1}{0.88-0.33\beta_1}\right)V_{be} \geq V_{be} \tag{2-7}$$

This wall longitudinal reinforcement is prescribed to extend at least one tension development length above and below the flanges of the embedded steel section. This wall reinforcement is prescribed to be confined by transverse reinforcement that meets ACI 318 Section 18.10.6. For cases in which the longitudinal reinforcement ratio is less than $400/f_y$, transverse reinforcement satisfying ACI 318-19 Section 18.10.6.5(b) through (e) over the distance calculated in accordance with ACI 318-19 Section 18.10.6.4(a) is required between a height of L_e below the bottom flange and L_e above the top flange of an embedded steel section. The vertical spacing of this transverse reinforcement is prescribed not to exceed the lesser of 8” and eight times the diameter of the smallest longitudinal reinforcement confined by this transverse reinforcement. Beam longitudinal and transverse reinforcement is prescribed to be distributed around the perimeter with total area in each direction of at least $0.002b_{wc}$ and spacing not exceeding 12”. The beam longitudinal reinforcement is prescribed not to extend into the wall and not to be included in the computation of flexural strength.

3. Experimental Program

3.1. Specimen Design

Four SRC coupling beams embedded into reinforced concrete walls were designed, constructed, and tested. Each of two test specimens, shown in Figure 3.1 and Figure 3.2, was comprised of two coupling beams, a wall, a footing, and a top block. For each test specimen, the coupling beams were tested separately with load simultaneously applied to the wall. The coupling beams were tested as cantilevers, with the point of load application representing mid-length of a full-length coupling beam. The coupling beams were nominally identical. The test variables were the wall longitudinal reinforcement and the level of wall demands applied. For the four tests, SRC-W1, SRC-W2, SRC-W3, and SRC-W4, the wall longitudinal reinforcement ratio at the boundary was 0.026, 0.026, 0.012, and 0.0031, respectively, noting that the value for SRC-W4 is the web reinforcement ratio due to the lack of boundary element. The ratio of applied wall demands to applied coupling beam shear were the same for SRC-W2, SRC-W3, and SRC-W4 and less than that of SRC-W1. More details on the wall demands are provided in Section 3.6. Each coupling beam, shown in Figure 3.3, had 12” by 18” cross-section and a W12x96 A992 structural steel section with the flanges trimmed to 5.5” width. The flanges were trimmed to achieve improved scaling, as the test beams represented a ½-scale 24” by 36” rectangular cross section reinforced with a W24x250 A992 steel section. The beams were tested as 30” cantilevers. Each wall had 12” by 96” cross-section, shown in Figure 3.4, with 90” clear height. The footings were 33” wide by 18” tall by 120” long, and the top blocks were 27” wide by 18” tall by 120” long.

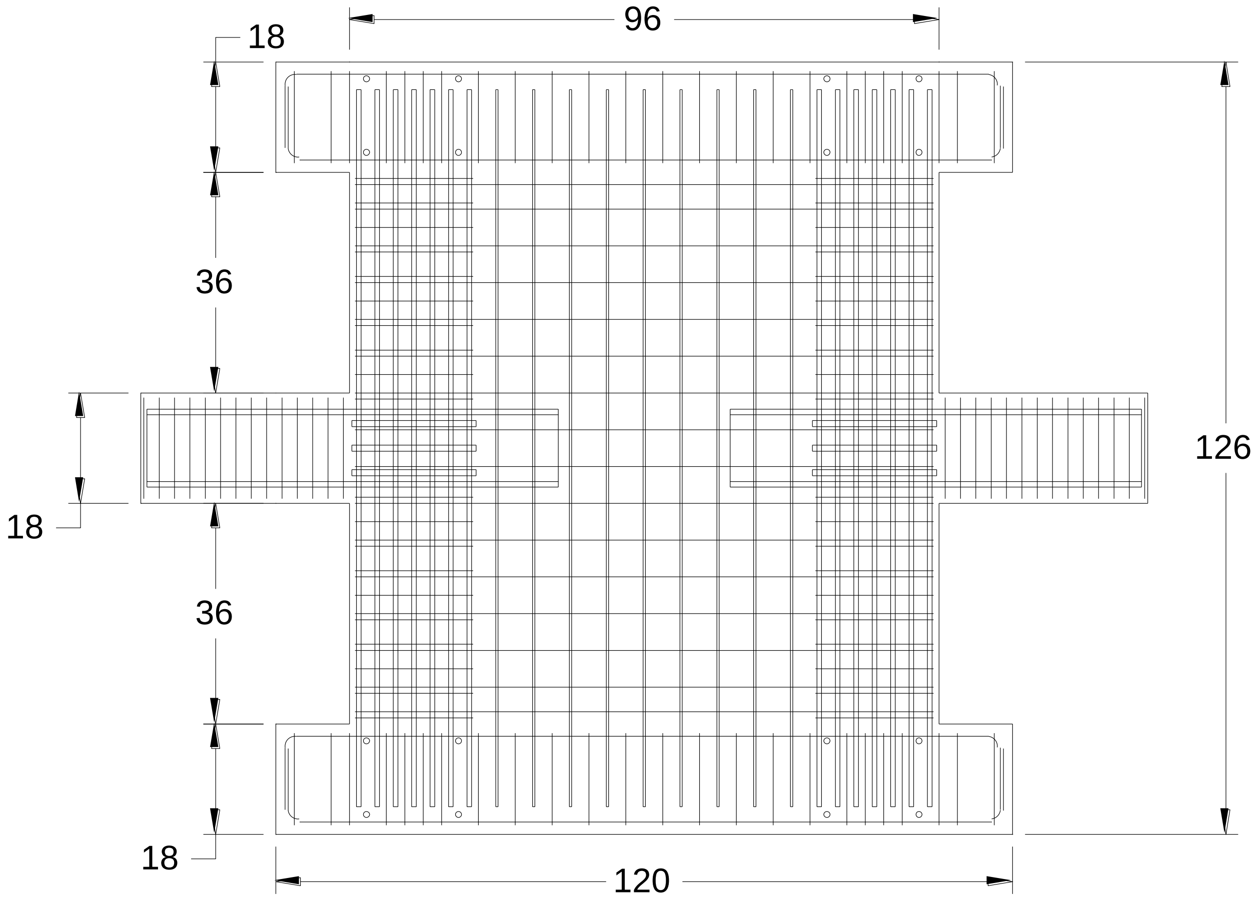

Figure 3.1. Elevation View of Test Specimen with SRC-W1 and SRC-W2

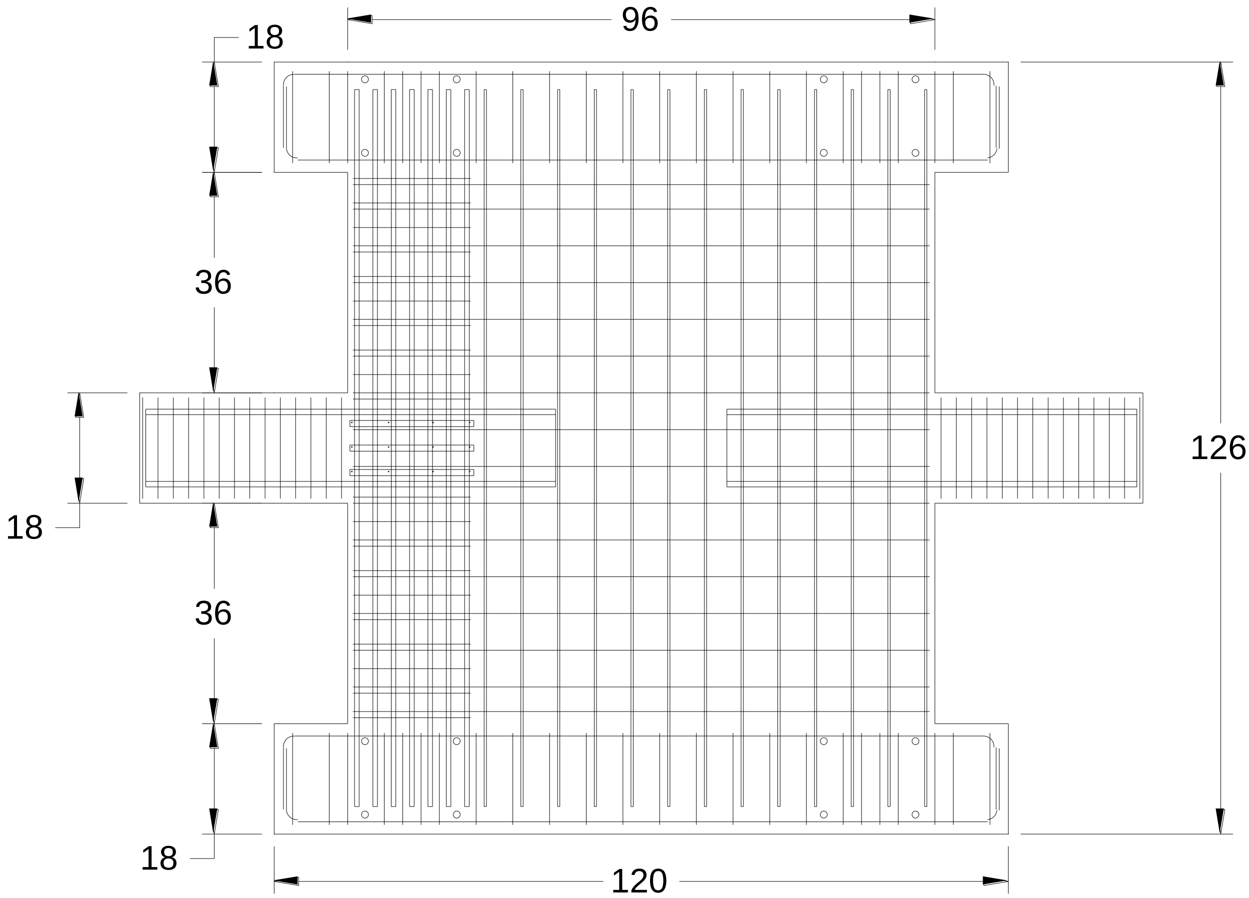

Figure 3.2. Elevation View of Test Specimen with SRC-W3 and SRC-W4

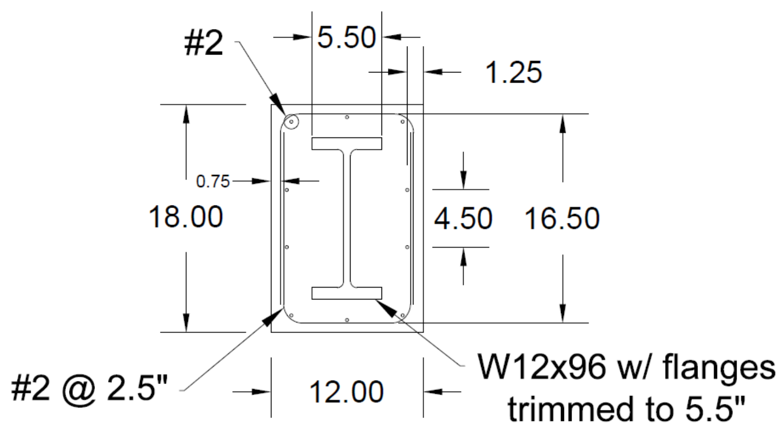

Figure 3.3. Coupling Beam Cross-Section

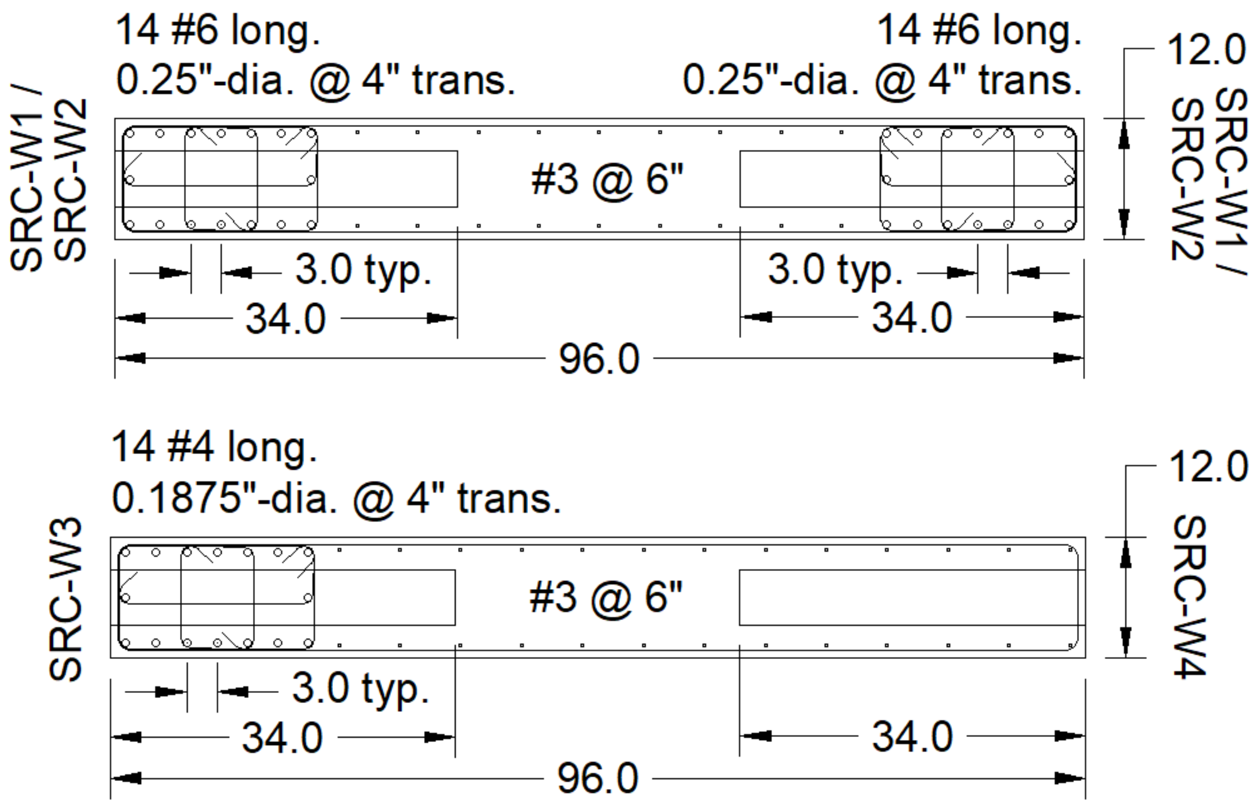

Figure 3.4. Wall Cross-Sections

There is a lack of previous research on the nonlinear wind behavior of SRC coupling beams, such that there is lack of design guidance. However, seismic design guidelines are provided in AISC 341-22 and were summarized in the previous chapter. In AISC 341-22, Section H5 applies to composite special shear walls, while Section H4 applies to composite ordinary shear walls. AISC 341-22 Section H4 provisions are expected to provide limited inelastic deformation capacity through yielding, as specified in AISC 341-22 Section H4.2. AISC 341-22 Section H5 provisions are expected to provide significant inelastic deformation capacity through yielding, such that the walls are specified to be designed including Chapter 18 of ACI 318, as specified in AISC 341-22 Section H5.2. ACI 318-19 Section 18.10.1.1 specifies that Section 18.10 applies to special structural walls. In this study, the coupling beams were tested to peak deformation demands of three times the yield rotation, with more details on loading protocol provided in Section 3.6. This level of demand is comparable to peak coupling beam demands under MCE-level earthquake for the 42-story reinforced concrete core wall building analyzed in Moehle et al (2011). The peak demands on the test beams were deemed to be more consistent with AISC 341-22 Section H5 design than AISC 341-22 Section H4 design. Therefore, the beams and walls were designed to satisfy AISC 341-22 Section H5.5 and ACI 318-19 Section 18.10.

0.25”-diameter A36 undeformed bar was used as reinforcement in the beam. This included ten longitudinal bars around the perimeter of the section and transverse reinforcement comprised of hoops spaced at 2.5” on center. Each hoop used as transverse reinforcement consisted of U-bars with long legs overlapping. The concrete clear cover to the beam transverse reinforcement was 0.75”. At full-scale, this reinforcement in the half-scale beam satisfied AISC 341-22 Section H4.5b.2(c) for a total area in each direction of at least $0.002b_{wc}$ and spacing not exceeding 12”. The longitudinal reinforcement was not embedded into the wall, as recommended by Barbachyn et al (2012) and prescribed by AISC 341-22, rather than embedded a short distance as shown in ACI 318-19 Fig. R18.10.7.b.

The specified compression strength of concrete, f'_c, used in the beams and wall was 5.5 ksi. Using R_y = 1.1 for A992, R_{yr} = 1.5 for A36, and R_c = 1.3 from AISC 341-22, M_{pbe} was computed to be 448 k-ft, and V_{ce} was computed to be 344 k for the beam. The clear cover at the end of the wall was 0.75” to 0.25”-diameter wall boundary transverse reinforcement and 0.625” to #3 U-bars spliced to wall shear reinforcement. Using the larger clear cover to determine g, V_{be} was computed to be 192 k for the flexure-controlled beam. L_e was computed to be 33.0" using Eq. (2-4). L_e begins from the inside of the wall boundary transverse reinforcement, which was located 1.0" from the beam-wall interface. Thus, the required embedment length from the beam-wall interface was 34.0", which was the length provided. Auxiliary transfer bars and end bearing plates were not provided in the embedment region. Web stiffeners were not provided in the steel section.

The minimum required strength of wall longitudinal reinforcement crossing the embedment length was determined to be 366 kips in accordance with Eq. (2-7). SRC-W1 and SRC-W2 had 14#6 and 4#3 Grade 60 longitudinal bars crossing the embedment length, as shown in Figure 3.4 and Figure 3.2, for a provided nominal strength of 396 kips, which was 1.08 times that required. This ratio was less than 1.0 for SRC-W3 and SRC-W4 to assess whether the quantity of reinforcement prescribed by AISC 341-22 could be reduced if wall demands are sufficiently low. SRC-W3 had 14#4 and 4#3 Grade 60 longitudinal bars crossing the embedment length for a provided nominal strength of 194.4 kips, which was 0.53 times that required. SRC-W4 had 12#3 Grade 60 longitudinal bars crossing the embedment length for a provided nominal strength of 79.2 kips, which was 0.22 times that required.

It was assumed that the test beams were not located in a wall location with a special boundary element. The corresponding boundary longitudinal reinforcement ratio of 0.026 for SRC-W1 and SRC-W2 and 0.012 for SRC-W3 exceeded $400/f_y = 0.0067$, such that an intermediate level of boundary transverse reinforcement was required by ACI 318-19 Section 18.10.6.5(b). The boundary element transverse reinforcement was configured as hoops and cross-ties with 0.75" clear cover that were spaced longitudinally at 4" on center with every other longitudinal bar restrained along the length of the wall. This satisfied the requirements of ACI 318-19 Section 18.10.6.5(b) at half-scale. The boundary element transverse reinforcement was 0.25”-diameter A36 undeformed bar for SRC-W1 and SRC-W2 and 0.1875”-diameter A36 undeformed bar for SRC-W3. This satisfied the requirements of ACI 318-19 Section 25.7.2.2, which specifies #3 or larger transverse reinforcement for #10 or smaller longitudinal reinforcement and #4 or larger transverse reinforcement for #11 or larger longitudinal reinforcement, at half-scale. The two longitudinal bars in each boundary located at the wall centerline were discontinuous at the embedment of the steel section. Wall boundary element transverse reinforcement was provided in the embedment zone using threaded rods and plates, as shown in Figure 3.5. The threaded rods and plates, which were spaced longitudinally at 4”, were sized to provide stiffness and strength not less than that of the boundary element transverse reinforcement above and below the embedded steel section. The threaded rods passed through holes pre-drilled into the web of the steel section prior to assembly. This detailing is consistent with that used by Motter et al (2017a). For SRC-W4, the longitudinal reinforcement ratio of 0.0031 was less than $400/f_y$ = 0.0067, such that an intermediate level of boundary transverse reinforcement was not required by ACI 318-19 Section 18.10.6.5(b). The wall boundary transverse reinforcement required by AISC 341-22 Section H5.5b between a height L_e below the bottom flange and L_e above the top flange was not provided for SRC-W4.

Wall web horizontal and vertical reinforcement was #3 spaced at 6”, and the resulting reinforcement ratio of 0.0031 exceeded the minimum of 0.0025 required by ACI 318-19 Section 18.10.2.1. The vertical web reinforcement extended to the end of the wall for SRC-W4. U-bars at the ends of the wall were spliced to the wall web horizontal reinforcement to satisfy ACI 318-19

Section 18.10.6.5(a). At the location of the embedded steel section, the U-bars did not pass through the web of the steel section, and a double U-bar detail was used, as shown in Figure 3.6.

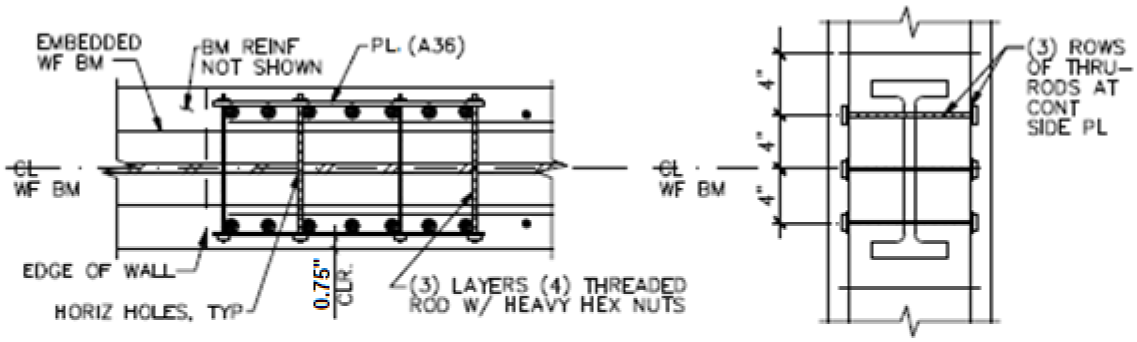

Figure 3.5. Embedment Detail

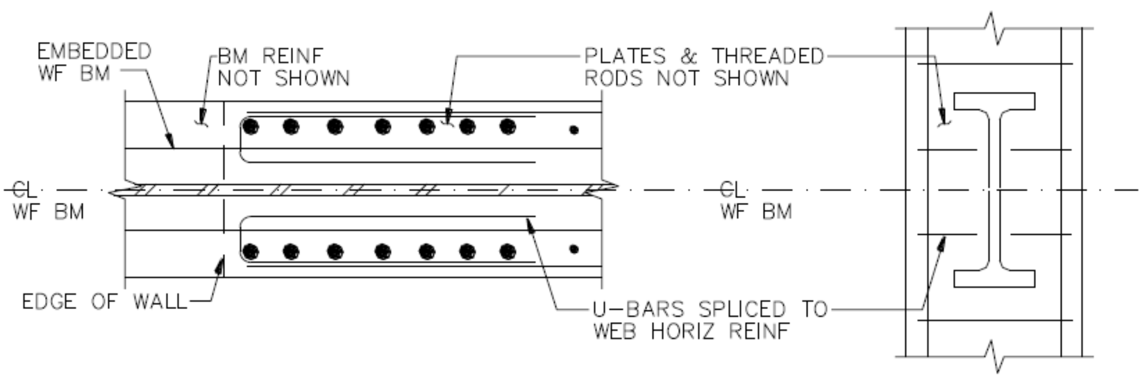

Figure 3.6. U-Bars Spliced to Web Horizontal Reinforcement at Embedded Steel Section

3.2. Construction

The test specimens were built indoors on a level surface. The first specimen, with SRC-W1 and SRC-W2, was constructed and tests were completed prior to construction of the second specimen, with SRC-W3 and SRC-W4. For each specimen, construction began with building of footing formwork and tying of the footing reinforcement cage, followed by placement of the reinforcement cage in the footing with spacers used to maintain clear cover. Formwork for one side of the wall and coupling beams was built, positioned, and braced to the floor. The wall boundary element reinforcement cages were assembled and placed, with the formwork used for positioning. For the specimen with SRC-W1 and SRC-W2, some reinforcement in the footing was removed and re-placed to accommodate placement of the wall boundary element reinforcement, which had #6 hooked longitudinal reinforcement. Wall web horizontal and vertical reinforcement were then tied into position individually. PVC was installed in the footing formwork to create voids that were later used for post-tensioning rods. The footing was poured, and the footing surface within the plan of the wall was roughened, as this was a construction joint. After several days, the footing formwork was removed.

Formwork for the coupling beams was built, positioned, and braced to the floor. Reinforcement cages for the coupling beams were tied. The steel sections and rebar cages were moved into position with spacers used to set cover, with photos provided in Figure 3.7 through Figure 3.9. The remaining face of formwork from the base of the wall to the top of the coupling beams was built, installed, and braced to the floor. Threaded rods for instrumentation were installed through the thickness of the wall and coupling beams, with holes drilled in the formwork to accommodate the threaded rods. Photos prior to subsequent concrete placement are provided in Figure 3.10. Concrete was pumped from the bottom of the wall to the height of the top of the coupling beams, including the coupling beams. The concrete surface in the wall at the height of the coupling beams was roughened, as this was a construction joint.

Formwork for the remaining face of the upper wall and for the top block was built, installed, and braced to the floor. The top block reinforcement cage was tied and placed into the formwork with spacers used to maintain clear cover. PVC was installed in the top block formwork. Threaded rods for instrumentation were installed in the wall. Concrete in the wall and top block was pumped from the top of the coupling beams to the top of the specimen. Photos of the test specimens after completion of construction and removal of formwork are provided in Figure 3.11. The construction process resulted in construction joints at the footing-wall interface and at the top of the coupling beams. A construction joint at the top of the coupling beams is consistent with standard practice in which construction joints are present between story levels.

Figure 3.7. Photo of Reinforcement in Wall and Coupling Beams for SRC-W1 and SRC-W2

Figure 3.8. Photo of Reinforcement in Wall and Coupling Beams for SRC-W3 (right) and SRC-W4 (left)

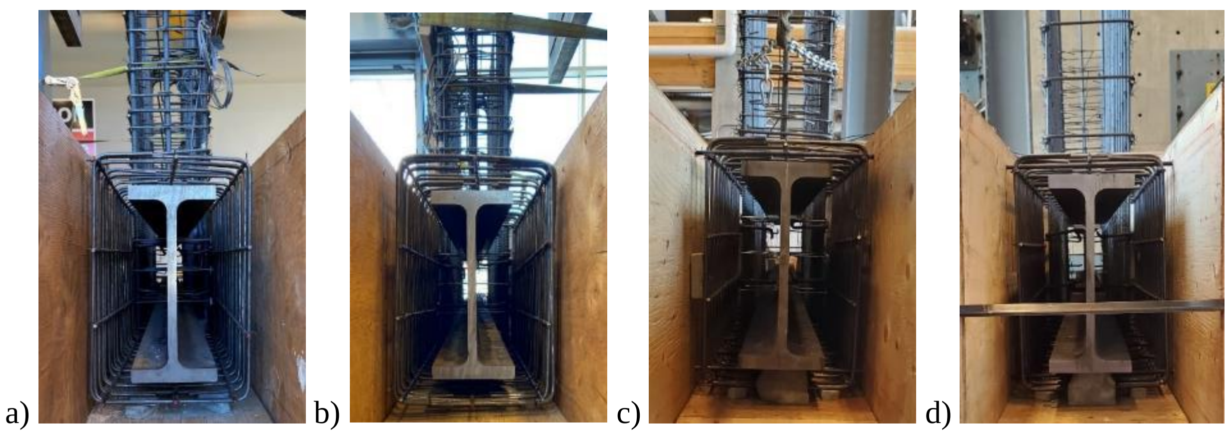

Figure 3.9. Photo of Coupling Beam Cross-Sections for a) SRC-W1, b) SRC-W2, c) SRC-W3, and d) SRC-W4

Figure 3.10. Photos Prior to Casting Concrete from Base of Wall to Top of Coupling Beams

(Left Photo: SRC-W1 and SRC-W2. Right Photo: SRC-W3 and SRC-W4.)

Figure 3.11. Photos of Test Specimens after Completion of Construction

(Left Photo: SRC-W1 and SRC-W2. Right Photo: SRC-W3 and SRC-W4.)

3.3. Material Properties

The specified compressive strength of concrete, f'_c, was 5.5 ksi. Concrete was provided by a local supplier. Each specimen was constructed in three separate lifts, as described in Section 3.2. For each concrete lift, 6”x12” concrete cylinders were prepared in accordance with ASTM C31 (2022). Compressive tests were conducted at 28 days as well as before and after each coupling beam test. Values of the tested compressive strength of concrete, $f'_{c,test}$, are provided in Table 3.1.

Table 3.1. Tested Compressive Strength of Concrete

Test Name	**Location**	**Age (days)**	**$f'_{c,test}$ (ksi)**				
			Test #1	Test #2	Test #3	Test #4	Average
SRC-W1	Lower Wall	220	7.43	7.06	7.04	6.95	7.12
		240	7.05	7.65	7.18	7.41	7.33
	Upper Wall	198	5.50	5.03	5.28	5.49	5.32
		218	5.53	5.52	5.73	5.52	5.58
SRC-W2	Lower Wall	342	7.39	7.67	7.57	7.57	7.55
		356	7.33	6.76	7.63	7.62	7.33
	Upper Wall	320	5.47	5.48	5.41	5.23	5.40
		334	5.43	5.61	5.49	4.98	5.37
SRC-W3	Lower Wall	98	4.74	4.59	3.95	5.02	4.57
		105	4.21	4.93	4.74	5.16	4.76
	Upper Wall	84	5.42	6.04	5.41	5.40	5.57
		91	5.86	5.17	4.89	4.99	5.25
SRC-W4	Lower Wall	154	5.30	4.93	4.98	5.47	5.17
		160	4.73	5.20	5.11	4.52	4.89
	Upper Wall	133	5.57	4.37	5.18	-	5.04
		139	5.86	6.08	5.60	-	5.47

The wall contained #6, #4, and #3 Grade 60 reinforcement compliant with either ASTM A615 or ASTM A706. The reinforcement was cut and bent by a local supplier, with test samples provided. 0.25”-diameter and 0.1875”-diameter A36 undeformed reinforcement was used in the beams and walls. This reinforcement was cut and bent in-house. Tensile testing was conducted on #6, #4, and #3 reinforcement samples, with results provided in Table 3.2 and Figure 3.12.

Table 3.2. Measured Strength and Elongation from Tensile Testing of Reinforcement

Reinforcement Size	Test No.	F_y (ksi)	F_u (ksi)	% Elong.
#6	Test #1	66.5	107.5	17.5
	Test #2	67.2	107.6	17.3
	Test #3	66.0	107.6	17.5
	Test #4	66.2	107.6	17.5
	Average	66.5	107.6	17.5
#4	Test #1	67.0	108.2	15.1
	Test #2	66.0	107.7	15.5
	Test #3	66.0	107.6	14.9
	Test #4	66.0	107.4	15.2
	Average	66.25	107.9	15.4
#3	Test #1	68.5	110.0	12.8
	Test #2	69.0	110.7	12.2
	Test #3	68.0	108.9	12.4
	Test #4	66.6	107.1	13.0
	Average	68.0	109.2	12.6

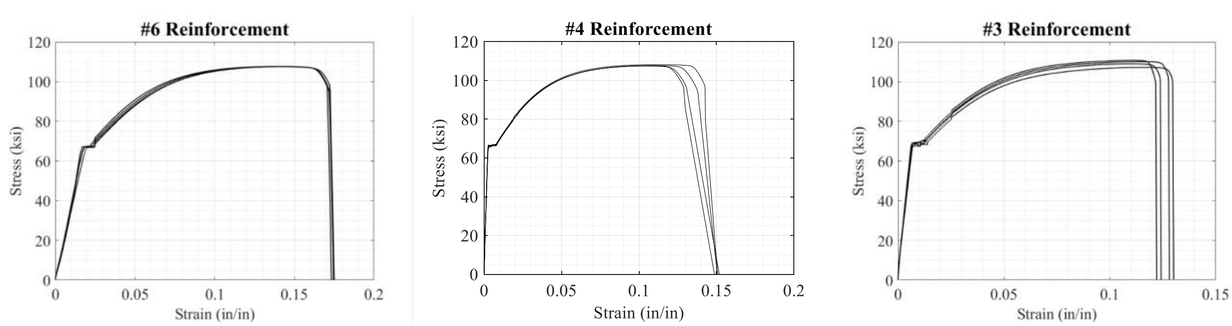

Figure 3.12. Measured Stress-Strain from Tensile Testing of Reinforcement

3.4. Test Set-Up

The test set-up is shown in Figure 3.13 and Figure 3.14 and is similar to that used by Motter et al (2017a) in previous seismic tests on SRC coupling beams. The test specimen was positioned atop a 20” wide by 39” tall by 120” long concrete spacer block to achieve sufficient clearance between the coupling beams and the floor for the actuator used to load the coupling beam. To level the test specimen and provide contact between concrete surfaces, grout was used between the spacer block and strong floor and between the spacer block and specimen footing. Using high-strength threaded rods, the footing was post-tensioned to the laboratory strong floor and was also post-tensioned in the transverse direction. A steel loading beam with welded base plate was installed at the top of the specimen, with grout used between the surfaces for contact and leveling. The steel loading beam was post-tensioned to the top block. The top block was post-tensioned in the transverse direction.

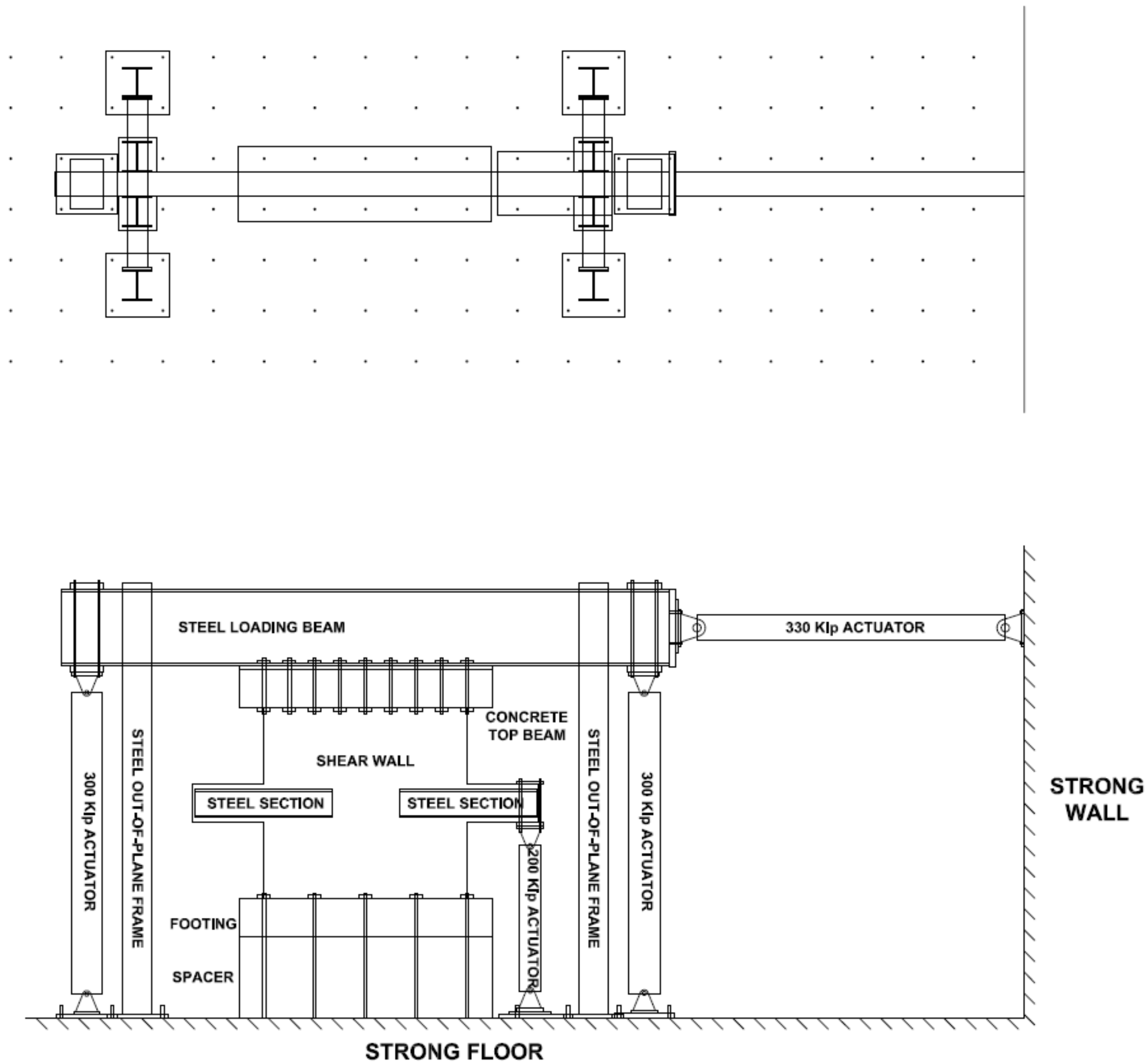

Figure 3.13. Test Set-Up a) Plan View and b) Elevation View

Figure 3.14. Photo of Test Set-Up

Four actuators were used in the test. An actuator with 200-kip capacity and ±10” stroke was connected from the strong floor to the coupling beam. This actuator was oriented vertically and located 30” from the face of the wall. This actuator was attached to the strong floor using an adaptor plate and attached to the coupling beam using a top and bottom plate post-tensioned to the coupling beam. 6” wide by ½” thick by 12” long bearing plates were used between the plates and the beam concrete to apply the load over the full beam thickness and a 6” width. Three actuators were connected to the steel loading beam. One of these was a 330-kip capacity actuator with ±20” stroke that was oriented horizontally and spanned from the strong wall to the loading beam. This actuator was attached to an adaptor plate that was post-tensioned to the strong wall and to a welded end plate on the loading beam. The other two actuators that were connected to the loading beam were oriented vertically and spanned from the loading beam to the strong floor. These were 268-kip capacity actuators with ±30” stroke. These two actuators were located 22’ feet apart at opposite ends of the loading beam. Spacers, consisting of short length steel I-beams, were used under each of these two actuators. These actuators had adaptor plates that were post-tensioned to the strong floor and post-tensioned to the loading beam.

Passive axial restraint was applied to the test beam. The axial restraint was comprised of 3/8” threaded rod running horizontally on each side of the wall and spanning from the end of the coupling beam being tested to the end of the coupling beam not being tested. Steel sections were used to spread load from the coupling beam to the threaded rods. This passive restraint was such that the axial compressive load on the coupling beam increased with increasing axial elongation, and the load was measured during testing using a load cell between the end of the coupling beam not being tested and the steel spreader beam. This axial restraint was expected to apply a low level of force with the intent of mitigating outward ratcheting of the test beam over repeated loading cycles. The approach was consistent with that used by Motter et al (2017a) in two of the four tests. Motter et al (2017a) had observed significant outward ratcheting in two of the tests and applied this type of axial restraint to mitigate outward ratcheting in the next two tests. The measured axial load was reported by Motter et al (2017a) to be sufficiently small to have minimal effect on the beam behavior through P-M interaction. This level of restraint is expected to be less than that provided by floor slabs and adjacent walls in actual coupling beams.

Out-of-plane restraint was installed near each end of the steel loading beam to mitigate out-of-plane deformation during testing. The out-of-plane restraint at each end consisted of a structural steel frame, comprised of two columns, a beam, and two short-length columns attached to the beam. These short-length columns were positioned in contact with the top and bottom flanges of the loading beam and had welded end plates that were then post-tensioned to the beam of the out-of-plane restraint frame. In addition to providing out-of-plane translational restraint, these columns were intended to resist torsion of the loading beam associated with out-of-plane rotation at the top of the wall. Grease was applied to the flanges of the loading beam and faces of the columns to mitigate frictional resistance to in-plane translation.

During testing of SRC-W2, bracing was installed to mitigate torsion and out-of-plane translation at the end of the test beam. This bracing, shown in Figure 3.15, was used for the entire test for SRC-W3 and SRC-W4. Two braces were used, and each brace consisted of a steel section with angled end plates that spanned from the column of the out-of-plane restraint frame to the lower base plate that was post-tensioned to the test beam. This bracing was oriented on an angle in a horizontal plane. The end plate at one end of each brace was bolted to the columns of the out-of-plane restraint frame. Grease was applied between the end plate at the other end of the brace and the edge of the lower base plate that was post-tensioned to the test beam.

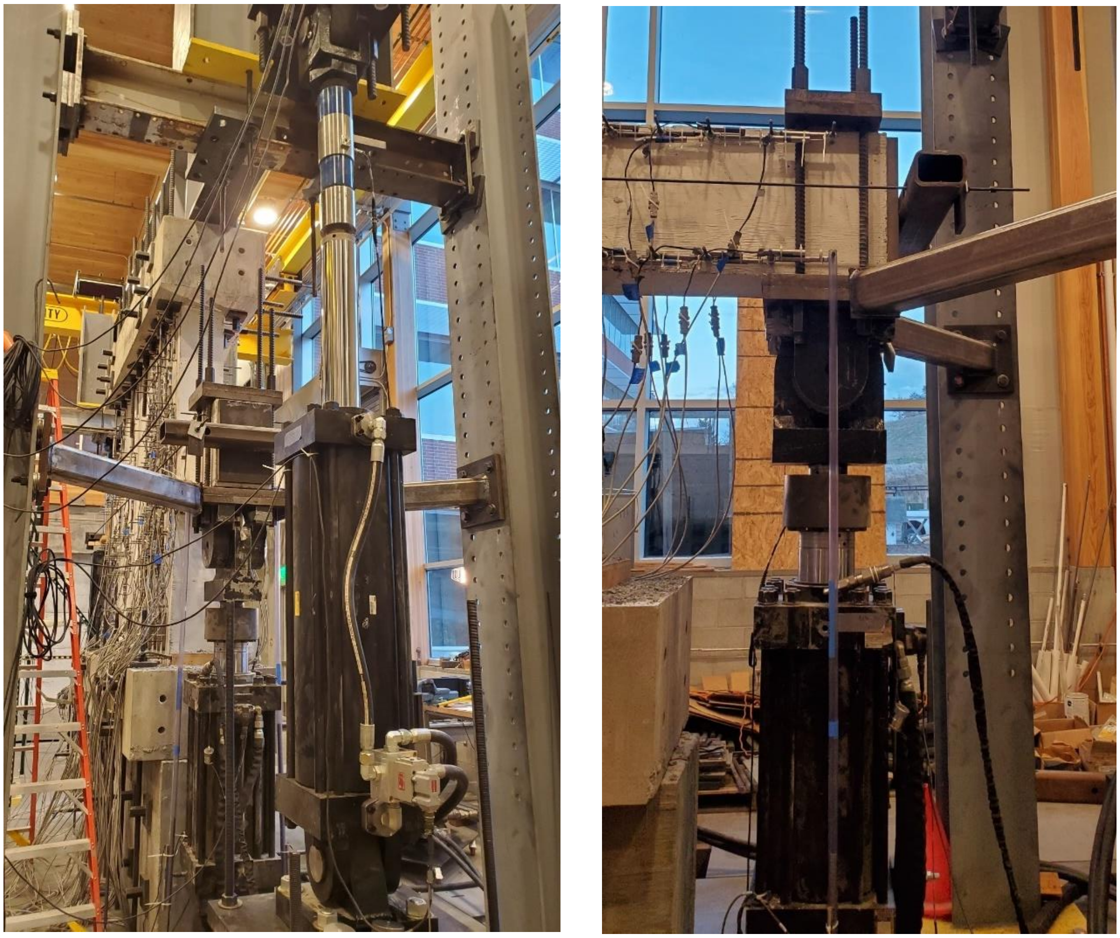

Figure 3.15. Photos of Out-of-Plane Test Beam Bracing

3.5. Instrumentation

Instrumentation was comprised of 95 linear variable differential transformers (LVDTs), one load cell on each of the four actuators, and one load cell to measure axial force in the test beam. Additionally, for the first specimen, with SRC-W1 and SRC-W2, there were 36 strain gauges on wall longitudinal reinforcement. The layout of LVDTs, shown in Figure 3.16, was selected to enable determination of the components of deformation from axial-flexure, shear, and interface axial-flexure and shear in the test beam and to determine the strain field and assess plane section behavior in the wall. The embedment model for the steel section reflected in AISC 341-22 is based on the assumption of plane section behavior over the embedment length, while a wall in bending is typically analyzed based on plane section behavior. The layout in instrumentation was selected to enable assessment of the extent to which plane section behavior in the wall is disturbed by embedment of the beam. The layout of strain gages used for the first specimen, with SRC-W1 and SRC-W2, is provided in Figure 3.17, with 18 strain gages provided on the longitudinal reinforcement in each of the two wall boundary elements. This layout of strain gages was selected to aid in the assessment of the local tensile increase or compressive reduction in strain in wall longitudinal reinforcement due to the effect of the embedment demands, which create local tension.

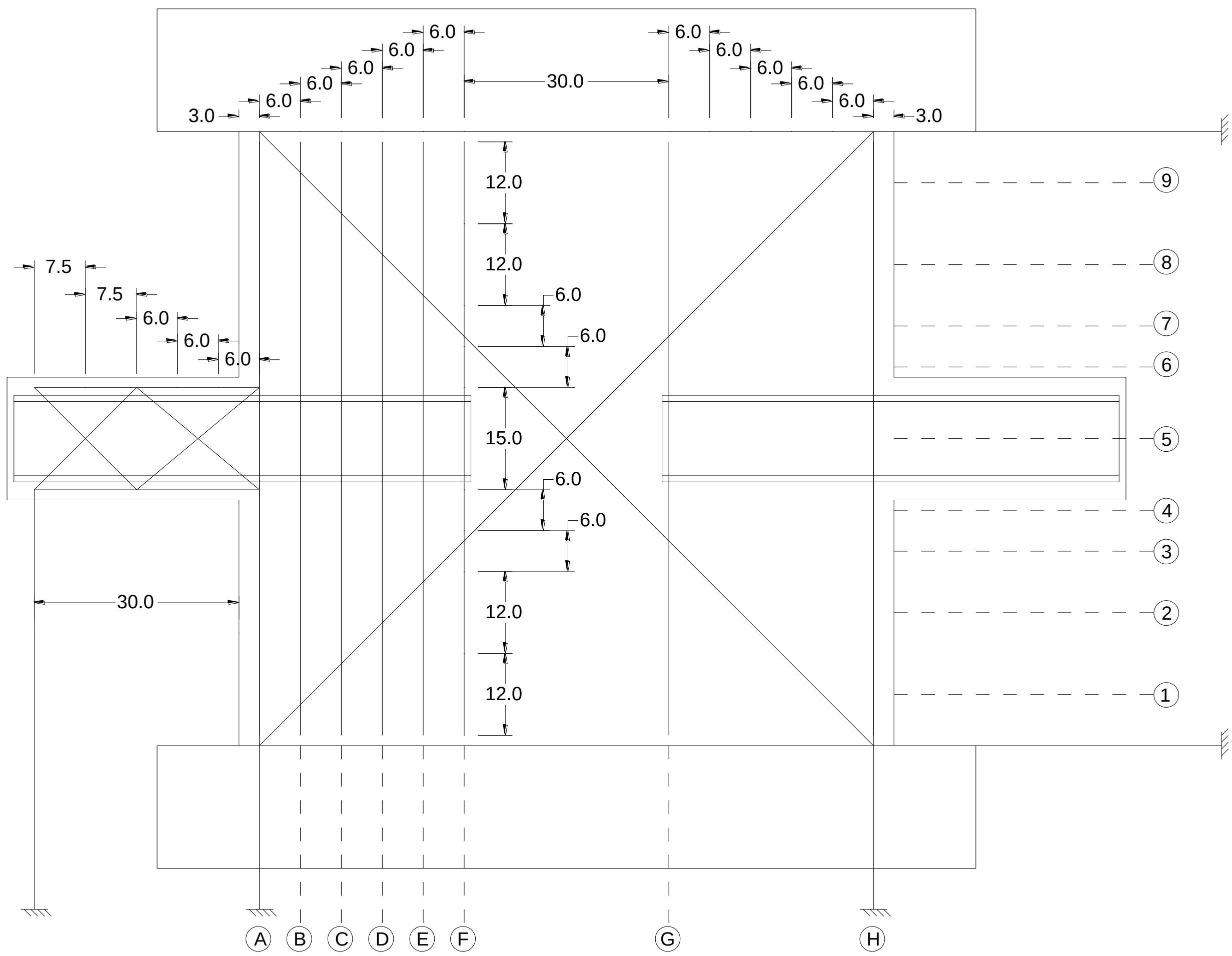

Figure 3.16. LVDT Layout

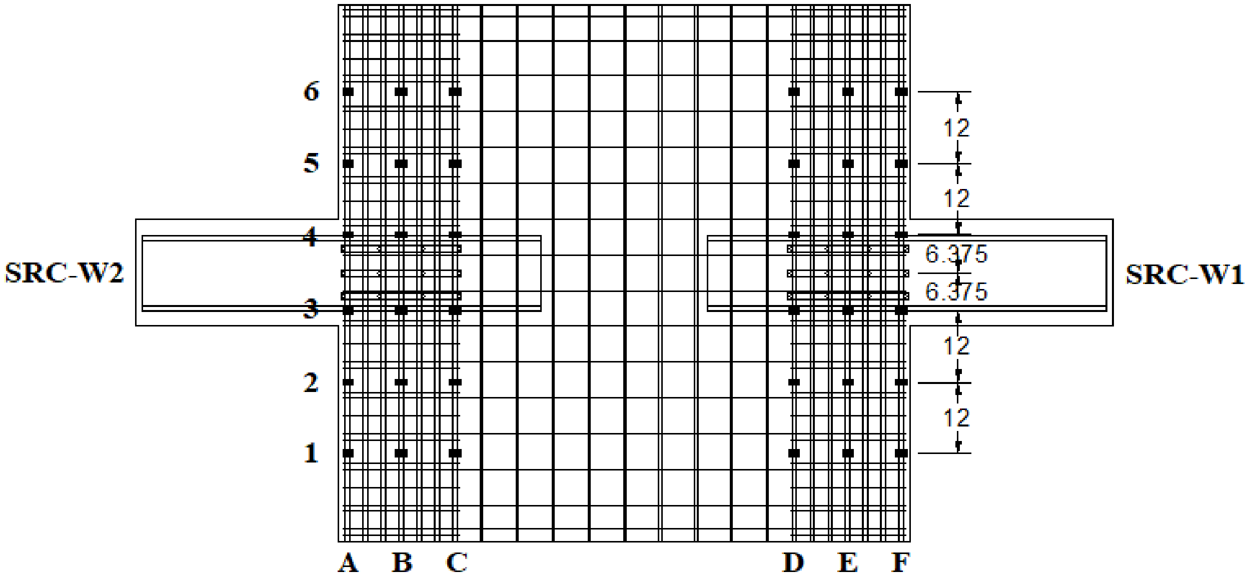

Figure 3.17. Strain Gage Layout for SRC-W1 and SRC-W2

3.6. Loading Protocol

During testing, reversed cyclic load was applied to the test beam, with reversed cyclic load and constant axial load applied to the wall. The loading protocol used for the test beam, shown in Figure 3.18, was comprised of 250 cycles at $0.15M_{pbe}$, 500 cycles at $0.40M_{pbe}$, 75 cycles at $0.75M_{pbe}$, five cycles at $1.2\theta_y$, three cycles at $1.5\theta_y$, two cycles at $2.0\theta_y$, two cycles at $2.5\theta_y$, and one cycle at $3.0\theta_y$, followed by the same sequence in reverse, where θ_y is the yield rotation. For SRC-W4, the loading protocol consisted of 250 cycles at $0.15M_{pbe}$, 500 cycles at $0.40M_{pbe}$, and two cycles at 6.0% chord rotation, as $0.75M_{pbe}$ was not reached prior to reaching 6.0% chord rotation during the first excursion after 500 cycles at $0.40M_{pbe}$. M_{pbe} was computed as 447.8 k-ft for SRC-W1, 450.7 k-ft for SRC-W2, 426.7 k-ft for SRC-W3, and 432.7 k-ft for SRC-W4 using 55 ksi expected yield strength for A992 steel and the average tested concrete compressive strength before the start of the test of 7.12 ksi for SRC-W1, 7.55 ksi for SRC-W2, 4.57 ksi for SRC-W3, and 5.17 ksi for SRC-W4. The corresponding $V@M_{pbe}$ was computed for a 2.5’ cantilever as 179.1 kips for SRC-W1, 180.3 kips for SRC-W2, 170.7 kips for SRC-W3, and 173.1 kips for SRC-W4. These values for $V@M_{pbe}$ were used to control the tests. θ_y was determined during testing. During the first positive excursion to $1.2\theta_y$, the measured chord rotation at $0.75M_{pbe}$ was multiplied by $M_y/(0.75M_{pbe})$ to determine θ_y, where M_y was the moment at which the tension flange fully yields (i.e., the strain on the inner face of the tension flange is equal to the yield strain), computed from moment-curvature analysis using the same material properties used for calculating M_{pbe}. This loading protocol was a modification of that used by Abdullah et al (2020). The protocol used by Abdullah et al (2020) had a peak rotation of $1.5\theta_y$, while the protocol used in this study had a peak rotation of $3.0\theta_y$.

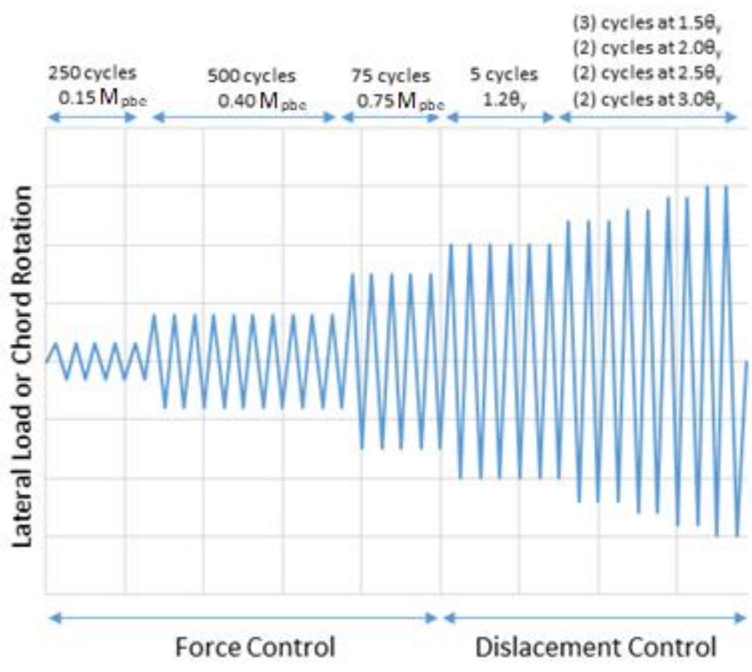

Figure 3.18. Loading Protocol

For the displacement-controlled cycles in the loading protocol, the chord rotation was computed as the beam displacement divided by the 30" cantilever length, with a correction for footing and wall deformation. The correction for footing deformation was made using the two vertical LVDTs on the footing to estimate rotation and vertical translation of the top plane of the footing. The correction for wall rotation was taken in a similar manner using the two sensors that spanned over the clear height of the wall, but the value was halved due to the coupling beam being located at mid-height of the wall.

The loads applied during testing are shown in Figure 3.19, with the resulting wall demands shown in Figure 3.20 through Figure 3.28 for the four tests. A constant axial gravity load of 328 kips was applied to the wall during all beam tests. This was determined as $0.04A_g f'_{c,test}$ = 328 kips using $f'_{c,test}$ = 7.12 ksi obtained from the lower wall concrete prior to the first beam test. Reversed cyclic lateral load was applied to the wall through force proportionality among actuators. The gravity load was applied using the two vertical actuators prior to the force proportionality, such that the gravity load was maintained during loading cycles. The change in moment from wall shear over a story height was equal to half of the moment created by the coupling beam in the wall. Assuming a 12' story height, which would be 6' at half-scale, the wall shear demand was programmed to be 6.5'/6'/2 = 0.542 times the beam shear demand. At the largest $V@M_{pbe}$ for the four test beams of 180.3 kips, the peak wall shear is 97.7 kips, which is roughly equal to $\sqrt{R_c f'_c}A_{cv}$ = 97.4 kips. Additional moment was applied to the wall using equal and opposite forces in the two vertical actuators. Each of these forces was programmed to be 0.275 times the beam shear demand for SRC-W1 and -0.034 times the beam shear demand for SRC-W2, SRC-W3, and SRC-W4, and these two actuators were located 22' apart. The wall demands for SRC-W1 were intended to be larger than typical demands at most locations in coupled walls but not so large as to produce wall yielding. At the expected beam strength of 179.1 kips for SCR-W1, the wall demands, excluding coupling beam demand, at mid-height were computed to produce a peak tensile strain of 0.30e_y and peak compressive strain of 0.00032, based on moment-curvature analysis, where e_y is the yield strain of the wall longitudinal reinforcement based on the tested strength provided in Table 3.2. For SRC-W2 at 180.3 kips, these strains were 0.08e_y in tension in the positive loading direction and 0.00011 in compression in the negative loading direction. For SRC-W3 at 170.7 kips, these strains were 0.12e_y in tension in the positive loading direction and 0.00017 in compression in the negative loading direction. For SRC-W4 at 173.1 kips, these strains were 0.21e_y in tension in the positive loading direction and 0.00016 in compression in the negative loading direction. The local demands are larger due to the influence of the coupling beam connection (Motter et al, 2017a,b).

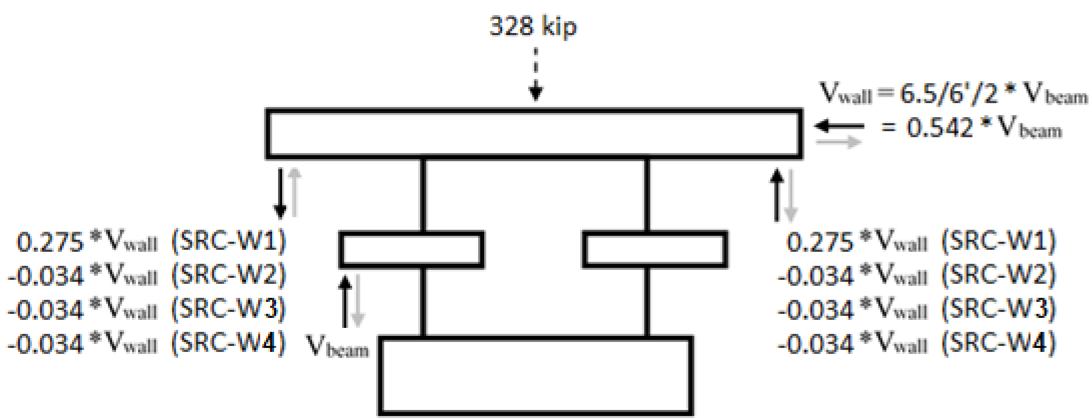

Figure 3.19. Applied Loads

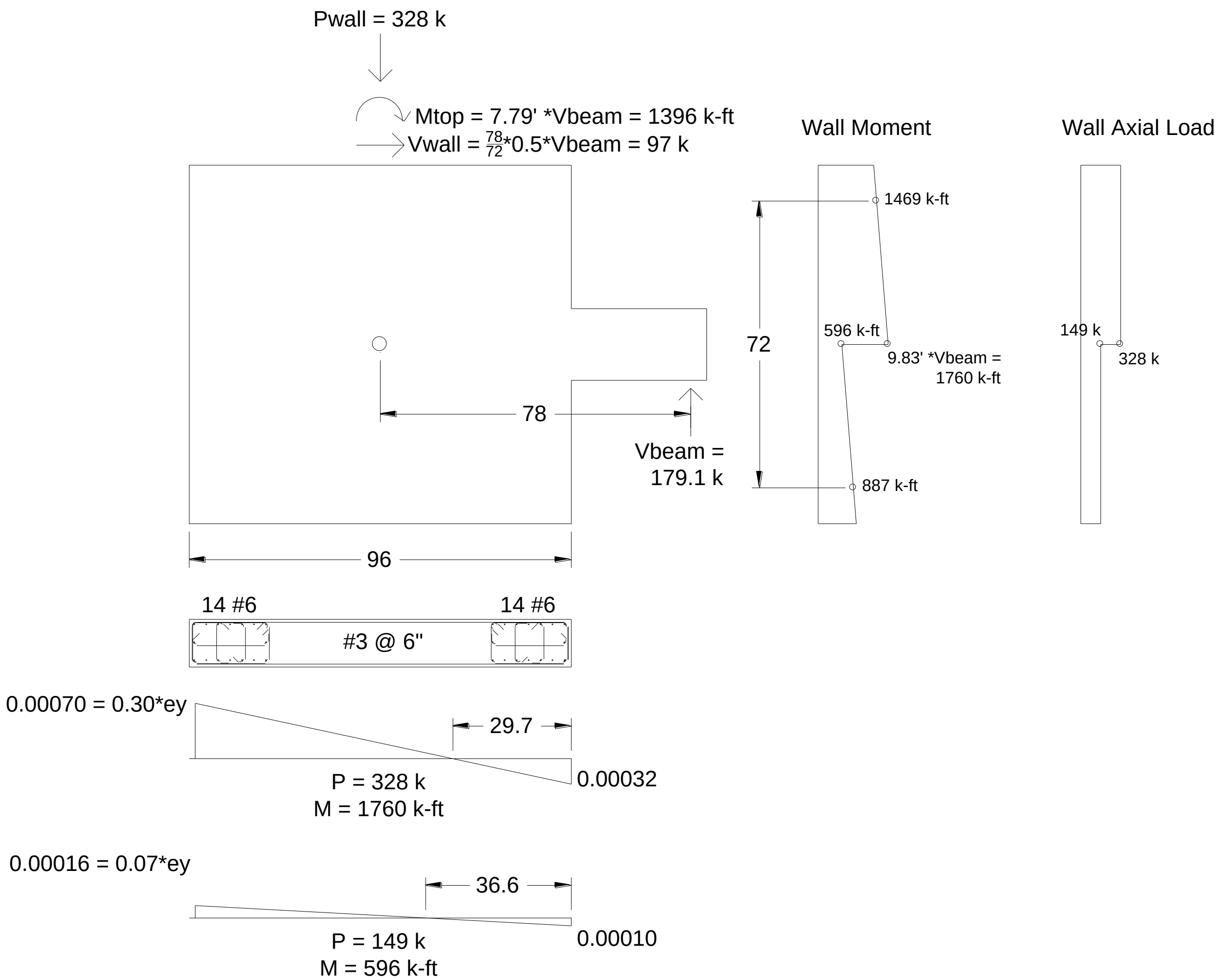

Figure 3.20. Wall Demands at $V@M_{pbe}$ for SRC-W1 in the Positive Loading Direction, with Strain Demands Determined from Moment-Curvature Analysis

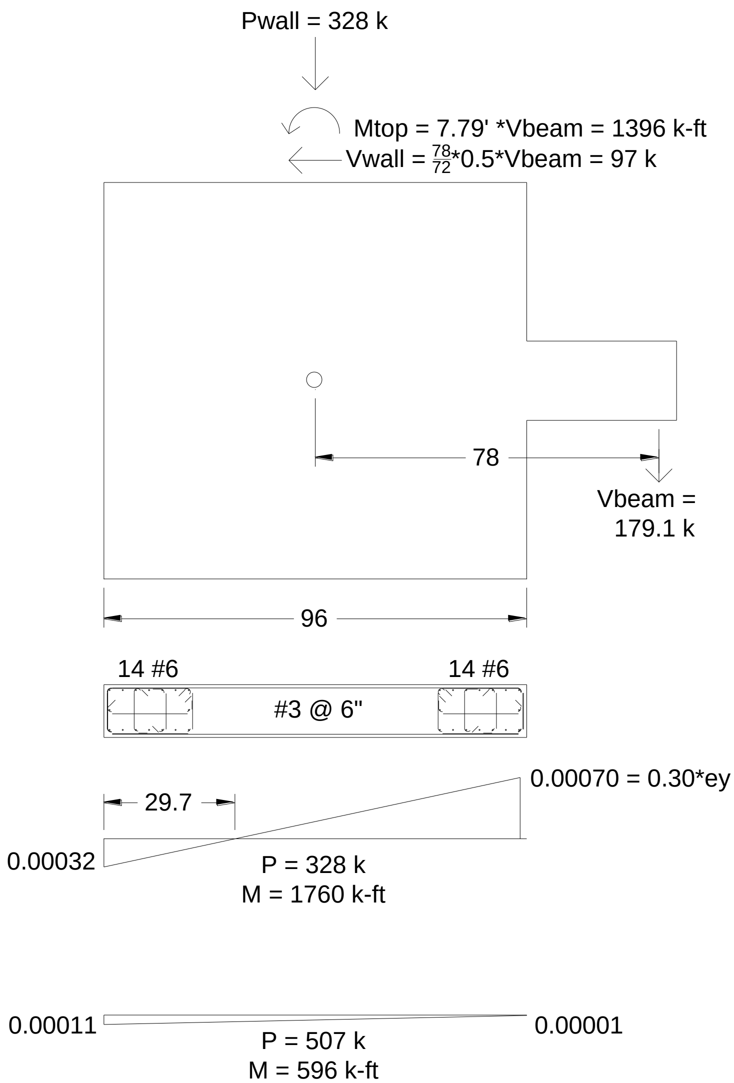

Figure 3.21. Wall Demands at *V@M* for SRC-W1 in the Negative Loading Direction, with Strain Demands Determined from Moment-Curvature Analysis

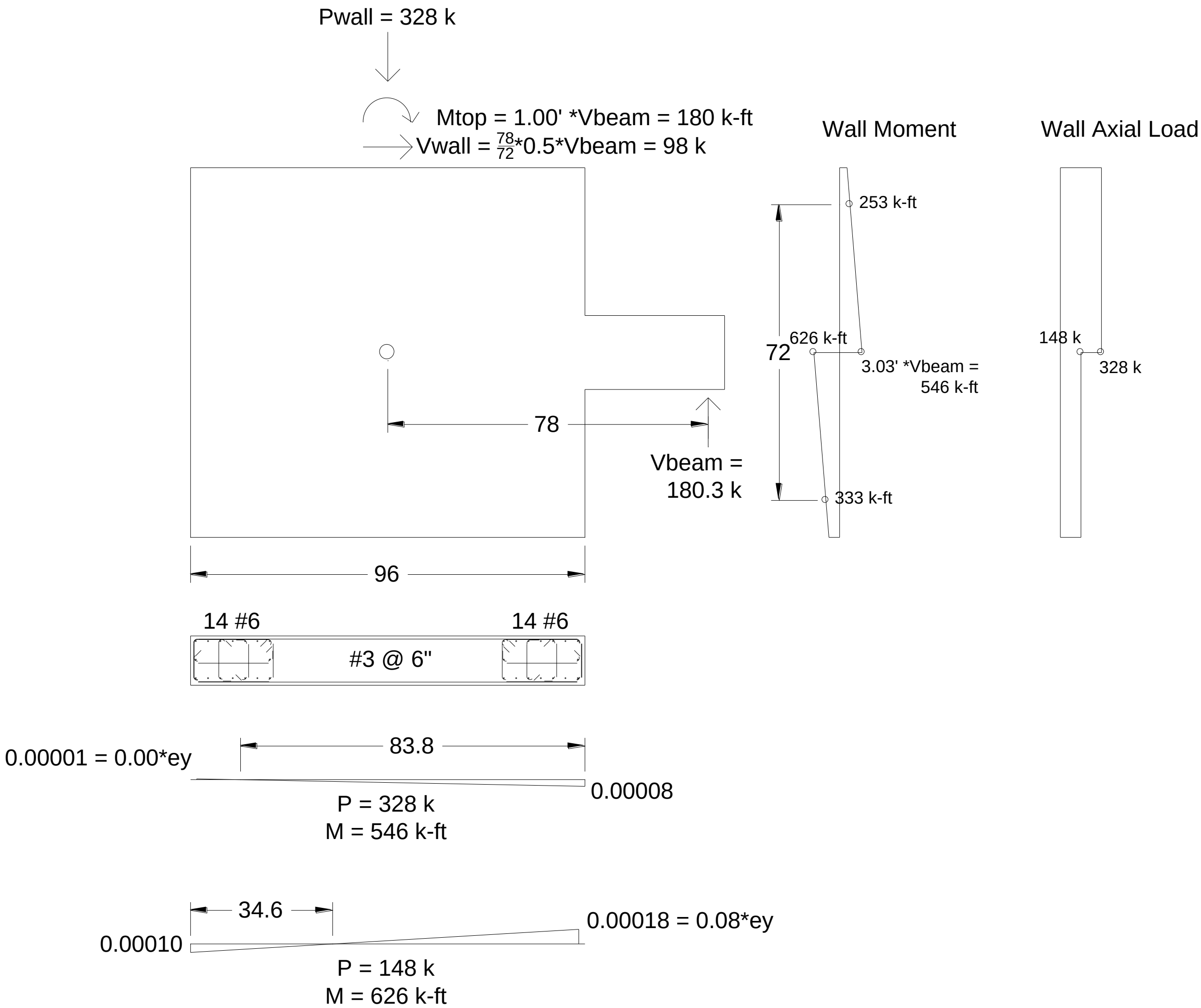

Figure 3.22. Wall Demands at $V@M_{pbe}$ for SRC-W2 in the Positive Loading Direction, with Strain Demands Determined from Moment-Curvature Analysis

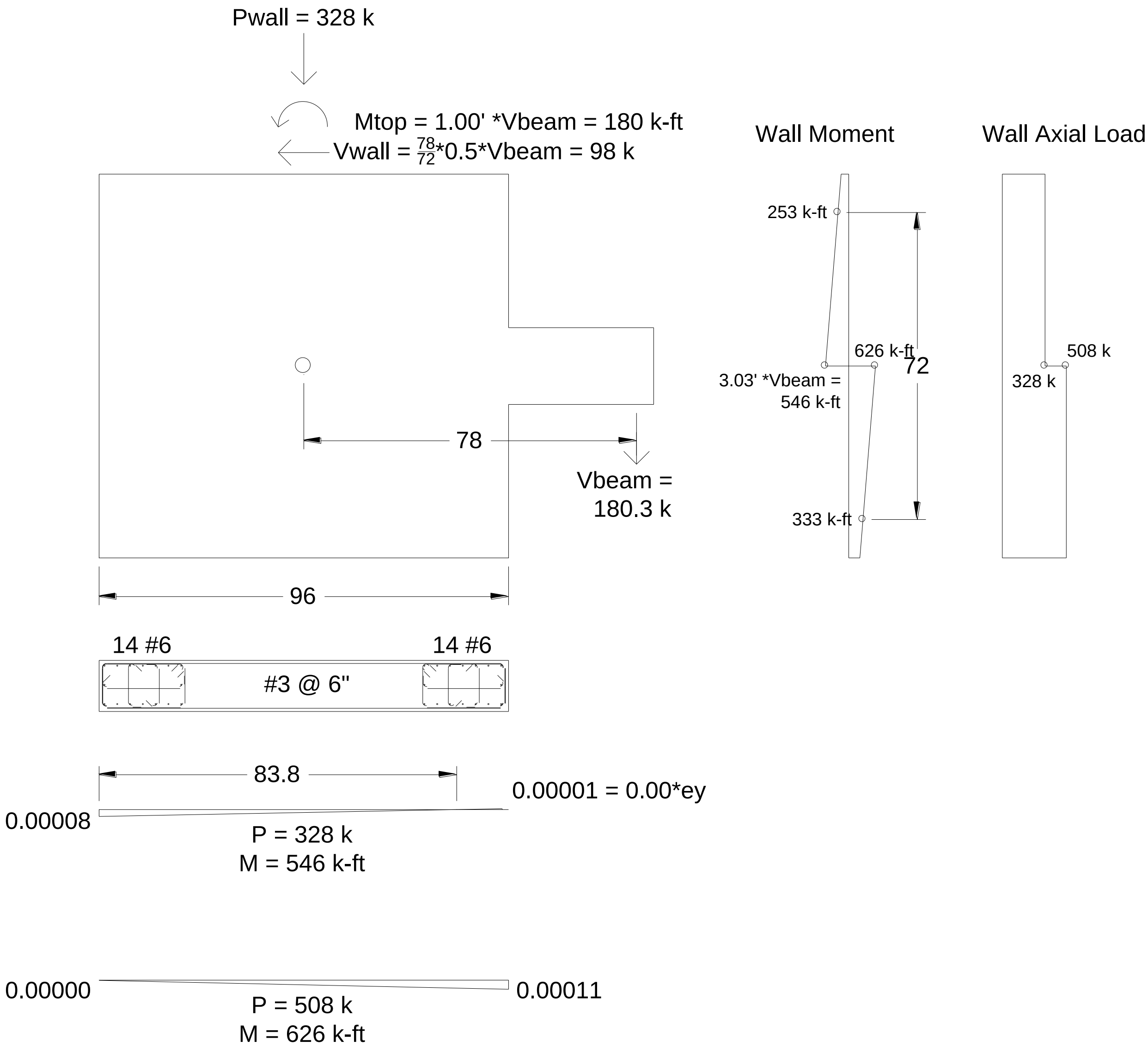

Figure 3.23. Wall Demands at *V@M*

Strain Demands Determined from Moment-Curvature Analysis

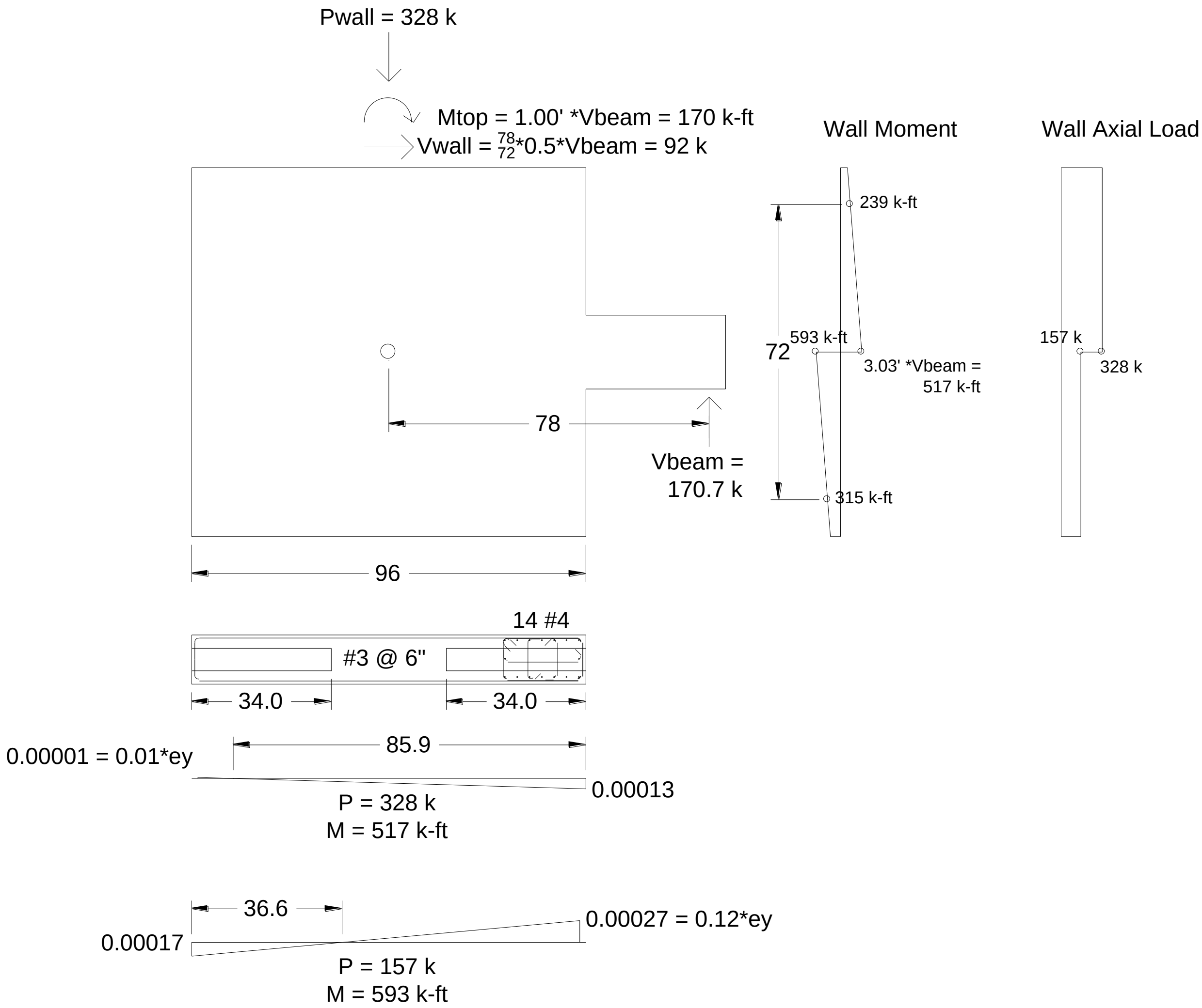

Figure 3.24. Wall Demands at *V@M* for SRC-W3 in the Positive Loading Direction, with Strain Demands Determined from Moment-Curvature Analysis

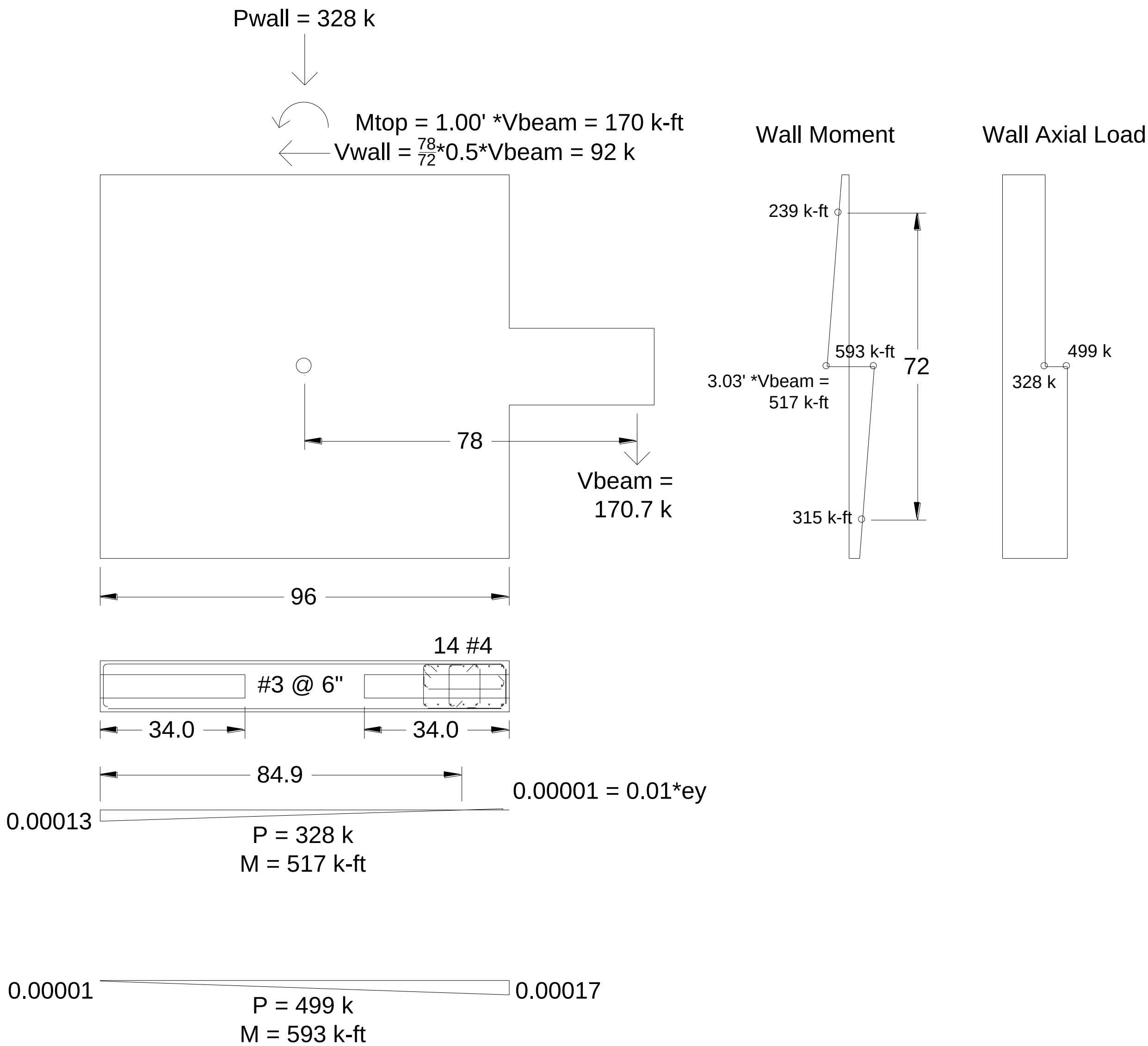

Figure 3.25. Wall Demands at $V@M_{pbe}$ for SRC-W3 in the Negative Loading Direction, with Strain Demands Determined from Moment-Curvature Analysis

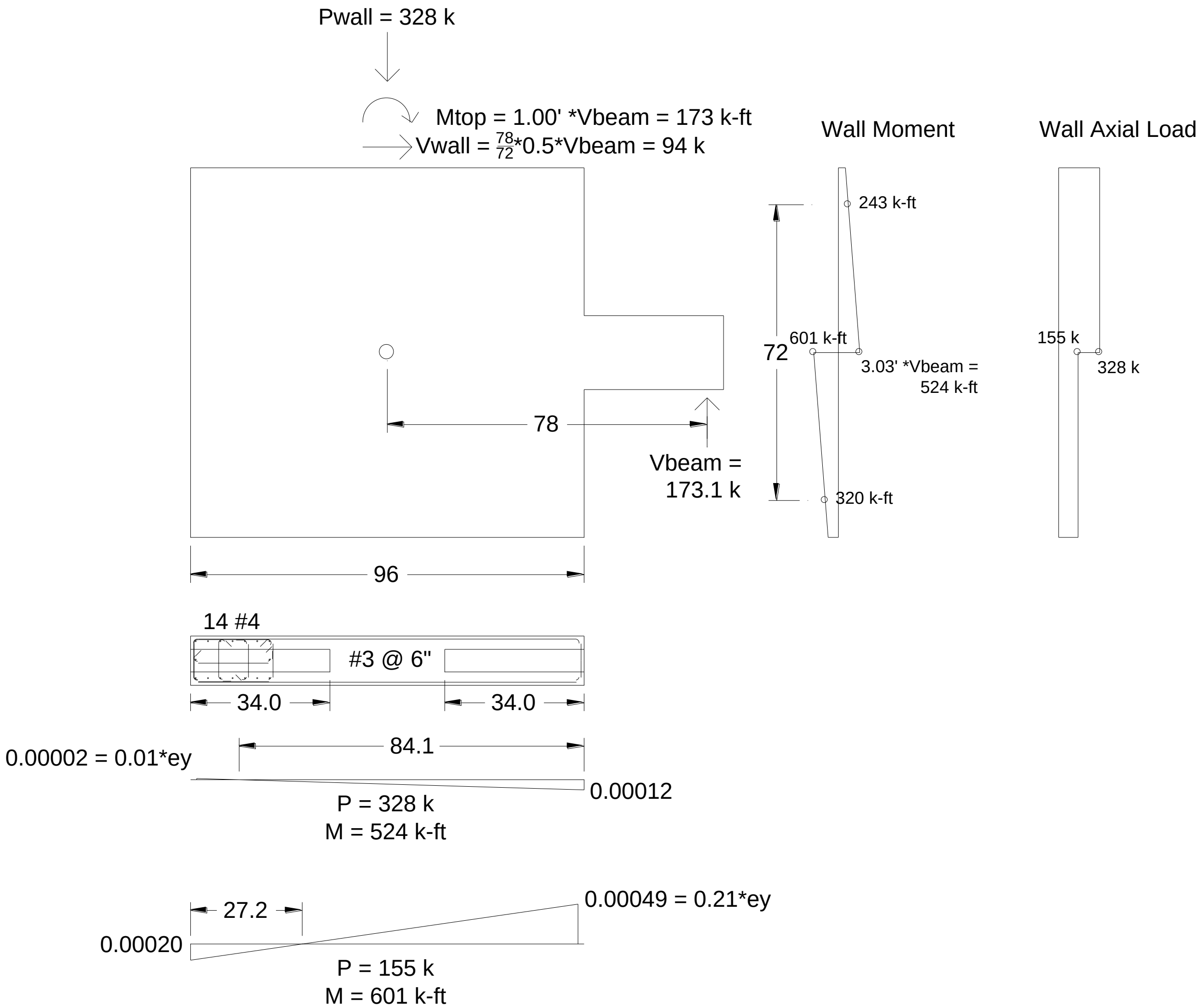

Figure 3.26. Wall Demands at $V@M_{pbe}$ for SRC-W4 in the Positive Loading Direction, with Strain Demands Determined from Moment-Curvature Analysis

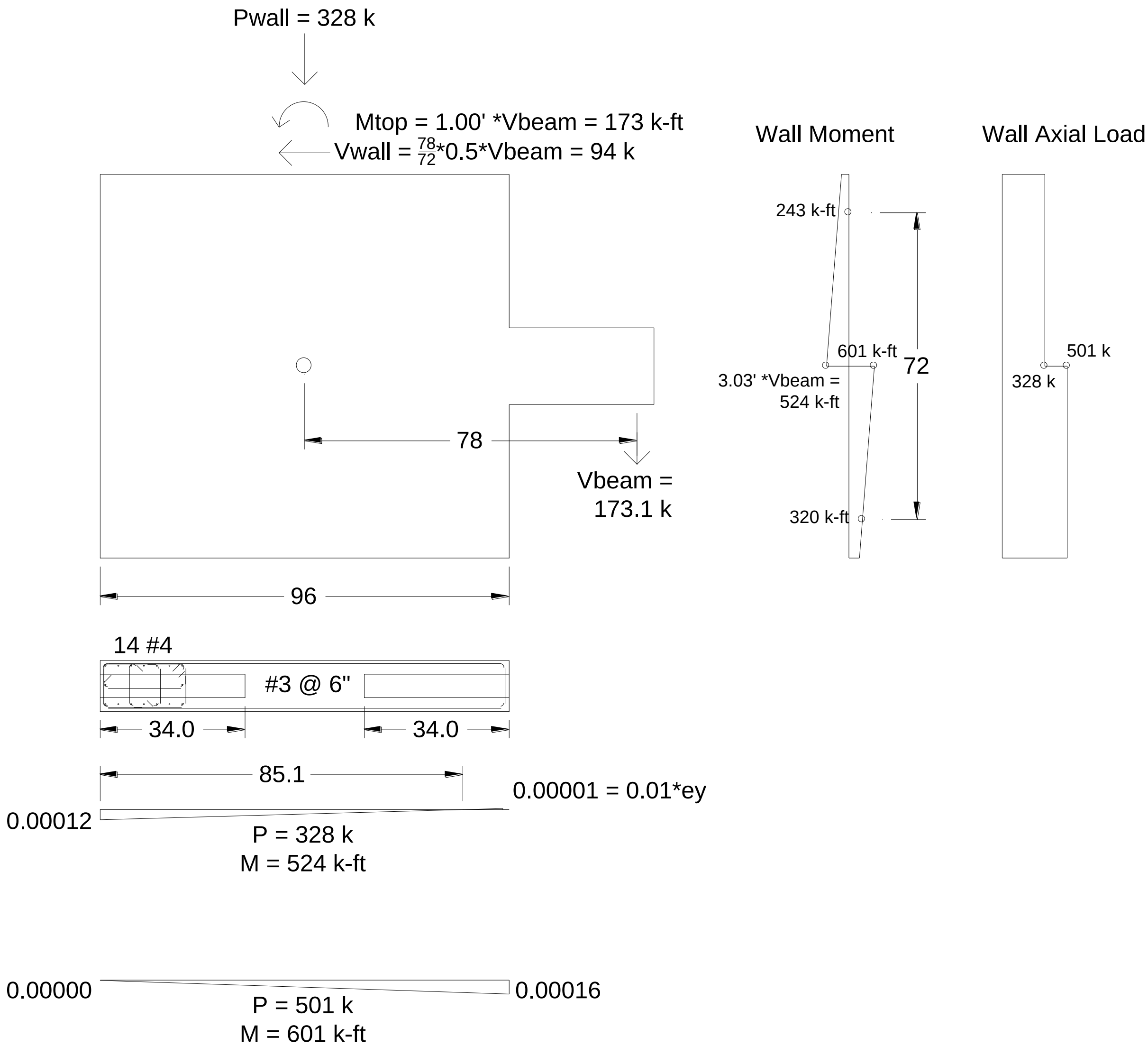

Figure 3.27. Wall Demands at *V@M_{pbe}* for SRC-W4 in the Negative Loading Direction, with Strain Demands Determined from Moment-Curvature Analysis

Figure 3.28. Wall Demands, Excluding Coupling Beam Demands, at Location of Coupling Beam, Determined from Moment-Curvature Analysis

4. Test Results

4.1. Observed Damage

Damage photos are provided in Figure 4.1 through Figure 4.4 for the beams and Figure 4.5 through Figure 4.8 for the wall. These photos were taken at zero rotation following completion of the cycle indicated on the figures. First and last cycles in each cycle group are shown for the beams, and the first cycle in each group is shown for the walls. Additional increments are shown for SRC-W4, which did not reach 0.75M_{pbe}. After the cycles at 1.5θ_y for SRC-W2, a brace to mitigate torsion and out-of-plane translation in the test beam was installed, as described in Section 3.5, and this changed the vantage point of the provided photos for subsequent cycles. Between loading cycles during testing, cracks were marked, and those 0.2 millimeters or larger were measured. For SRC-W1 and SRC-W3, cracks in the positive loading direction were marked in black, and cracks in the negative loading direction were marked in red. For SRC-W2 and SRC-W4, cracks in the positive loading direction were marked in blue, and cracks in the negative loading direction were marked in green. Locations and measured widths of cracks that were 0.2 millimeters or larger are provided in Figure 4.9 through Figure 4.13 and Table 4.1 through Table 4.5, respectively. Beam crack widths were reported as the largest values measured at the top and bottom beam surfaces, reported as “End”, and at the face, reported as “Face”. Wall crack widths were reported as the largest values measured at the end surface of the wall, reported as “End”, and at the face, reported as “Face”.

For SRC-W1, SRC-W2, and SRC-W3, damage concentrated at the beam-wall interface. This was the only location with concrete spalling, with minimal damage in the beam span. For SRC-W1, the crack across the beam-wall interface was the only crack to exceed 2.0 millimeters and was measured as 19 millimeters for cycles at $3.0\theta_y$. For SRC-W3, this was the only crack to exceed 1.0 millimeter and reached a maximum of 25 millimeters in the positive loading direction and 27 millimeters in the negative loading direction for cycles at $3.0\theta_y$. For SRC-W1 and SRC-W2, the next largest cracks formed horizontally along the flanges of the steel section. For SRC-W1, the lower crack reached 0.35 millimeters and the top crack reached 1.0 millimeter for cycles at $3.0\theta_y$. For SRC-W2, these cracks were measured as nearly 2.0 millimeters at upper flange locations. For SRC-W3, vertical cracks formed along the beam flanges during the first group of cycles at $0.75M_{pbe}$ and remained less than 0.3 millimeters throughout the test. For SRC-W1, wall cracks differed for positive and negative loading. Positive loading resulted in extensive cracks on the side of the wall opposite the test beam. Negative loading resulted in diagonal cracks extending to the top of the wall on the side of the wall with the test beam, while there were limited cracks at the base. SRC-W2 was tested after SRC-W1 with lower wall loads, and new wall cracks did not appear until the displacement-controlled cycles. However, several existing wall cracks opened earlier than observed during testing of SRC-W1. For SRC-W3, significantly more wall cracks developed in the positive loading direction than the negative loading direction. Horizontal cracks opened on the side of the wall opposite the test beam, similar to SRC-W1 but not to the same extent. As the test progressed, new cracks in the wall formed above the beam, while increases in cracks widths below the beam were more limited. Unlike SRC-W1, diagonal cracks were not observed in the wall during negative loading. Horizontal cracks in the embedment region near the centerline of the steel section formed during the second group of 75 cycles at $0.75M_{pbe}$. Relative to SRC1 and SRC2 tested by Motter et al (2017a), extensive ratcheting of the beams was not observed, indicating the effectiveness of the axial restraint.

Observed damage for SRC-W4 differed significantly from the other three tests, as significant wall damage was observed. For cycles at 0.15M_{pbe}, the crack pattern for SRC-W4 was similar to the other tests, with the largest cracks forming at the beam-wall interface and smaller cracks along the flanges of the steel section forming as horizontal cracks with some vertical cracks branching from them. For cycles at 0.4M_{pbe}, concrete spalled at the beam-wall interface and within the embedment region. The level of spalling was such that the cracks used for crack measurements were changed after the 30th cycle at 0.4M_{pbe}, reflected by Figure 4.12 and Figure 4.13 and Table 4.4 and Table 4.5. The largest cracks formed at the beam-wall interface, with the crack width reaching more than 50 millimeters in the negative loading direction and 25 millimeters in the positive loading direction. As shown in Figure 4.4, spalling of cover concrete in the embedment region initiated and progressed significantly during the 500 cycles at 0.4M_{pbe}, with the wall reinforcement and steel section visible. Horizontal cracks in the wall were observed above the embedment region, indicated as 3+W and 4+W in Figure 4.13 and Table 4.5. These cracks reached a maximum width of 1.5 millimeters, which occurred during the first cycle at 6.0% rotation. The damage in the wall was such that the beam did not reach 0.75M_{pbe}. Despite the significant damage in the embedment region, buckling of wall longitudinal reinforcement was not observed.

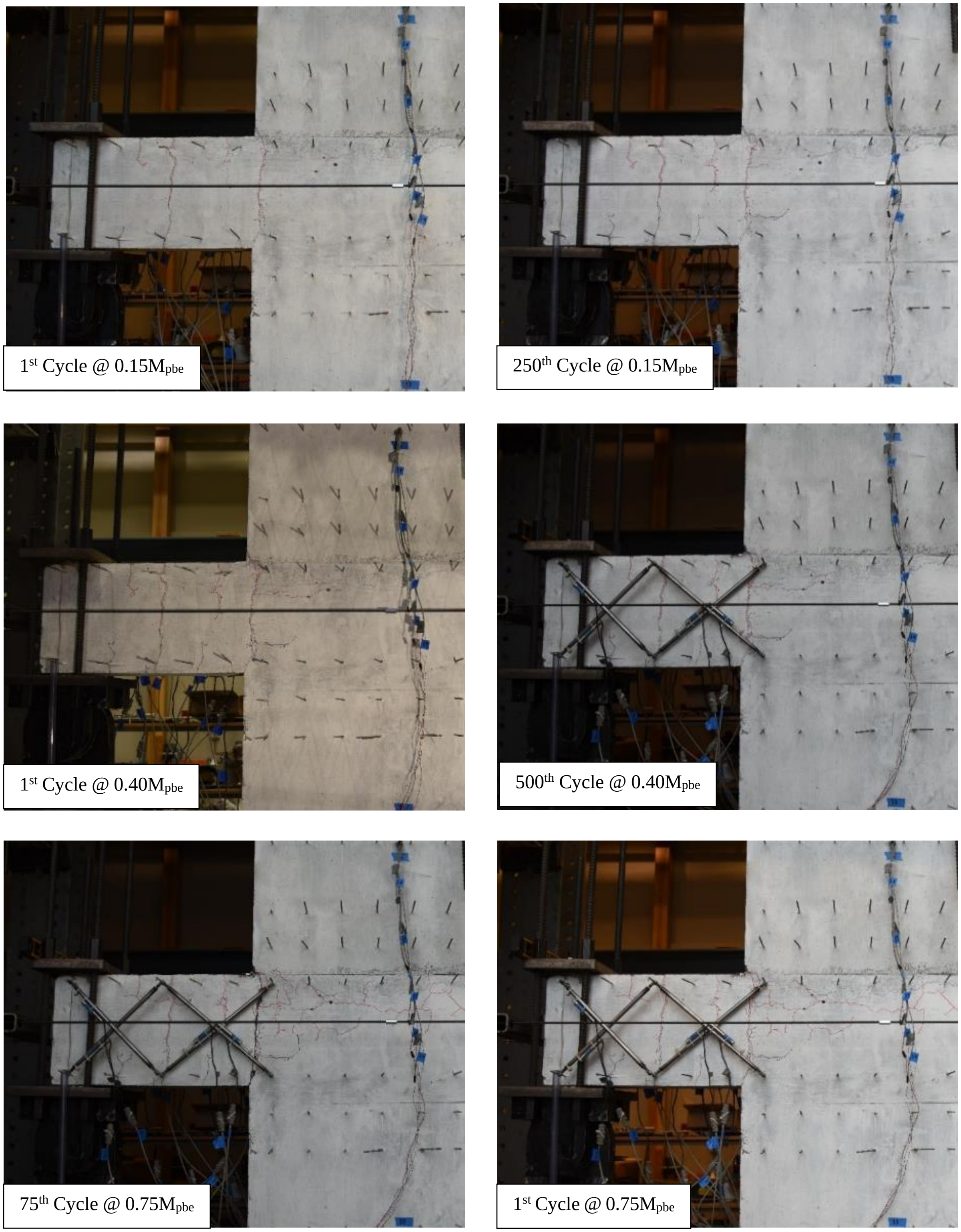

Figure 4.1. Damage Photos for SRC-W1

Figure 4.1. Damage Photos for SRC-W1 (continued)

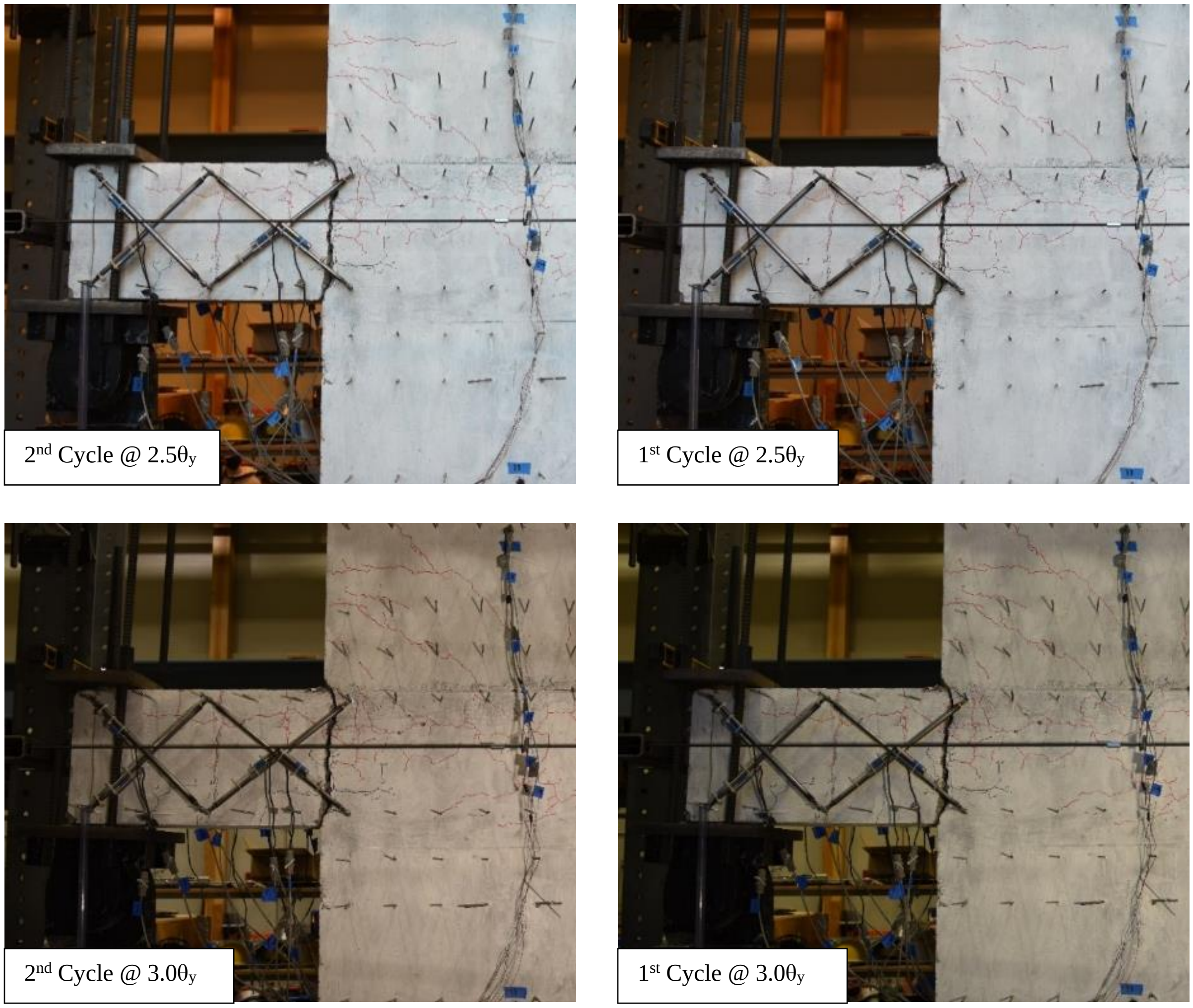

Figure 4.1. Damage Photos for SRC-W1 (continued)

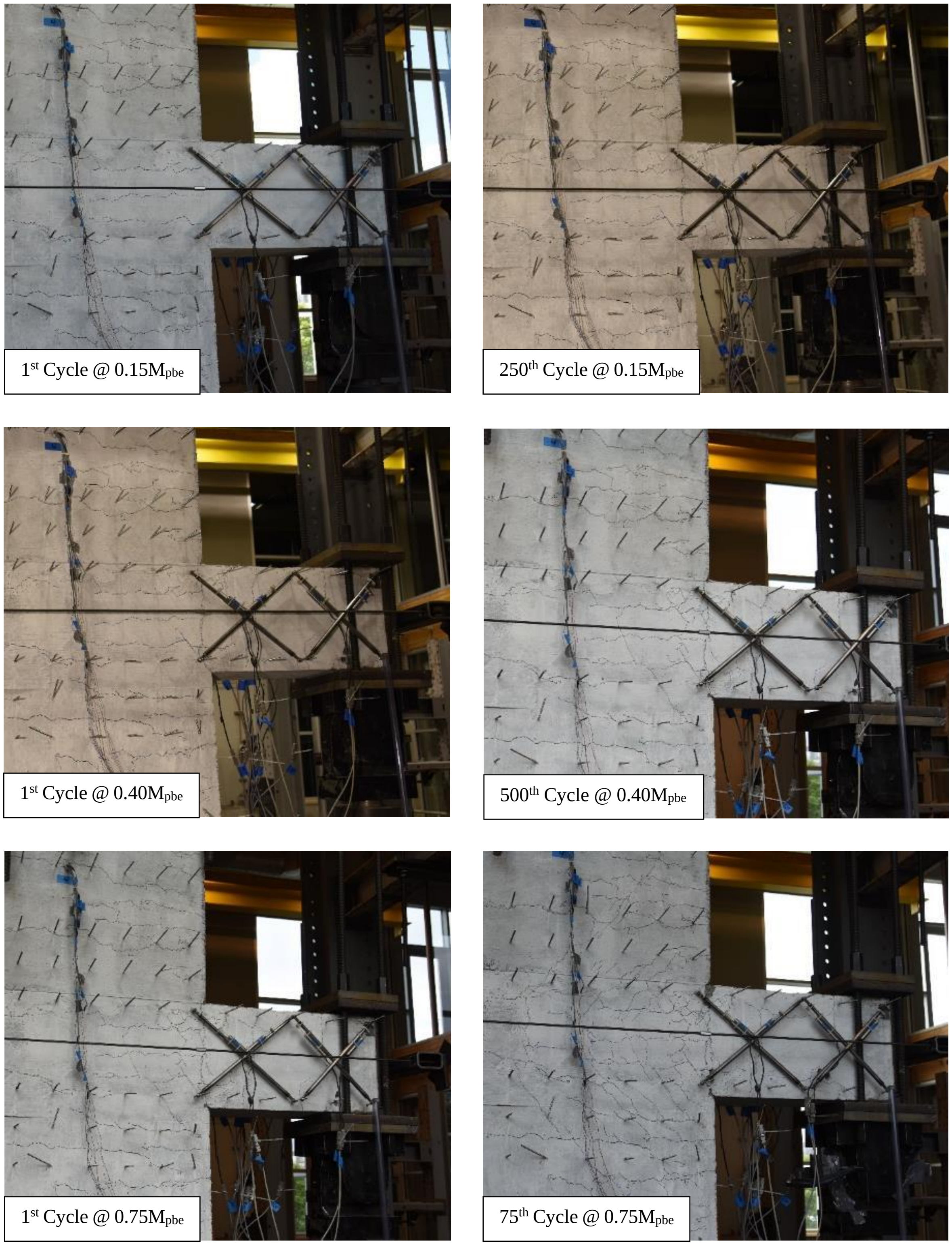

Figure 4.2. Damage Photos for SRC-W2

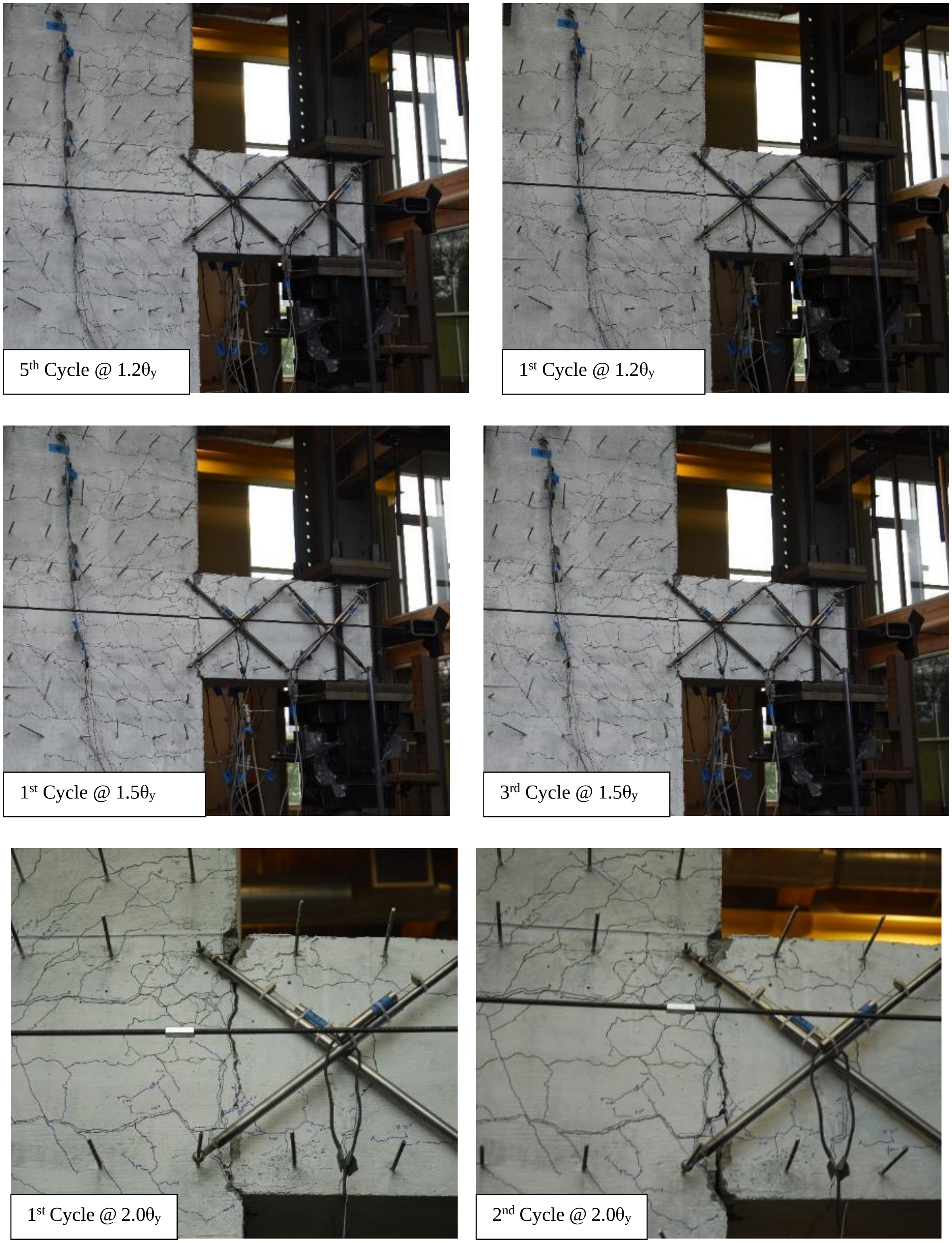

Figure 4.2. Damage Photos for SRC-W2 (continued)

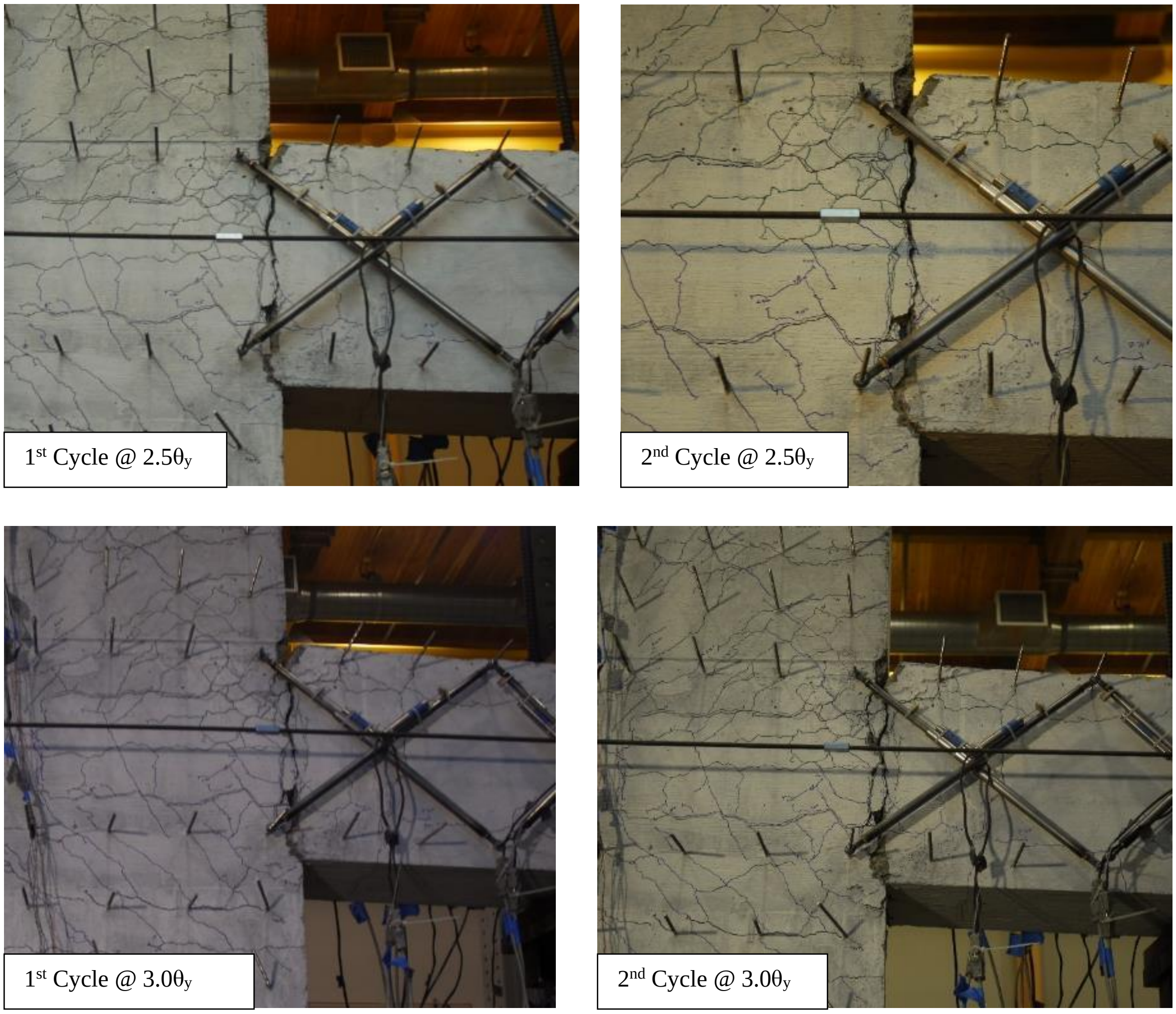

Figure 4.2. Damage Photos for SRC-W2 (continued)

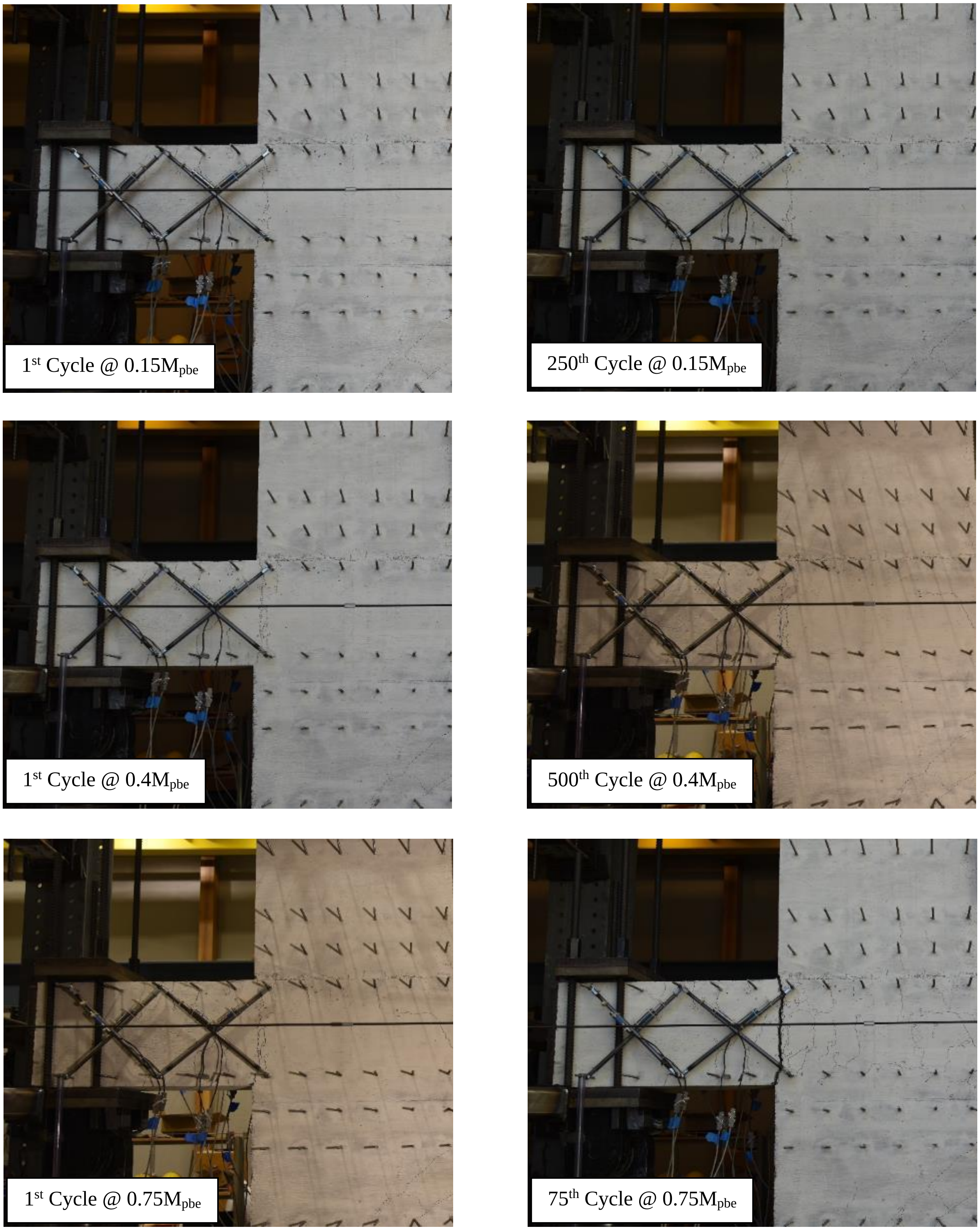

Figure 4.3. Damage Photos for SRC-W3

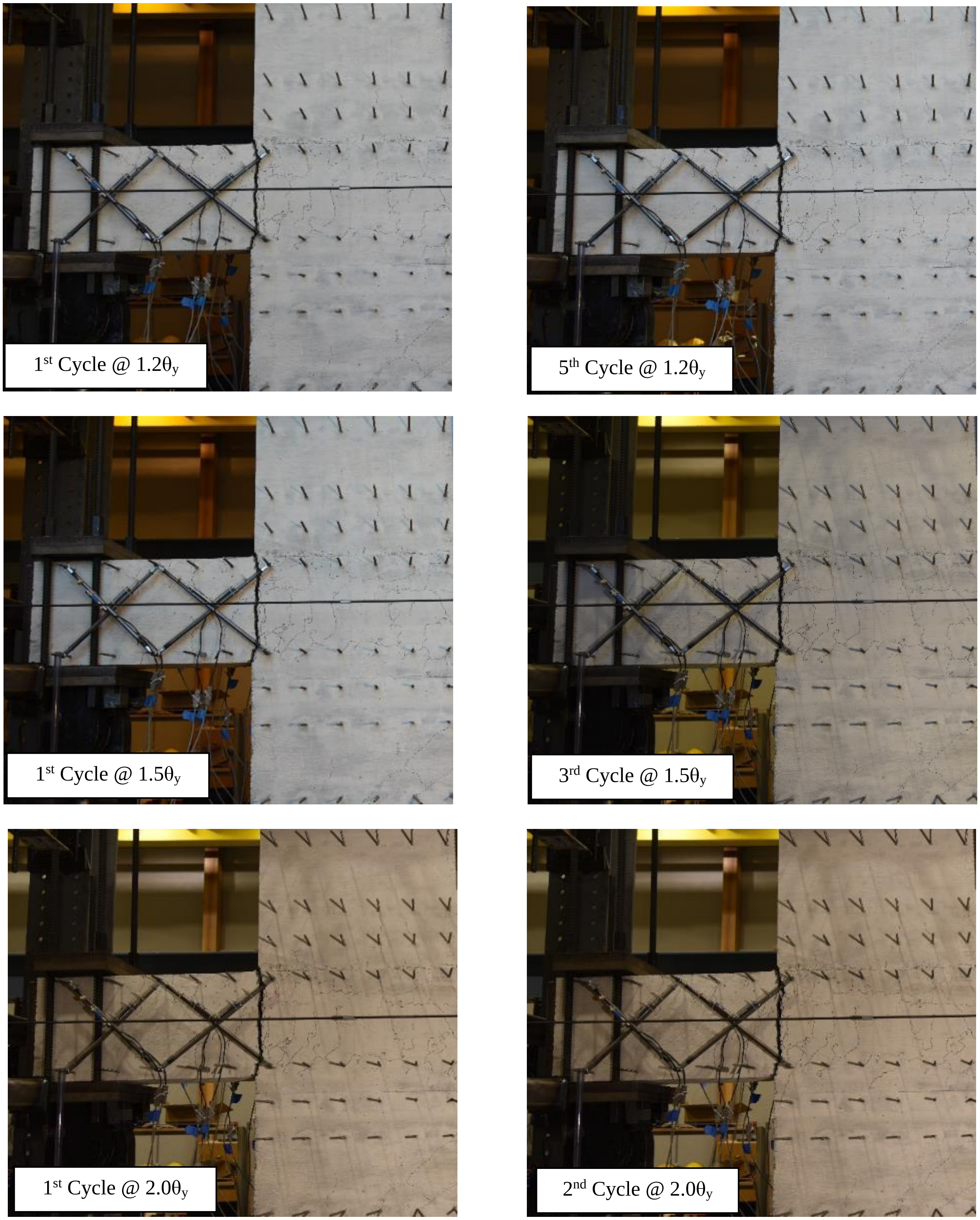

Figure 4.3. Damage Photos for SRC-W3 (continued)

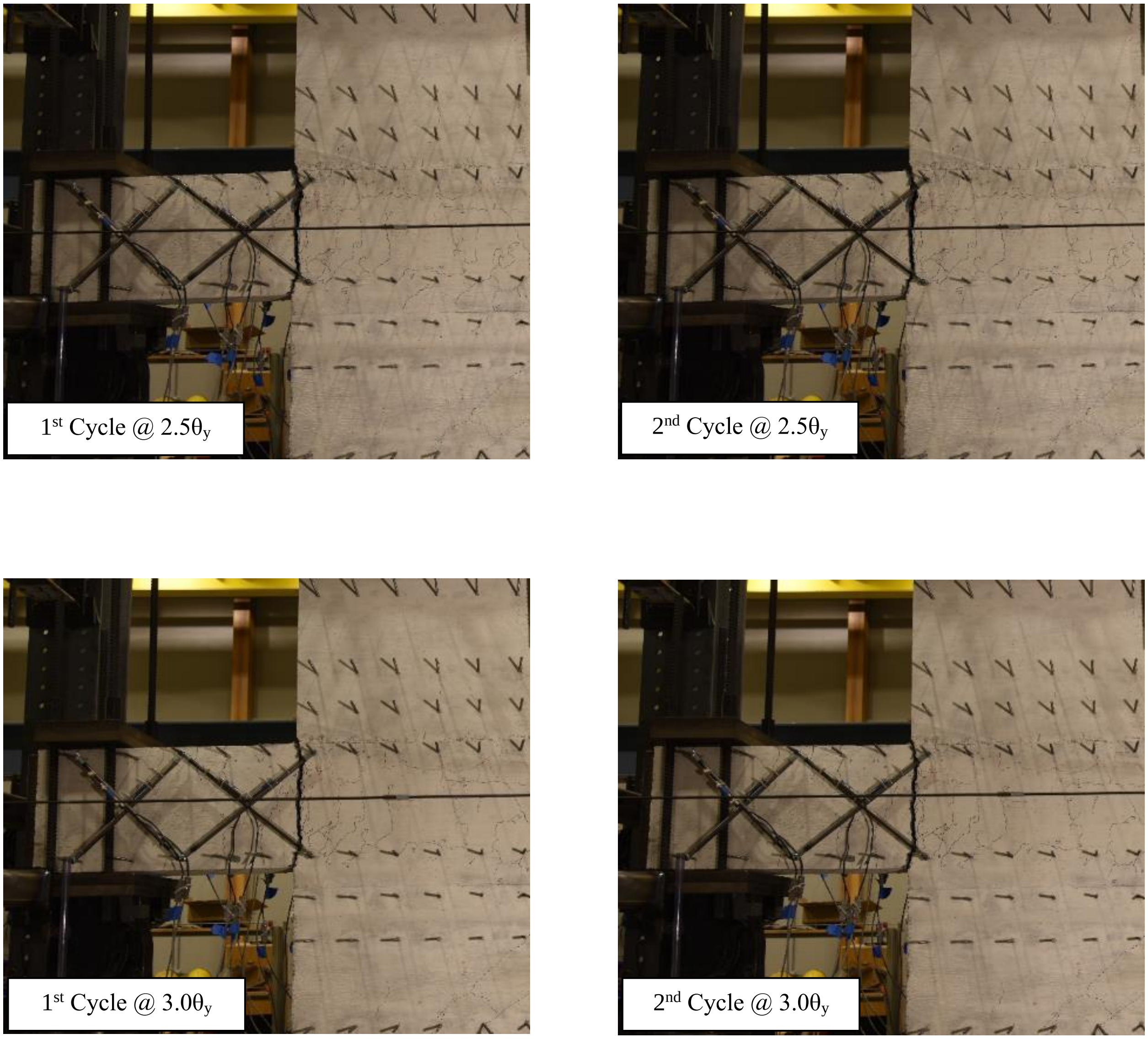

Figure 4.3. Damage Photos for SRC-W3 (continued)

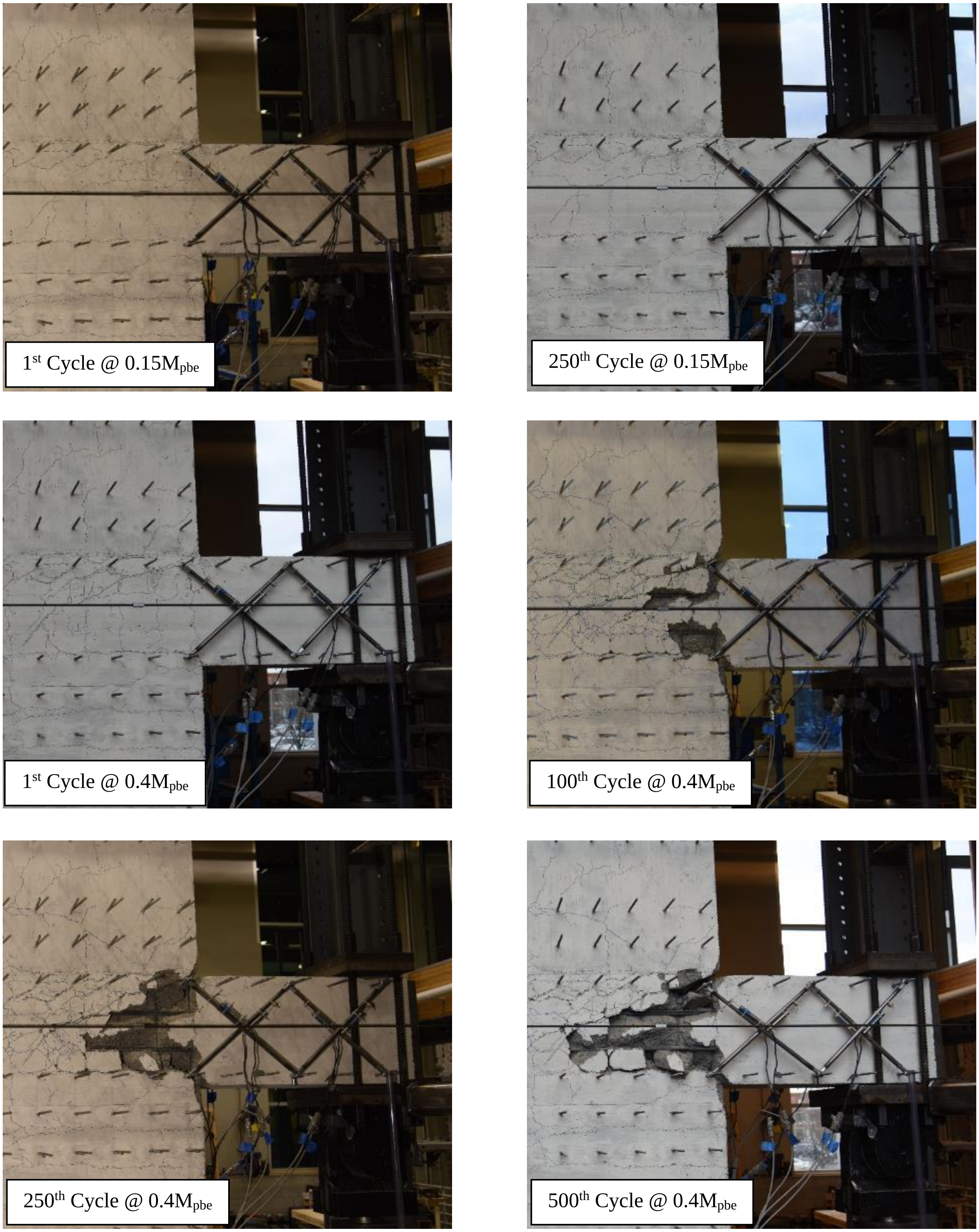

Figure 4.4. Damage Photos for SRC-W4

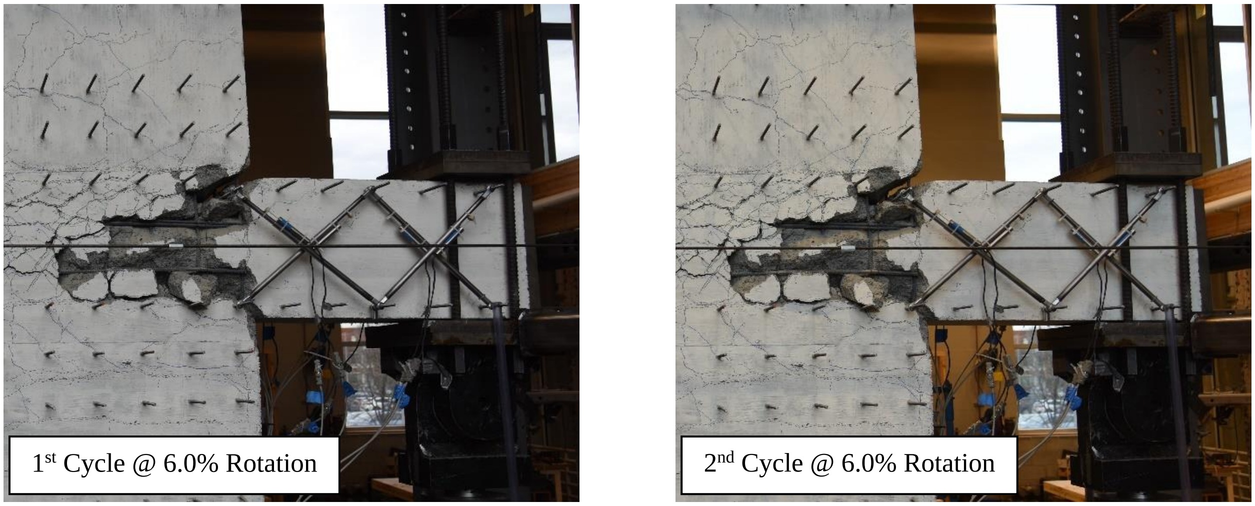

Figure 4.4. Damage Photos for SRC-W4 (continued)

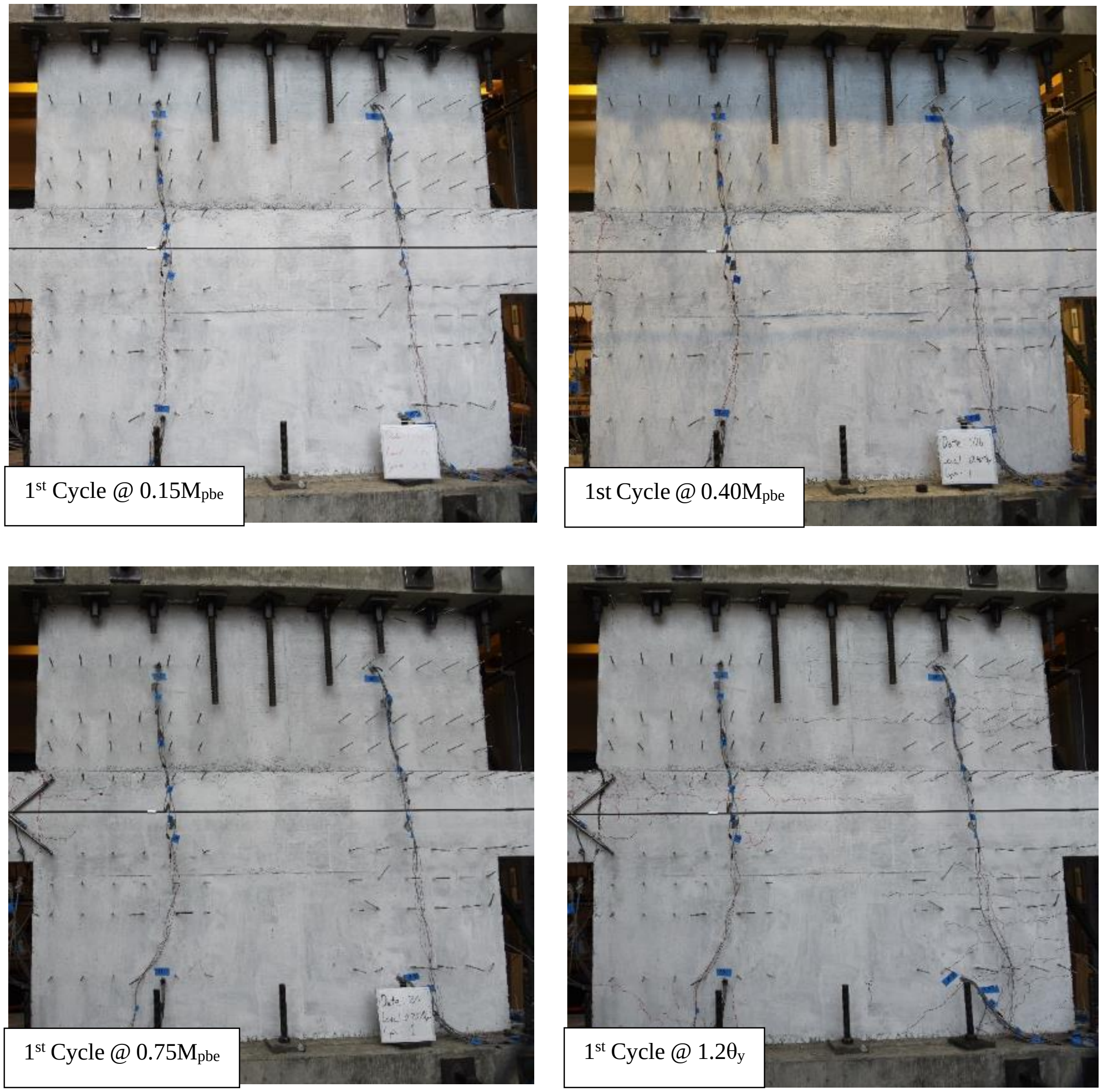

Figure 4.5. Wall Damage Photos for SRC-W1

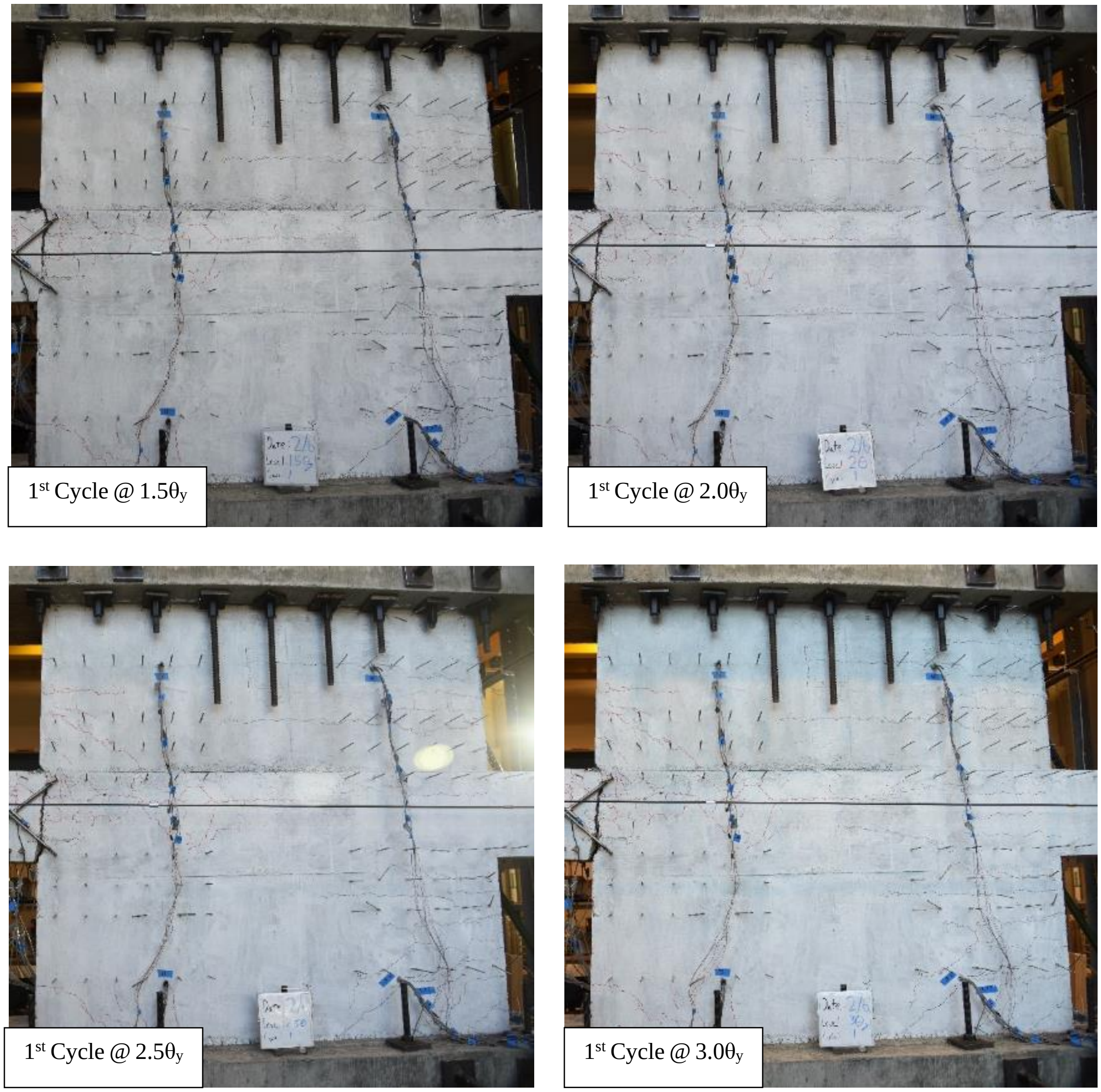

Figure 4.5. Wall Damage Photos for SRC-W1 (continued)

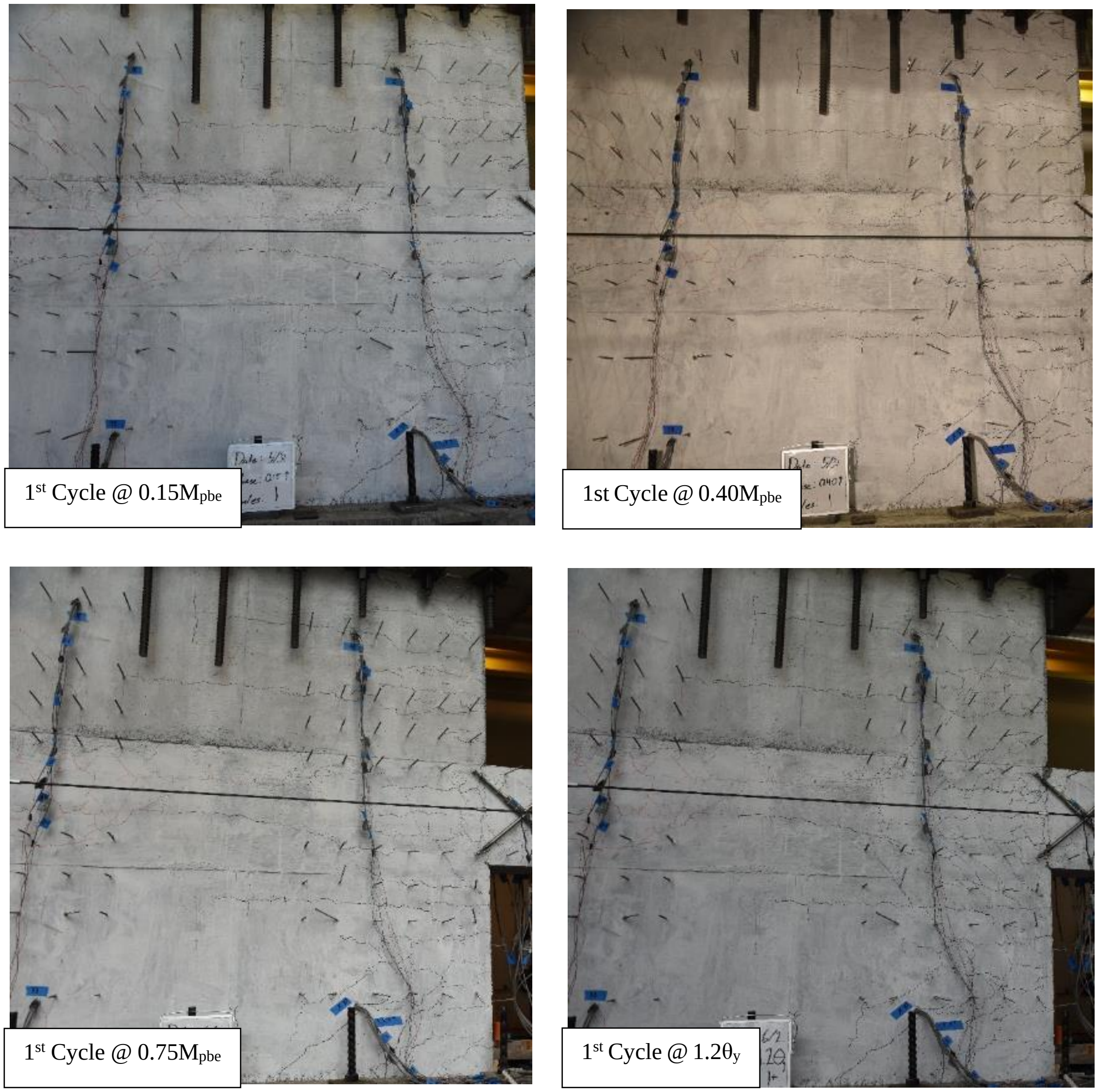

Figure 4.6. Wall Damage Photos for SRC-W2

Figure 4.6. Wall Damage Photos for SRC-W2 (continued)

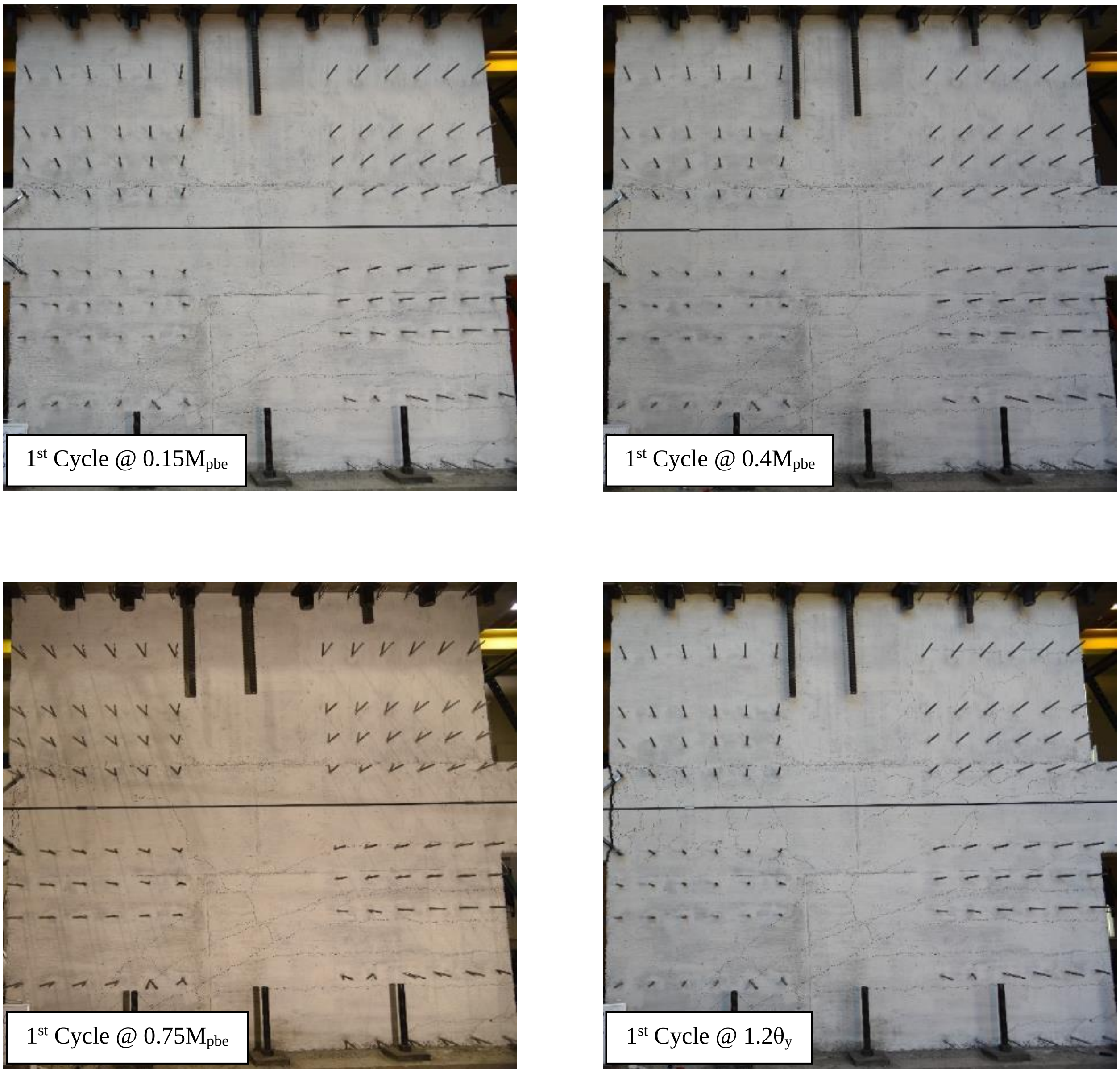

Figure 4.7. Wall Damage Photos for SRC-W3

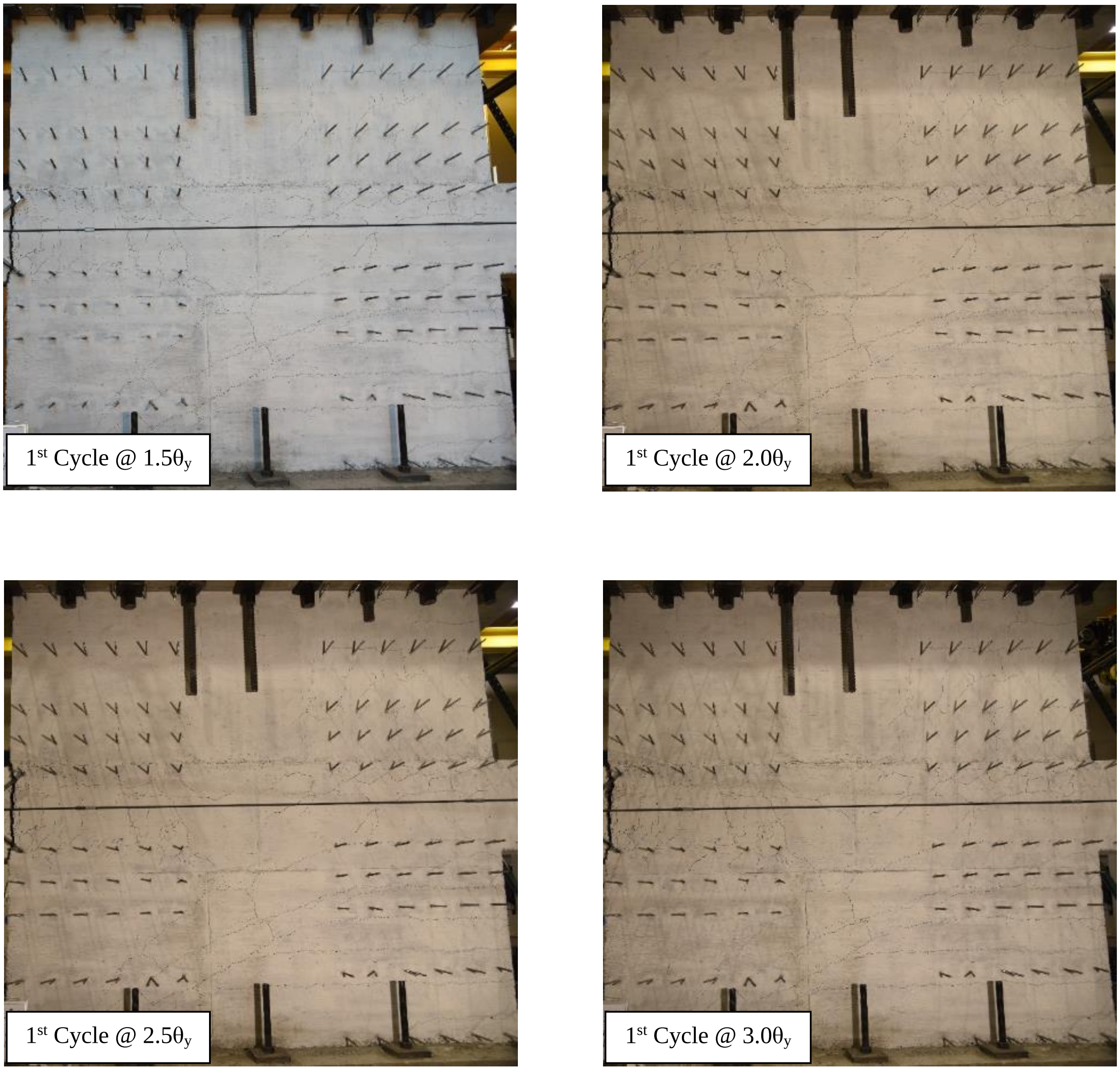

Figure 4.7. Wall Damage Photos for SRC-W3 (continued)

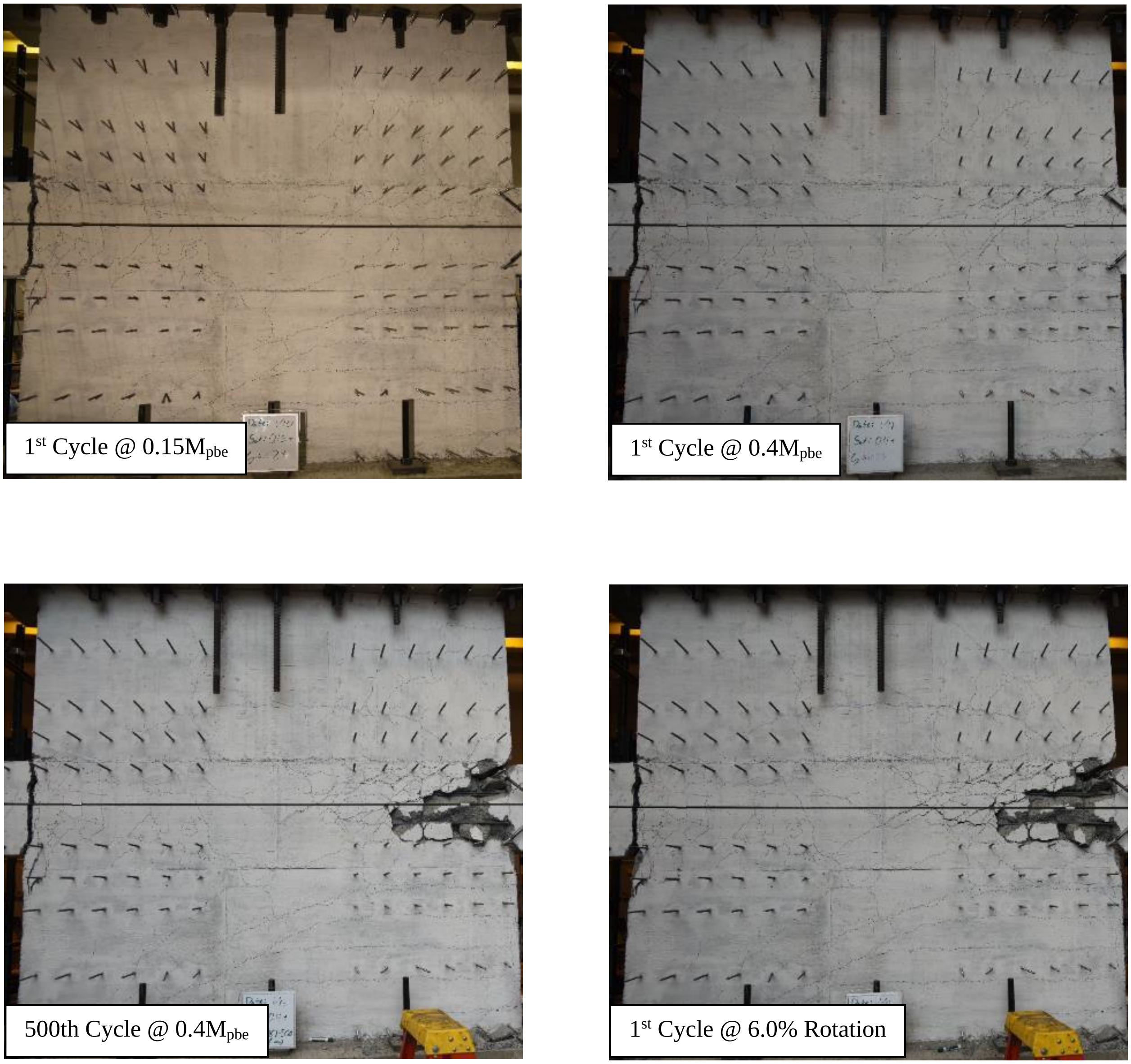

Figure 4.8. Wall Damage Photos for SRC-W4

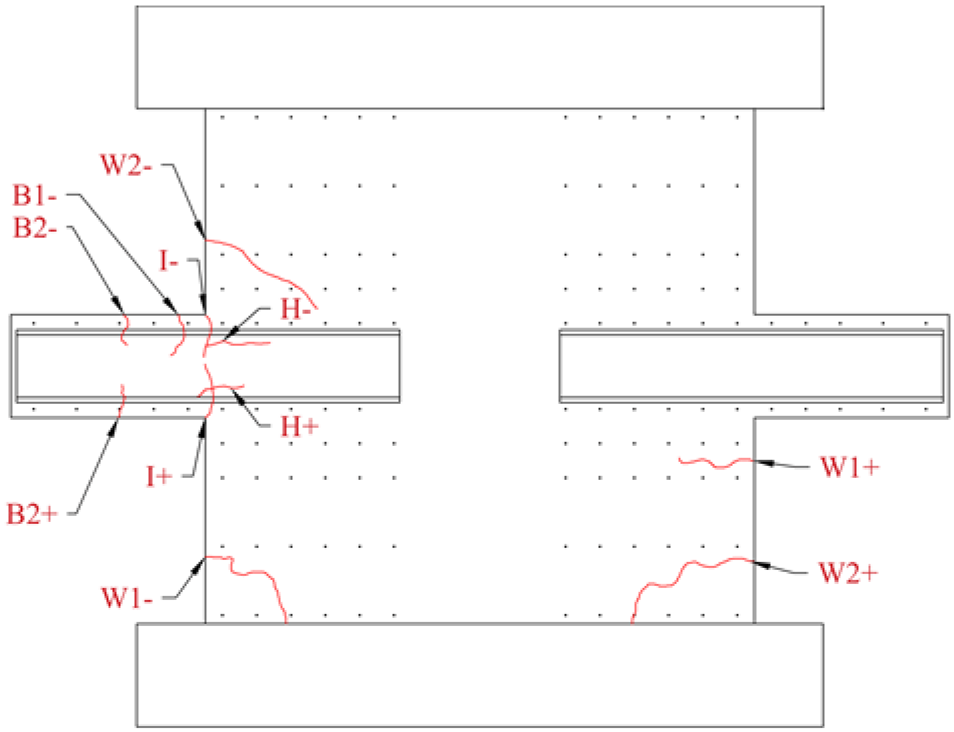

Figure 4.9. Location of Cracks 0.2 Millimeters or Larger for SRC-W1

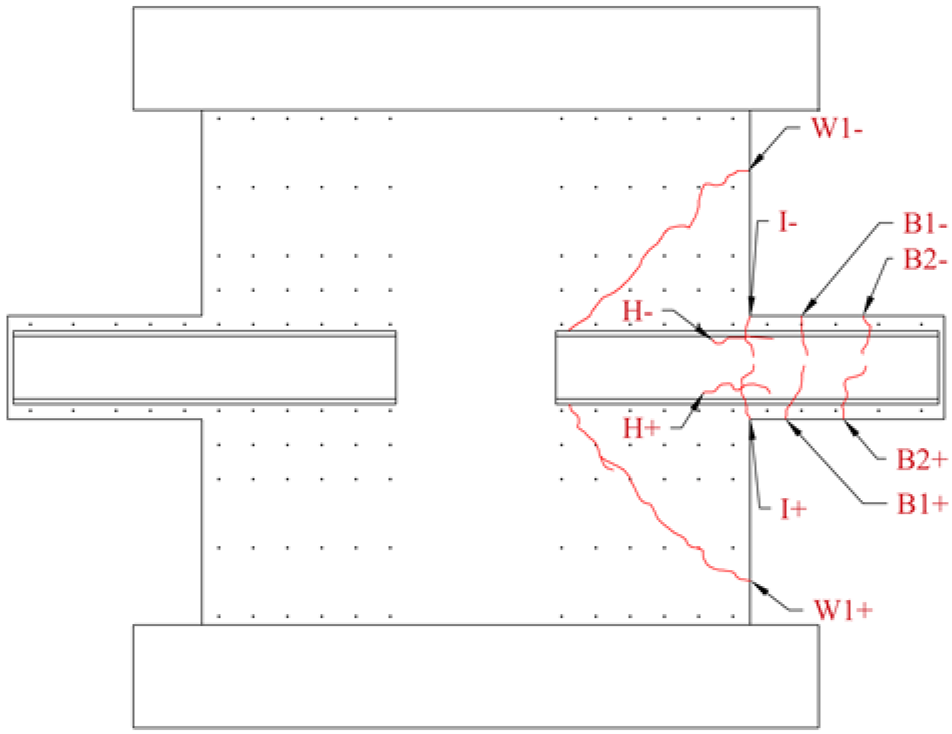

Figure 4.10. Location of Cracks 0.2 Millimeters or Larger for SRC-W2

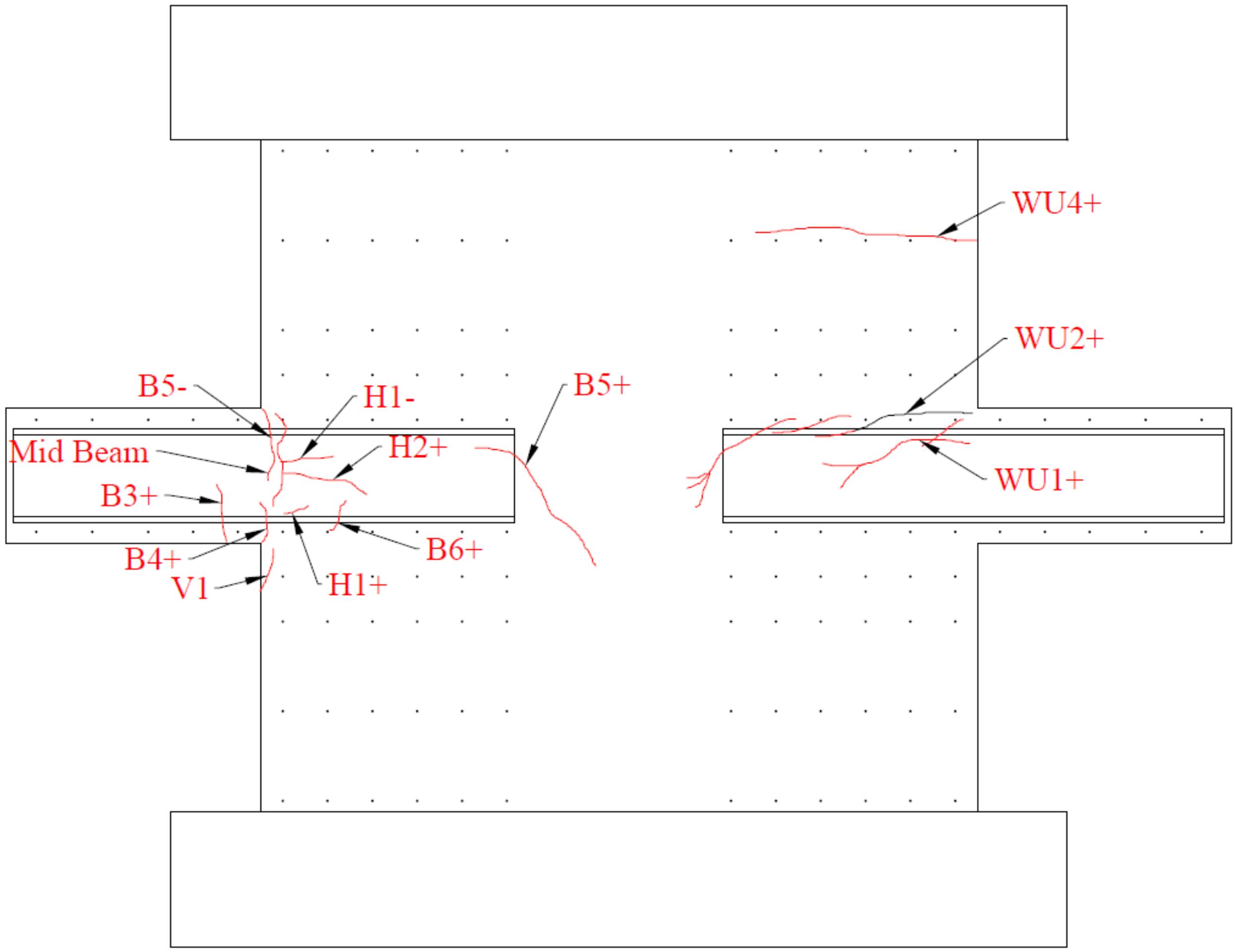

Figure 4.11. Location of Cracks 0.2 Millimeters or Larger for SRC-W3

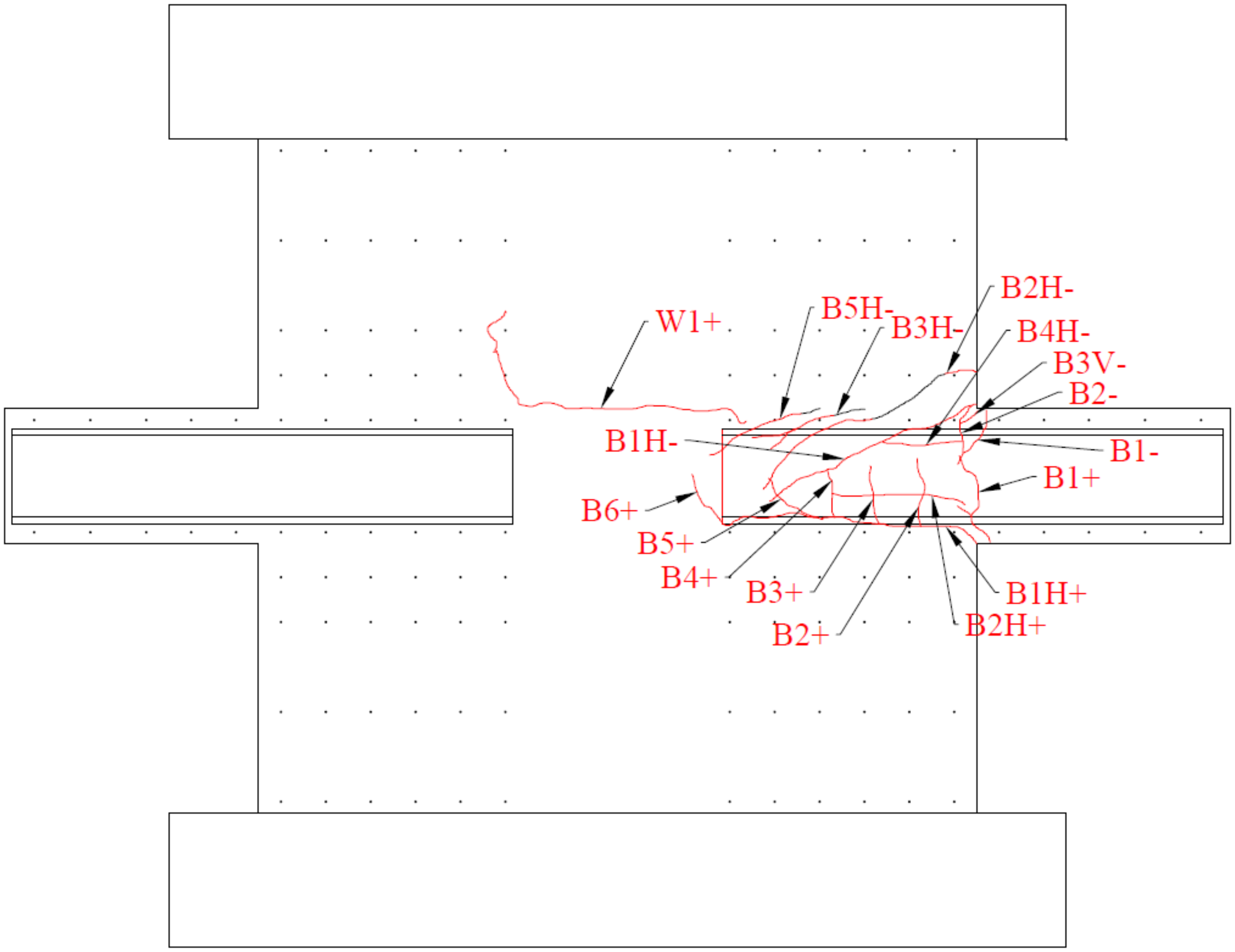

Figure 4.12. Location of Cracks 0.2 Millimeters or Larger for SRC-W4 through the 30th Cycle at $0.4M_{pbe}$

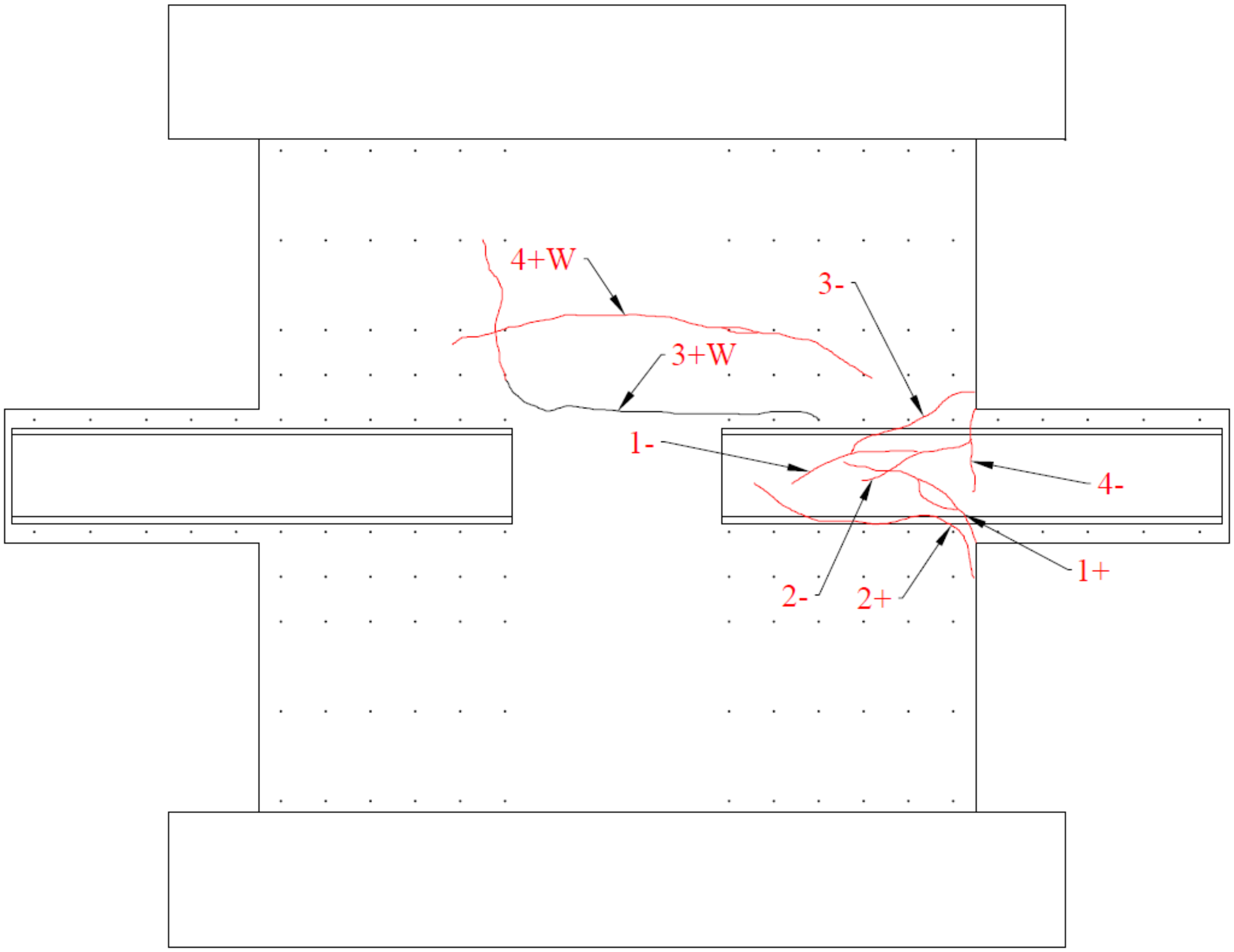

Figure 4.13. Location of Cracks 0.2 Millimeters or Larger for SRC-W4 following the 30th Cycle at $0.4M_{pbe}$

Table 4.1. Measured Crack Widths (Millimeters) for SRC-W1

Crack:	I1+		I1-		B2+		B2-		H+		H-		W1+		W2+	
Group/Cycle	End	Face	End	Face	End	Face	End	Face	End	Face	End	Face	Face	End	Face	End
0.15M_p First	0.4	0.2	0.2	0.3	H	H	H	0.2	-	-	-	-	-	-	-	-
0.15M_p Last	0.6	0.4	0.5	0.35	H	0.25	H	0.2	H	H	H	H	-	-	-	-
0.4M_p First	1	0.5	1.5	0.6	0.2	0.25	H	0.2	H	H	H	H	-	-	-	-
0.4M_p Last	1.5	0.8	1.5	0.8	0.25	0.2	0.2	0.2	0.2	H	H	H	-	-	-	-
0.75M_p First	2.5	1.5	2.5+	1.5	0.3	0.25	0.25	0.2	0.25	H	0.3	H	-	-	-	-
0.75M_p Last	7	4	7	4	0.35	0.25	0.3	0.25	0.25	H	0.4	H	H	0.25	H	0.2
1.2θ_y First	9	5	10	4	0.35	0.25	0.3	0.25	0.25	H	0.5	H	H	0.25	H	0.2
1.2θ_y Last	9	6	10	5.5	0.35	0.25	0.3	0.25	0.35	H	0.6	H	H	0.25	H	0.25
1.5θ_y First	11	7	12	6	0.3	0.25	0.3	0.25	0.3	H	0.7	H	H	0.2	H	0.25
1.5θ_y Last	12	8	13	7	0.3	0.25	0.3	0.25	0.3	H	0.7	H	H	0.2	H	0.25
2.0θ_y First	15	12	17	9	0.3	0.25	0.3	0.25	0.3	H	0.8	H	H	0.2	H	0.2
2.0θ_y Last	16	12	17	10	0.3	0.25	0.3	0.25	0.3	H	0.8	H	H	0.2	H	0.2
2.5θ_y First	19	14	21	11	0.3	0.25	H	H	0.35	H	0.8	H	H	0.2	H	0.2
2.5θ_y Last	20	15	21	15	0.35	0.25	H	H	0.35	H	0.8	H	H	0.2	H	0.25
3.0θ_y First	23	17	24	17	0.35	0.25	H	H	0.35	H	0.8	H	H	0.2	H	0.25
3.0θ_y Last	23	17	24	17	0.35	0.25	H	H	0.3	H	1	H	H	0.2	H	0.25
2.5θ_y First	21	14	21	17	0.4	0.3	H	H	0.35	H	1	H	H	0.2	H	0.2
2.5θ_y Last	20	14	21	14	0.4	0.3	H	H	0.35	H	0.6	H	H	0.2	H	0.2
2.0θ_y First	17	15	18	12	0.4	0.25	H	H	0.4	H	0.6	H	H	0.2	H	0.2
2.0θ_y Last	17	11	17	12	0.5	0.2	H	H	0.35	H	0.6	H	H	0.2	H	0.2
1.5θ_y First	14	11	15	13	0.5	0.2	H	H	0.35	H	0.6	H	H	0.2	H	0.2
1.5θ_y Last	13	11	13	11	0.35	0.2	H	H	0.35	H	0.5	H	H	0.2	H	0.2
1.2θ_y First	12	10	13	11	0.4	0.25	H	H	0.35	H	0.6	H	H	0.2	H	0.2
1.2θ_y Last	11	11	12	10	0.4	0.2	H	H	0.6	H	0.35	H	H	0.2	H	2
0.75M_p First	13	10	13	11	0.4	0.2	H	H	0.4	H	0.8	H	H	0.2	H	0.2
0.75M_p Last	12	10	13	9	0.5	0.2	H	H	0.35	H	0.6	H	H	0.2	H	0.2
0.4M_p First	6	7	9	10	0.4	0.2	H	H	H	H	0.3	H	H	0.2	H	0.2
0.4M_p LAst	5	8	8	8	0.4	0.2	H	H	H	H	0.3	H	H	0.2	H	0.2
0.15M_p First	4	8	8	8	0.35	H	H	H	H	H	H	H	H	0.2	H	0.2
0.15M_p Last	4	5	7	6	0.35	H	H	H	H	H	H	H	H	0.2	H	0.2

Table 4.2. Measured Crack Widths (Millimeters) for SRC-W2

Crack:	I1+		I1-		B1+		B2+		B1-		B2-		W1+		W1-		H+		H-	
Group/Cycle	End	Face	End	Face	End	Face	End	Face	End	Face	End	Face	End	Face	End	Face	Face	End	Face	End
0.15Mp First	-	-	0.6	0.3	-	-	-	-	-	-	-	-	-	-	-	-	-	-	-	-
0.15Mp Last	0.8	0.4	0.7	0.35	-	-	-	-	-	-	-	-	-	-	-	-	-	-	-	-
0.4Mp First	1.5	0.4	1.5	0.5	H	H	H	H	H	0.25	H	H	-	-	-	-	-	-	-	-
0.4Mp Last	1.5	0.5	2	0.6	H	H	H	H	H	0.3	H	H	-	-	-	-	-	-	-	-
0.75Mp First	3	0.8	3.5	1.5	0.3	0.2	0.2	H	0.35	0.2	0.2	0.2	-	-	-	-	-	-	-	-
0.75Mp Last	4.5	1.4	4.5	1.5	0.35	0.25	0.2	H	0.35	0.2	0.2	0.2	0.25	0.4	0.25	0.4	0.2	0.4	0.2	0.5
1.2θy First	9	2	8	2	H	H	H	H	0.2	0.25	0.2	H	0.2	0.4	0.25	0.4	0.2	0.8	H	0.6
1.2θy Last	9	2	8	2	H	H	H	H	0.2	0.2	0.2	H	0.2	0.4	0.25	0.4	0.2	0.8	H	0.6
1.5θy First	11	2.5	11	3	H	H	H	H	0.2	0.25	0.25	0.2	0.2	0.6	0.2	0.4	0.2	1	0.2	1
1.5θy Last	11	2.5	11	3	H	H	H	H	0.2	0.25	0.25	0.2	0.2	0.6	0.2	0.4	0.2	0.9	0.2	1.5
2.0θy First	13	5	14	5	H	H	H	H	0.2	0.25	0.25	0.2	0.25	0.6	0.3	0.5	0.25	1	0.25	0.8
2.0θy Last	13	5	13	6	H	H	H	H	0.2	0.25	0.25	0.2	0.25	0.5	0.2	0.4	0.25	1.5	0.25	1.25
2.5θy First	14	7.5	16	6	H	H	H	H	0.25	0.25	0.2	0.25	0.25	0.6	0.25	0.5	0.25	1.25	0.25	1
2.5θy Last	14	6	18	7	H	H	H	H	0.25	0.25	0.2	0.25	0.25	0.6	0.25	0.4	0.25	1.5	0.25	1.25
3.0θy First	20	9	22	6	H	H	H	H	0.2	0.25	0.25	0.2	0.25	0.6	0.25	0.5	0.25	2	0.25	3
3.0θy Last	21	9	22	6	H	H	H	H	0.2	0.25	0.25	0.2	0.25	0.6	0.25	0.4	0.25	1.5	0.25	3
2.5θy First	17	7	17	6	H	H	H	H	0.25	0.25	0.2	0.25	0.25	0.6	0.25	0.4	0.25	1.75	0.6	3
2.5θy Last	19	8	18	6	H	H	H	H	0.25	0.25	0.2	0.25	0.25	0.6	0.25	0.4	0.25	1.5	0.6	3.5
2.0θy First	15	7	17	9	H	H	H	H	0.2	0.25	0.25	0.2	0.25	0.6	0.25	0.35	0.25	1.5	0.25	3.5
2.0θy Last	15	7	18	10	H	H	H	H	0.2	0.25	0.25	0.2	0.25	0.5	0.25	0.35	0.25	1.5	0.25	3.5
1.5θy First	10	6	12	7	H	H	H	H	0.2	0.25	0.25	0.2	0.25	0.5	0.25	0.4	0.25	1	0.25	3
1.5θy Last	11	5	12	7	H	H	H	H	0.2	0.25	0.25	0.2	0.2	0.4	0.25	0.4	0.25	1.5	0.25	3
1.2θy First	11	8	9	8	H	H	H	H	0.2	0.25	0.25	0.2	0.2	0.4	0.2	0.35	0.25	1	0.2	1
1.2θy Last	10	8	10	8	H	H	H	H	0.2	0.25	0.25	0.2	0.2	0.35	0.2	0.3	0.2	0.9	0.25	1
0.75Mp First	15	7	16	8	H	H	H	H	0.2	0.25	0.25	0.2	0.25	0.45	0.2	0.35	0.2	1.25	0.2	1.5
0.75Mp Last	14	12	14	8	H	H	H	H	0.2	0.25	0.25	0.2	0.2	0.6	0.25	0.5	0.25	1.75	0.2	1.5
0.4Mp First	8	7	9	6	H	H	H	H	0.2	0.25	0.25	0.2	0.25	0.4	0.2	0.4	0.25	1.5	0.2	1.5
0.4Mp LAst	9	6	10	6	H	H	H	H	0.2	0.25	0.25	0.2	0.25	0.4	0.2	0.35	0.25	1.25	0.2	1.5
0.15Mp First	6	6	6	5	H	H	H	H	0.2	0.25	0.25	0.2	0.2	0.35	0.2	0.3	H	1	0.2	1
0.15Mp Last	6	5	6	5	H	H	H	H	0.2	0.25	0.25	0.2	0.2	0.3	0.2	0.3	H	0.8	0.2	1

Table 4.3. Measured Crack Widths (Millimeters) for SRC-W3

Crack:	B3+		B4+		B5+		B6+	B5-		Mid Beam	WU1+		WU2+		WU4+		V1	H1-		H1+		H2+	
Group/Cycle	End	Face	End	Face	End	Face	Face	End	Face	Face	End	Face	End	Face	End	Face	Face	End	Face	End	Face	End	Face
0.15Mp First	H	H	H	H	-	-	-	H	H	-	-	-	-	-	-	-	-	-	-	-	-	-	-
0.15Mp First	0.15	H	0.15	0.2	-	-	-	0.2	0.25	-	-	-	-	-	-	-	-	-	-	-	-	-	-
0.4Mp First	0.15	H	0.5	0.3	-	-	-	0.8	0.6	-	-	-	-	-	-	-	-	-	-	-	-	-	-
0.4Mp First	0.15	H	0.8	0.5	0.2	0.2		1	0.8	0.35	-	-	-	-	-	-	-	-	-	-	-	-	-
0.75Mp First	0.15	H	2	1	0.2	0.25	H	2.5	1.8	0.6	-	-	-	-	-	-	-	-	-	-	-	-	-
0.75Mp First	0.4	0.3	14	13	0.25	0.3	H	15	14	12	0.2	0.2	-	-	-	-	-	-	-	-	-	-	-
1.2θMp First	0.4	0.3	16	14	0.25	0.3	0.2	16	15	13	0.2	0.2	0.3	-	-	-	-	-	-	-	-	-	-
1.2θMp Last	0.4	0.3	16	14	0.25	0.3	0.2	17	15	13	0.2	0.2	0.35	0.2	-	-	-	-	-	-	-	-	-
1.5θMp First	0.4	0.3	17	15	0.25	0.3	0.2	18	17	14	0.2	0.2	0.35	0.2	-	-	-	-	-	-	-	-	-
1.5θMp Last	0.4	0.3	18	16	0.25	0.35	0.25	19	17	14	0.2	0.2	0.35	0.2	0.15	H	-	-	-	-	-	-	-
2.0θMp First	0.4	0.3	19	17	0.25	0.35	0.25	21	19	15	0.2	0.2	0.35	0.2	0.15	H	-	-	-	-	-	-	-
2.0θMp Last	0.4	0.3	20	18	0.25	0.35	0.25	21	19	15	0.2	0.2	0.35	0.2	0.15	H	-	-	-	-	-	-	-
2.5θMp First	0.4	0.3	22	18	0.25	0.35	0.25	24	21	16	0.2	0.2	0.35	0.2	0.15	H	-	-	-	-	-	-	-
2.5θMp Last	0.4	0.3	22	18	0.25	0.35	0.25	24	23	16	0.2	0.2	0.35	0.2	0.15	H	-	-	-	-	-	-	-
3.0θMp First	0.4	0.3	27	20	0.25	0.35	0.25	27	23	18	0.2	0.2	0.35	0.2	0.15	H	-	-	-	-	-	-	-
3.0θMp Last	0.4	0.3	27	20	0.25	0.35	0.25	27	25	18	0.2	0.2	0.35	0.2	0.15	H	-	-	-	-	-	-	-
2.5θMp First	0.4	0.3	22	20	0.25	0.35	0.25	25	25	19	0.2	0.2	0.35	0.2	0.15	H	2	-	-	-	-	-	-
2.5θMp Last	0.4	0.3	23	20	0.25	0.35	0.25	25	23	18	0.2	0.2	0.35	0.2	0.15	H	2	-	-	-	-	-	-
2.0θMp First	0.4	0.3	22	20	0.25	0.3	0.2	23	22	17	0.2	0.2	0.35	0.2	0.15	H	2.5	-	-	-	-	-	-
2.0θMp Last	0.4	0.3	23	20	0.25	0.3	0.2	23	20	18	0.2	0.2	0.35	0.2	0.15	H	2.5	-	-	-	-	-	-
1.5θMp First	0.4	0.3	21	19	0.3	0.25	0.2	21	20	19	0.2	0.2	0.35	0.2	0.15	H	2.5	-	-	-	-	-	-
1.5θMp Last	0.4	0.3	21	19	0.3	0.25	0.2	21	20	19	0.2	0.2	0.35	0.2	0.15	H	2.5	-	-	-	-	-	-
1.2θMp First	0.4	0.3	20	19	0.3	0.25	0.2	21	20	18	0.2	0.2	0.35	0.2	0.15	H	2.5	-	-	-	-	-	-
1.2θMp Last	0.4	0.3	20	19	0.3	0.25	0.2	21	20	18	0.2	0.2	0.35	0.2	0.15	H	2.5	-	-	-	-	-	-
0.75Mp First	0.4	0.3	21	20	0.3	0.25	0.2	21	20	18	0.2	0.2	0.35	0.2	0.15	H	2.5	0.5	0.25	0.2	H	0.5	0.25
0.75Mp First	0.4	0.3	26	24	0.3	0.25	0.2	27	25	23	0.2	0.2	0.35	0.2	0.15	H	2.5	0.5	0.25	0.2	0.2	0.5	0.25
0.4Mp First	0.4	0.3	24	22	0.3	0.25	H	24	23	21	0.2	0.2	0.35	0.2	0.15	H	3	0.3	0.2	0.2	H	H	H
0.4Mp First	0.4	0.3	24	23	0.3	0.25	H	25	23	23	0.2	0.2	0.35	0.2	0.15	H	3	0.3	0.2	0.2	H	H	H
0.15Mp First	0.2	H	23	23	0.2	0.2	H	23	23	23	0.2	0.2	0.35	0.2	H	H	-	0.25	H	0.2	H	H	H
0.15Mp First	0.2	H	23	23	0.2	0.2	H	23	23	23	0.2	0.2	0.35	0.2	H	H	-	0.25	H	0.2	H	H	H

Table 4.4. Measured Crack Widths (Millimeters) for SRC-W4 through the 30th Cycle at $0.4M_{pbe}$

Crack:	Group/Cycle	0.15Mp First	0.15Mp First	0.4Mp First	0.4Mp (30)
B1+	End	0.4	0.8	2.5	8
	Face 1	0.2	0.25	0.4	0.1
	Face 2	-	-	-	1
B2+	End	0.3	0.4	0.25	0.3
	Face	0.15	0.2	0.1	0.1
B3+	End	H	0.15	0.2	0.2
	Face	H	0.1	0.1	H
B4+	Face	H	H	0.3	0.25
	End	H	H	0.2	0.15
B5+	End	-	-	0.25	1
	Face	-	-	0.15	0.6
B6+	Face	-	-	0.2	0.35
	End	-	-	H	H
B1H+	1*	-	-	-	8
	2	-	-	1.5	1.5
	3	-	-	1.25	2.5
	4	-	-	0.5	1.5
	5	-	-	0.25	0.3
B2H+	1	-	-	-	0.6
	2	-	-	-	0.6
	3	-	-	-	0.3
W1+	1	-	-	-	0.6
	2	-	-	-	1
	3	-	-	-	0.6
B1V-	End	0.5	0.8	4	10
	Face	0.2	0.3	0.6	3
B2V-	End	0.15	0.15	0.15	H
	Face	0.4	0.4	0.5	0.3
B3V-	End	-	-	-	10
B1H-	1	1	1.25	2.5	0.4
	2	0.35	0.4	1.5	1
	3	-	-	0.4	1.5
	4	-	-	0.25	0.4
B2H-	1	-	-	-	0.35
	2	-	-	0.4	0.6
	3	-	-	0.5	0.2
	4	-	-	0.25	0.35
B3H-	1	-	-	0.15	0.35
	2	-	-	0.4	0.8
	3	-	-	0.15	0.4
B4H-	1	-	-	-	5
	2	-	-	-	1.5
B5H-	1	-	-	-	0.4
	2	-	-	-	0.8
	3	-	-	-	0.3

Table 4.5. Measured Crack Widths (Millimeters) for SRC-W4 through the 30th Cycle at 0.4M_{pbe}

Crack:	Group/Cycle	0.4Mp (40)	0.4Mp (100)	0.4Mp (250)	0.4Mp (500)	0.75Mp (1)	0.75Mp (2)
1+	1*	8	8	10	10	22	25
	2	0.6	1				
	3	1	6				
	4	1	0.4				
2+	1	2.5					
	2	3	3.5				
	3	1.5	1.5	1.5			
	4	1	0.5	0.3			
3+W	1	0.6	0.5	0.6	0.4	1.5	0.6
	2	1	1	0.6	0.6	1.5	0.35
	3	0.6	0.6	0.8	0.8	1.5	0.8
4+W	1	0.25	0.3	0.3	0.3	0.6	0.35
	2	0.5	0.6	0.5	0.5	1.5	1.5
	3	0.4	0.5	0.5	0.5	0.8	0.6
1-	1	10	10	10	10	50	50
	2	3	2				
	3	2.5					
	4	1.5	2				
	5	1.5	2	2.5			
2-	1	2.5					
	2	1.5	2				
3-	1	1	3.5				
	2	1	1.5	1.5			
	3	0.35	0.5	0.4			
4-	1	0.6	0.5	0.5			

4.2. Load-Deformation

Load-deformation responses for the tested beams are provided in Figure 4.14. Cyclic stiffness degradation occurred during repeated loading cycles at a given increment, particularly during the groups of 75 cycles at $0.75M_{pbe}$, as shown in Figure 4.15. θ_y, determined as described in Section 3.6, was 1.90% chord rotation for SRC-W1, 1.55% chord rotation for SRC-W2 and SRC-W3, and indeterminate for SRC-W4, as $0.75M_{pbe}$ was not reached. For the three tests in which θ_y was determined, peak deformation demand was $3\theta_y$, as discussed in Section 3.6, resulting in peak deformation of 5.70% for SRC-W1 and 4.65% for SRC-W2 and SRC-W3. For these three tests, the demands during displacement-controlled cycles led to a reduction in stiffness for the second batches of load-controlled cycles relative to the initial batches of load-controlled cycles at a given increment. The hysteretic loops for SRC-W2 had slightly more pinching than SRC-W1 and SRC-W3, although the level of pinching in both tests was small, as was the level of strength degradation. The shape of the hysteretic loops is generally consistent with SRC1 tested by Motter et al (2017a), which is reflective of favorable embedment behavior and sufficient wall longitudinal reinforcement relative to the wall demands. The peak strength reached in these three tests was 173.5 kips in the positive direction and 179.8 kips in the negative direction for SRC-W1, 178.0 kips in the positive direction and 180.4 kips in the negative direction for SRC-W2, and 160.5 kips in the positive direction and 171.0 kips in the negative direction for SRC-W3. The stock beam used for steel sections in SRC-W1 and SRC-W2 differed from the stock beam used for steel sections in SRC-W3 and SRC-W4, which may have impacted the difference in strength for SRC-W3 relative to SRC-W1 and SRC-W2. As mentioned in Section 3.1, V_{be} for the test beams was computed to be 192 kips. This computed value is intended to be an upper bound for beam strength and is used for capacity design of the embedment length and wall longitudinal reinforcement. The post-yield strength increase was larger for these three test beams than for SRC1 tested by Motter et al (2017a). This was likely due to improved concrete contact in compression at the beam-wall interface for the case of reduced axial elongation, as axial restraint reduced axial elongation for these three test beams relative to SRC1, which was tested without axial restraint. More information on axial elongation is provided in Section 4.5.

This study did not include testing on SRC coupling beams that were designed using provisions in AISC 341-22 H4 and tested to peak deformation demands more consistent with ordinary walls. As mentioned in Section 3.1, the maximum deformation demands of $3\theta_y$ were deemed to be more consistent with the seismic design provisions in AISC 341-22 Section H5 for special walls than AISC 341-22 Section H4 for ordinary walls, such that the provisions in H5 were used for design of the test specimens. It is recommended that nonlinear wind design of steel reinforced concrete (SRC) coupling beams follow the seismic provisions in AISC 341-22 Section H5. Advanced levels of deformation demand under wind demands were reached for SRC-W1, SRC-W2, and SRC-W3 without significant strength degradation of initial cycles at new peak deformation demands or significant pinching in the load-deformation response. Similar to seismic design, a specified deformation capacity limit on the coupling beam is likely unnecessary for nonlinear wind design. However, based on the available data, the use of a deformation capacity limit of 6.0% chord rotation could be considered, based on modest extrapolation of data for SRC-W1.

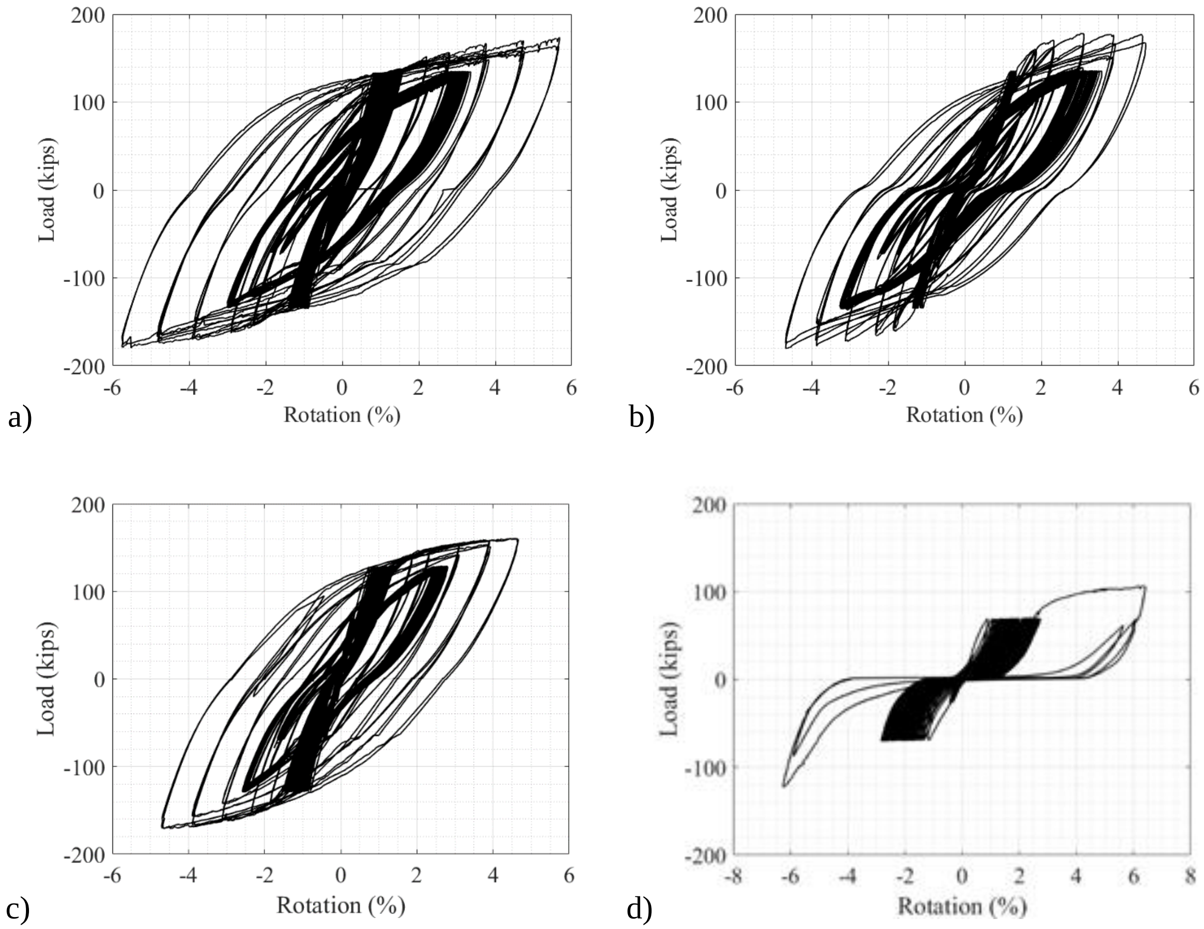

Figure 4.14. Load-Deformation for a) SRC-W1, b) SRC-W2, c) SRC-W3, and d) SRC-W4

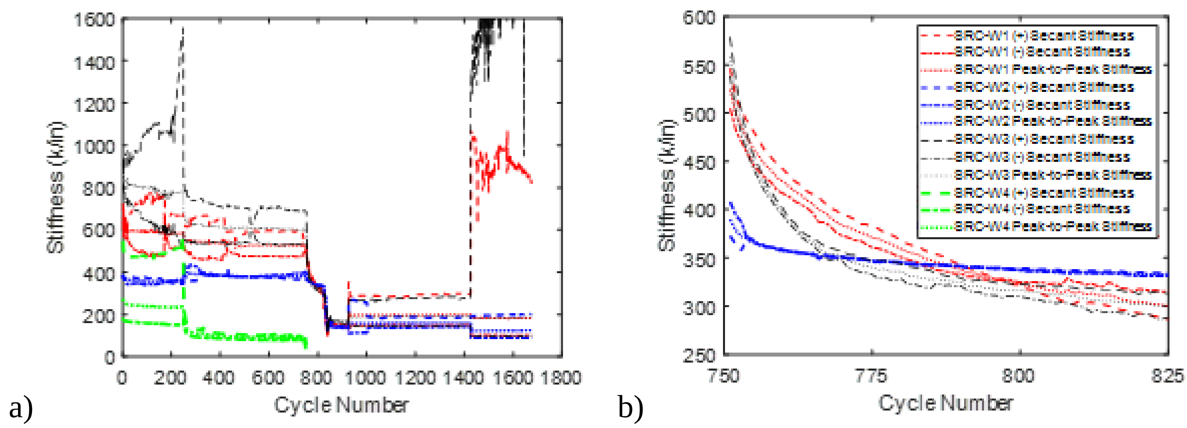

Figure 4.15. Effective Stiffness for a) All Cycles and b) Cycles at 0.75M_{pbe}

The behavior of SRC-W4 differed significantly from the other three tests. SRC-W4 and SRC-W3 were nominally identical tests, with the exception of the quantity of wall longitudinal reinforcement crossing the embedment length and the quantity of wall boundary transverse reinforcement. For SRC-W4, the wall longitudinal reinforcement was insufficient to prevent yielding at the connection, with the embedded steel section prying the wall open. Measured yielding occurred in the wall, with more details provided in Section 4.7. The significant stiffness degradation in the beam during the 500 cycles at $0.4M_{pbe}$ was consistent with that for the wall, as described in Section 4.7. For the 500 cycles at $0.4M_{pbe}$, the largest chord rotation reached by the beam was 2.57% in the positive loading direction and 2.98% in the negative loading direction. During the next positive excursion following the 500 cycles at $0.4M_{pbe}$, the beam reached 6.0% chord rotation prior to reaching $0.75M_{pbe}$. Two loading cycles were conducted at 6.0% chord rotation prior to stopping the test. Significant pinching was observed in the load-displacement hysteresis, with minimal load resistance for the second cycle at 6.0% until approaching the extents of the previous cycle at 6.0% rotation. This type of hysteresis is characteristic of gapping behavior. In this case, the beam pried the wall apart on the initial cyclic excursion to 6.0% with a gap remaining. The peak strength developed in the beam, 106.3 kips in the positive loading direction and 122.8 kips in the negative loading direction, was limited by the yielding in the wall and was significantly less than the other three tests. The combination of wall demands and wall reinforcement for SRC-W3 and SRC-W4 was adequate and inadequate, respectively, to produce favorable performance in the coupled wall.

It is recommended that the quantity of wall longitudinal reinforcement crossing the embedment length prescribed by AISC 341-22 Section H5 be reduced by 50% for cases in which wall demands do not exceed that applied for SRC-W3. This recommendation applies for both seismic and wind design, as favorable performance of SRC-W3 under wind demands to a peak deformation of 4.65% chord rotation was observed. The poor performance of SRC-W4 did not support further reduction to the quantity of wall reinforcement crossing the embedment length or reduction to the quantity of wall boundary transverse reinforcement required by AISC 341-22 Section H5. The peak wall moment and tensile strain demands for SRC-W3 were $0.29M_y$ and 0.00019 tensile strain in outermost reinforcement at the coupling beam mid-height and an average of $0.04M_y$ and -0.00001 tensile strain (0.00001 compressive strain) in outermost reinforcement over one story height, taken as half a story above and below the coupling beam mid-height. These demands were determined from moment-curvature analysis for the moment and axial load, with moment and axial load diagrams determined based on transfer of coupling beam moment and shear to the wall at mid-height of the coupling beam. The moment-curvature analysis used the Hognestad (1951) concrete model, with the compressive strength of concrete taken as the average tested value for SRC-W3, which was 4.67 ksi. The M_y indicated here was based on reaching 70 ksi, the expected yield strength of A615 Grade 60 reinforcement (PEER TBI, 2017), in the outermost longitudinal reinforcement. The tested yield strength of the reinforcement was not used here, since the demands were less than yielding.

Measured torsional rotation at the point of load application in the test beams is provided in Figure 4.16 through Figure 4.19. This torsional rotation was determined from two LVDTs located at opposite beam faces and both located at the point of load application. Torsional rotation was smaller for SRC-W1 than the other three tests. For SRC-W2 and SRC-W3, the torsional rotation remained relatively small through the pre-yielding load-controlled cycles but grew larger during the displacement-controlled cycles. After the cycles at $1.5\theta_y$ for SRC-W2, a brace was installed on the beam to mitigate additional torsion. The brace was used for SRC-W3 and SRC-W4 for the duration of the test, and the torsion was less for SRC-W3 than SRC-W2. The peak measured torsional rotation was 1.8% for SRC-W2 and 0.94% for SRC-W3. The peak measured torsional rotation for SRC-W4 reached 1.1% during the $0.4M_{pbe}$ cycles and 1.8% overall. The larger torsional rotation for SRC-W4 than SRC-W3 was potentially due to wall damage.

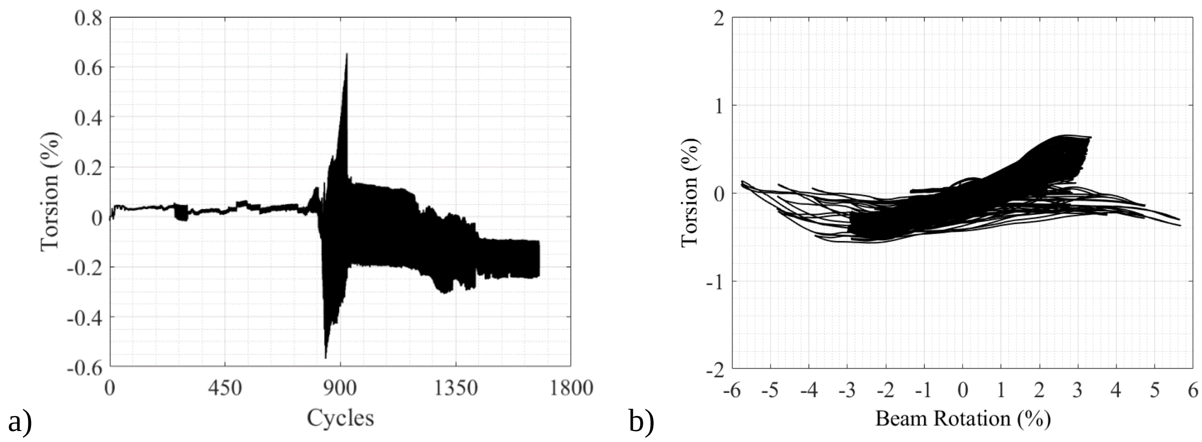

Figure 4.16. Measured Torsion in SRC-W1 at the Point of Shear Load Application Relative to a) Cycle Number, and b) Beam Rotation

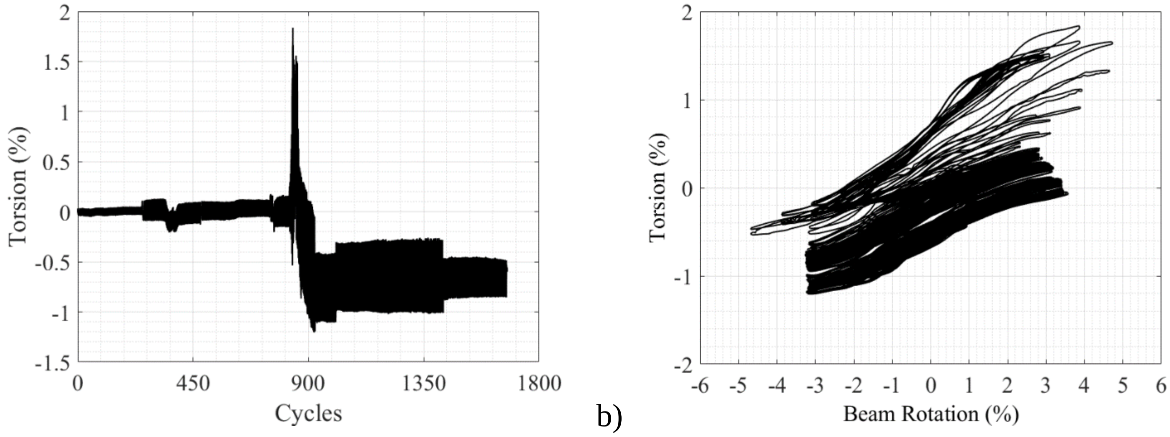

a) b)

Figure 4.17. Measured Torsion in SRC-W2 at the Point of Shear Load Application Relative to a) Cycle Number, and b) Beam Rotation

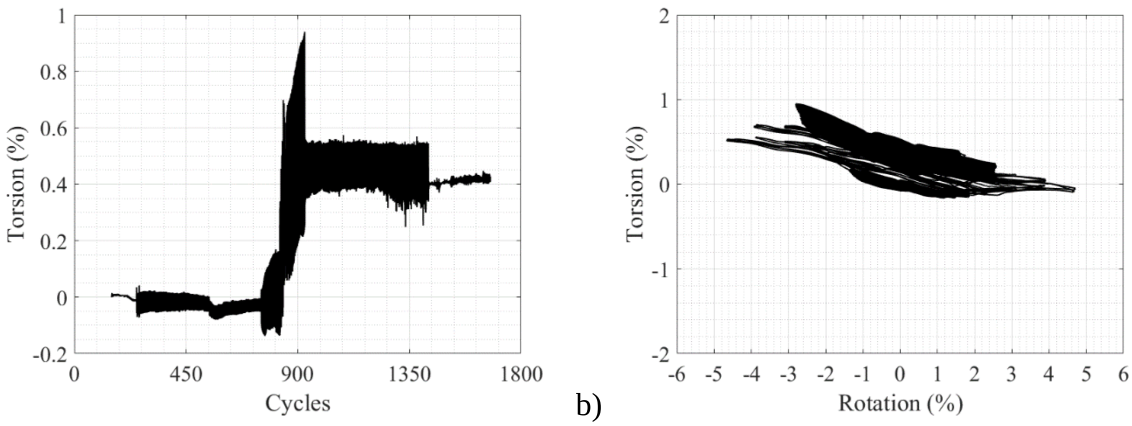

a) b)

Figure 4.18. Measured Torsion in SRC-W3 at the Point of Shear Load Application Relative to a) Cycle Number, and b) Beam Rotation

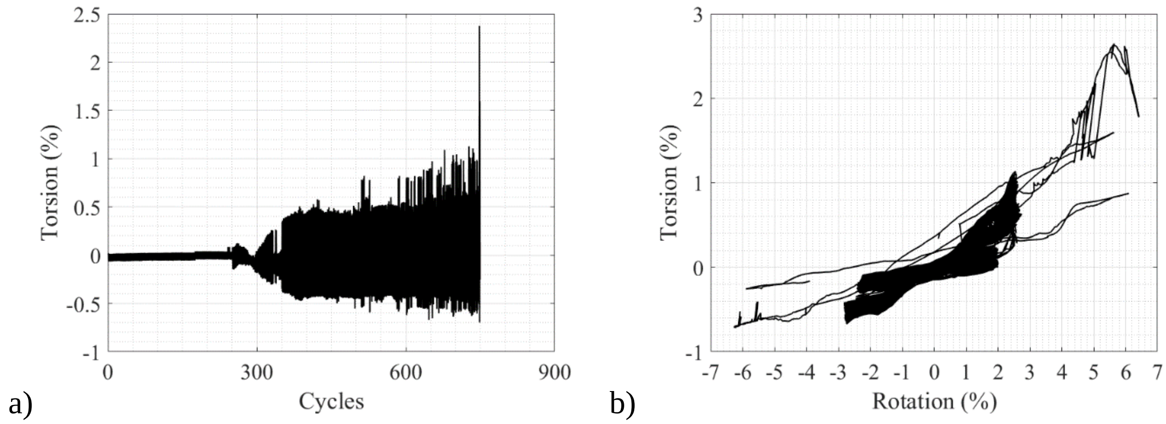

Figure 4.19. Measured Torsion in SRC-W4 at the Point of Shear Load Application Relative to a) Cycle Number, and b) Beam Rotation

4.3. Dissipated Energy

Plots of the cumulative dissipated energy and dissipated energy per cycle are provided in Figure 4.20 for the four tests, with the average dissipated energy per cycle at each loading increment provided in Table 4.6. Dissipated energy was computed as the area enclosed by the load-deformation hysteretic loops in Figure 4.14, with the chord rotation converted to beam displacement at the point of loading application. The dissipated energy per cycle was reasonably consistent for SRC-W1, SRC-W2, and SRC-W3 during the load-controlled cycles. During the displacement-controlled cycles, the energy dissipation was largest for SRC-W1 due to the larger yield displacement and resulting larger chord rotations in the testing protocol. The energy dissipation for SRC-W2 was smaller than SRC-W3 during the displacement-controlled cycles but significantly larger during the subsequent 75 cycles at 0.75M_{pbe}. The total energy dissipated for SRC-W2 at the completion of testing was larger despite the slightly increased level of pinching evident in the hysteric plots in Figure 4.14. The dissipated energy per cycle was highest for SRC-W4 likely due to energy being dissipated in the connection, as beam chord rotation and damage at the connection increased during repeated loading cycles significantly more than in the other three tests. The increase in cumulative dissipated energy for the two cycles to 6.0% rotation was relatively minor relative to the increase in dissipated energy over repeated cycles at $0.4M_{pbe}$. The total cumulative dissipated energy was significantly less for SRC-W4 than the other three tests at the completion of testing, despite SRC-W4 being the only test that reached 6.0% chord rotation. The poor energy dissipation for SRC-W4 was a result of the damage at the connection.

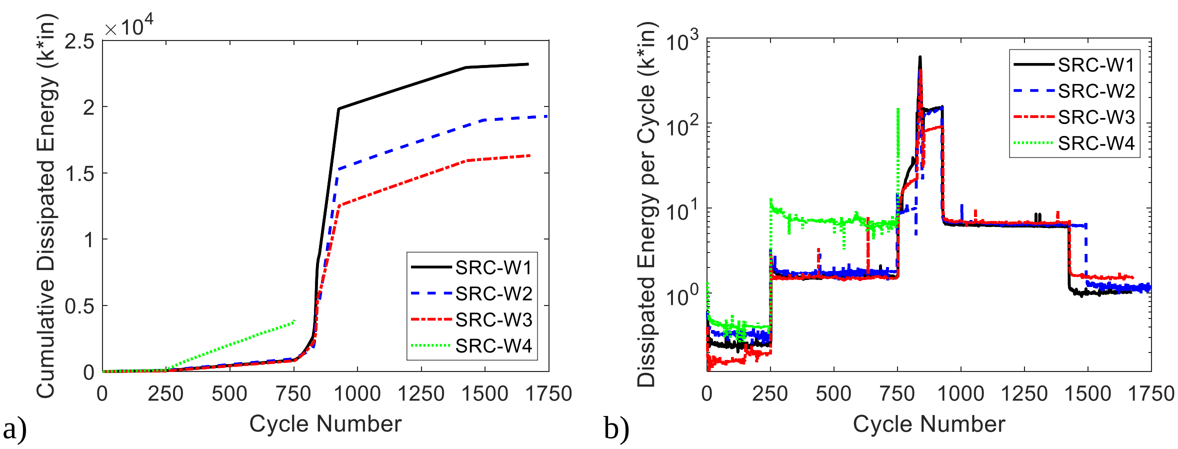

Figure 4.20. a) Cumulative Dissipated Energy, and b) Dissipated Energy per Cycle

Table 4.6. Average Dissipated Energy per Cycle at Each Loading Increment

Loading Increment	Average Dissipated Energy per Cycle (k*in^2)			
	SRC-W1	SRC-W2	SRC-W3	SRC-W4
$0.15M_{pbe}$	0.25	0.33	0.17	0.41
$0.40M_{pbe}$	1.60	1.74	1.53	7.16
$0.75M_{pbe}$	23.7	9.5	17.9	NA
$1.2\theta_y$	113.2	48.8	59.9	NA
$1.5\theta_y$	197.3	99.4	111.3	NA
$2.0\theta_y$	329.2	195.5	209.6	NA
$2.5\theta_y$	463.6	297.4	319.6	NA
$3.0\theta_y$	600.1	401.1	430.0	NA
$2.5\theta_y$	450.3	270.8	302.7	NA
$2.0\theta_y$	288.7	150.9	170.8	NA
$1.5\theta_y$	147.0	59.7	74.5	NA
$1.2\theta_y$	79.3	25.9	32.5	NA
$0.75M_{pbe}$	145.8	134.6	86.2	NA
$0.40M_{pbe}$	6.30	6.59	6.83	NA
$0.15M_{pbe}$	1.02	1.19	1.55	NA

4.4. Moment-Rotation

Moment-rotation at the beam-wall interface is provided in Figure 4.21. The characteristics of the hysteretic plots are similar to those of the load-deformation plots in Figure 4.14. The majority of the beam deformation was from interface rotation. More information on sources of deformation is provided in Section 4.6. Much of the rotation at the beam-wall interface comes from slip of the embedded steel section. Rotation measured at the first location entirely within the beam span is provided in Figure 4.22 and provides a better indication of the bending in the beam. This location was centered at 9” from the beam-wall interface, as shown in Figure 3.16. Minimal rotation was measured at this location, suggesting that the majority of the measured rotation at the beam-wall interface was due to slip.

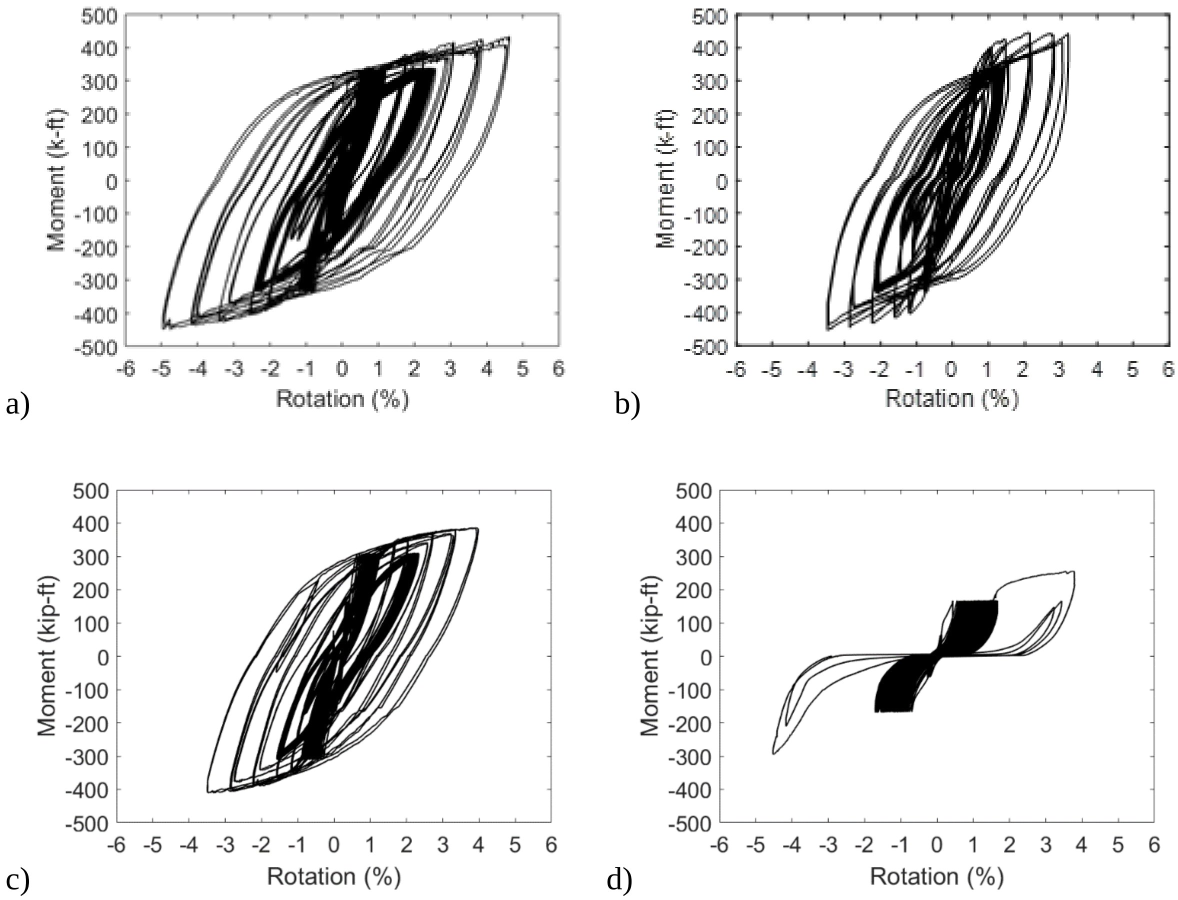

Figure 4.21. Moment-Rotation at Beam-Wall Interface for a) SRC-W1, b) SRC-W2, c) SRC-W3, and d) SRC-W4

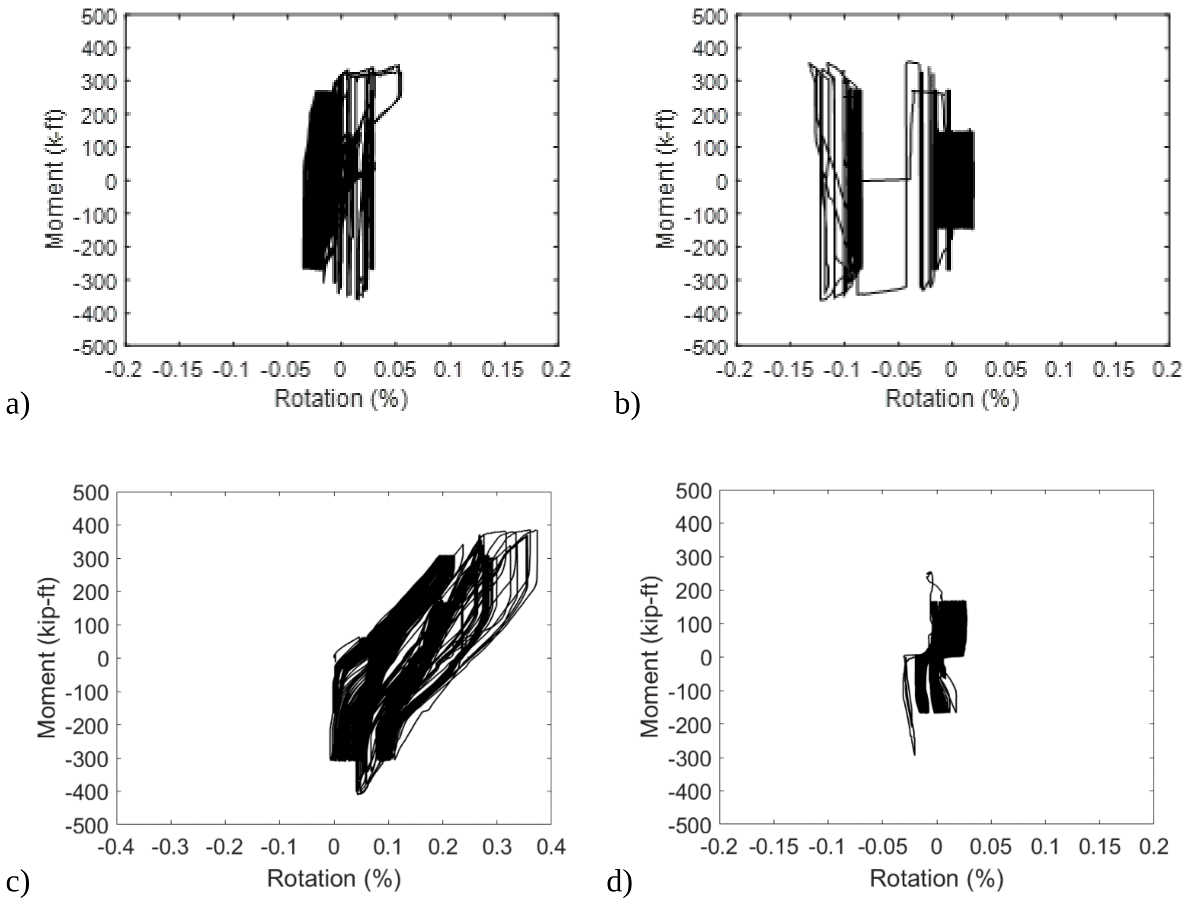

Figure 4.22. Moment-Rotation at First Sensor Location in Beam for a) SRC-W1, b) SRC-W2, c) SRC-W3, and d) SRC-W4

4.5. Axial Elongation and Axial Load

Plots of axial load versus coupling beam rotation are provided in Figure 4.23. The initial axial load was roughly 2.0 kips, as this was needed to hold the axial restraint system in place prior to the start of testing. For the first half of the testing protocol, the increase in axial load with beam deformation was roughly linear for SRC-W1 and SRC-W2 but not SRC-W3. Increase in axial load for repeated loading cycles at a given increment was more significant for SRC-W3 than SRC-W1 and more significant for SRC-W1 than SRC-W2. The axial load did not exceed 15 kips and was less than $0.015A_g f'_{c,test}$ for all four tests, where A_g is the gross area of the beam cross-section. Plots of axial elongation versus coupling beam rotation are provided in Figure 4.24. The axial elongation did not exceed 1.0" in any test. This was less than that measured for SRC1 and SRC2, without axial restraint, tested by Motter et al (2017a), although these two beams were tested to higher levels of chord rotation. The increase in axial elongation with repeated loading cycles at a given increment was less for SRC-W1, SRC-W2, SRC-W3, and SRC-W4 with axial restraint than for SRC1 and SRC2 without axial restraint.

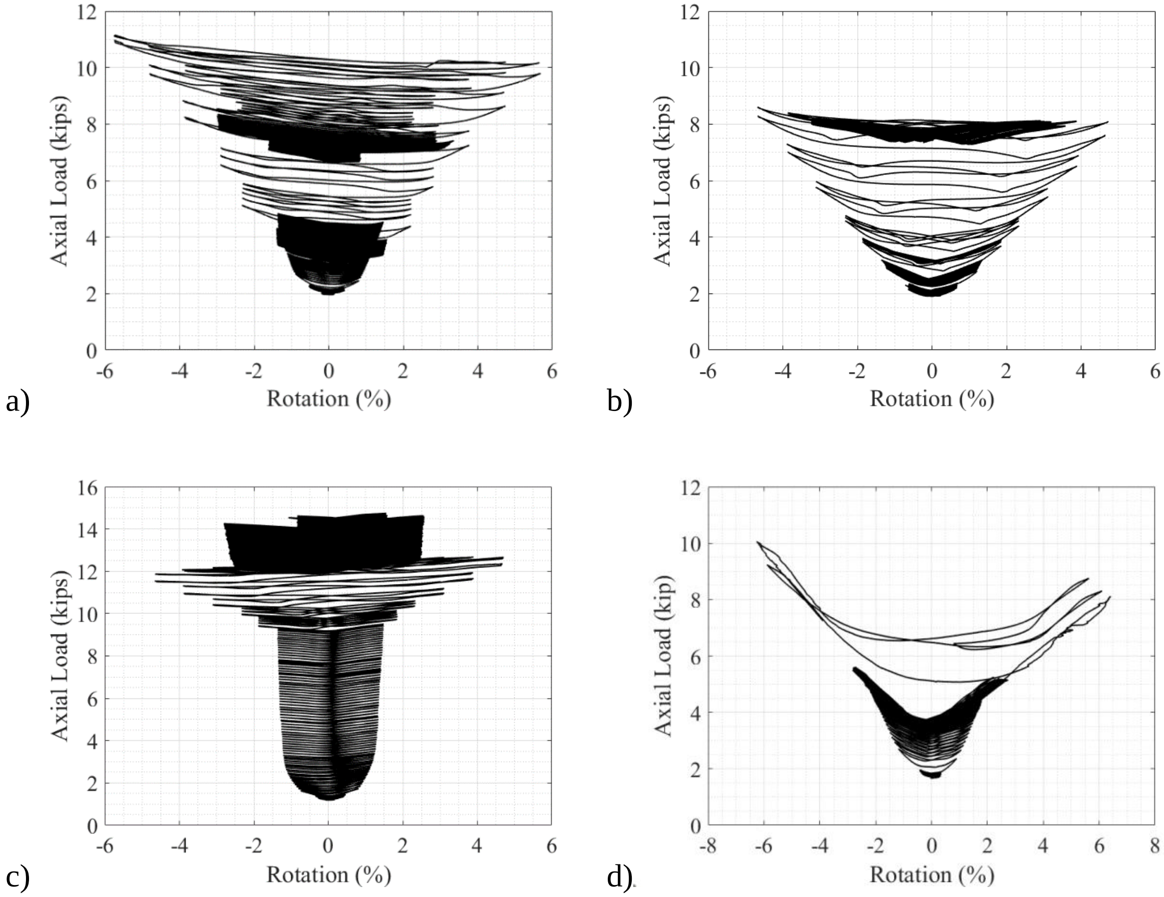

Figure 4.23. Axial Load versus Rotation for a) SRC-W1, b) SRC-W2, c) SRC-W3, and d) SRC-W4

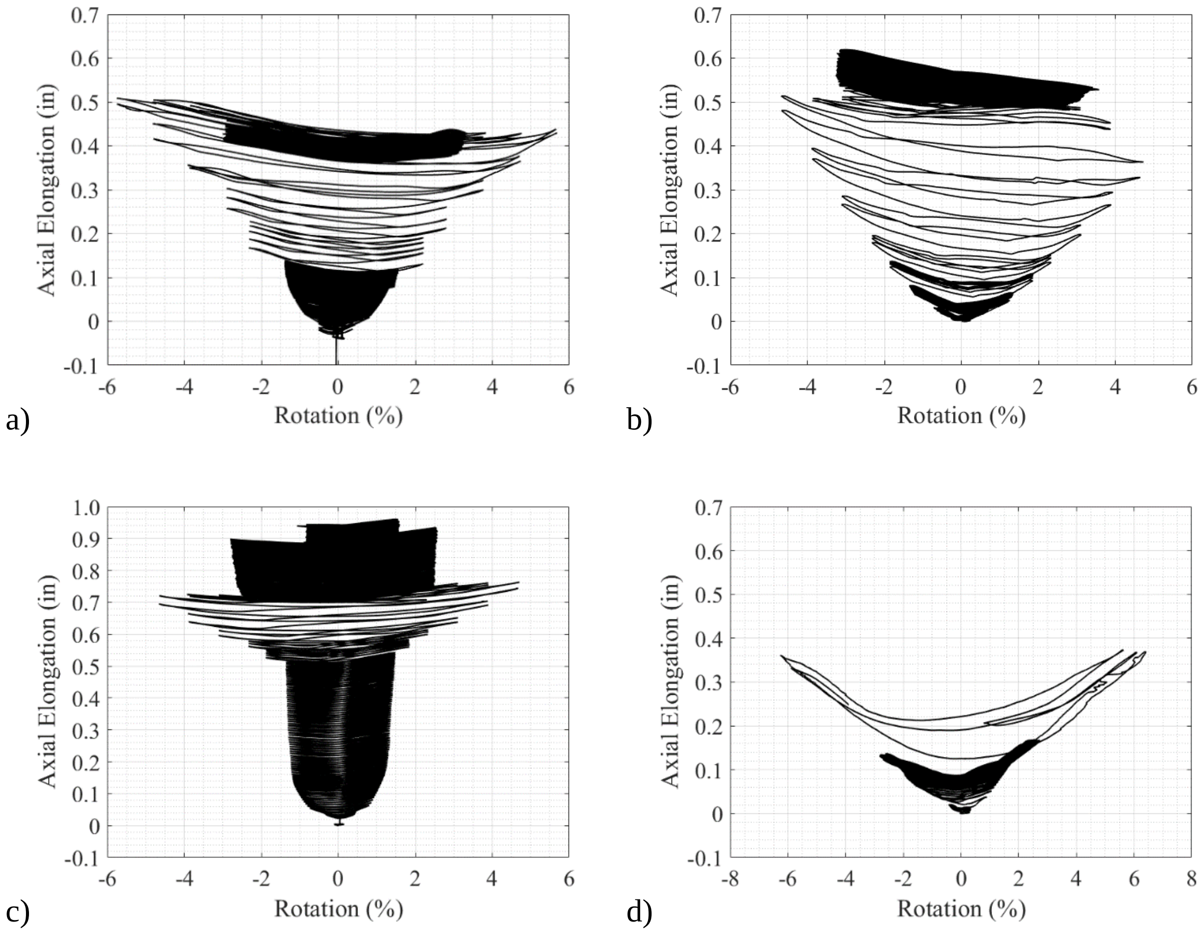

Figure 4.24. Axial Elongation versus Rotation for a) SRC-W1, b) SRC-W2, c) SRC-W3, and d) SRC-W4

4.6. Components of Beam Deformation

The components of beam deformation are provided in Figure 4.25 for SRC-W1, SRC-W2, and SRC-W3 for the first cycle of each cycle group. The slip component was taken as the rotation measured at the beam-wall interface multiplied by the 30” span length. Although the sensors at this location spanned 6”, measured deformation in the beam span was minimal, as indicated by the flexural deformation in Figure 4.25 and as described in Section 4.4, suggesting that the majority of the deformation at the beam-wall interface was due to slip. The flexural deformation was determined through integration of the curvature measured along the length of the beam, with average curvature used over the length of sensor pairs. This was achieved by multiplying the rotation from each pair of sensors located fully within the beam span by the length from the midpoint of the sensor pair to the point of load application and summing the resulting deformations. The exception was the sensor pair located closest to the point of load application, in which the rotation was multiplied by two-thirds of the sensor lengths rather than one-half of the sensor lengths. The shear deformation was determined using the procedure described by Massone and Wallace (2004), in which geometry is used to remove the measured flexural deformation from the measured values in a pair of diagonal sensors to determine the resulting shear deformation over the length of the pair of diagonal sensors. The component labeled “Other” in Figure 4.25 was determined as the difference between the beam displacement and the combined displacement from slip, flexure, and shear.

It is evident from the plots in Figure 4.25 that the majority of the beam deformation was due to slip. This is consistent with results reported by Motter et al (2017a). For SRC-W1 and SRC-W3, the slip was larger in the positive than negative loading direction, and the “Other” component was larger in the negative than the positive direction. The slip component exceeded 100% in the positive loading direction, corresponding with the “Other” component providing a negative contribution. This is consistent with the behavior observed for SRC2 reported by Motter et al (2013). This behavior may be indicative of more beam plasticity at the beam-wall interface in the positive than negative loading direction, suggesting that plasticity may be moving into the embedment in the negative loading direction due to wall tension at the embedment region. This was associated with a reduction in the force developed in the negative loading direction relative to the positive loading direction for SRC2 but not for SRC-W1 and SRC-W3. For SRC-W2, components of deformation were more symmetric, consistent with SRC1 tested by Motter et al (2017a). The lower wall moments for SRC-W2 relative to SRC-W1 and the increased wall reinforcement for SRC-W2 relative to SRC-W3 may have contributed to this behavior.

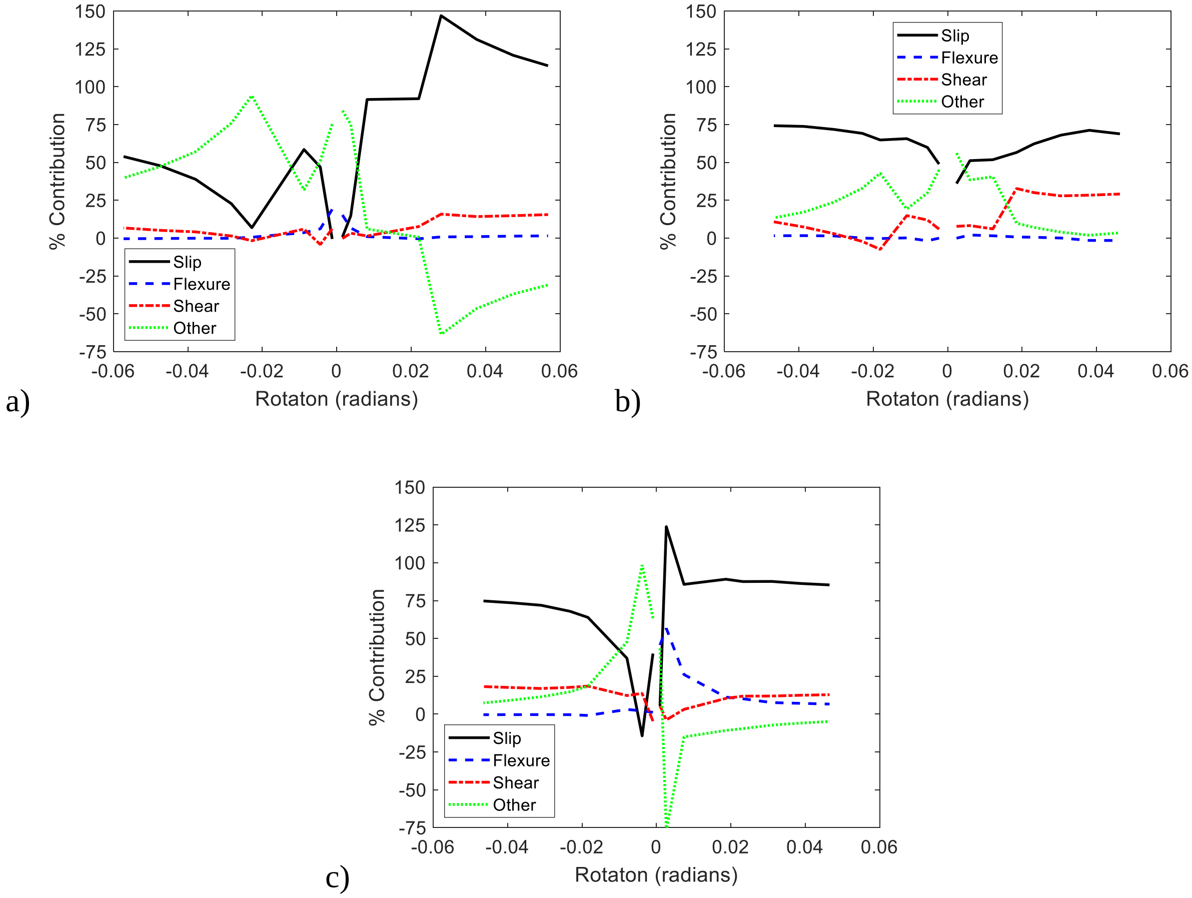

Figure 4.25. Components of Deformation for a) SRC-W1, b) SRC-W2, c) SRC-W3

4.7. Wall Load-Deformation

Plots of wall load-deformation are provided in Figure 4.26. Rotation was determined using measured data from two LVDTs, one near each edge of the wall, spanning the clear height of the wall from the top of the bottom block to the bottom of the top block. The rotation is provided in the plots as radians times 100%. It is evident from the plots that deformation in the wall was minimal relative to rotational demand in the test beams for SRC-W1, SRC-W2, and SRC-W3. For SRC-W4, the rotation in the wall was significant, reaching 0.49% during the 500 cycles at $0.4M_{pbe}$ and reaching 1.30% during the two subsequent cycles to 6.0% coupling beam chord rotation. The wall ratcheted in one direction, with tension on the side of the wall with the test beam, as the beam pried the wall at the connection. As noted in Section 3.6, a correction was made to beam rotation to account for wall rotation. Based on the measured wall rotation shown in Figure 4.26, this correction was small for SRC-W1, SRC-W2, and SRC-W3 but more significant for SRC-W4. The peak measured wall rotation for SRC-W1, SRC-W2, and SRC-W3 was less than that measured for SRC1 tested by Motter et al (2017a). The peak measured wall rotation for SRC-W4 was comparable to that for SRC4 tested by Motter et al (2017a). Buckling of longitudinal reinforcement in the wall was not observed for SRC-W4, suggesting that local tension demands created in the wall by the SRC coupling beam may have exceeded the compressive demands due to applied wall demand. Buckling of longitudinal reinforcement in the wall was observed for SRC4, which had larger moment applied to the wall than SRC-W4. Although ratcheting was evident in the wall load-deformation response for both tests, the difference in wall rotation for positive and negative cycles was more significant for SRC4, likely due to the larger wall demands.

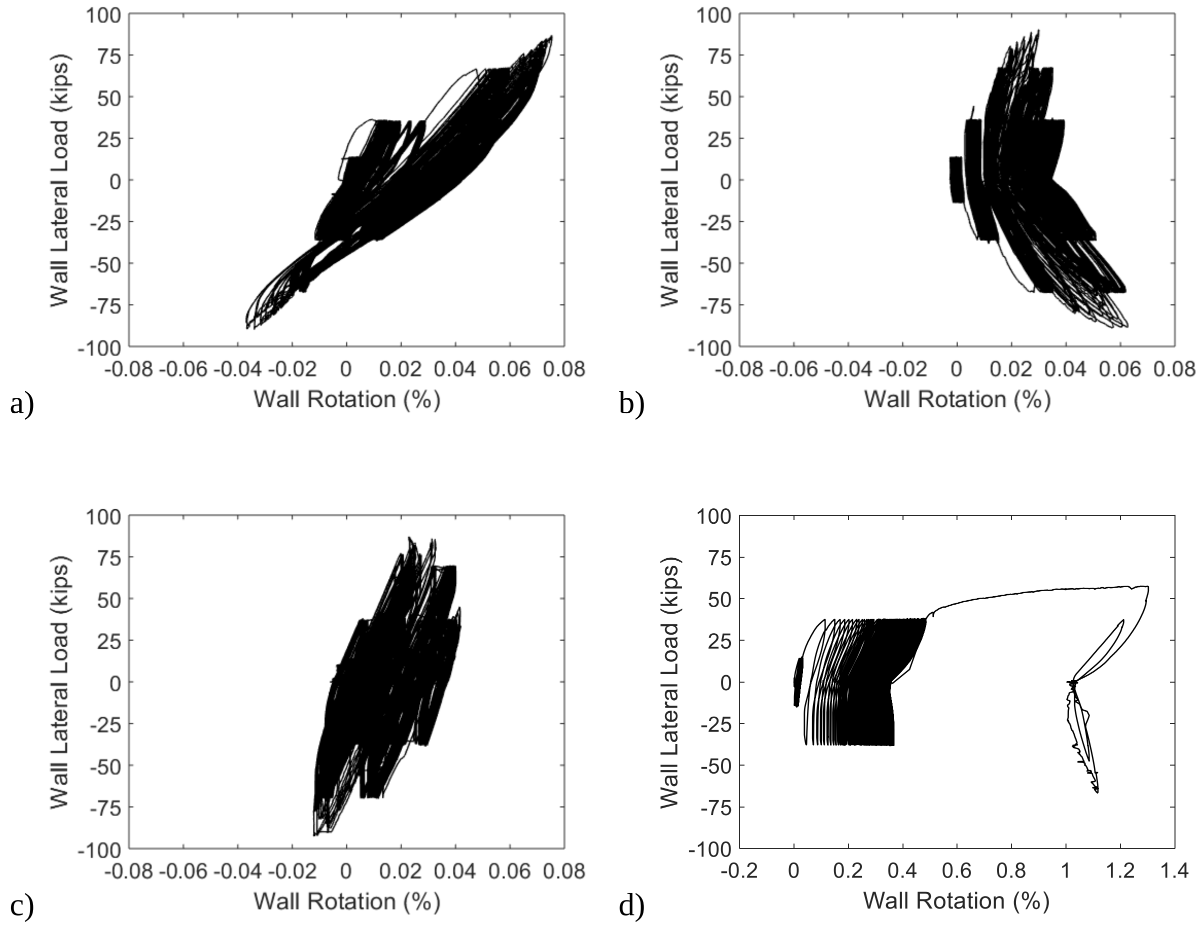

Figure 4.26. Wall Rotation for a) SRC-W1, b) SRC-W2, c) SRC-W3, and d) SRC-W4

It was shown in Section 4.2 that stiffness degradation was significant in the beams within groups of cycles prior to yielding, particularly during the 75 cycles at $0.75M_{pbe}$ for SRC-W1, SRC-W2, and SRC-W3 and during the cycles at lower levels for SRC-W4. For SRC-W1, SRC-W2, and SRC-W3, plots of secant stiffness during the first group of 75 cycles at $0.75M_{pbe}$ for both the wall and the beams are provided in Figure 4.27, with the wall secant stiffness determined from the data in Figure 4.26. The stiffness values provided in Figure 4.27 were normalized to the stiffness of the final cycle in this group of 75. It is evident from the data shown in Figure 4.27 that stiffness degradation at this loading level was most significant in the beam for SRC-W1 and SRC-W3. The stiffness degradation for the wall was larger for SRC-W2 than SRC-W1 over the first 15 cycles in this group, with much of this difference coming from the first to second cycles. The level of stiffness degradation in the beam for SRC-W2 was comparable to that in the wall during testing of SRC-W1. The level of stiffness degradation in the wall for SRC-W3 was lower than that for SRC-W1 and SRC-W2, as degradation of stiffness in the wall did not occur for SRC-W3 over these 75 cycles.

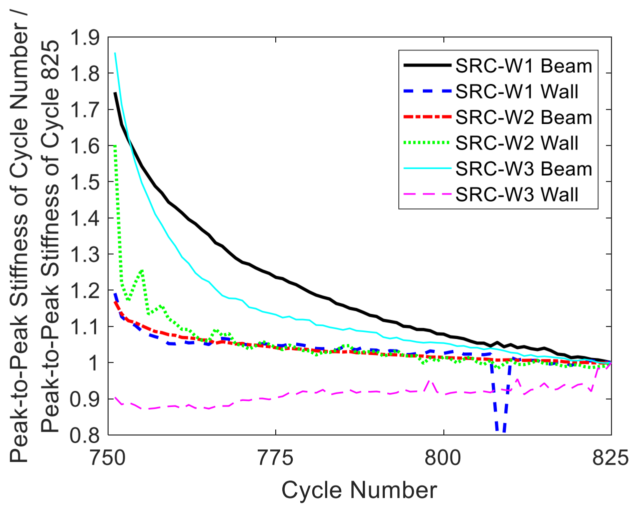

Figure 4.27. Stiffness Degradation during First Group of 75 Cycles at $0.75M_{pbe}$

4.8. Wall Strain Profiles

Wall strain profiles, based on LVDT measurements, at the locations shown in Figure 3.16 are provided in Figure 4.28 through Figure 4.35. The strain profiles were formulated using strain values at the peak of each first cycle at each increment of load or displacement applied. The plots for SRC-W2 and SRC-W4 do not include residual strain after completion of testing of SRC-W1 and SRC-W3, respectively, as some LVDT locations changed within the wall between tests to accommodate the consistent LVDT layout relative to the test beam, as shown in Figure 3.16. Plane-section behavior is often not evident in Figure 4.28 through Figure 4.31, with larger strains measured at the end of the wall with the embedded beam. For SRC-W1, SRC-W2, and SRC-W3, the measured strains were generally less than the yield strain, which was computed for each test based on the measured yield stress in the reinforcement, provided in Table 3.2, and an elastic modulus for steel of 29,000 ksi. The peak compressive strains occurred in the vicinity of the embedded steel section and approached the yield strain for the three tests. For SRC-W4, yielding was measured in compression at locations below the coupling beam, and yielding was measured in tension at locations in Row 3 through Row 8. The majority of these locations were above and below the embedded steel section, but there were also locations on the other side of the wall. The largest tensile strains for this beam were measured at Row 5, the location at which the sensors spanned across the embedded steel section, and reached peak values between 5% and 6% at locations closest to the beam-wall interface.

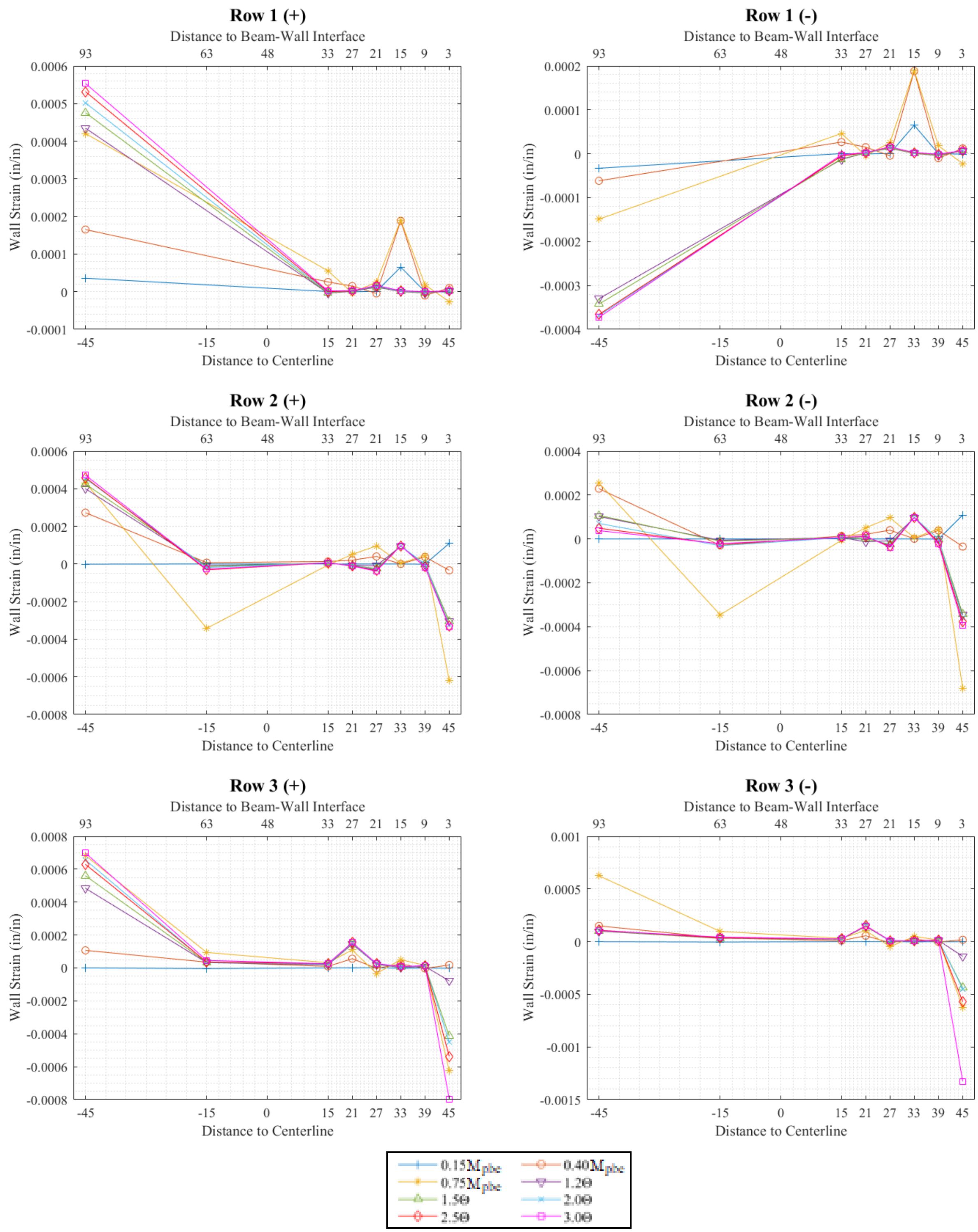

Figure 4.28. Wall Strain along Cross-Sections for SRC-W1

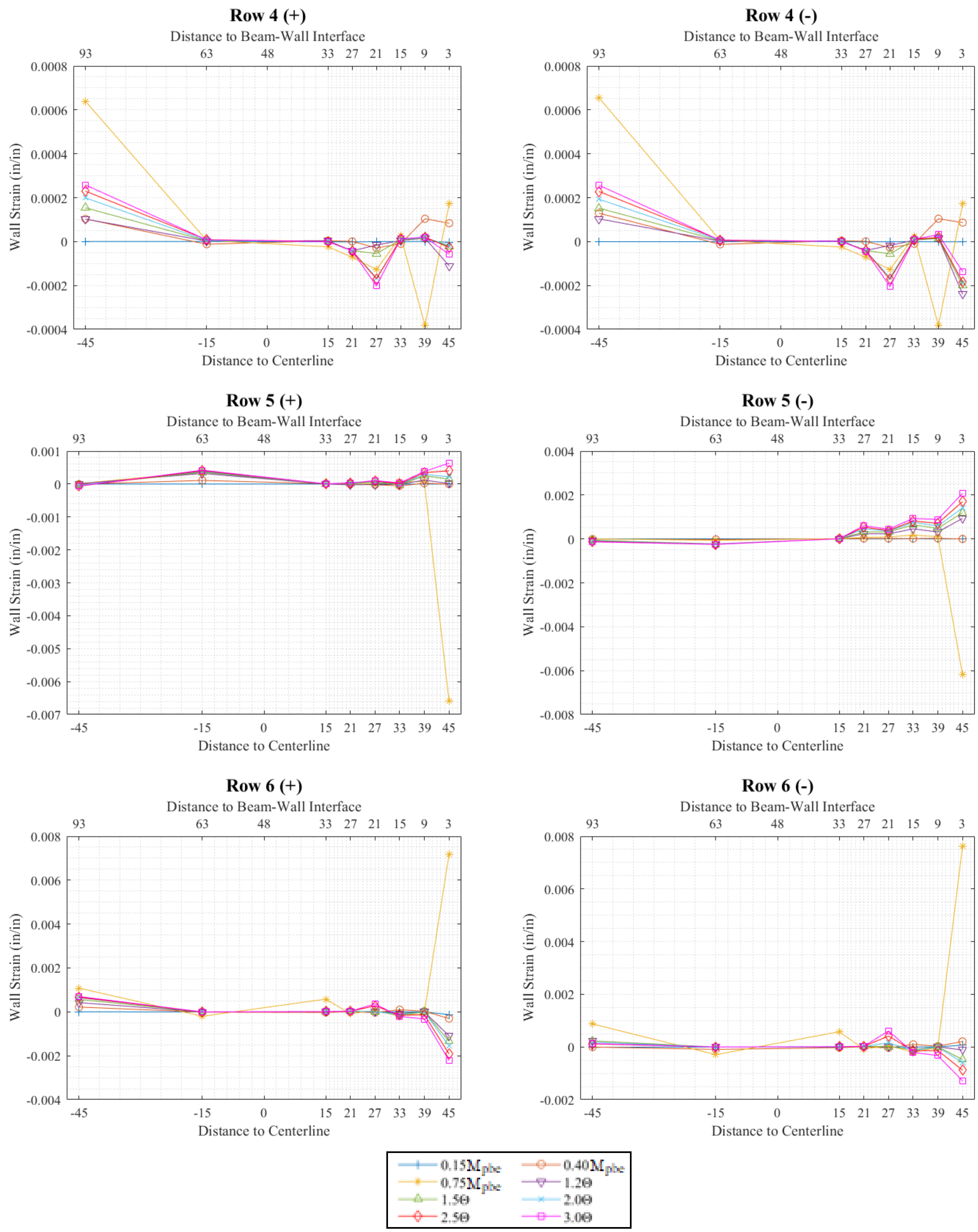

Figure 4.28. Wall Strain along Cross-Sections for SRC-W1 (continued)

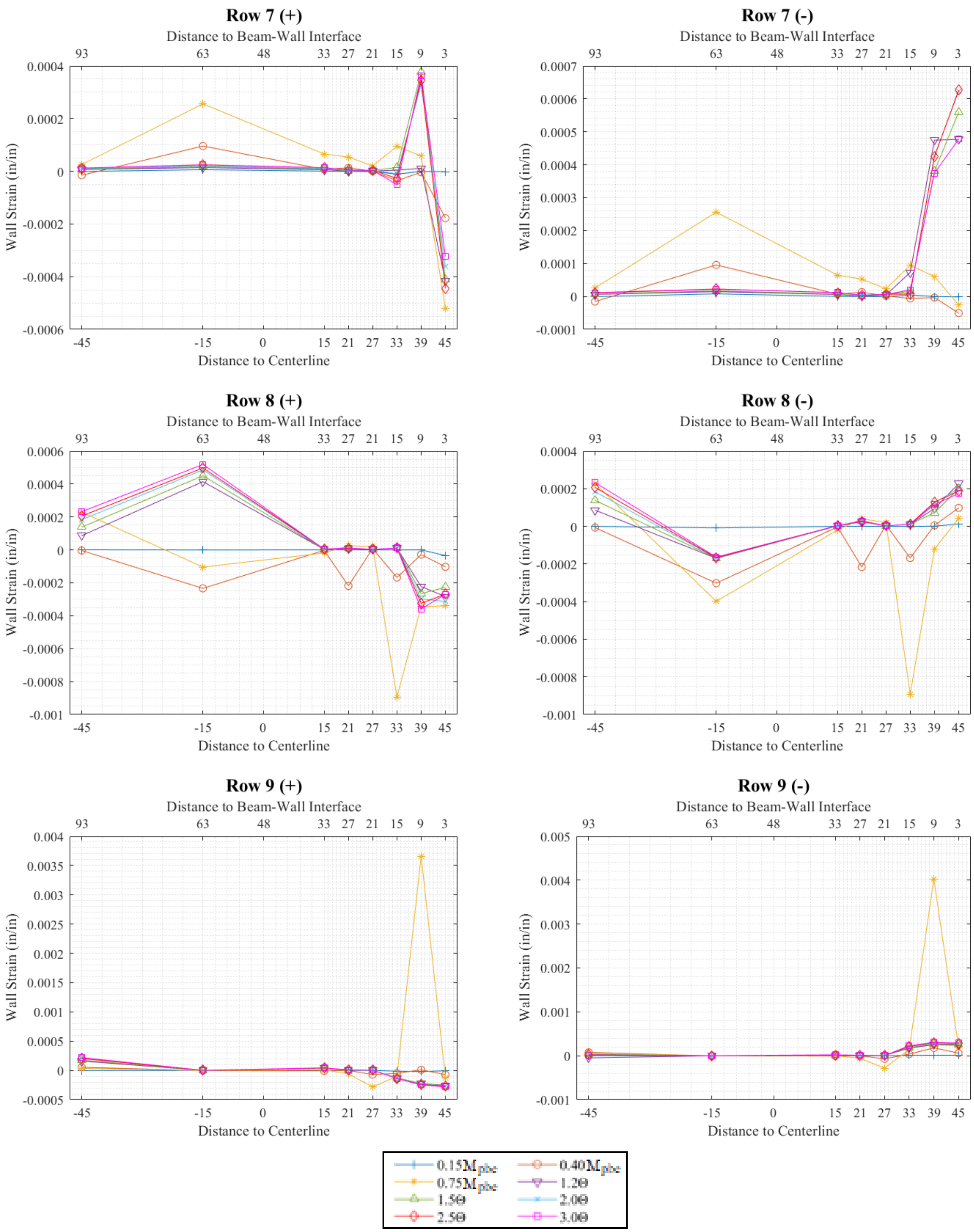

Figure 4.28. Wall Strain along Cross-Sections for SRC-W1 (continued)

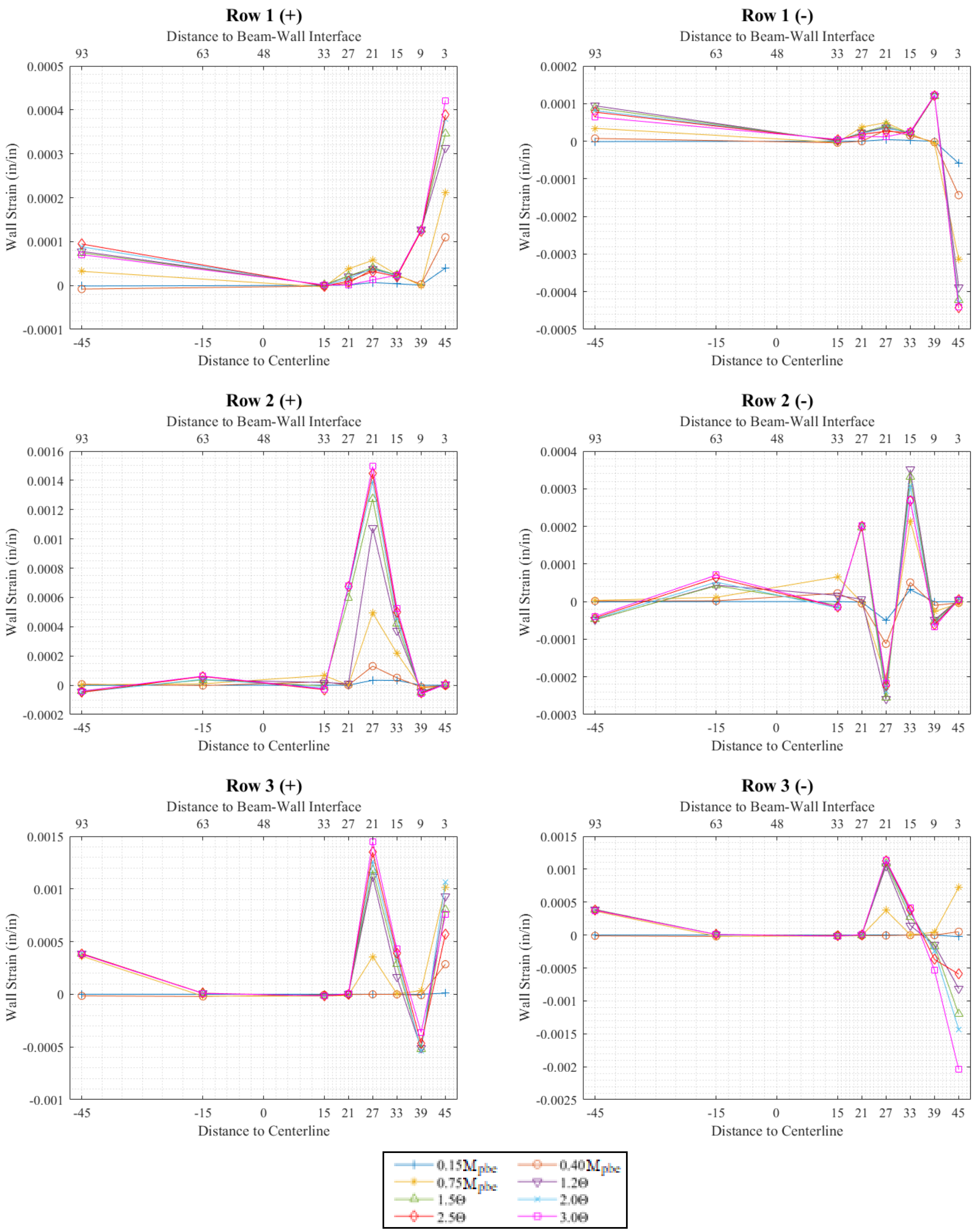

Figure 4.29. Wall Strain along Cross-Sections for SRC-W2

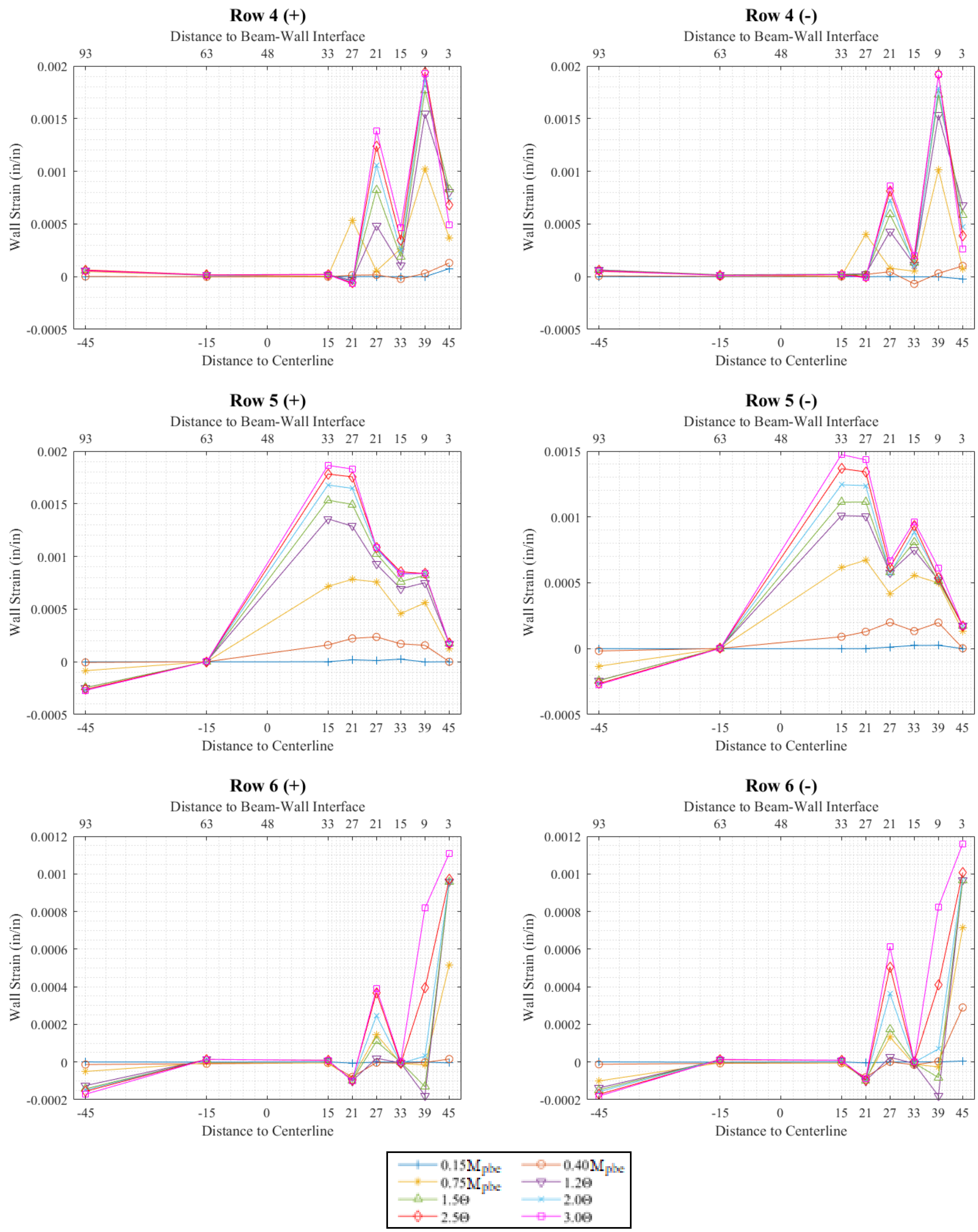

Figure 4.29. Wall Strain along Cross-Sections for SRC-W2 (continued)

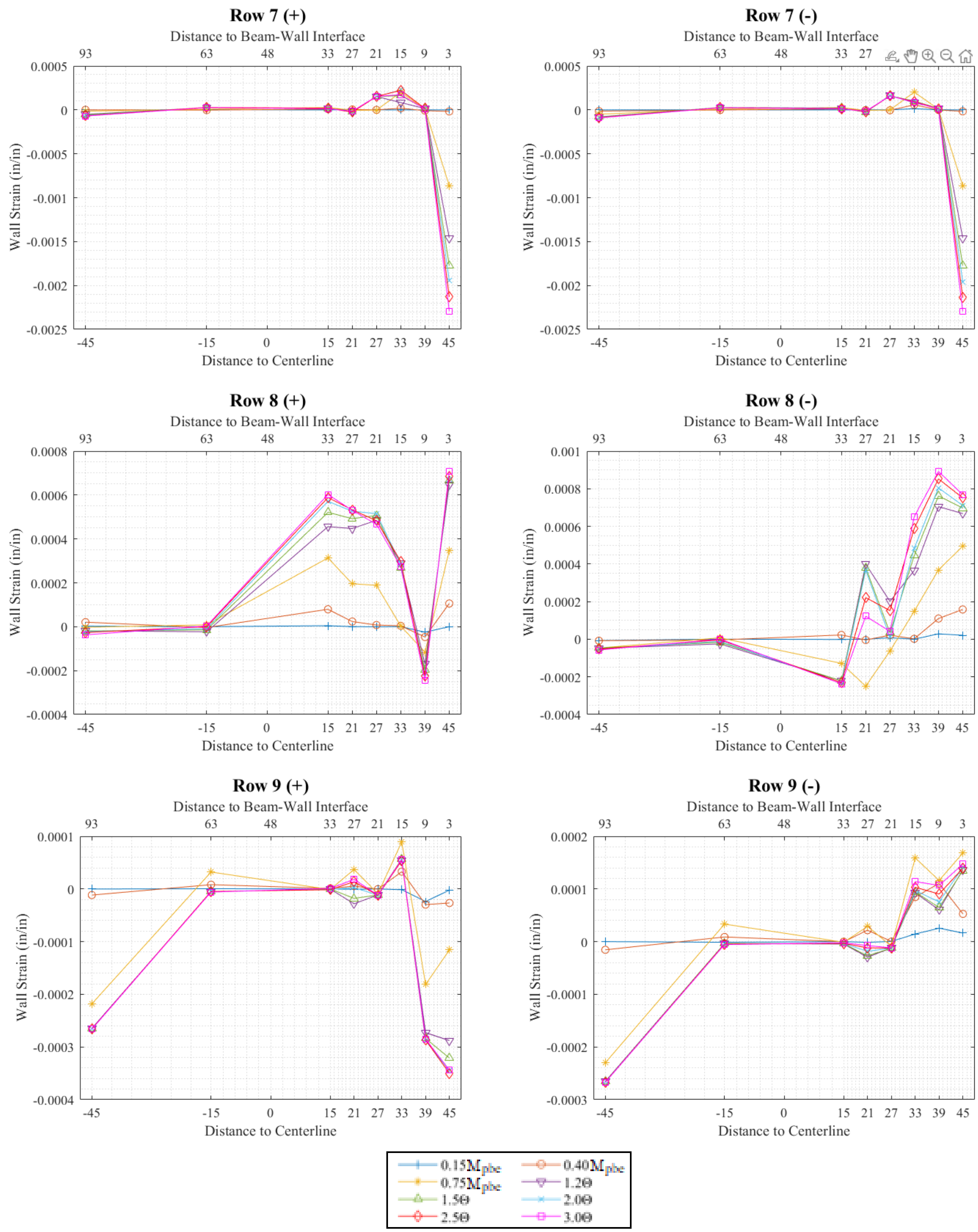

Figure 4.29. Wall Strain along Cross-Sections for SRC-W2 (continued)

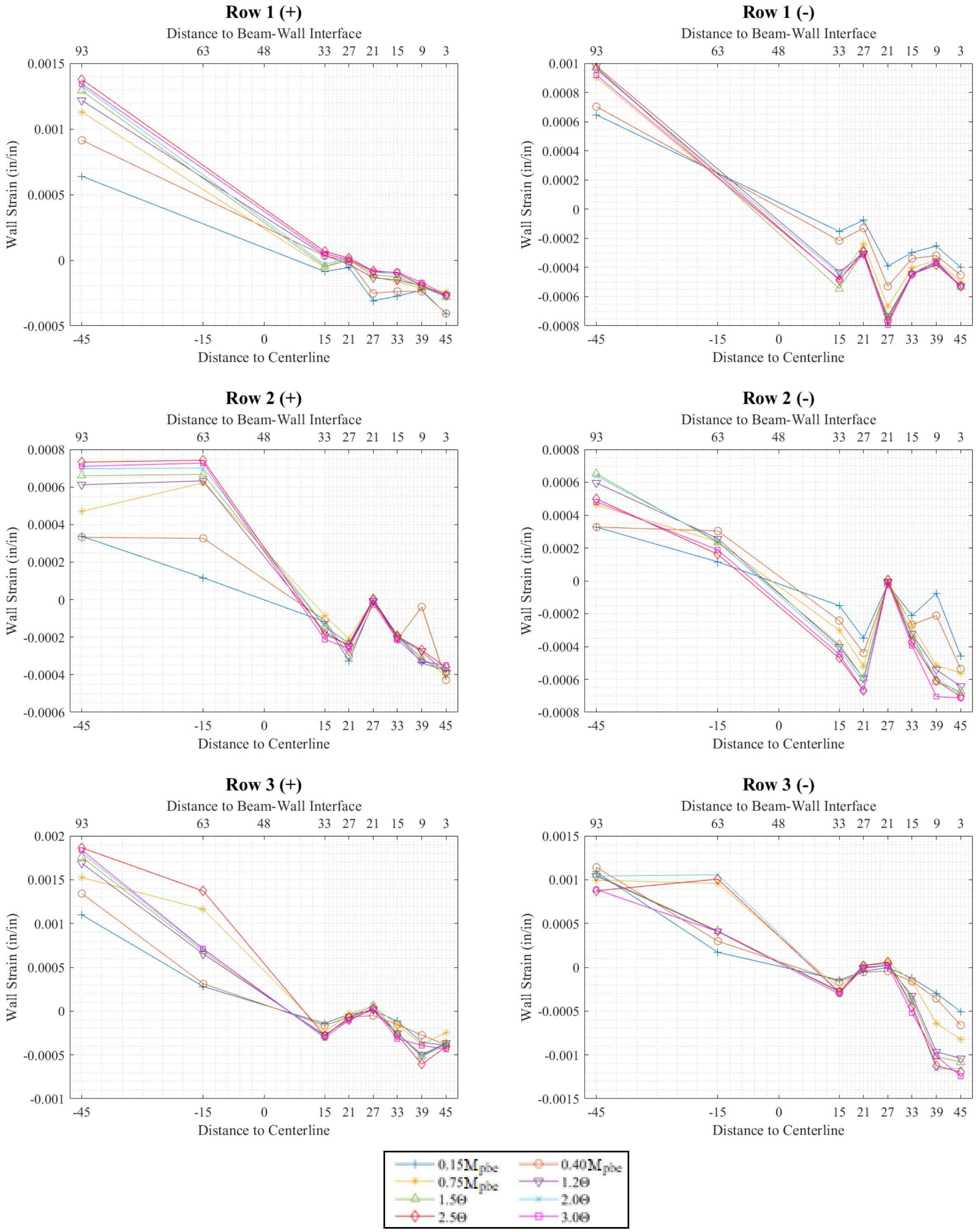

Figure 4.30. Wall Strain along Cross-Sections for SRC-W3

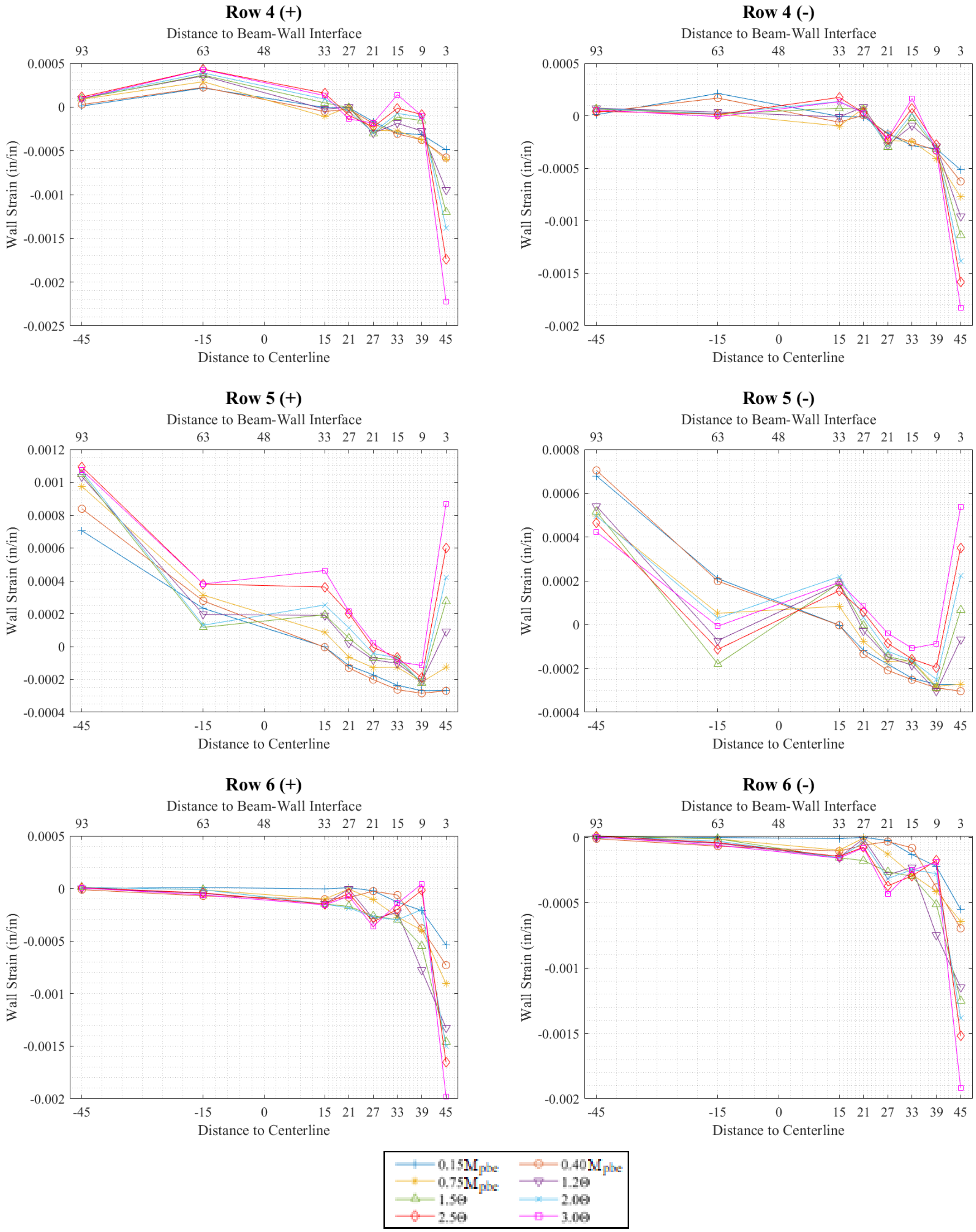

Figure 4.30. Wall Strain along Cross-Sections for SRC-W3 (continued)

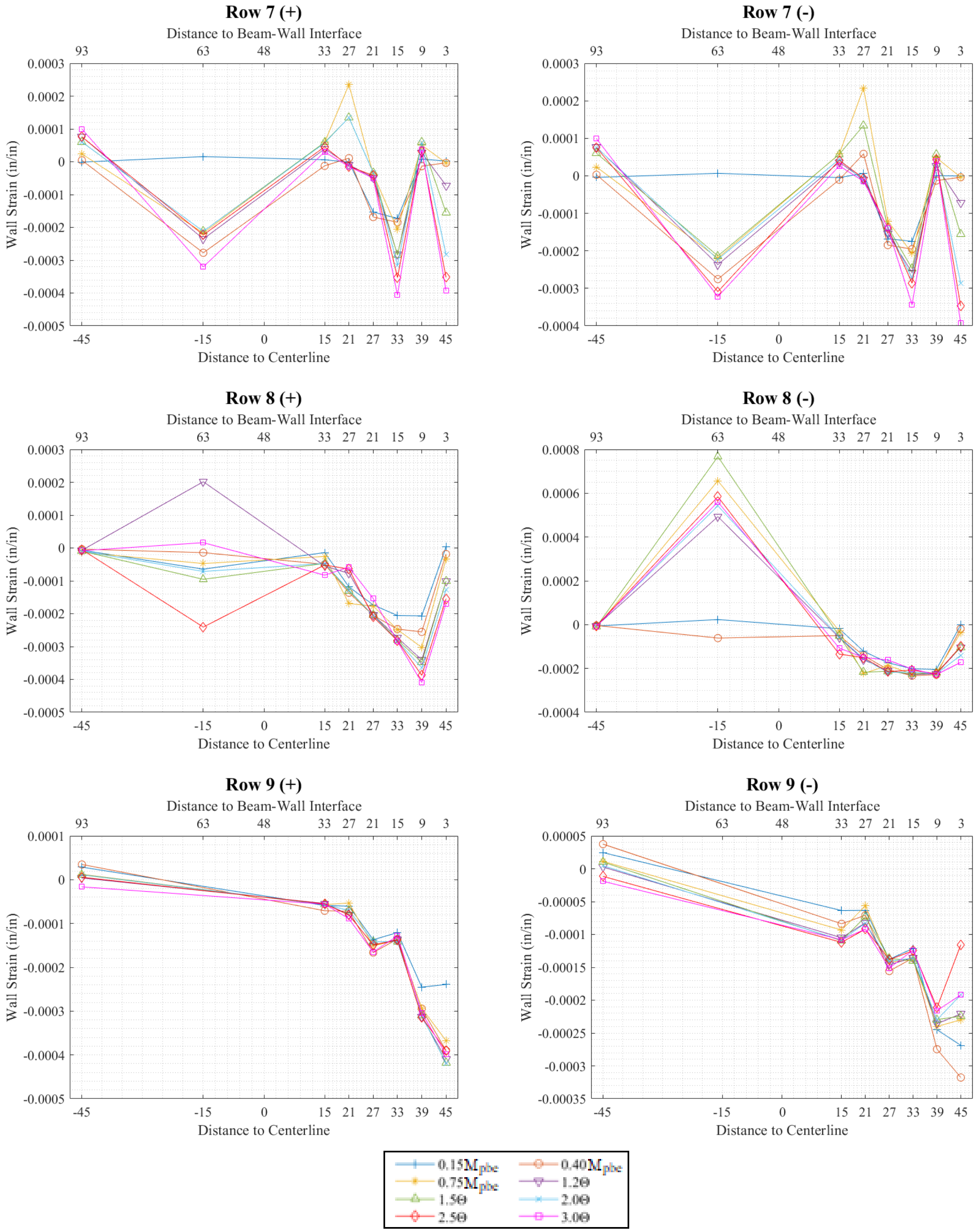

Figure 4.30. Wall Strain along Cross-Sections for SRC-W3 (continued)

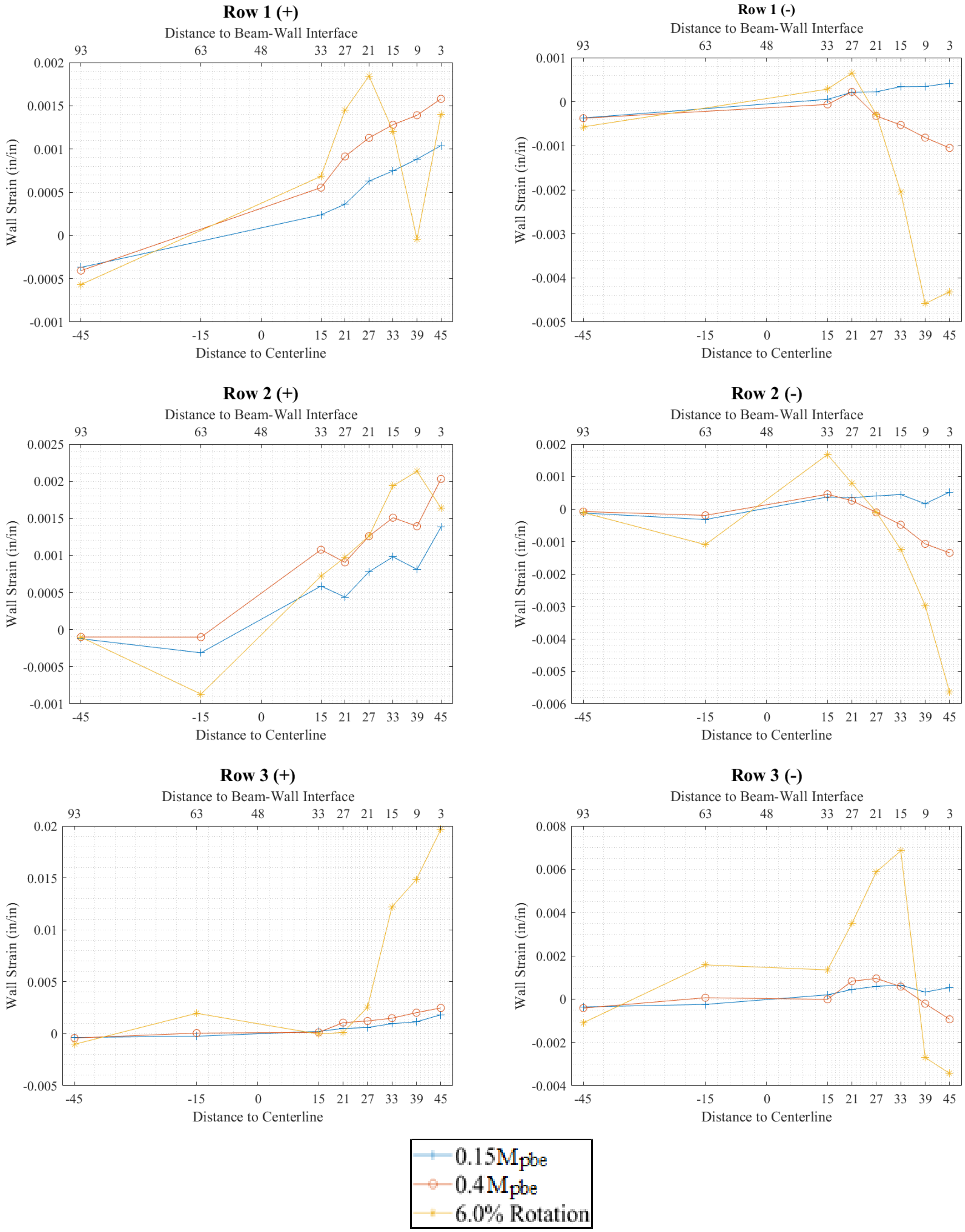

Figure 4.31. Wall Strain along Cross-Sections for SRC-W4

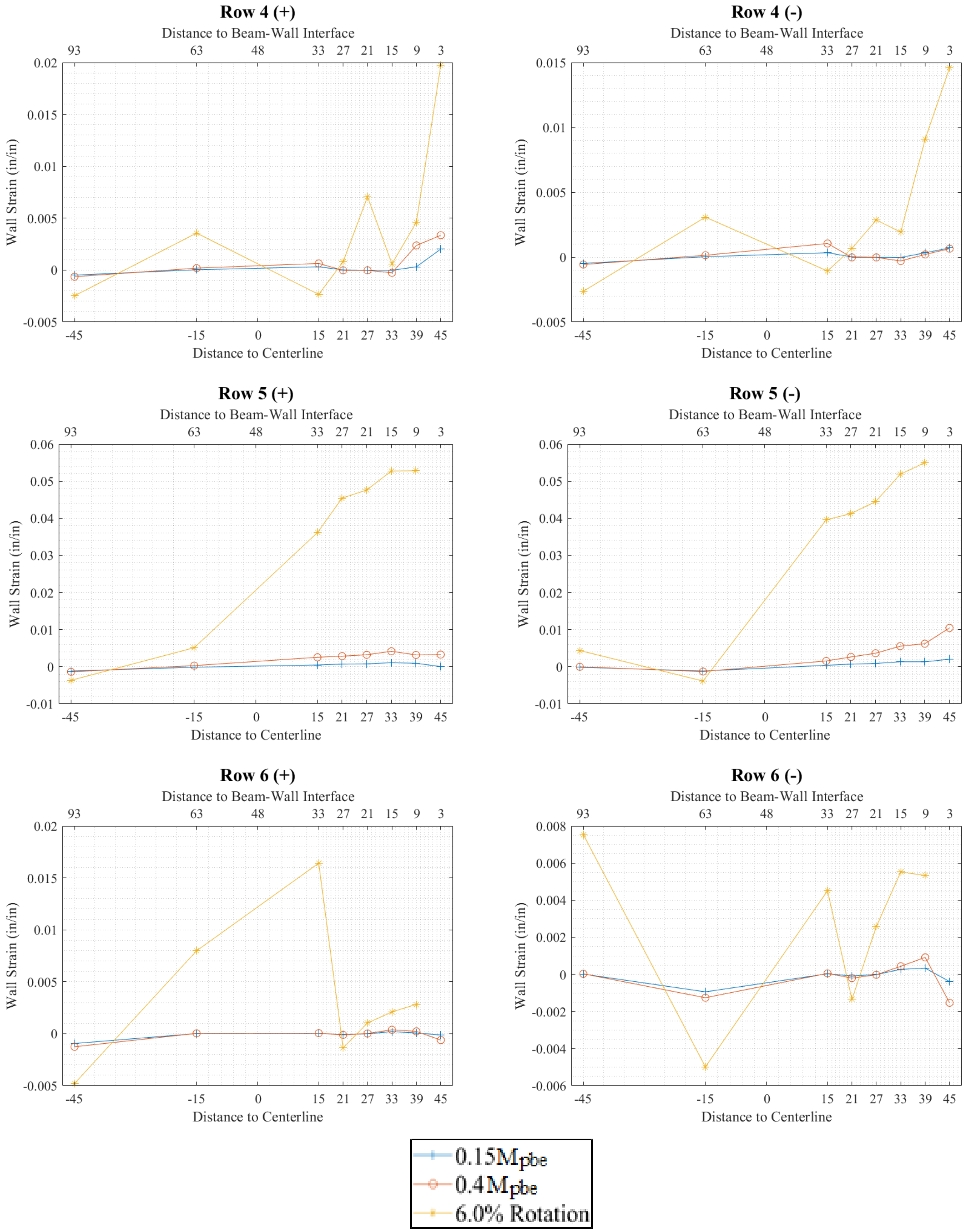

Figure 4.31. Wall Strain along Cross-Sections for SRC-W4 (continued)

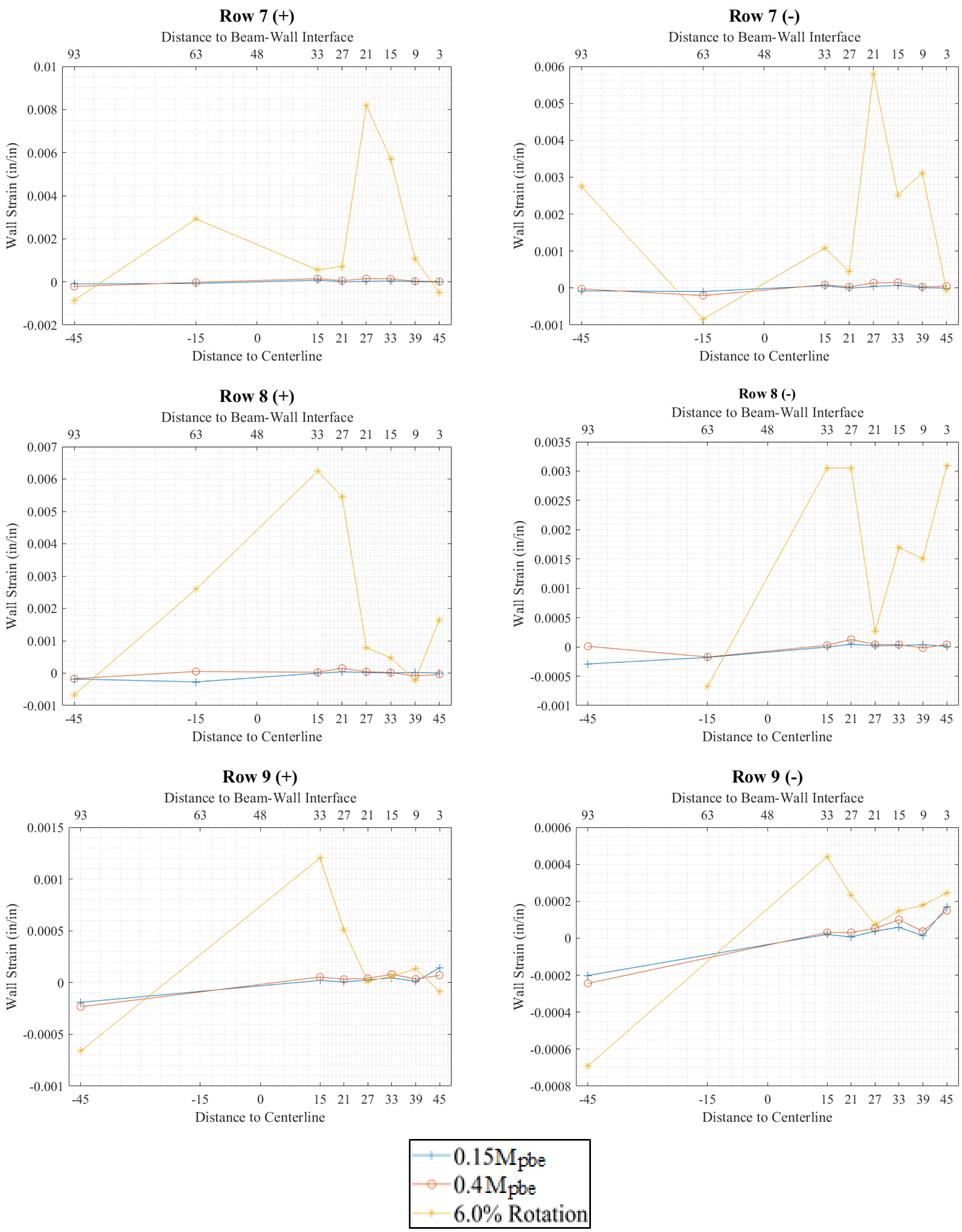

Figure 4.31 Wall Strain along Cross-Sections for SRC-W4 (continued)

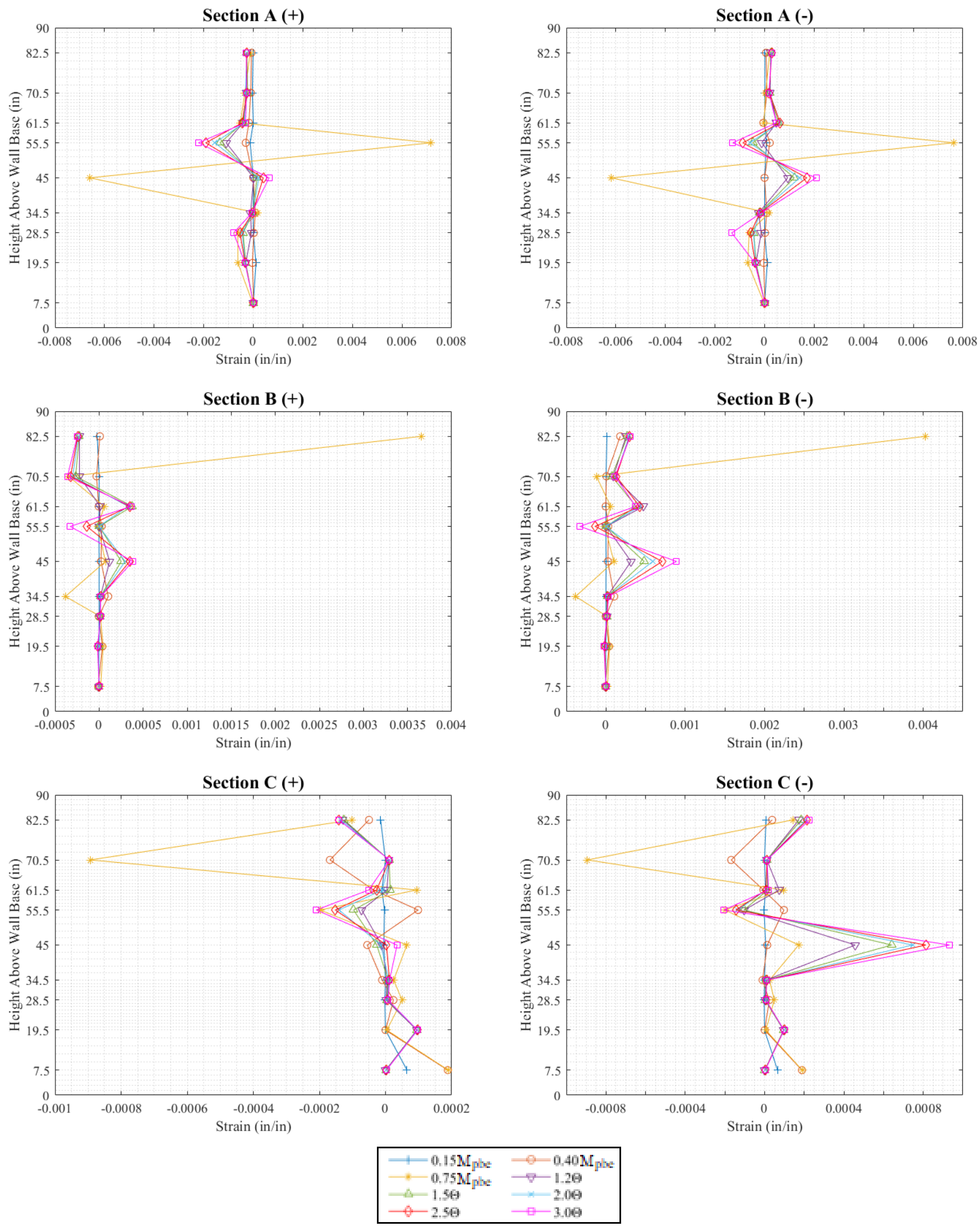

Figure 4.32. Wall Strain over Height for SRC-W1

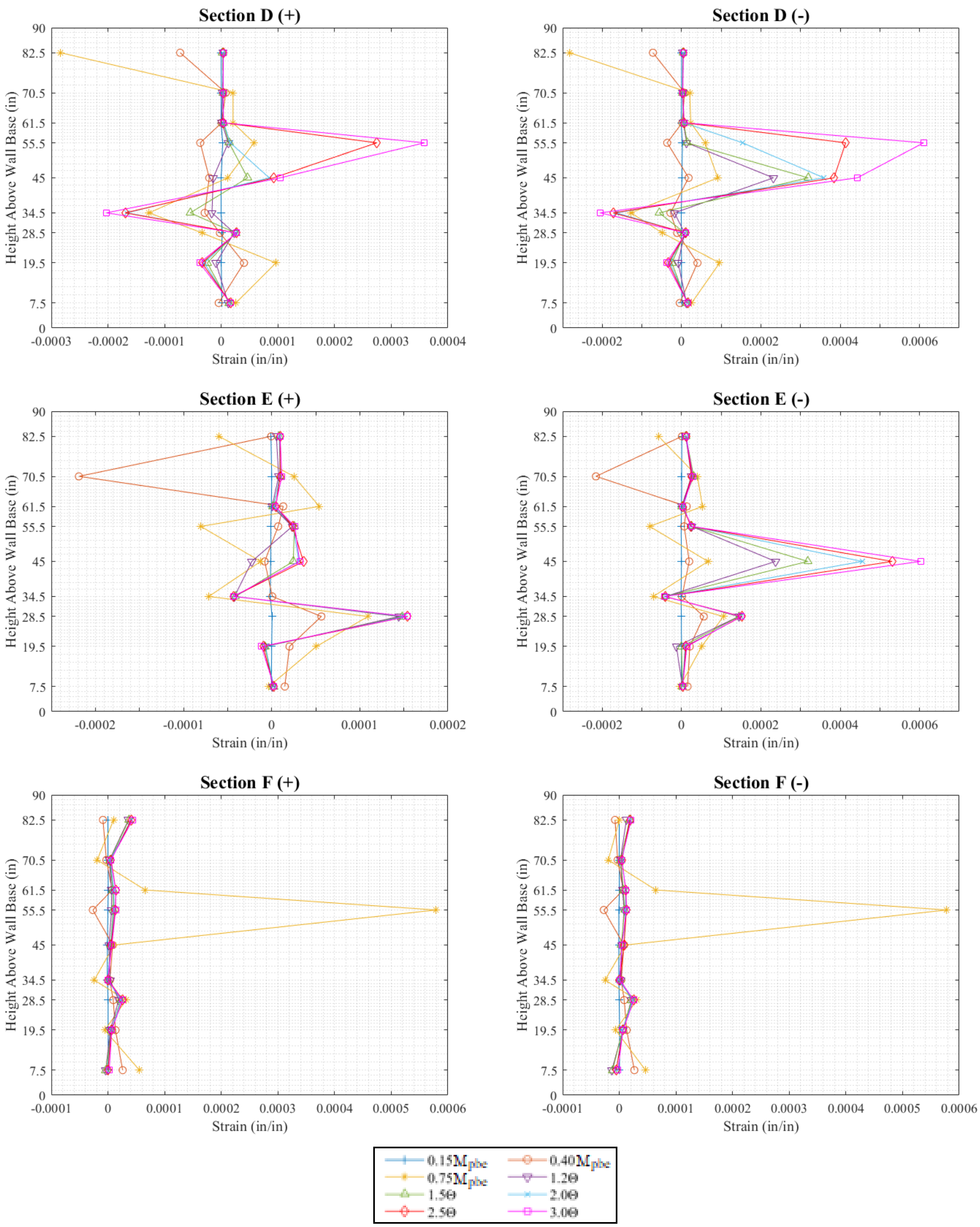

Figure 4.32. Wall Strain over Height for SRC-W1 (continued)

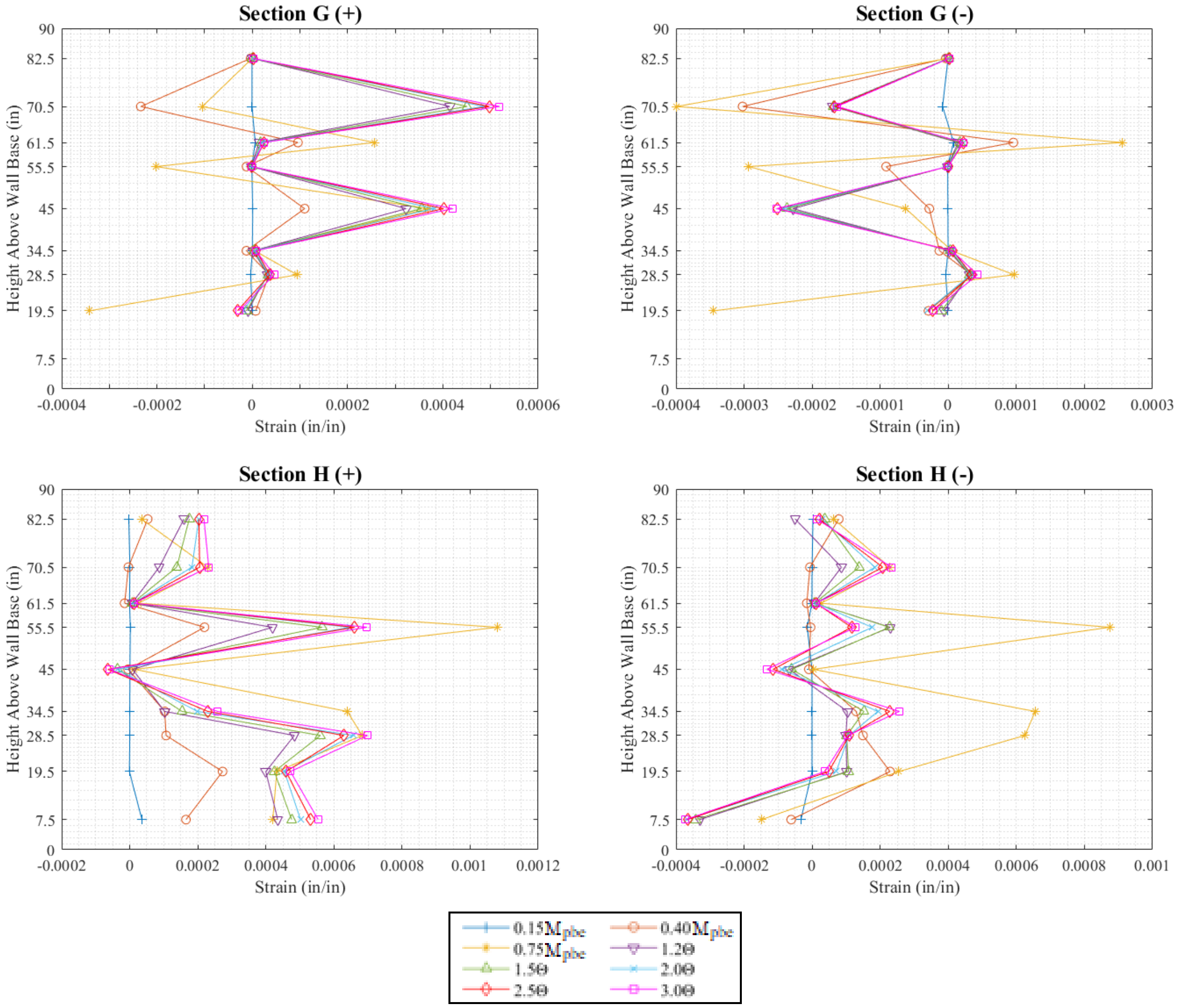

Figure 4.32. Wall Strain over Height for SRC-W1 (continued)

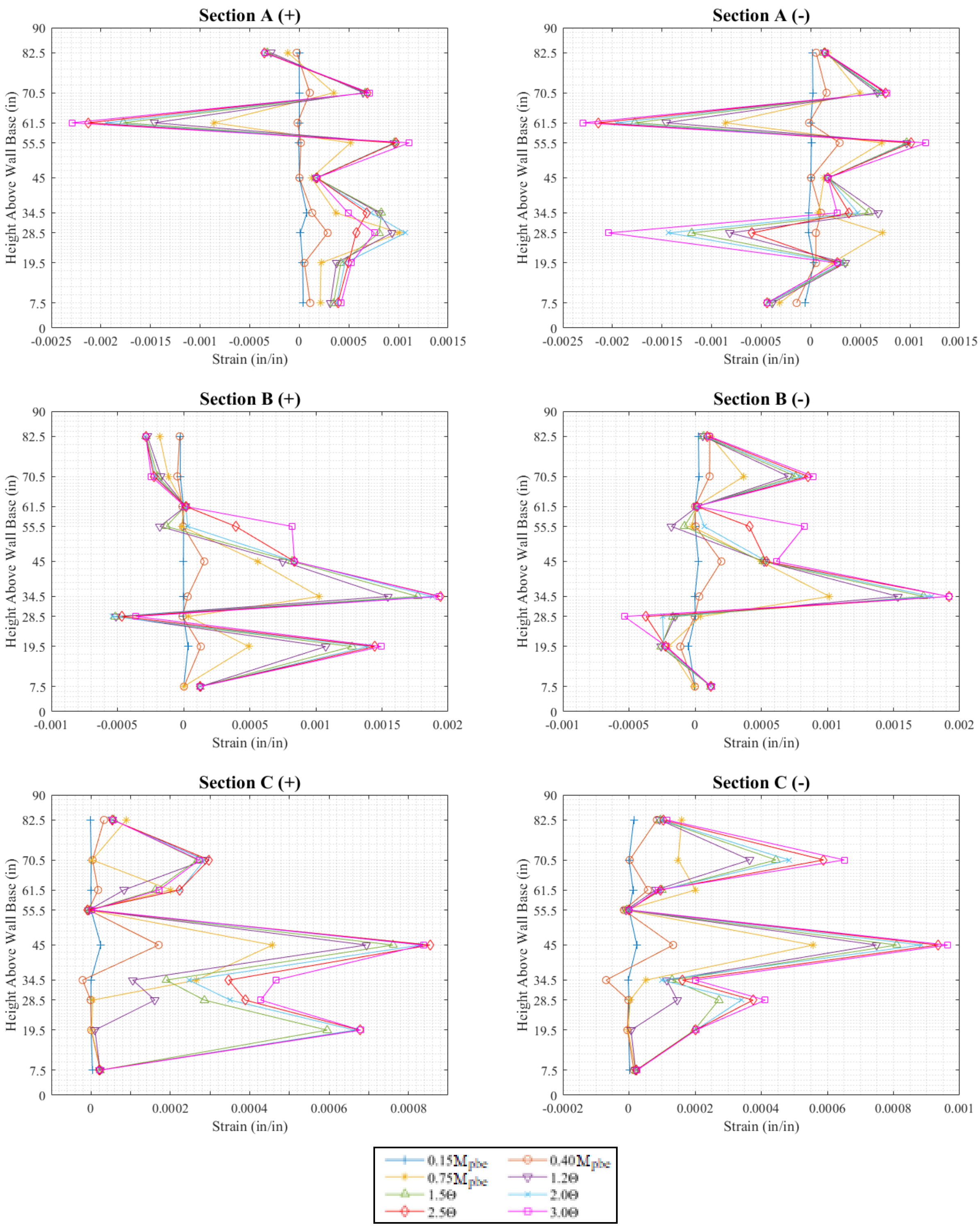

Figure 4.33. Wall Strain over Height for SRC-W2

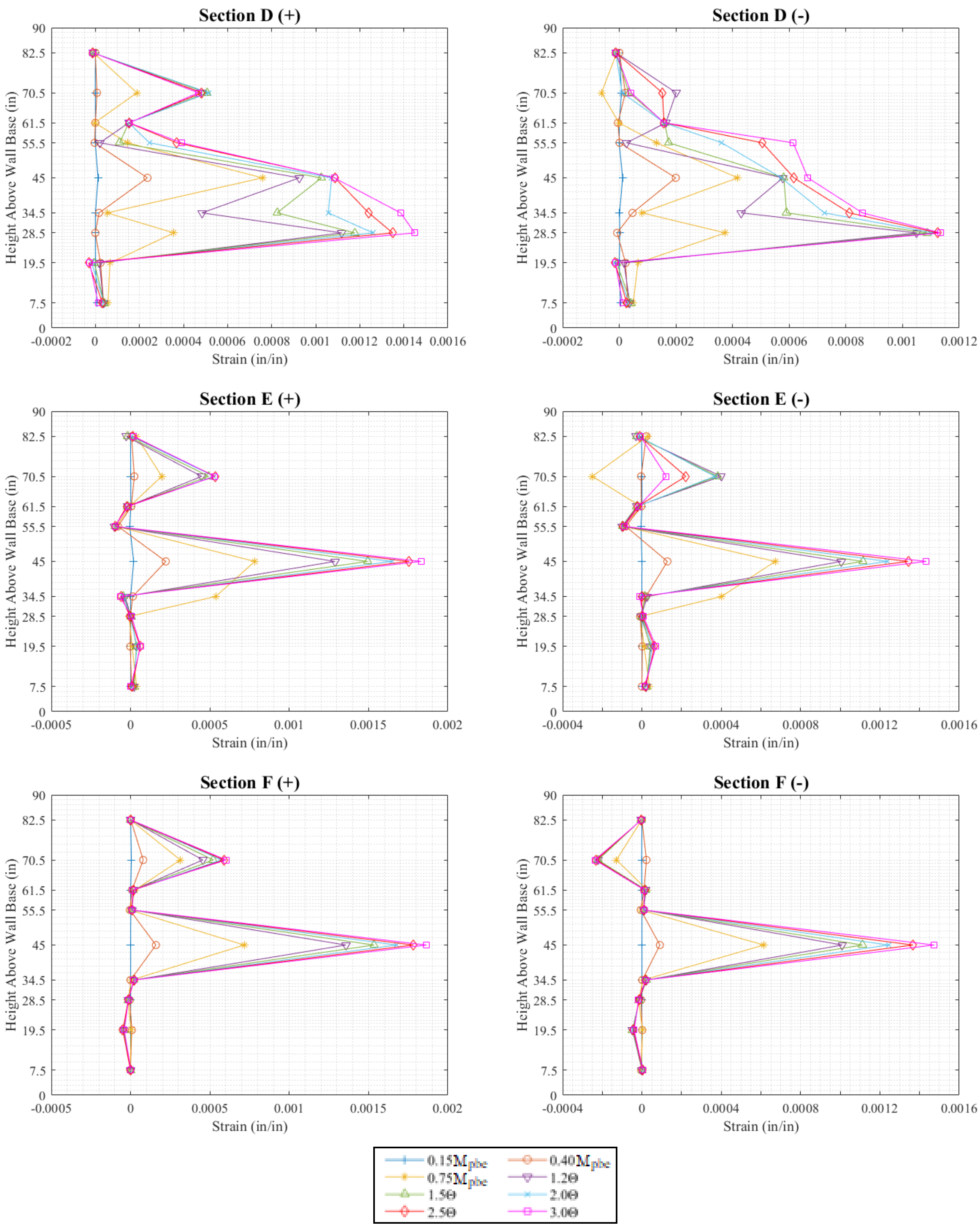

Figure 4.33. Wall Strain over Height for SRC-W2 (continued)

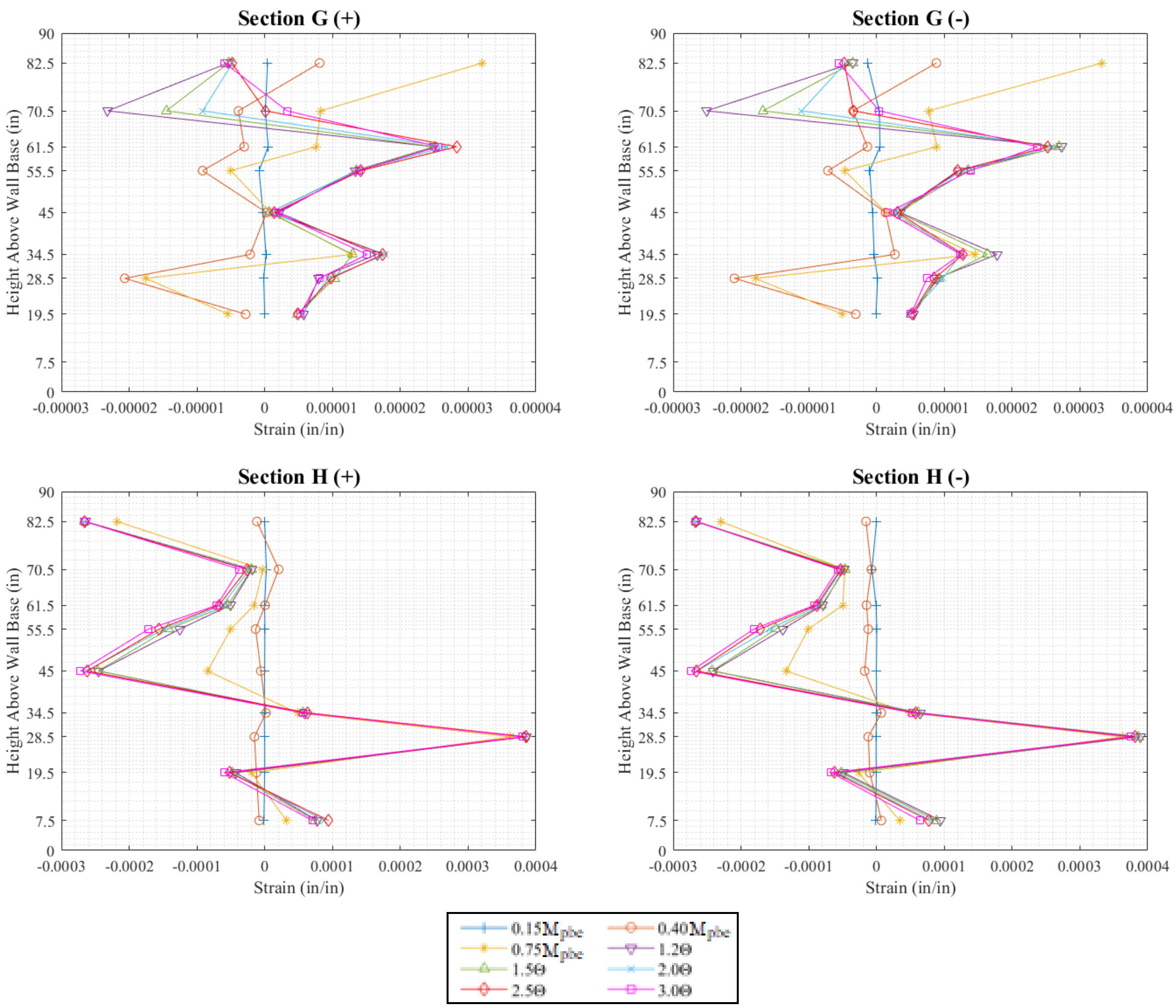

Figure 4.33. Wall Strain over Height for SRC-W2 (continued)

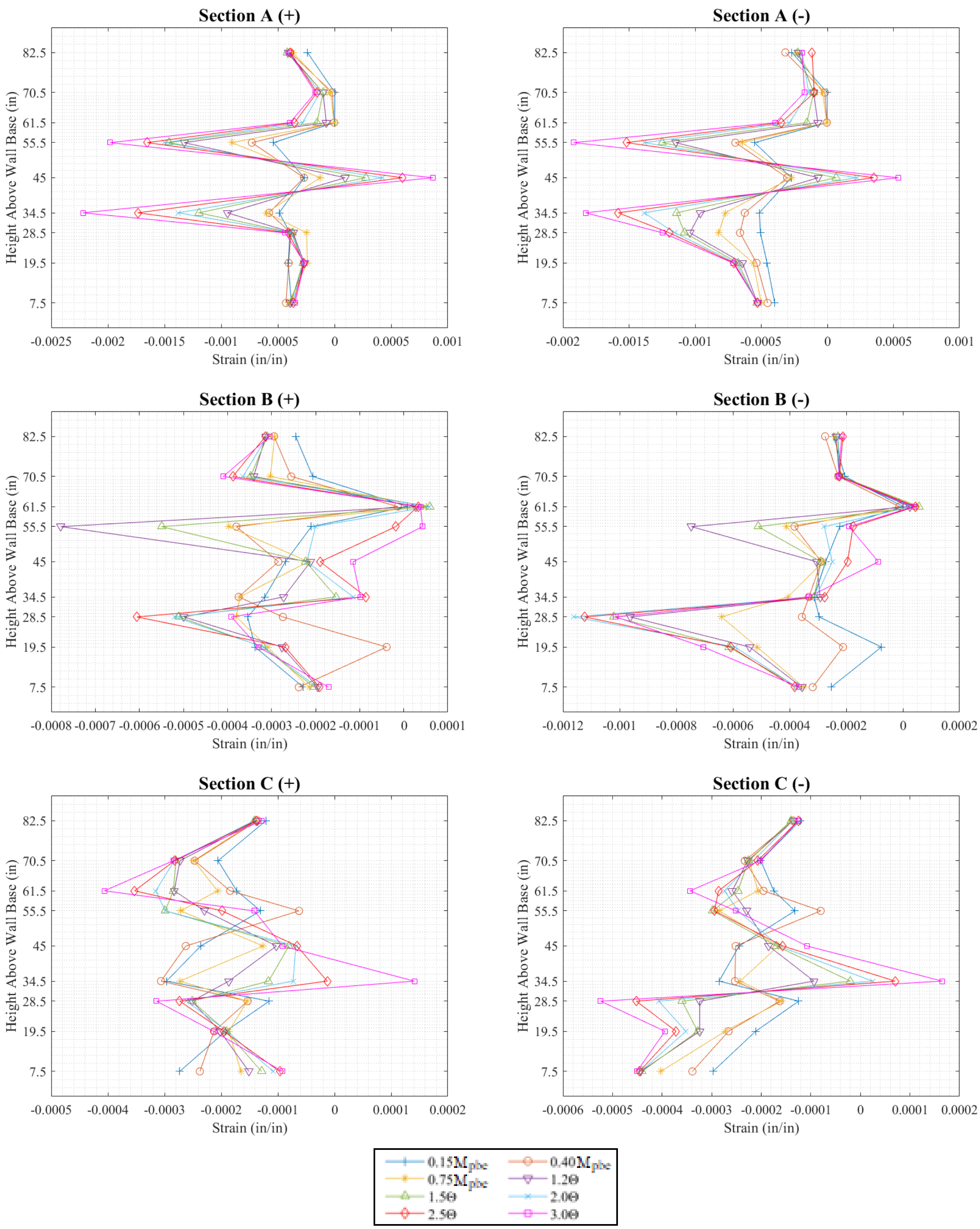

Figure 4.34. Wall Strain over Height for SRC-W3

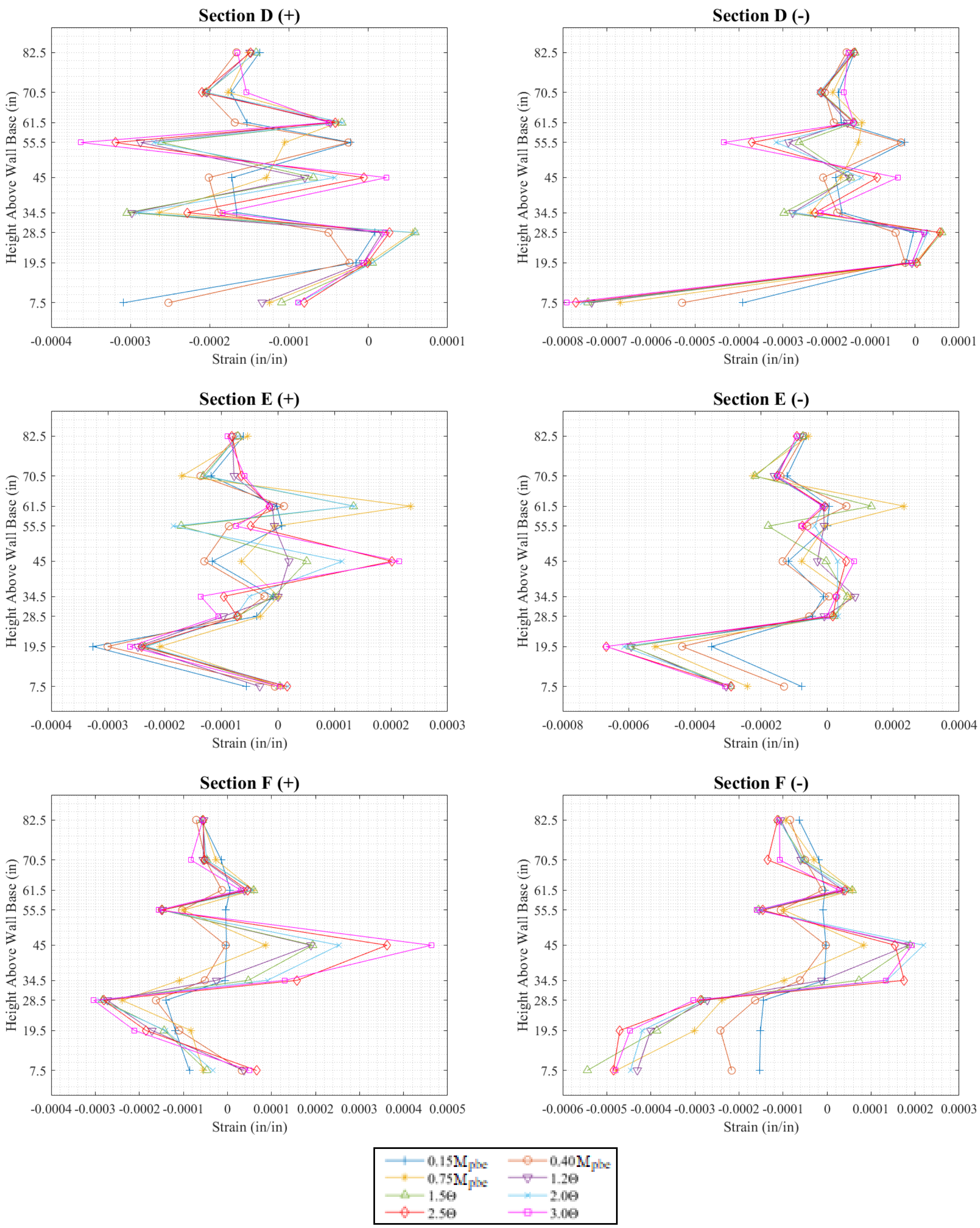

Figure 4.34. Wall Strain over Height for SRC-W3 (continued)

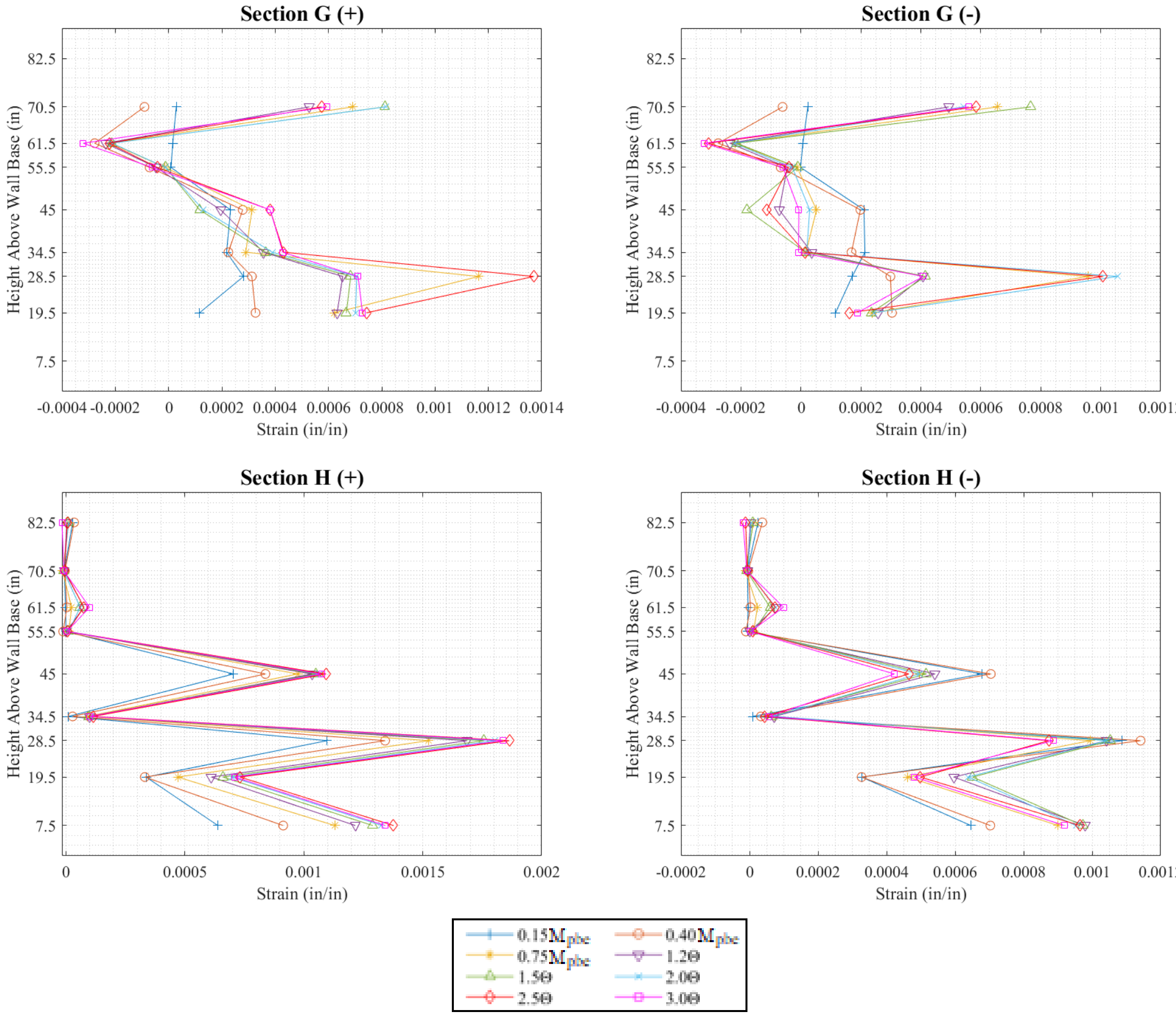

Figure 4.34. Wall Strain over Height for SRC-W3 (continued)

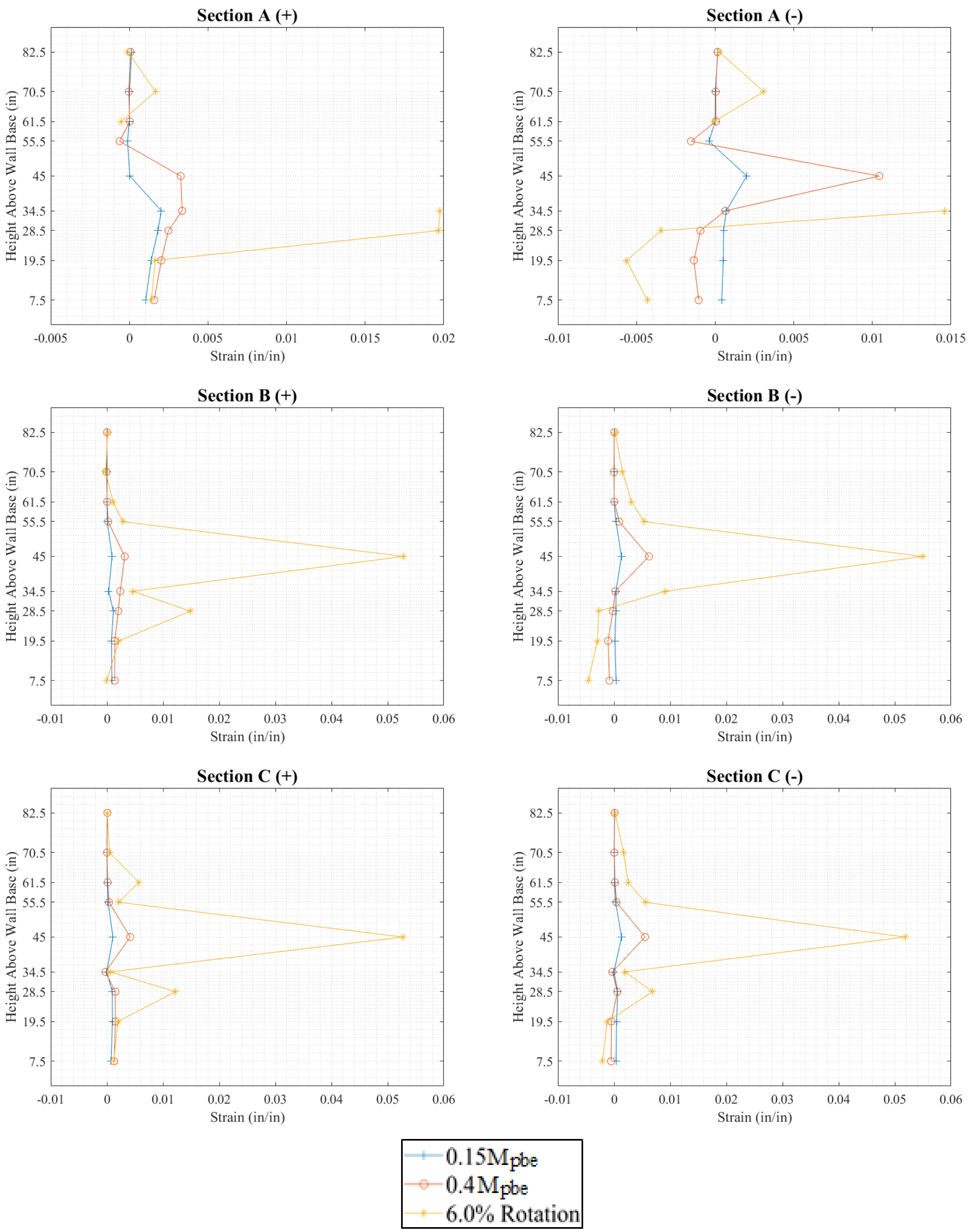

Figure 4.35. Wall Strain over Height for SRC-W4

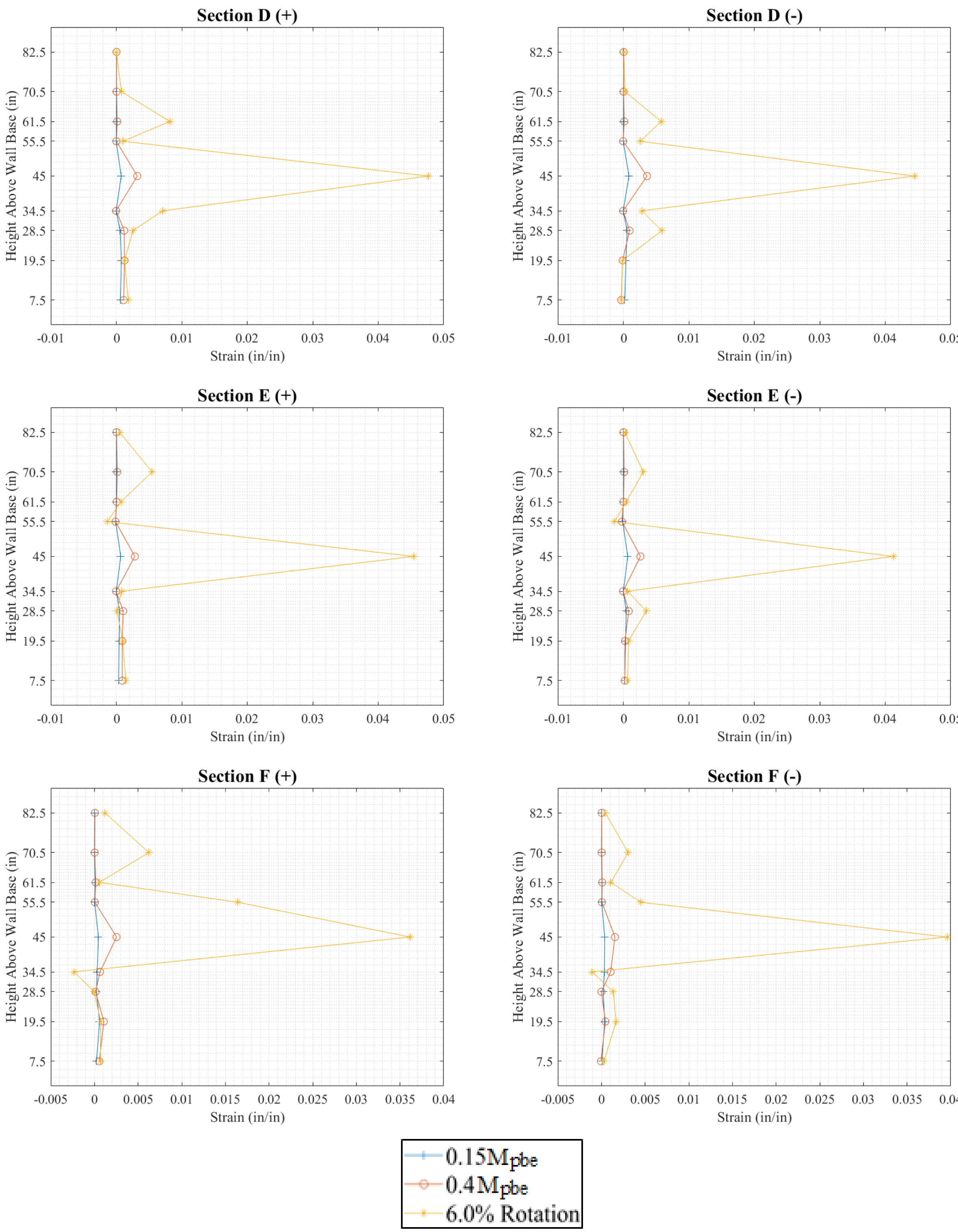

Figure 4.35. Wall Strain over Height for SRC-W4 (continued)

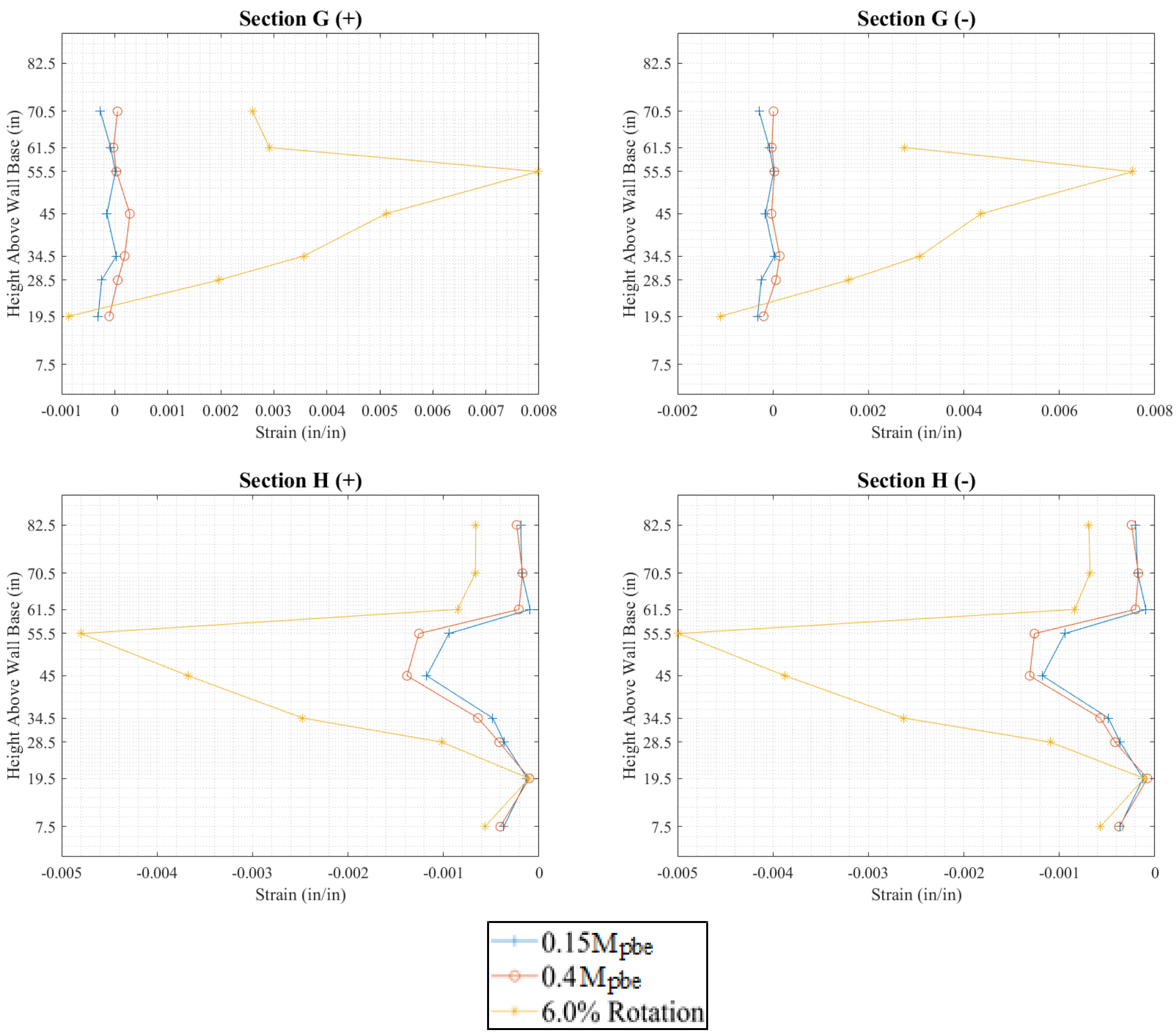

Figure 4.35. Wall Strain over Height for SRC-W4 (continued)

4.9. Wall Reinforcement Strain

For SRC-W1 and SRC-W2, which included strain gauges on wall longitudinal reinforcement, wall strain profiles at the locations shown in Figure 3.17 are provided in Figure 4.36 through Figure 4.39. The strain profiles were formulated using strain values at the peak of each first cycle at each increment of load or displacement applied. The plots for SRC-W2 include residual strain after completion of testing of SRC-W1. Plane-section behavior is not evident in Figure 4.36 through Figure 4.39.

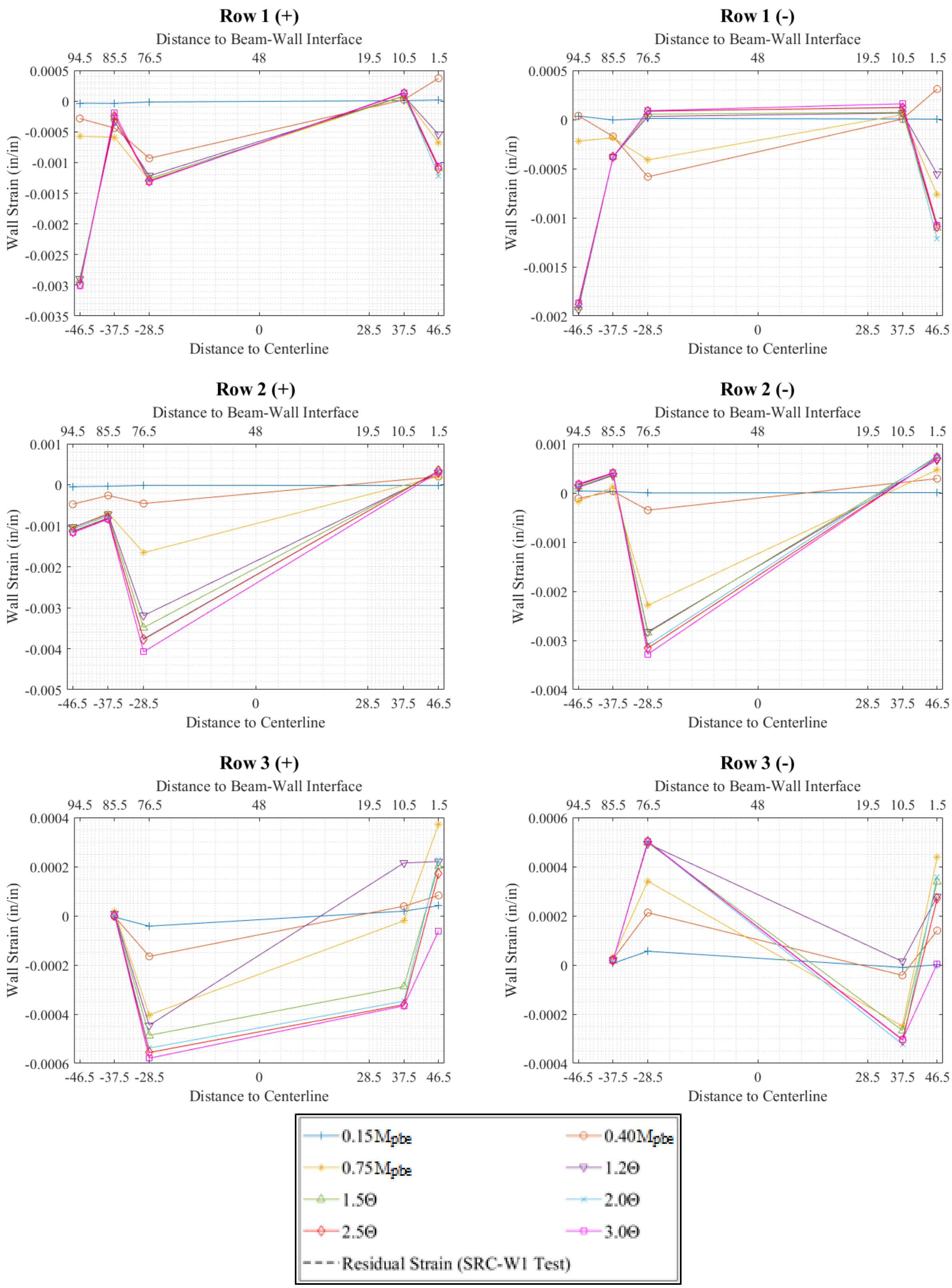

Figure 4.36. Wall Longitudinal Reinforcement Strain along Cross-Sections for SRC-W1

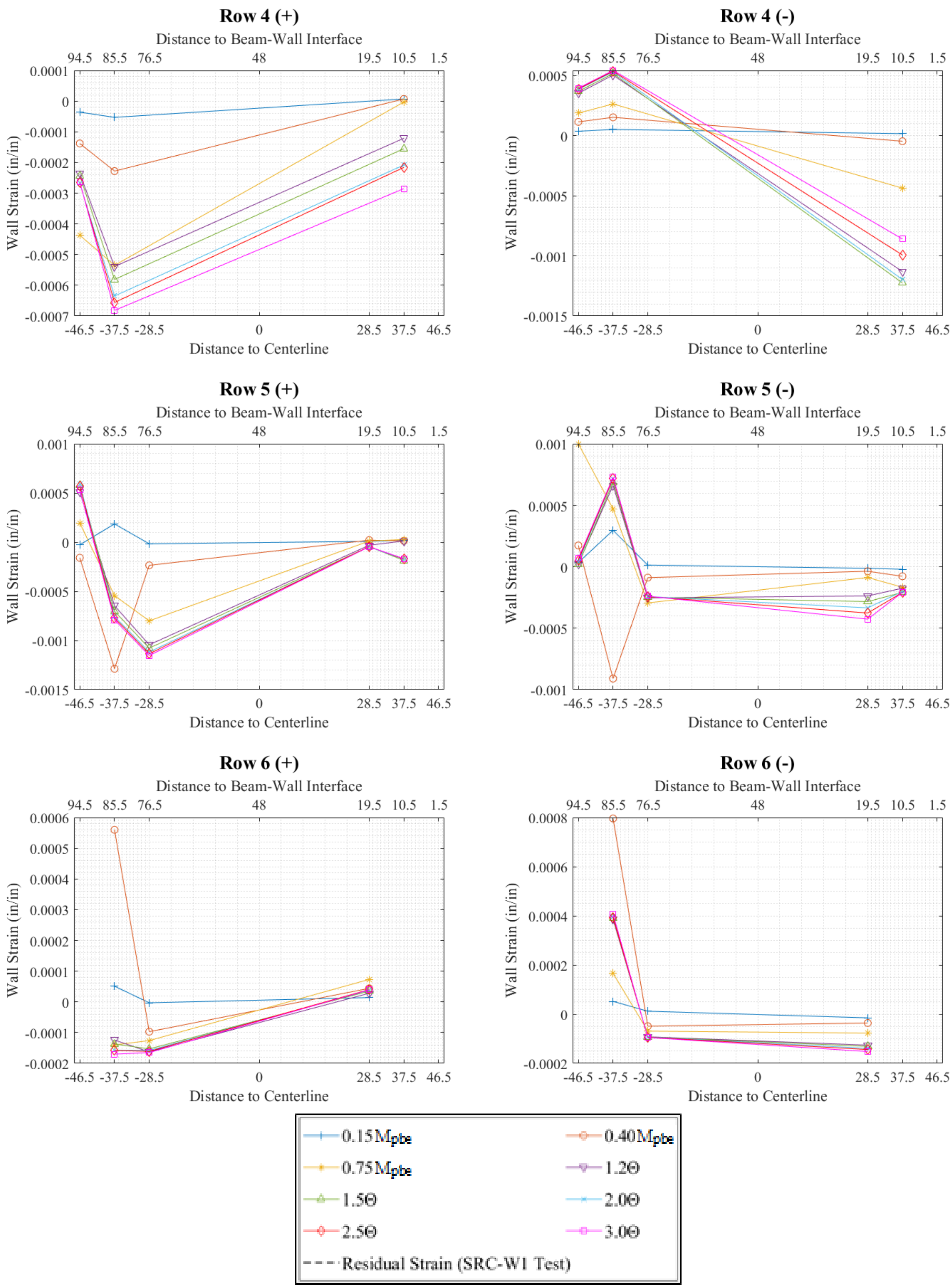

Figure 4.36. Wall Longitudinal Reinforcement Strain along Cross-Sections for SRC-W1 (cont.)

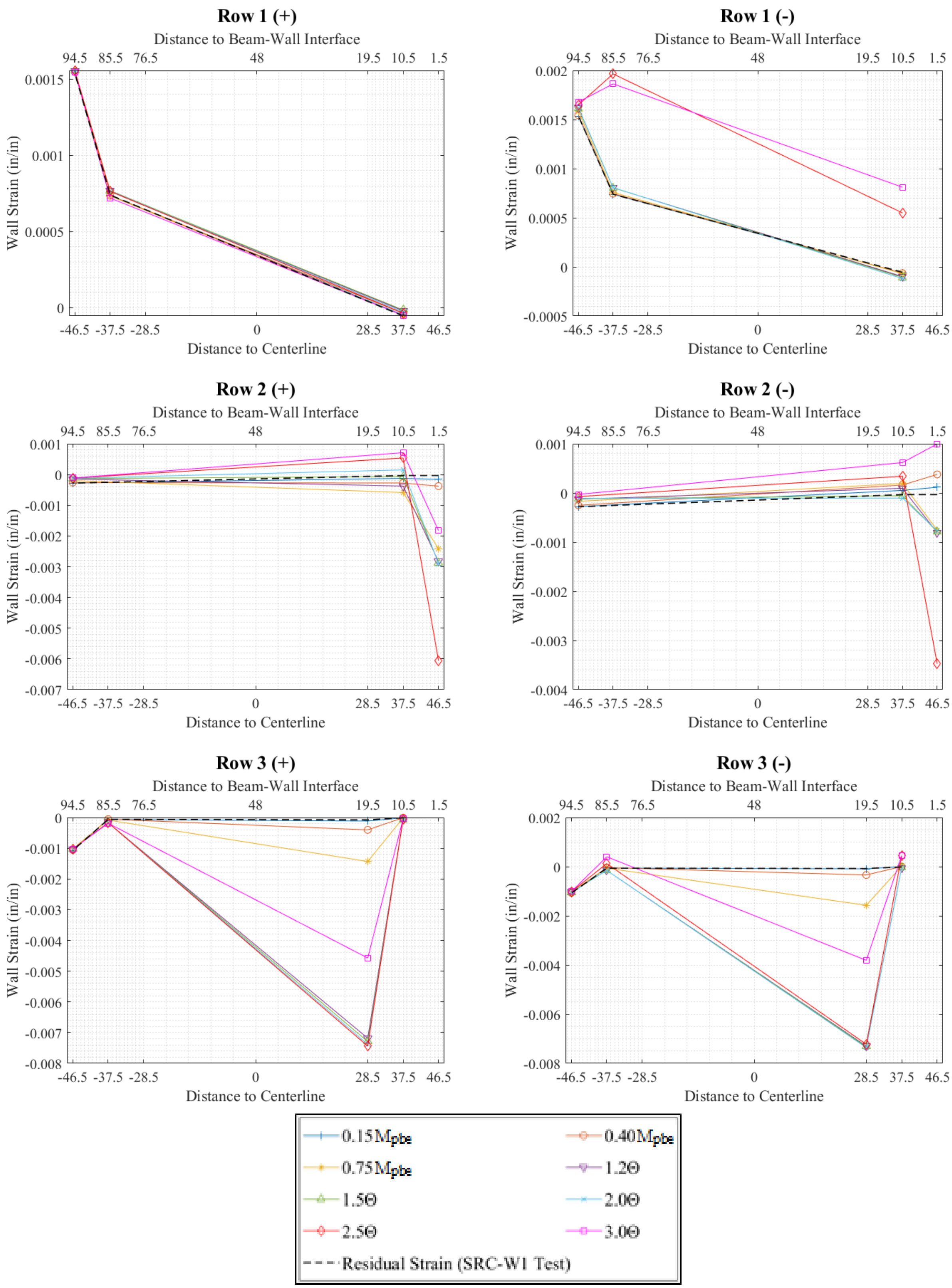

Figure 4.37. Wall Longitudinal Reinforcement Strain along Cross-Sections for SRC-W2

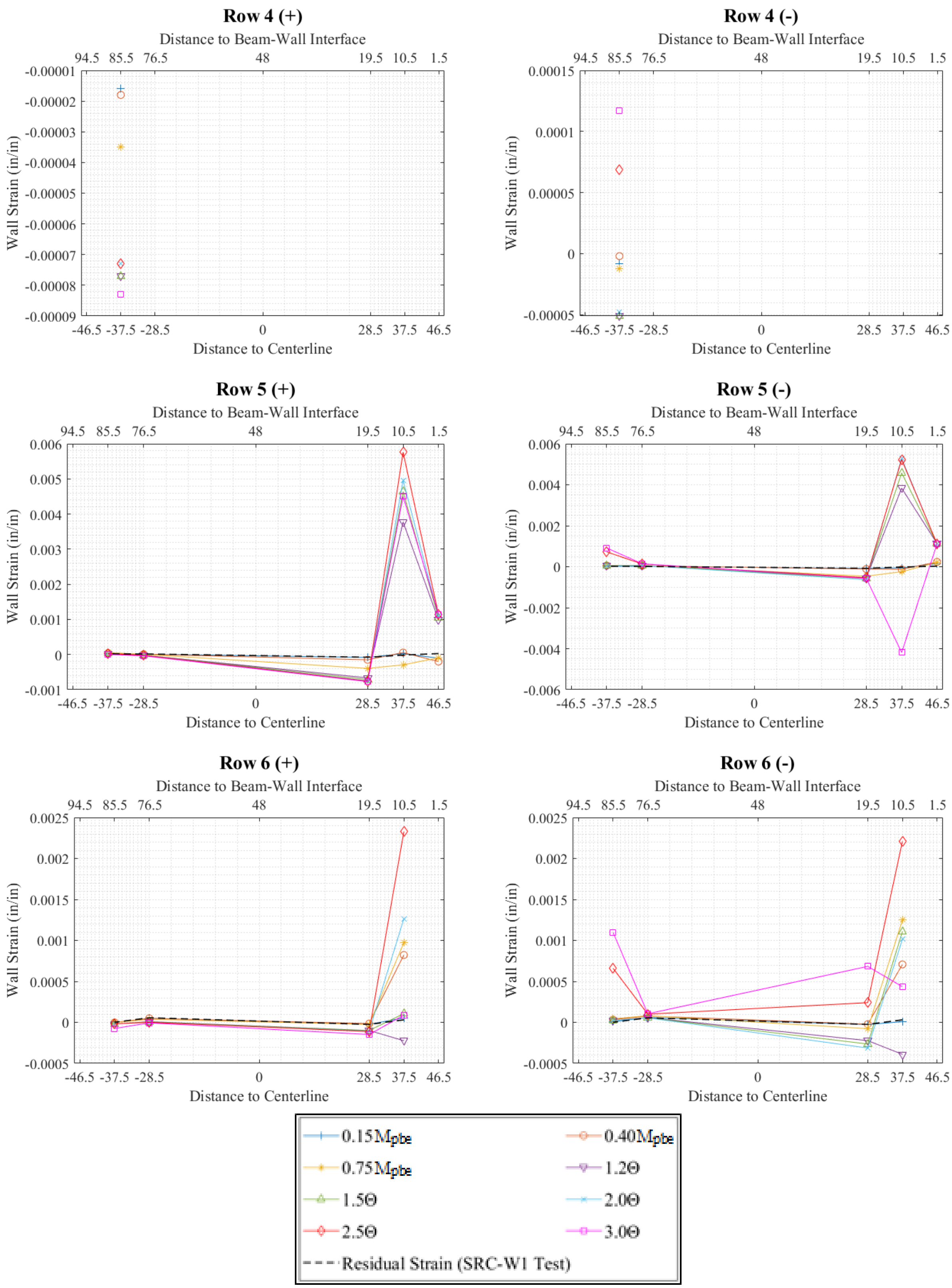

Figure 4.37. Wall Longitudinal Reinforcement Strain along Cross-Sections for SRC-W2 (cont.)

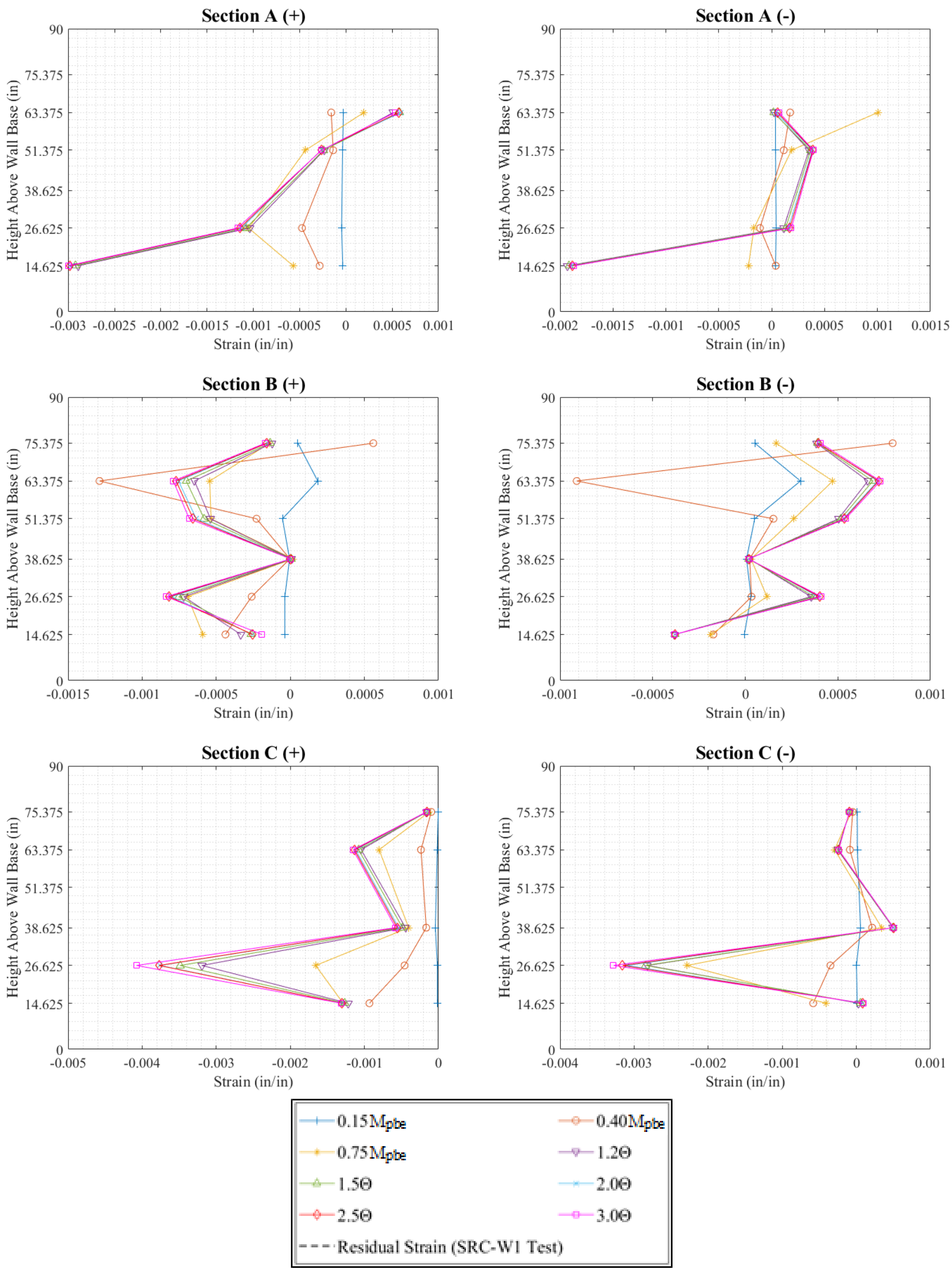

Figure 4.38. Wall Longitudinal Reinforcement Strain over Height for SRC-W1

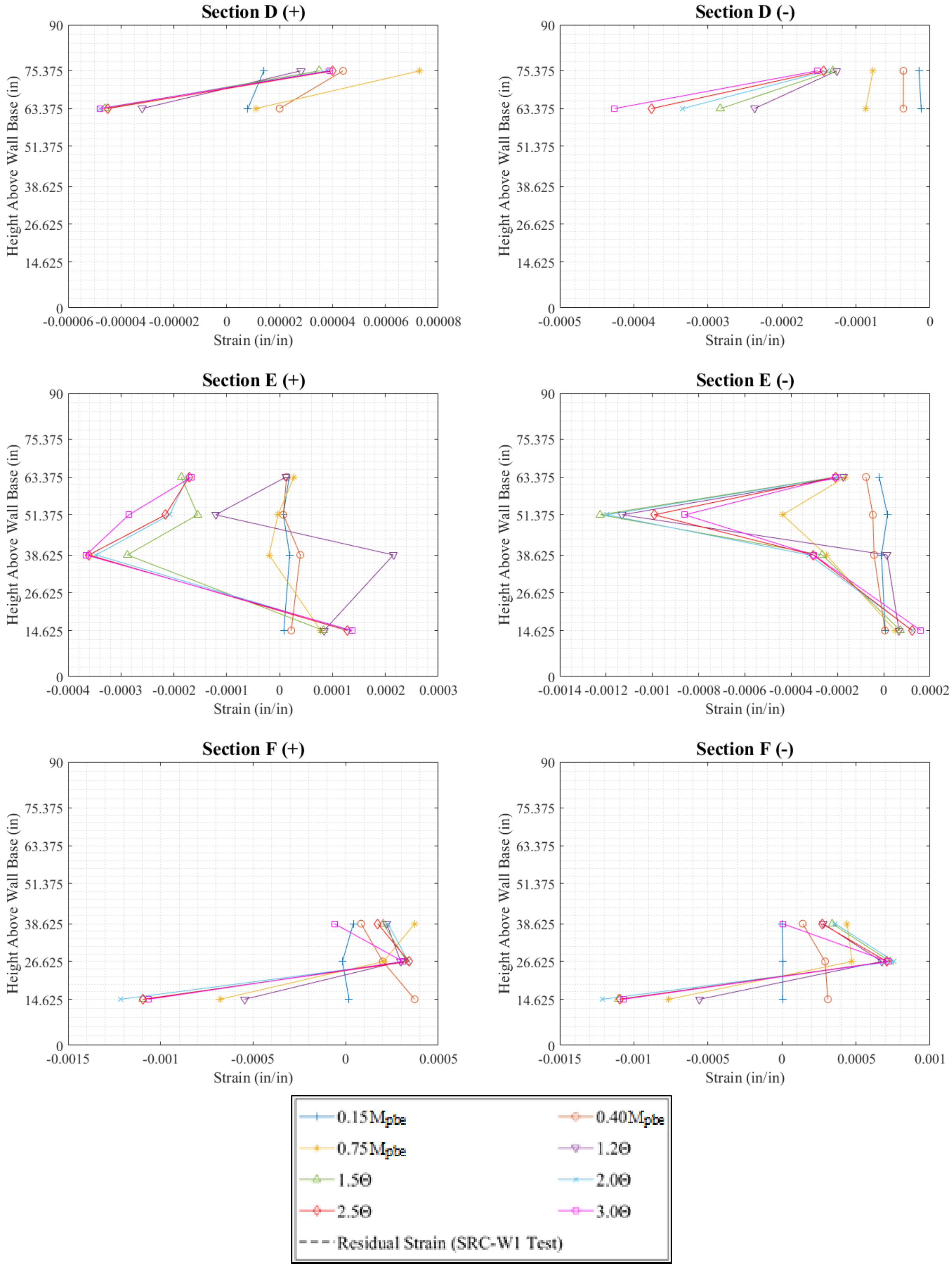

Figure 4.38. Wall Longitudinal Reinforcement Strain over Height for SRC-W1 (continued)

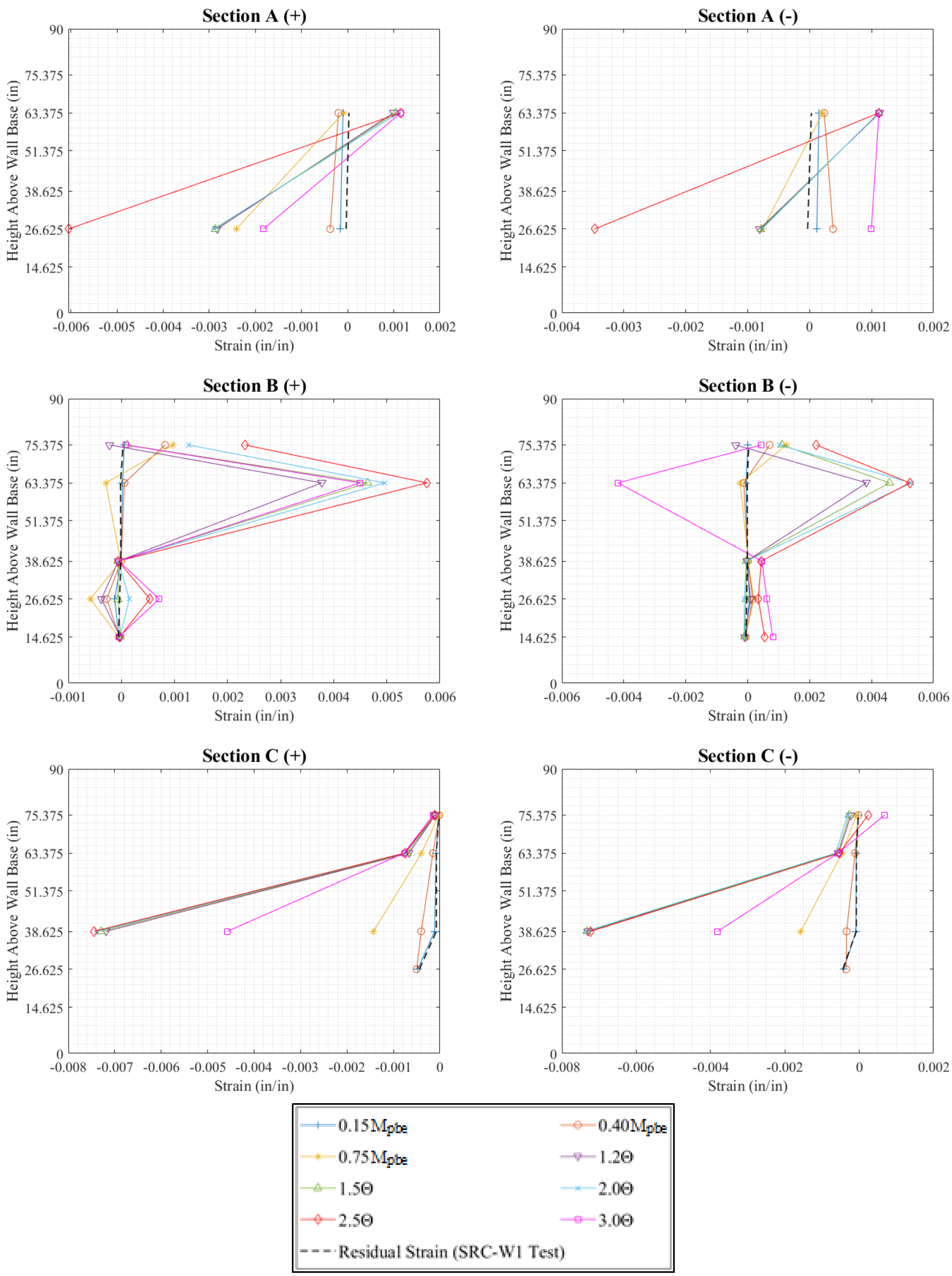

Figure 4.39. Wall Longitudinal Reinforcement Strain over Height for SRC-W2

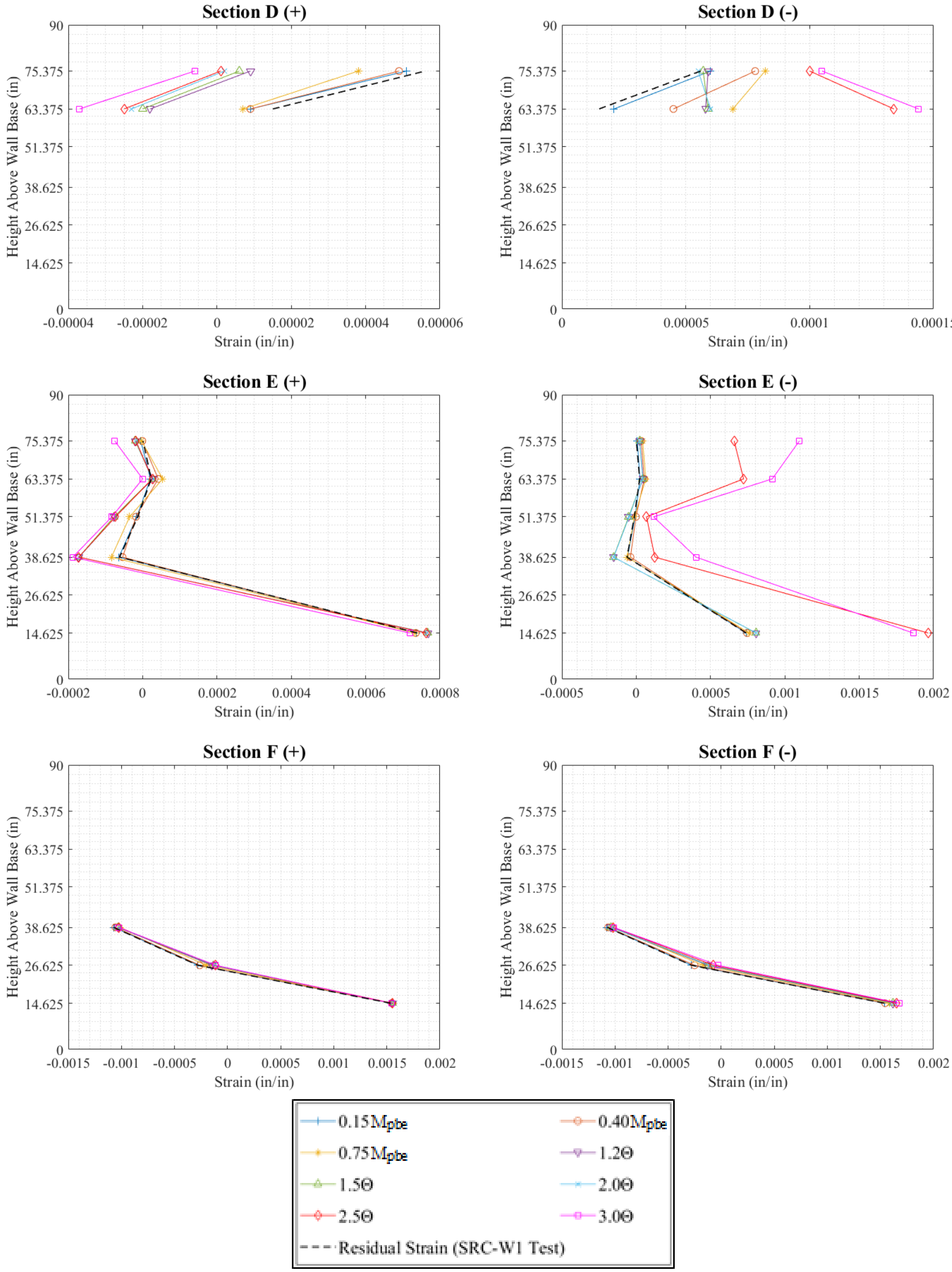

Figure 4.39. Wall Longitudinal Reinforcement Strain over Height for SRC-W2 (continued)

5. Modeling Recommendations

5.1. Effective Stiffness

It was shown in Section 4.6 and Section 4.4 that the majority of the coupling beam elastic deformation was measured at the beam-wall interface due to slip of the steel section. This was consistent with results from Motter et al (2017a) for seismic tests on SRC coupling beams. Motter et al (2017b) recommended an effective stiffness based on flexural rigidity of:

$$(EI)_{eff} = \frac{M_p L}{6\theta_y} \tag{5-1}$$

or:

$$(EI)_{eff} = 0.06\alpha E_s I_{trans} \tag{5-2}$$

where M_p is the plastic moment of the section using a Whitney stress block for concrete in compression, L is the beam length, θ_y is the yield rotation, taken as 0.0133 radians of chord rotation, α is the span-to-depth ratio of the beam, E_s is the elastic modulus of steel, and I_{trans} is the transformed moment of inertia, transforming concrete to steel. AISC 341-22, consistent with PEER TBI (2017), recommended an effective stiffness based on flexural and shear rigidity of:

$$(EI)_{eff} = 0.07\alpha(EI)_{trans} \tag{5-3}$$

$$(GA)_{eff} = 1.0G_sA_{sw} \tag{5-4}$$

where $(EI)_{trans}$ is the flexural rigidity of the cracked transformed section, G_s is the shear modulus of steel, and A_{sw} is the area of the web of the steel section.

The predicted and measured chord rotation at $0.75M_{pbe}$ are provided in Table 5.1 for SRC-W1 and SRC-W2 tested in this study, CB6 tested by Abdullah et al (2020), and SRC1 and SRC2 tested by Motter et al (2017a). SRC-W4 from this study and SRC3 and SRC4 from Motter et al (2017a) were excluded from this comparison, as the wall yielded prior to reaching $0.75M_{pbe}$, leading to significant reduction in beam stiffness at $0.75M_{pbe}$ for these tests. Although wall yielding did not occur for SRC2, $0.75M_{pbe}$ was not reached for SRC2 in the negative loading direction due to the strength reduction from wall demands reducing beam fixity. Therefore, a measured chord rotation at $0.75M_{pbe}$ for SRC2 was not provided in Table 5.1 in the negative loading direction.

Table 5.1. Measured and Predicted Chord Rotation for Test Beams at $0.75M_{pbe}$

Test Name	Reference	Predicted			Measured			
		Eq. (5-1)	Eq. (5-2)	AISC	1st +	1st -	75th +	75th -
SRC-W1	This Study	0.0100	0.0103	0.0105	0.0079	-0.0092	0.0160	-0.0135
SRC-W2	This Study	0.0100	0.0103	0.0105	0.0121	-0.0110	0.0135	-0.0135
SRC-W3	This Study	0.0100	0.0104	0.0105	0.0074	-0.0079	0.0136	-0.0148
CB6	Abdullah et al (2020)	0.0100	0.0089	0.0113	0.0055	-0.0056	0.0088	-0.0087
SRC1	Motter et al (2017a)	0.0100	0.0105	0.0107	0.0151	-0.0149	NA	NA
SRC2	Motter et al (2017a)	0.0100	0.0105	0.0107	0.0080	NA	NA	NA

The wall demands at $0.75M_{pbe}$ for each test, determined from moment-curvature analysis, are provided in Figure 5.1. The demands for CB6, which are not shown, were constant compression, as this test did not include a cyclically loaded wall. The measured stiffness for this test was roughly equal in the positive and negative loading direction. For SRC-W1, the stiffness was 16% lower in the negative than the positive loading direction. In the positive loading direction, SRC1 had significantly lower stiffness than the other tests, which may have been a result of the significantly lower compressive force in the wall, as shown in Figure 5.1. Assuming linear stress-strain behavior in the embedment concrete at $0.75M_{pbe}$, the front embedment force for SRC1 was estimated as 375 kips, which was more than double the 160 kip compressive force in the wall. This was not the case for the other beams, with wall compressive forces of 405 kips for SRC2, 386 kips for SRC-W1, and 328 kips for SRC-W2 and SRC-W3. The significantly lower wall compressive force for SRC1 likely led to the reduction in stiffness, including the reduced stiffness in the negative loading direction.

For the four beams tested under wind loading, namely SRC-W1, SRC-W2, SRC-W3, and CB6, the level of stiffness degradation differed at $0.75M_{pbe}$. The ratio of the stiffness of the 75th and final cycle to the 1st cycle was 0.63 and 0.64 for CB6, 0.49 and 0.68 for SRC-W1, 0.90 and 0.81 for SRC-W2, and 0.54 and 0.53 for SRC-W3 in the positive and negative loading directions, respectively. For the measured moment-rotation at the beam-wall interface, shown in Figure 4.21, these ratios were 0.34 and 0.80 for SRC-W1, 0.95 and 0.90 for SRC-W2, and 0.51 and 0.33 for SRC-W3 in the positive and negative loading directions, respectively. SRC-W1 had larger wall demands than SRC-W2 with the same quantity of wall longitudinal reinforcement crossing the embedment, and SRC-W3 had the same wall demands as SRC-W2 with less wall longitudinal reinforcement crossing the embedment. A higher level of wall compression relative to the quantity of wall longitudinal reinforcement, even if cyclic compression, may be associated with a higher level of stiffness degradation, given that stiffness degradation for SRC-W2 was less than the other tests at this loading level.

For the first cycle at $0.75M_{pbe}$ for SRC-W1, SRC-W2, and SRC-W3, the average ratio of measured stiffness to predicted stiffness is 1.08 using Eq. (5-1), 1.12 using Eq. (5-2), and 1.14 using AISC 341-22 (Eq. (5-3) and Eq. (5-4)), based on the values in Table 5.1. These values were 1.80, 1.60, and 2.04, respectively, for the Abdullah et al (2020) test, which did not include a cyclically loaded wall. It is recommended that the effective stiffness used for seismic design, which is provided in AISC 341-22, be adjusted for nonlinear wind design to account for stiffness degradation. This could be achieved through the use of a stiffness degradation factor that matches the behavior shown in Figure 4.15b. However, most commercially available computer software used by practicing engineers does not have such a feature for stiffness degradation. Thus, it is recommended that an average stiffness be used. For the 75 cycles at $0.75M_{pbe}$, the average ratio of secant stiffness to initial cycle secant stiffness was 0.66 and 0.71 for SRC-W1, 0.93 and 0.85 for SRC-W2, and 0.53 and 0.65 for SRC-W3 in the positive and negative loading directions, respectively. Seismic protocols have significantly fewer cycles, with three cycles used in past tests by Motter et al (2017a) for loading at this level. For the first three cycles at $0.75M_{pbe}$, the average ratio of secant stiffness to initial cycle secant stiffness was 0.95 and 0.96 for SRC-W1, 0.98 and 0.97 for SRC-W2, and 0.95 and 1.01 SRC-W3. For the six sets of values, the average ratio of the value for 75 cycles to the value for three cycles is 0.74. Therefore, it is recommended that the effective stiffness for nonlinear wind design be taken as 0.75 times the value determined using AISC 341-22 for seismic design.

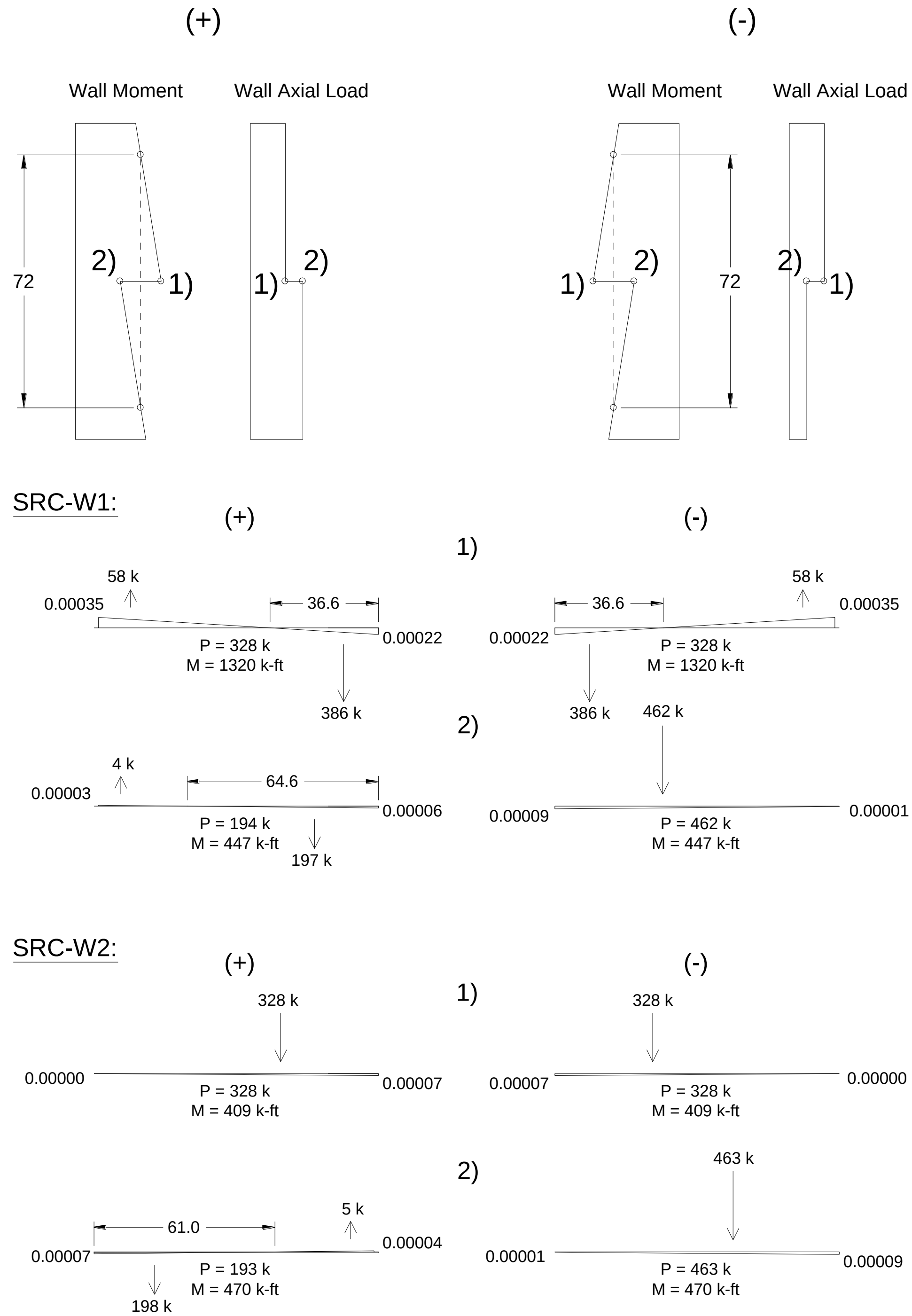

Figure 5.1. Wall Demands at $0.75M_{pbe}$, Excluding Coupling Beam Demands, at Location of Coupling Beam (Coupling Beam on Right), Determined from Moment-Curvature Analysis

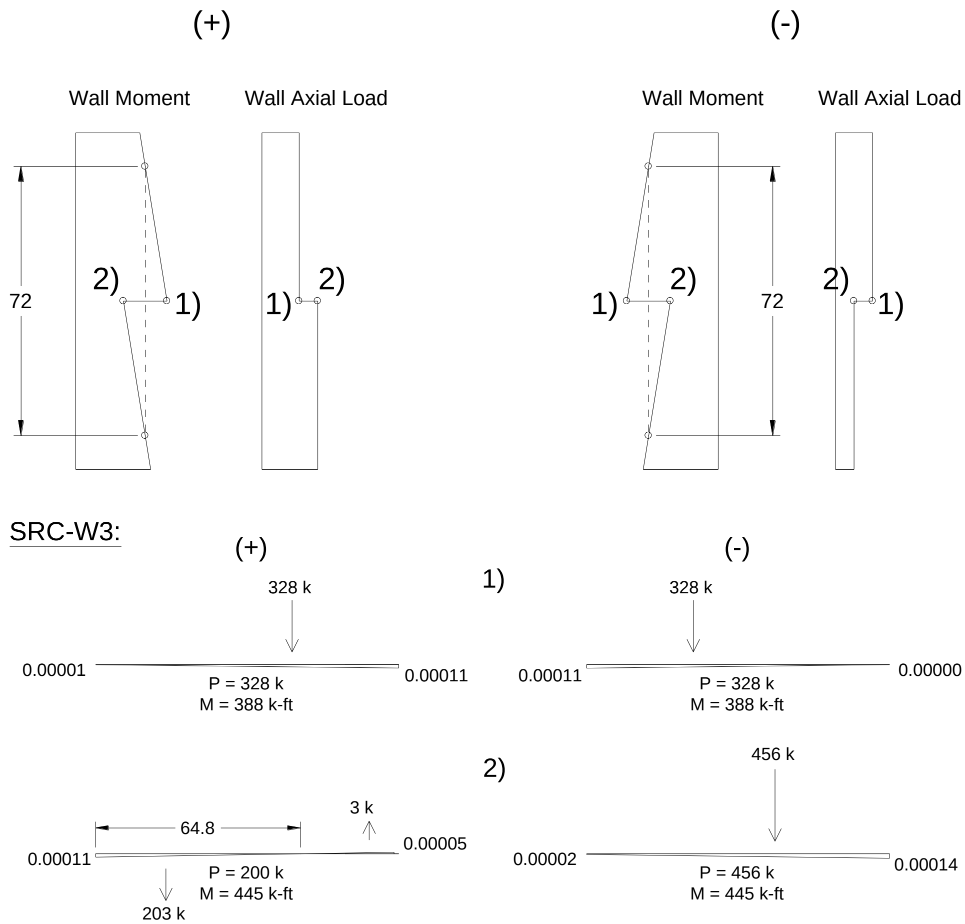

Figure 5.1. Wall Demands at 0.75M_{pbe}, Excluding Coupling Beam Demands, at Location of Coupling Beam (Coupling Beam on Right), Determined from Moment-Curvature Analysis (continued)

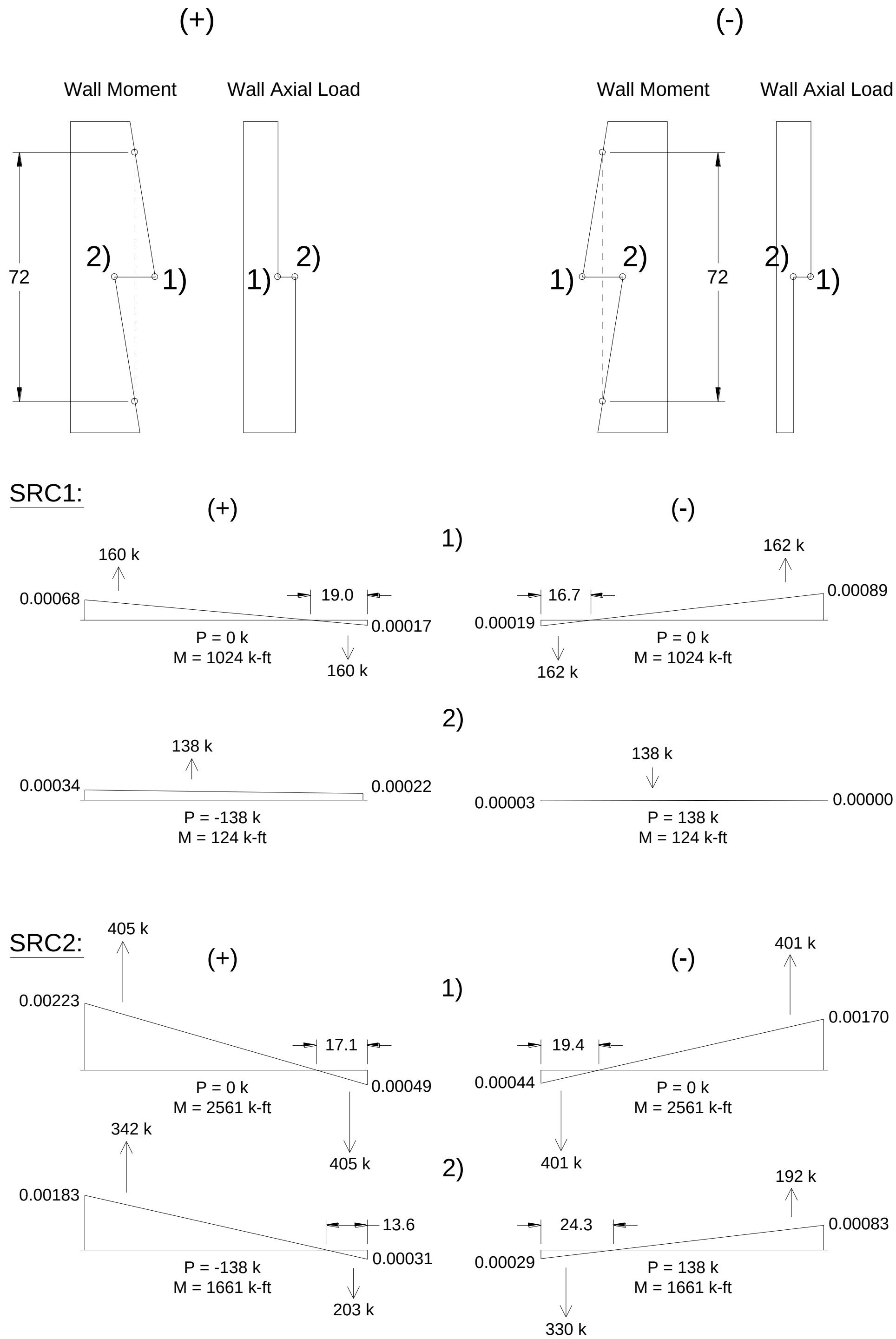

Figure 5.1. Wall Demands at 0.75M_{pbe}, Excluding Coupling Beam Demands, at Location of Coupling Beam (Coupling Beam on Right), Determined from Moment-Curvature Analysis

(continued)

5.2. Backbone Models

Nonlinear backbone models are typically fit to load-deformation test data to formulate models that are suitable for implementation into commercially available computer software. This is commonplace for seismic tests, which typically have a few loading cycles at each increment, often resulting in a lack of significant stiffness degradation prior to yielding. As discussed in the previous section, stiffness degradation for repeated loading cycles at a given increment in the wind loading protocol was significant for the tests conducted in this study, particularly for cycles at $0.75M_{pbe}$. Most commercially available software used for nonlinear modeling of structural behavior with moment-rotation or shear-deformation hinges does not include a feature for degrading stiffness at repeated loading cycles to the same level. This creates debate as to how best to fit a typical backbone model to these test data. If the backbone model is fit based on test data at initial cycles, the energy under the model would be more than the test data. If the backbone model is fit based on test data at final cycles, the energy under the model would be less than the test data. It is recommended to fit the backbone model based on average values of all cycles at each increment. This would promote equal area under the curve for the backbone model and test data. Equal area is consistent with the approach for backbone modeling currently being proposed by ACI Committee 374 (ACI 374.3R-16) for performance-based seismic design.

To fit the backbone model to test data, a linearized backbone of the test data was first formulated by connecting data points at each loading increment, as shown in Figure 5.2 with resulting data provided in Table 5.2. Backbone models fit to data based on first cycles, final cycles, and average cycles are provided in Figure 5.2 and Table 5.3. In each of these cases the backbone model considered only cyclic increments larger than previous increments, such that cycles in the loading protocol after the two cycles at $3.0\theta_y$ were excluded. The backbone model was bilinear up to the maximum shear force, V_{max}, similar to the backbone model described in ASCE/SEI 41 Section 7.4.3.2.4. The first line connected the origin to the yield force, $V_{y,test}$, and intersected the test data backbone at 0.6 of the yield force. The second line connected the yield force to the peak shear force. The yield force was determined such that the area under the test data backbone and model backbone were equal up to the peak shear force. The backbones from SRC-W1, SRC-W2, and SRC-W3 are provided on the same plot in Figure 5.3 for comparative purposes. Less difference in stiffness at yield between the initial and final cycle backbone was evident for SRC-W2 relative to SRC-W1 and SRC-W3.

For SRC-W1, SRC-W2, and SRC-W3, ratios of tested strength to predicted strength are provided in Table 5.4, with values for $V@M_y$ and $V@M_{pbe}$ consistent with the values in Section 3.6. The plastic rotation in the test, $\theta_{plastic}$, also provided in Table 5.4, was the difference between the maximum rotation and the rotation at yield. For the values in Table 5.4, the average $V_{y,test}$ / $V@M_y$ is 0.97, the average V_{max} / $V@M_{pbe}$ is 0.98, and the average $\theta_{plastic}$ is 4.05. A suggested bilinear backbone model for the SRC coupling beams for nonlinear wind design uses the effective stiffness from AISC 341-22 multiplied by 0.75, a yield strength of $V@M_y$, and a post-yield stiffness, $k_{plastic}$, in units of force per radian chord rotation, of:

$$k_{plastic} = \frac{V@M_{pbe} - V@M_y}{0.04} \quad (5\text{-}5)$$

with calculation of M_{pbe} and M_y based on expected material properties for concrete compressive strength and yield strength of the flange steel, which could differ for built-up versus rolled sections. The hysteretic behavior used in the model should be determined by modeling the tests with calibration to the energy dissipation provided in Figure 4.20 and Table 4.6. While the suggested backbone model is reflective of behavior observed in the tests, the tests did not include the influence of axial restraint from floors and walls on coupling beam behavior. Axial restraint is expected to alter the load-deformation response in the coupling beam, and it is recommended that future research examine the influence of axial restraint.

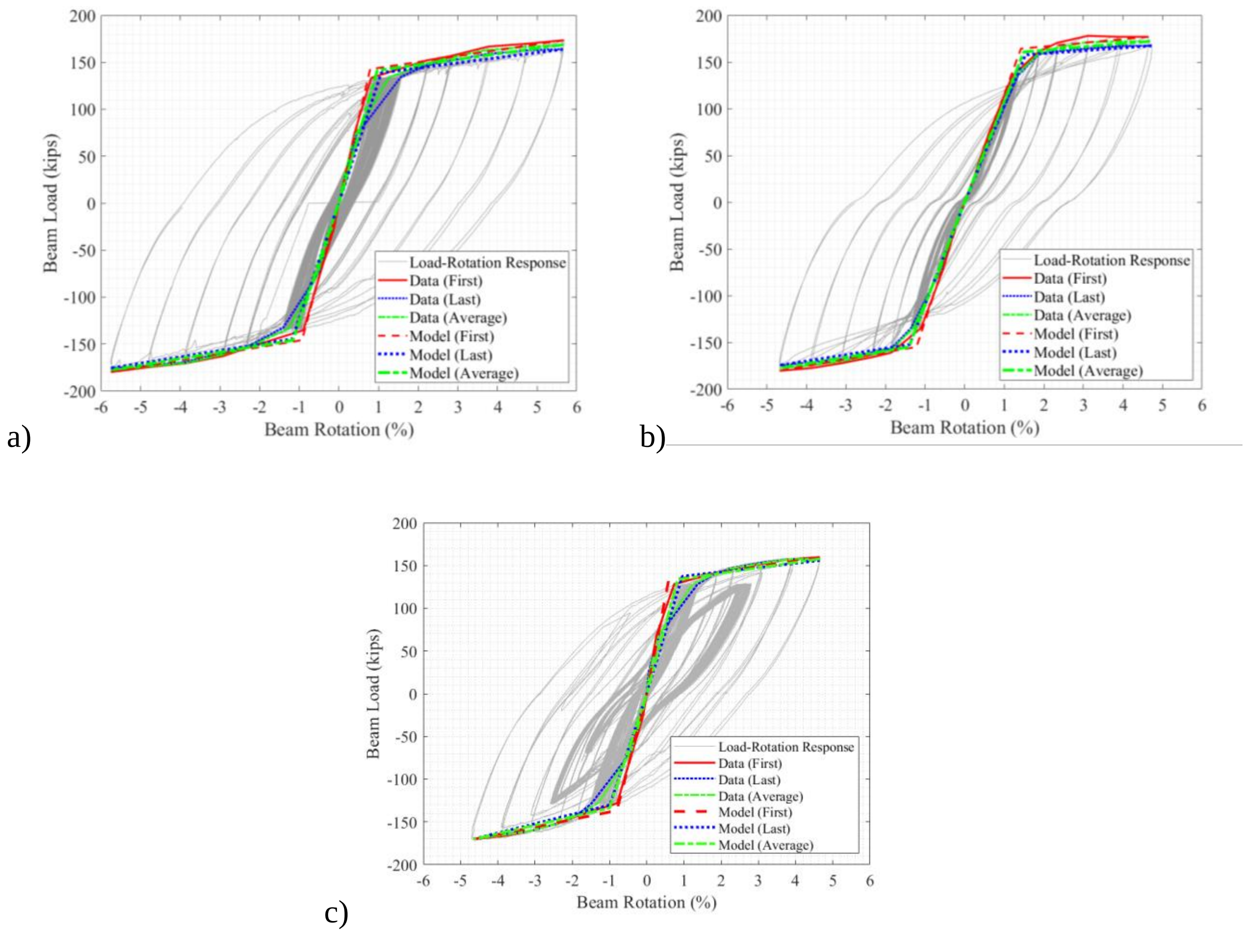

Figure 5.2. Backbone Models Fit to Test Data for a) SRC-W1, b) SRC-W2, and c) SRC-W3

Table 5.2. Load-Rotation Coordinates of Test Data Backbones

SRC-W1						SRC-W2						SRC-W3					
First		Last		Average		First		Last		Average		First		Last		Average	
Rot. (%)	Load (Kips)	Rot. (%)	Load (Kips)	Rot. (%)	Load (Kips)	Rot. (%)	Load (Kips)	Rot. (%)	Load (Kips)	Rot. (%)	Load (Kips)	Rot. (%)	Load (Kips)	Rot. (%)	Load (Kips)	Rot. (%)	Load (Kips)
5.68	173.5	5.65	164	5.67	168.8	4.65	177.0	4.73	167.4	4.69	172.2	4.65	159.7	4.65	155.8	4.65	157.7
4.74	169.8	4.71	162.7	4.67	166.2	3.89	177.0	3.94	167	3.84	172	3.88	157.5	3.88	157.5	3.88	157.5
3.77	166.7	3.76	158.9	3.7	162.8	3.12	178.0	3.11	164.4	3.07	171.2	3.10	151.9	3.10	153.3	3.10	152.6
2.8	156.6	2.81	152	2.72	154.1	2.33	170.5	2.33	161.4	2.31	164.9	2.32	146.2	2.33	147.3	2.33	146.8
2.21	152	2.21	146.7	2.19	148.4	1.86	160.5	1.87	158.6	1.85	158.2	1.86	141.5	1.86	141.0	1.86	140.9
0.82	133.4	1.57	134.6	1.27	134	1.21	135.7	1.35	135.5	1.31	135.3	0.74	128.2	1.37	128.2	1.24	128.2
0.38	72.5	0.42	71.1	0.39	70.8	0.60	72.2	0.69	72.3	0.64	72.3	0.26	68.3	0.33	68.5	0.32	68.5
0.15	27.5	0.14	27.3	0.13	27.3	0.24	27.1	0.26	27.1	0.25	27.1	0.09	25.8	0.05	25.6	0.08	25.8
0	0	0	0	0	0	0	0	0	0	0	0	0	0	0	0	0	0
-0.12	-26.7	-0.17	-26.7	-0.17	-26.7	-0.23	-27.1	-0.25	-27	-0.26	-27.1	-0.10	-25.8	-0.16	-25.6	-0.14	-25.7
-0.44	-71.3	-0.49	-72.7	-0.51	-72.5	-0.54	-72.1	-0.6	-72.2	-0.62	-72.2	-0.39	-68.3	-0.43	-68.9	-0.42	-68.5
-0.89	-135.2	-1.4	-132.4	-1.26	-133.3	-1.11	-134.8	-1.35	-134.5	-1.3	-134.6	-0.79	-128.1	-1.48	-128.5	-1.29	-127.5
-2.32	-154.2	-2.3	-152.7	-2.3	-153.6	-1.86	-161.1	-1.86	-156.6	-1.85	-158.2	-1.84	-142.8	-1.84	-141.0	-1.85	-141.9
-2.91	-162.7	-2.9	-159.5	-2.9	-160.9	-2.32	-165.7	-2.32	-160.2	-2.31	-162.9	-2.33	-151.0	-2.32	-151.2	-2.33	-151.2
-3.87	-170.5	-3.92	-169.6	-3.84	-170.1	-3.12	-172.3	-3.11	-167.8	-3.08	-170	-3.10	-160.3	-3.10	-160.2	-3.10	-160.2
-4.80	-174.7	-4.82	-172.8	-4.74	-173.7	-3.87	-177.4	-3.89	-171.3	-3.88	-174.4	-3.88	-166.6	-3.87	-164.9	-3.88	-165.4
-5.75	-179.8	-5.75	-175.6	-5.75	-177.7	-4.68	-180.4	-4.68	-174.6	-4.68	-177.5	-4.65	-170.3	-4.65	-170.0	-4.65	-170.2

Table 5.3. Load-Rotation Coordinates of Bilinear Backbone Models

	SRC-W1		**SRC-W2**		**SRC-W3**	
	Rotation (%)	**Load (Kips)**	**Rotation (%)**	**Load (Kips)**	**Rotation (%)**	**Load (Kips)**
First	5.68	173.5	4.65	177.0	4.65	159.7
	0.79	142.7	1.42	164.3	0.59	132.4
	0.00	0.0	0.00	0.0	0.00	0.0
	-0.93	-145.8	-1.22	-154.9	-0.80	-136.7
	-5.75	-179.8	-4.68	-180.4	-4.65	-170.3
Last	5.65	164.0	4.73	167.4	4.65	155.8
	1.07	138.7	1.54	157.7	0.96	137.3
	0.00	0.0	0.00	0.0	0.00	0.0
	-1.18	-144.5	-1.39	-152.2	-0.99	-130.1
	-5.75	-175.6	-4.68	-174.6	-4.65	-170.0
Average	5.67	168.8	4.69	172.2	4.65	157.7
	0.97	141.4	1.49	160.8	0.83	133.5
	0.00	0.0	0.00	0.0	0.00	0.0
	-1.16	-145.9	-1.41	-155.0	-1.00	-133.9
	-5.75	-177.7	-4.68	-177.5	-4.65	-170.2

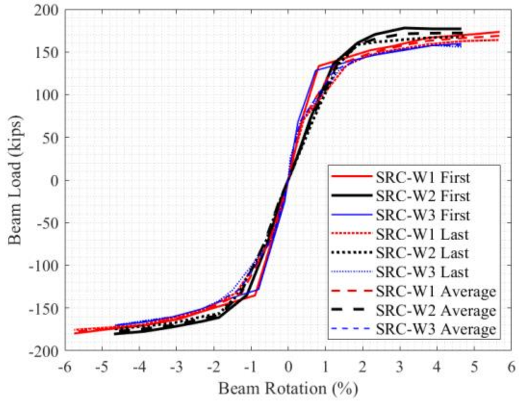

a)

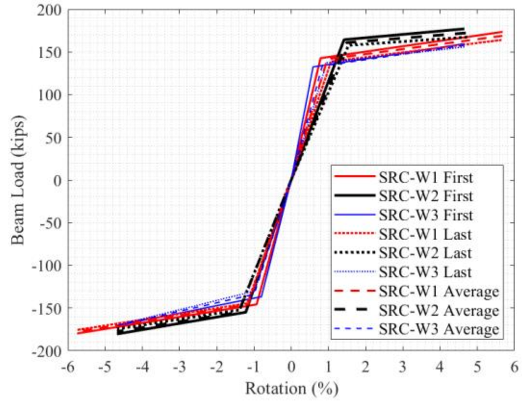

b)

Figure 5.3. Backbone Models using a) Data at Cycle Peaks, b) Bilinear Fit

Table 5.4. Strength and Plastic Deformation of Bilinear Backbone Models

Test Name	$V_{y,test}$ / $V@M_y$		V_{max} / $V@M_{pbe}$		$\theta_{plastic}$ (%)	
	(+)	(-)	(+)	(-)	(+)	(-)
SRC-W1	0.94	0.96	0.97	1.00	4.89	4.82
SRC-W2	1.07	1.01	0.98	1.00	3.23	3.46
SRC-W3	0.91	0.94	0.94	1.00	4.06	3.85

6. Summary and Conclusions

Four steel reinforced concrete (SRC) coupling beams, SRC-W1, SRC-W2, SRC-W3, and SRC-W4 were tested quasi-statically under fully reversed cyclic wind demands. Each test specimen included two test beams and one wall, with the steel sections in the test beams embedded into opposite ends of the reinforced concrete structural wall. The beams were tested individually as cantilevers, with SRC-W1 tested prior to SRC-W2 in one wall and SRC-W3 tested prior to SRC-W4 in another wall. Passive axial compressive restraint was applied to each beam during testing. The beams and walls were designed in accordance with AISC 341-22 Section H5, with the exception of the wall longitudinal reinforcement crossing the embedment length for SRC-W3 and SRC-W4, which had 0.53 and 0.22, respectively, times the strength required, and, for SRC-W4, the lack of wall boundary transverse reinforcement at the embedment region. The walls had reinforcement detailing that was compliant with ACI 318-19 Section 18.10.6.5. The test beams were nominally identical, with the only test variable being the wall demand and quantity of wall reinforcement. During each test, the wall was subjected to constant axial gravity load and fully reversed-cyclic lateral load that was linearly proportional to the load in the test beam. The ratio of wall shear to beam shear was the same for all tests. The ratio of applied wall moment to beam shear was the same for SRC-W2, SRC-W3, and SRC-W4 and was larger for SRC-W1. The loading cycles applied to SRC-W1, SRC-W2, and SRC-W3 consisted of 250 cycles at $0.15M_{pbe}$, 500 cycles at $0.40M_{pbe}$, 75 cycles at $0.75M_{pbe}$, five cycles at $1.2\theta_y$, three cycles at $1.5\theta_y$, two cycles at $2.0\theta_y$, two cycles at $2.5\theta_y$, and one cycle at $3.0\theta_y$, followed by the same sequence in reverse, where θ_y was the yield rotation, and M_{pbe} was the expected flexural strength calculated using the plastic stress distribution or the strain compatibility method. The loading cycles applied to SRC-W4 consisted of 250 cycles at $0.15M_{pbe}$, 500 cycles at $0.40M_{pbe}$, and two cycles at 6.0% chord rotation, as $0.75M_{pbe}$ was not reached prior to reaching 6.0% chord rotation during the first excursion after 500 cycles at $0.40M_{pbe}$. Data were collected during the tests using measurements from LVDTs, strain gages, and load cells, as well as crack measurements and photos of damage.

Based on analysis of measured data, as well as analysis of results from previous tests, the following conclusions were reached on SRC coupling beams:

- It is recommended that nonlinear wind design of steel reinforced concrete (SRC) coupling beams follow the seismic provisions in AISC 341-22 Section H5, with exceptions noted in subsequent points. This study did not include testing on SRC coupling beams that were designed using provisions in AISC 341-22 Section H4 and tested to peak deformation demands more consistent with ordinary walls.
- Consistent with seismic behavior, damage to AISC 341-22 Section H5 compliant beams concentrates at the beam-wall interface for wind demand, with the crack width growing as deformation demand increases. For these beams, the majority of the coupling beam deformation was measured to occur at this location, and damage in the embedment region was limited to cracking.
- A minimum area of wall longitudinal reinforcement crossing the embedment length is prescribed in AISC 341-22 for seismic design. For cases in which an insufficient quantity of wall longitudinal reinforcement is provided, wall yielding can occur, with damage at the embedded connection. The quantity of reinforcement prescribed by AISC 341-22 Section H5 was determined to be overly conservative in some instances, based on test results for

SRC-W3. For SRC-W3, the wall demands were sufficiently low that a 47% reduction in the quantity of reinforcement determined from AISC 341-22 Section H5 resulted in favorable performance that was similar to SRC-W1 and SRC-W2, which had a quantity of wall reinforcement that satisfied the AISC 341-22 Section H5 provision. However, a 78% reduction in this quantity of reinforcement in combination with a lack of wall boundary transverse reinforcement for SRC-W4 resulted in unfavorable performance, even for relatively modest levels of applied wall demand. It is recommended that the quantity of wall longitudinal reinforcement crossing the embedment length prescribed by AISC 341-22 Section H5 be reduced by 50% for cases in which wall demands do not exceed that applied for SRC-W3. The peak wall moment and tensile strain demands for SRC-W3 were $0.29M_y$ and 0.00019 tensile strain in outermost reinforcement at the coupling beam mid-height and an average of $0.04M_y$ and -0.00001 tensile strain (0.00001 compressive strain) in outermost reinforcement over one story height, taken as half a story above and below the coupling beam mid-height. These demands were determined from moment-curvature analysis for the moment and axial load, with moment and axial load diagrams determined based on transfer of coupling beam moment and shear to the wall at mid-height of the coupling beam. The M_y indicated here was based on reaching 70 ksi, the expected yield strength of A615 Grade 60 reinforcement (PEER TBI, 2017), in the outermost longitudinal reinforcement.

- Minimal axial compressive force is needed in the coupling beam to reduce outward ratcheting and alter the post-yield stiffness in the load-deformation response. The measured axial load in the test beams did not exceed $0.015A_g f'_{c,test}$, where A_g is the gross area of the beam cross-section and $f'_{c,test}$ is the tested compressive strength of concrete. At this level of axial load, the effect of P-M interaction on beam strength was determined to be minimal. The increase in axial elongation with repeated loading cycles at a given increment was less for the tests in this study with axial restraint than for SRC1 and SRC2, tested by Motter et al (2017a), without axial restraint. The post-yield strength increase was larger for SRC-W1, SRC-W2, and SRC-W3 than for SRC1, which was the only test beam in that test program that was fully compliant with AISC 341-22 Section H5. This was likely due to improved concrete contact in compression for the case of reduced axial elongation.

- Stiffness for the first cycle at $0.75M_{pbe}$ was examined using the results from SRC-W1, SRC-W2, and SRC-W3 from this study and three beams from other studies. The difference between stiffness in the positive and negative direction was more significant for larger cyclic wall demands, with higher stiffness in the positive direction due to wall demands producing compression at the embedment region. The average of the positive and negative stiffness was larger for walls with higher compression force in the wall on the positive excursion.
- Stiffness degradation in SRC coupling beams subjected to repeating loading cycles is significant. This was particularly true for repeated loading cycles at $0.75M_{pbe}$ prior to yielding. The ratio of stiffness on the 75th cycle to stiffness on the first cycle was 0.49 in the positive and 0.68 in the negative for SRC-W1, 0.90 in the positive and 0.81 in the negative for SRC-W2, and 0.54 in the positive and 0.53 in the negative for SRC-W3. Abdullah et al (2020) tested an SRC coupling beam embedded into concrete blocks subjected to constant compression, and these ratios were 0.63 and 0.64 for the two loading directions. SRC-W1 had larger wall demands than SRC-W2 with the same quantity of wall longitudinal reinforcement crossing the embedment, and SRC-W3 had the same wall

demands as SRC-W2 with less wall longitudinal reinforcement crossing the embedment. A higher level of wall compression relative to the quantity of wall longitudinal reinforcement, even if cyclic compression, may be associated with a higher level of stiffness degradation, given that stiffness degradation for SRC-W2 was less than the other tests at this loading level. Less stiffness degradation of the beam may correspond to more stiffness degradation in the wall, as the stiffness degradation in the wall at this loading level was larger for SRC-W2 than SRC-W1 and SRC-W3, with the level of stiffness degradation in the beam for SRC-W2 comparable to that in the wall during testing of SRC-W1. Additional test data are needed to further examine these items. The ratio of the average stiffness for the 75 cycles at $0.75M_{pbe}$ to the average stiffness for the first three of these cycles, which is more reflective of a seismic testing protocol, averaged 0.74 for SRC-W1, SRC-W2, and SRC-W3. It is recommended that the effective stiffness for nonlinear wind design be 75% of that prescribed in AISC 341-22 for seismic design.

- The yield rotation, θ_y, for the test beams was larger than that of previous seismic tests, although this was dependent on the definition of yield rotation. For the test beams, θ_y was determined during testing. During the first positive excursion to $1.2\theta_y$, the measured chord rotation at $0.75M_{pbe}$ was multiplied by $M_y/(0.75M_{pbe})$ to determine θ_y, where M_y was the moment at which the tension flange fully yields (i.e., the strain on the inner face of the tension flange is equal to the yield strain), computed from moment-curvature using the same material properties used for computation of M_{pbe}. For this definition of θ_y, the cyclic stiffness degradation during the first batch of 75 cycles at $0.75M_{pbe}$ significantly increased θ_y relative to previous seismic tests.

- Despite the significant stiffness degradation for repeated loading cycles at a given increment, SRC coupling beams can reach advanced levels of deformation demand under wind demands without significant strength degradation of initial cycles at new peak deformation demands or significant pinching in the load-deformation response. Peak deformation demand was 5.70% for SRC-W1 and 4.65% for SRC-W2 and SRC-W3, with favorable performance observed. Strength degradation of initial cycles at new peak deformation demands was not observed in the tests, with the peak measured load in each test attained on the first loading cycle to the peak deformation level. Similar to seismic design, a specified deformation capacity limit on the coupling beam is likely unnecessary for nonlinear wind design. However, based on the available data, the use of a deformation capacity limit of 6.0% chord rotation could be considered, based on modest extrapolation of data for SRC-W1.
- The ASCE/SEI Prestandard for Performance-Based Wind Design specifies the formulation of nonlinear models to capture structural response. Backbone models that represent load-deformation response of structural components are typically used for this purpose. For SRC coupling beams in which cyclic stiffness degradation for repeated cycles at a given increment is not explicitly modeled, it is recommended to use a backbone model based on average values of all cycles at each increment, as this would lead to equal area under the curve for the backbone model and test data. Backbone models for the four tests are provided in Section 5.2. A bilinear backbone model for nonlinear wind design was suggested that uses an effective stiffness of 75% of that prescribed in AISC 341-22, a computed yield moment from moment-curvature, a computed expected strength from AISC 341-22, and a post-yield slope based on 4.0% chord rotation from yield to expected strength.

References

Abdullah, S., Aswegan, K., Jaberansari, S., Klemencic, R., and Wallace, J. (2020). “Performance of Reinforced Concrete Coupling Beams Subjected to Simulated Wind Loading.” ACI Structural Journal, 117(3): 283-295.

ACI (American Concrete Institute). (2019). “Building code requirements for structural concrete.” ACI 318-19, Farmington Hills, MI.

ACI 374.3R-16 (2016). “Guide to Nonlinear Modeling Parameters for Earthquake-Resistant Structures”. American Concrete Institute, Farmington Hills, MI.

AISC. (2022). “Seismic provisions for structural steel buildings.” ANSI/AISC 341-22, Chicago, IL.

AISC. (2022). “Specification for structural steel buildings.” ANSI/AISC 360-22, Chicago, IL.

ASCE/SEI. (2016). “Minimum design loads for buildings and other structures.” ASCE/SEI Standard 7-16, Reston, VA.

ASCE/SEI (2019). “Prestandard for performance-based wind design.” American Society of Civil Engineers, Reston, VA.

ASTM C31/C31M-22. Standard Practice for Making and Curing Concrete Test Specimens in the Field. American Society of Testing and Materials, West Conshohocken, PA.

Barbachyn, S.M., Kurama, Y.C., and Novak, L.C. (2012). "Analytical Evaluation of Diagonally Reinforced Concrete Coupling Beams under Lateral Loads." ACI Structural Journal, 109(4): 497-507.

Gong, B. and Shahrooz, B. M. (2001a). "Concrete-steel composite coupling beams. I: Component testing." J. Struct. Eng., 10.1061/(ASCE) 0733-9445(2001)127:6(625), 625–631.

Gong, B. and Shahrooz, B. M. (2001b). "Concrete-steel composite coupling beams. II: Subassembly testing and design verification." J. Struct. Eng., 10.1061/(ASCE)0733-9445(2001)127:6(632), 632–638.

Harries, K.A., Mitchell, D., Cook, W.D., and Redwood, R.G. (1993). "Seismic Response of Steel Beams Coupling Concrete Walls." Journal of Structural Engineering. 119(12), 3611-3629.

Harries, K.A., Mitchell, D., Redwood, R.G., and Cook, W.D., (1997). "Seismic Design of Coupled Walls – A Case for Mixed Construction." Canadian Journal of Civil Engineering. 24, 448-459.

Hognestad, E. (1951). "A Study of Combined Bending and Axial Load in Reinforced Concrete Members." Bulletin 399, University of Illinois Engineering Experiment Station, Urbana, IL.

Marcakis, K. and Mitchell, D. (1980). Precast Concrete Connections with Embedded Steel Members. Precast Concrete Institute (PCI) Journal. 25:4, 88-116.

Massone, L. M. and Wallace, J. W. (2004). “Load-Deformation Response of Slender Reinforced Concrete Walls.” ACI Structural Journal, 101(1), 103–113.

Mattock, A.H. and Gaafar, G.H. (1982). Strength of Embedded Steel Sections as Brackets. ACI Journal. 79:9, 83-93.

Moehle, J., Bozorgnia, Y., Jayaram, N., Jones, P., Rahnama, M., Shome, N., Tuna, Z., Wallace, J., Yang, T., Zareian, F. (2011). Case Studies of the Seismic Performance of Tall Buildings Designed by Alternative Means. Task 12 Report for the Tall Buildings Initiative. PEER Report 2011/05, CSSC Report 11-02. Pacific Earthquake Engineering Research Center, Berkeley, CA.

Motter, C.J., Fields, D.C., Hooper, J.D., Klemencic, R., and Wallace, J.W. (2013). Design Recommendations for Steel Reinforced Concrete (SRC) Coupling Beams. UCLA SGEL Research Report 2013-06, University of California, Los Angeles.

Motter, C. J., Fields, D. C., Hooper, J. D., Klemencic, R., and Wallace, J.W. (2017a). “Steel-reinforced concrete coupling beams. I: Testing.” J. Struct. Eng., 143(3): 04016191.

Motter, C. J., Fields, D. C., Hooper, J. D., Klemencic, R., and Wallace, J.W. (2017b). "Steel reinforced concrete coupling beams. Part II: Modeling." J. Struct. Eng., 143(3): 04016192.

Paulay, T., and Binney J.R. (1974). "Diagonally Reinforced Coupling Beams of Shear Walls," ACI Special Publication 42-46, Farmington Hills, MI.

PEER (Pacific Earthquake Engineering Research Center) TBI (Tall Buildings Initiative). (2017). "Guidelines for performance-based seismic design of tall buildings." PEER Rep. 2017/06, Univ. of California, Berkeley, CA.

Shahrooz, B. M., Remetter, M. E., and Qin, F. (1993). "Seismic design and performance of composite coupled walls." J. Struct. Eng., 119(11), 3291–3309.

Nonlinear Wind Design of Steel Reinforced Concrete (SRC) Coupling Beams: Design Recommendations

Alexander Hill

Jacob Forbes

Christopher J. Motter

Washington State University

RGA #06-19

CHARLES PANKOW FOUNDATION

Building Innovation through Research

aci Foundation Building the Future

MAGNUSSON KLEMENCIC ASSOCIATES FOUNDATION

Acknowledgements

This research was supported by funding from the Charles Pankow Foundation, with co-funding from the American Concrete Institute (ACI) Foundation and the Magnusson Klemencic Associates (MKA) Foundation. The authors express their gratitude to the Charles Pankow Foundation, ACI Foundation, and MKA Foundation. Any opinions, findings, and conclusions expressed in this material are those of the authors and do not necessarily reflect those of the Charles Pankow Foundation, ACI Foundation, or MKA Foundation. Thanks are extended to the members of the industry advisory panel, comprised of Viral Patel, Rafael Sabelli, Gregory Deierlein, Mark Denavit, Brad Malmsten, John Peronto, Roberto Leon, Amit Varma, Ron Klemencic, David Fields, John Hooper, Kevin Aswegan, Sean Clifton, Juliana Rochester, Russell Larsen, Jordan Jarrett, and Bahram Shahrooz. This study on steel reinforced concrete (SRC) coupling beams was conducted in parallel with a companion study on steel coupling beams conducted at the University of Cincinnati. Sushil Kunwar, Bahram Shahrooz, and Patrick Fortney are thanked for collaborative discussions. This research is dedicated to the memory of Patrick J. Fortney.

Design Recommendations

The study conducted by Hill et al (2023) on nonlinear wind behavior of steel reinforced concrete (SRC) coupling beams included testing and analysis of data for four tests, namely SRC-W1, SRC-W2, SRC-W3, and SRC-W4. The formulation of design recommendations for nonlinear wind behavior of SRC coupling beams were included in Chapter 4 and Chapter 5 of Hill et al (2023). A summary is provided here:

- It is recommended that nonlinear wind design of steel reinforced concrete (SRC) coupling beams follow the seismic provisions in AISC 341-22 Section H5, with exceptions noted in subsequent points. The loading protocol used for the tests had a maximum displacement demand of three times the yield rotation. As described in Hill et al (2023), this level of displacement demand was deemed to be more consistent with the seismic design provisions in AISC 341-22 Section H5 for special walls than AISC 341-22 Section H4 for ordinary walls, such that the provisions in H5 were used for design of the test specimens. The exception was a reduction to the quantity of wall longitudinal reinforcement crossing the embedment, which was reduced for SRC-W3 and SRC-W4, and the quantity of wall boundary transverse reinforcement, which was reduced for SRC-W4, to examine potential instances in which these provisions may be overly conservative. The study conducted by Hill et al (2023) did not include testing on SRC coupling beams that were designed using provisions in AISC 341-22 Section H4 and tested to peak deformation demands more consistent with ordinary walls. The study conducted by Hill et al (2023) also did not include testing on the reduction of wall boundary transverse reinforcement relative to that required by AISC 341-22 Section H5 for SRC coupling beams that were otherwise compliant with provisions in AISC 341-22 Section H5.

- It is recommended that the quantity of wall longitudinal reinforcement crossing the embedment length prescribed by AISC 341-22 Section H4 and Section H5 be reduced by 50% for cases in which wall demands do not exceed that applied for SRC-W3. This recommendation applies for seismic and wind design, as favorable performance of SRC-W3 under wind demands to a peak deformation of 4.65% chord rotation was observed. The poor performance of SRC-W4 did not support further reduction to the quantity of wall reinforcement crossing the embedment length or reduction to the quantity of wall boundary transverse reinforcement required by AISC 341 Section H5. The peak wall moment and tensile strain demands for SRC-W3 were $0.29M_y$ and 0.00019 tensile strain in outermost reinforcement at the coupling beam mid-height and an average of $0.04M_y$ and -0.00001 tensile strain (0.00001 compressive strain) in outermost reinforcement over one story height, taken as half a story above and below the coupling beam mid-height. These demands were determined from moment-curvature analysis for the moment and axial load, with moment and axial load diagrams determined based on transfer of coupling beam moment and shear to the wall at mid-height of the coupling beam. The moment-curvature analysis used the Hognestad (1951) concrete model, with the compressive strength of concrete taken as the average tested value for SRC-W3, which was 4.67 ksi. The M_y indicated here was based on reaching 70 ksi, the expected yield strength of A615 Grade 60 reinforcement (PEER TBI, 2017), in the outermost longitudinal reinforcement. The tested yield strength of the reinforcement was not used here, since the demands were less than yielding.

- The load-deformation response of SRC coupling beams under nonlinear wind demand was found to be generally consistent with seismic demand, with the exception of stiffness degradation, which was substantially greater for wind demand due to the additional loading cycles. It is recommended that the effective stiffness for nonlinear wind design be 75% of that prescribed in AISC 341-22 for seismic design.
- A bilinear backbone model for nonlinear wind design is suggested, with effective stiffness of 75% of that prescribed in AISC 341-22 for seismic design, a yield force computed using moment-curvature analysis at full yielding of the tension flange using expected material properties, and a post-yield slope determined using Eq. (5-5) from Hill et al (2023). It is recommended that the hysteretic model be determined by modeling the tests with calibration to dissipated energy test data for SRC-W1, SRC-W2, and SRC-W3 provided in Figure 4.20 and Table 4.6 of Hill et al (2023).
- The peak deformation reached during testing was 5.7% chord rotation for SRC-W1. Aside from the difference in stiffness degradation, the load-deformation response of SRC-W1, SRC-W2, and SRC-W3 was similar to SRC1 tested by Motter et al (2017a) using a seismic protocol to deformation demands in excess of 12%. Strength degradation for initial loading cycles to larger increments was minimal-to-none in all of these tests. Similar to seismic design, a specified deformation capacity limit on the coupling beam is likely unnecessary for nonlinear wind design. However, based on the available data, the use of a deformation capacity limit of 6.0% chord rotation could be considered, based on modest extrapolation of data for SRC-W1. The peak deformation demands reached in the coupling beam are expected to be limited by the deformation demands reached in the walls.

References

AISC. (2022). “Seismic provisions for structural steel buildings.” ANSI/AISC 341-22, Chicago, IL.

Hill, A., Forbes, J., and Motter, C.J. (2023). “Nonlinear Wind Design of Steel Reinforced Concrete (SRC) Coupling Beams: Final Report.” Charles Pankow Foundation, McLean, VA.

Hognestad, E. (1951). “A Study of Combined Bending and Axial Load in Reinforced Concrete Members.” Bulletin 399, University of Illinois Engineering Experiment Station, Urbana, IL.

Motter, C. J., Fields, D. C., Hooper, J. D., Klemencic, R., and Wallace, J.W. (2017a). “Steel-reinforced concrete coupling beams. I: Testing.” J. Struct. Eng., 143(3): 04016191.

PEER (Pacific Earthquake Engineering Research Center) TBI (Tall Buildings Initiative). (2017). “Guidelines for performance-based seismic design of tall buildings.” PEER Rep. 2017/06, Univ. of California, Berkeley, CA.